SAKARYA ÜNİVERSİTESİ

FEN BİLİMLERİ ENSTİTÜSÜ DERGİSİ

Sakarya University Journal of Science (SAUJS)

SAKARYA ÜNİVERSİTESİ

e-issn: 2147-835X

Volume: 29

Issue: 1

February 2025

VOLUME: 29 ISSUE: 1
E-ISSN 2147-835X

FEBRUARY 2025
https://dergipark.org.tr/tr/pub/saufenbilder

SAKARYA UNIVERSITY JOURNAL OF SCIENCE

SAKARYA
ÜNİVERSİTESİ

Section Editor (Civil Engineering)

Section Editor (Chemistry)

Section Editor (Biology)

Section Editor (Mathematics)

Section Editor (Computer Science and Engineering)

Muhammed Maruf Öztürk
Computer Science and Engineering
Süleyman Demirel University
Isparta - Türkiye
muhammedozturk@sdu.edu.tr

Mustafa Akpinar
Computer Science and Engineering
High Tech Collages
United Arab Emirates
mustafakpinar@gmail.com

Section Editor (Physics)

Ceren Tayran
Department Physics
Gazi University
Ankara - Türkiye
c.tayran@gazi.edu.tr

Section Editor (Industrial Engineering)

Feyza Gürbüz
Department Industrial Engineering
Erciyes University
Kayseri - Türkiye
feyza@erciyes.edu.tr

Mehmet Emin Aydın
Department Industrial Engineering
University of The West of England Bristol
England
mehmet.aydin@uwe.ac.uk,

Barış Yüce
Department Industrial Engineering
University of Exeter
United Kingdom
b.yuce@exeter.ac.uk

Benjamin Durakovic
Department Industrial Engineering
International University of Sarajevo
Bosnia and Herzegovina
bdurakovic@ius.edu.ba

Section Editor (Mechanical Engineering)

Elif Eker Kahveci
Department of Mechanical Engineering
Sakarya University
Sakarya - Türkiye
eeker@sakarya.edu.tr

Erman Aslan
Department of Mechanical Engineering
Kocaeli University
Kocaeli - Türkiye
erman.aslan@kocaeli.edu.tr

Abderrahmane Benbrik
Department of Mechanical Engineering
M'hamed Bougara University
Egypt
abderrahmane.benbrik@univ-boumerdes.dz

Ali Cemal Benim
Department of Mechanical Engineering
Düsseldorf University of Applied Sciences
Germany
alicemal@prof-benim.com

Shi-Chune Yao
Department of Mechanical Engineering
Carnegie Mellon University
USA
sy0d@andrew.cmu.edu

Section Editor (Environmental Sciences and Engineering)

Senay Çetin Doğruparmak
Department of Environmental Engineering
Kocaeli University
Kocaeli - Türkiye
senayc@kocaeli.edu.tr

Section Editor (Food Science)

Aslı Uçar
Department of Food Sciences
Ankara University
Ankara - Türkiye
aucar@ankara.edu.tr

Section Editor (Electrical and Electronics Engineering)

Francesco De Paulis
Department of Electrical and Electronics Engineering
L'Aquila University
Italy
francesco.depaulis@univaq.it

Rıfkı Terzioğlu
Department of Electrical and Electronics Engineering
Bolu Abant Izzet Baysal University
Bolu - Türkiye
rifkiterzioğlu@ibu.edu.tr

Section Editor (Architecture)

Section Editor (Materials Science)

English Language Editor

Editorial Assistant

Statistical Editor

Indexing

Contents

Research Article

Sakarya Üniversitesi Fen Bilimleri Dergisi
Sakarya University Journal of Science

ISSN : 2147-835X
Publisher : Sakarya University

Vol. 29, No. 1, 1-17, 2025
DOI: https://doi.org/10.16984/saufenbilder.1349956

Research Article

Offensive Language Detection in Turkish Language by Using NLP

Bekir Furkan Kesgin*, Rüştü Murat Demirer

Bahcesehir University, Faculty of Engineering, Department of Computer Engineering, Istanbul, Türkiye, furkan_bfk@hotmail.com, rustumurat.demirer@ou.bau.edu.tr
*Corresponding Author

ARTICLE INFO

Keywords:
Cyberhate
Social media
Natural language processing
Classification algorithms
Cyberbullying

Article History:
Received: 25.08.2023
Revised: 12.01.2025
Accepted: 12.01.2025
Online Available: 12.02.2025

ABSTRACT

The growing use of social media has increased online harassment, cyberhate, and the use of offensive language. This poses significant challenges for effectively detecting and addressing such issues. Natural Language Processing (NLP) has seen considerable advancements; however, automatically identifying offensive language remains a complex task due to the ambiguous and informal nature of user-generated content and the social context in which it occurs. In this thesis, our goal is to develop methods for automatic detection of offensive language in social media. Multiple classification algorithms, including Multinomial Naive Bayes, Gaussian Naive Bayes, SVM, Logistic Regression, and LSTM, are implemented and evaluated. Key measures including accuracy, F1 score, and AUC score are used to evaluate how well these algorithms work. Results show that the Random Forest Classifier obtains an AUC score of 0.65 and an accuracy of 0.82 without word2vec. On the other hand, LSTM demonstrates a competitive AUC score of 0.78 when compared to the Random Forest Classifier. These findings provide insights into the effectiveness of different algorithms for offensive language detection. The research contributes to the field by providing valuable tools and insights to enhance Turkish language processing and prioritize online safety, particularly in combating cyberbullying and fostering a tolerant online environment. The findings also pave the way for future research endeavors in natural language processing and have practical implications for protecting individuals and promoting a secure online space.

1. Introduction

The power of language has played a crucial role in human evolution, enabling communication, fostering development, and driving progress. One significant advancement in language processing is the Enigma technology, which emerged during World War II to decode enemy messages. Initially, there were concerns among computer scientists regarding the outcomes of natural language processing (NLP). Some researchers believed in the progress through statistics and probability, while others emphasized the importance of predefined rules for computers [1]

of expression but also reinforces prejudices, fosters discrimination, and incites violence. Many platforms have community standards and reporting mechanisms, but additional measures may be needed to ensure the safety and well-being of users [3].

Addressing hate speech poses challenges in languages other than English due to the lack of readily available data models. While English has been extensively researched and has abundant data, Turkish, for example, faces a scarcity of data. Creating data for Turkish is crucial to identify and minimize the psychological impacts of improper language, especially on young individuals [2].

The anonymity of cyberspace has allowed people to express themselves freely, but it has also led to the spread of hateful and discriminatory messages. Hate speech not only violates freedom

Cite as: B. F. Kesgin, R. M. Demirer (2025). Offensive Language Detection in Turkish Language by Using NLP, *Sakarya University Journal of Science*, 29(1), 1-17. https://doi.org/10.16984/saufenbilder.1349956

Hate speech can exacerbate mental health issues and pose risks to individuals who may be susceptible to negative actions. Identifying and removing hate speech is therefore vital for people's well-being [4].

With the increasing use of social media, cyberbullying has become a prominent issue.

However, research on cyberbullying in languages other than English, such as Turkish, is limited. This restriction hampers comprehensive studies and solutions for Turkish-speaking individuals.

While the right to free expression permits the use of abusive language on social media, this situation is untenable. Developing automated solutions is necessary to filter the growing amount of content and mitigate the negative consequences, especially for young users.

Language differences, such as the use of suffixes in Turkish and prefixes in English, have implications for word creation and meaning [5].

In summary, language plays a significant role in human progress, but challenges remain in addressing hate speech and cyberbullying. Further research, data availability, and automated solutions are needed to promote a safer and more inclusive online environment.

The research contributes to following items;

1. Collecting offensive words from the internet and processing input data for stemming, suffixes, censoring, and various options.
2. Collection of numerous data from famous internet websites by using the words that are generated.
3. Making encoding to make appropriate for deep learning models.
4. To classify items, GaussianNB, MultinomialNB, Logistic Regression, XGBClassifier, LSTM, SVC, etc. are used.
5. Results are shown by accuracy, f-1 score with confusion matrix on the offensive text of Turkish language.
6. This research helps Turkish language processing and help with making application who have kids. Because cyberbullying in the Turkish language is not good enough to detect it.

2. Neural Network Architectures Implemented in Natural Language Processing

Natural language processing may be defined as the modeling of rule-based human language and its transmission to a computer. It is a machine learning technique that can understand and comprehend human language. Artificial neural networks include NLP as a subclass. It provides us with a sophisticated language processing approach that blends machine learning with deep learning. Linguists put a lot of work into training models since natural language processing involves more than simply code and incorporates a lot of information about humans. It is one of the functions in the background of programs that may recognize real-world voice instructions and transform them to text.

As we looked at the encodings available in machine learning, we discovered that word2vec and one hot encoding were the best fit for our data set. According to Ma and Zhang (2015), utilizing Word2Vec on huge data is preferable due to performance and the utilization of NLP regions [6].

2.1. Encoding

In NLP, it is necessary to convert textual data into a numerical format for machine learning models to process it. This conversion process is called encoding and can be performed at either the word or character level. The encoding method used is important for effective data processing and analysis.

2.2. Word2Vec

Word2Vec works by extracting words from a phrase one at a time and assigning numbers to the most frequently used ones. It is an encoding strategy that establishes a context inside itself by examining the words to the right and left of the term where it is utilized semantically (Mikolov, T., Chen, K., Corrado, G. S., Dean, J., 2013). Figure 1 shows the semantic links between word pairs like king and queen or man and woman,

demonstrating Word2Vec's capacity to capture analogical relationships.

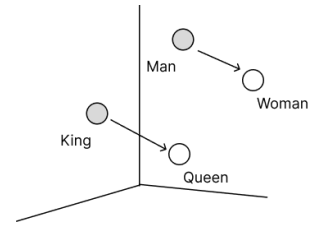

Figure 1. Word2vec example

In Word2Vec, the vector size determines the amount of features used to represent a word. As the number of features increases, so does the vector's size. A larger vector size allows for more complex word representations, but it requires more computer power and data. In contrast, a lower vector size produces more basic word representations with fewer information, but it requires less processing power and data.

Word2Vec is a technique used in natural language processing that represents words with numerical vectors. These vectors contain attributes that indicate the meaning of a word. Figure 2 shows how Word2Vec may capture geographical associations such as nations and capitals. These examples demonstrate how Word2Vec learns word associations and similarities, making it ideal for a wide range of NLP applications [7].

Figure 2. Example of word2vec

2.2.1. Index based encoding

Index-based encoding is an encoding method that helps to make categorical data more meaningful to a model. Unlike word2vec, it adds data to the vector space within itself, instead of defining the data within a one-dimensional object. It does this by encoding all values with values as 0 and 1. Index-based encoding is a method used in NLP to encode a word or text by connecting each word to a word index 6 in the dictionary. This approach is more memory-efficient and performs faster processing, depending on the size of the vocabulary.

In mathematical terms, index-based encoding considers the size of the dictionary as n and assigns a numerical index to each word, with the index number being a whole number between 0 and n-1. For instance, if a dictionary has 10,000 words, each word will be assigned a sequential index number ranging from 0 to 9,999.

Compared to other encoding methods like one-hot encoding or binary encoding, index-based encoding provides a smaller representation for word vectors. The data is pre-processed before beginning the real analysis in order to make algorithms easier to use and increase efficiency [8]. Figure 3 provides a practical example of index-based encoding, where each word in a dictionary is assigned a unique numerical index, demonstrating its memory-efficient representation.

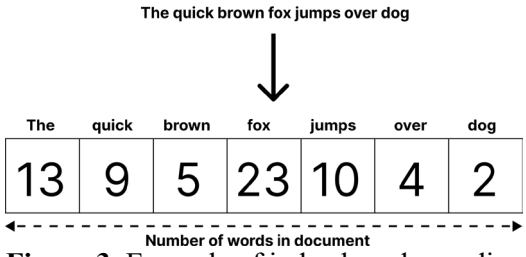

Figure 3. Example of index based encoding

Mathematic of Classifiers

The classifier can be represented mathematically as a formula in $\mathcal{D}$ space:
$S_n = \{(\mathbf{x}_1, y_1), (\mathbf{x}_2, y_2), \ldots, (\mathbf{x}_n, y_n)\}$ in $\mathcal{X} \times \mathcal{Y}$ space relevant to unsupervised learning approach. Because this distribution is unknown.
$\mathbf{x}$ are word2vec or index based encoded vectors. They are subspace of $\mathcal{X} \subseteq [0,1]^d$ and $\mathcal{Y} = \{y_1, y_2, y_3, \ldots\}$ label space we focus on binary classification ($\tau = 2$) to obtain classification error.

$$R_{\mathcal{D}}(h) = \Pr_{(\mathbf{x},y)\sim\mathcal{D}}[h(\mathbf{x}) \neq y]$$
$$= E_{(\mathbf{x},y)\sim\mathcal{D}}\left[\mathbb{I}[h(\mathbf{x}) \neq y]\right]$$
$$= E_{\mathbf{x}\sim\mathcal{D}_{\mathcal{X}}}\left[\sum_{j=1}^{\tau} \eta_j(\mathbf{x})\mathbb{I}[h(\mathbf{x}) \neq j]\right]$$

$$R^*_{\mathcal{D}} = E_{\mathbf{x}}\left[\min_{j\in[\tau]}\{1-\eta_j(\mathbf{x})\}\right] \text{ and } h^*_{\mathcal{D}}(\mathbf{x}) = \arg\max_{j\in[\tau]}\{\eta_j(\mathbf{x})\}$$

$R^*_{\mathcal{D}}$ is the minimum set of the classification. Where probability condition is

$\eta j(x) = Pr[y = j|x]$ for $j \in [\tau]$ of $y = j$ over offensive or non-offensive $\mathbf{x}$ with distribution of $\mathcal{D}$, and $\sum_{j=1}^{\tau=2} \eta_j(\mathbf{x}) = 1$ E is the expectation error in this formula and $E_{\mathbf{x}}$ this get the average of data inside the bracket. $R_{\mathcal{D}}(h)$ over whole training of this size. The function $\mathbb{I}[\cdot]$ is referred to as the indicator function, and it outputs 1 when the statement it evaluates will be true and 0 when it's false.

$h(\mathbf{x})$ is the hypothesis whether word offensive or non-offensive.

$\mathcal{D}$ is the training dataset which includes both offensive – non-offensive corpus data and unknown in practice [9].

2.3. Decision trees

Decision trees are a common technique in natural language processing (NLP) for tasks including sentiment analysis, text categorization, and named entity identification [10]. A decision tree is a type of model made up of leaf nodes, branches, and internal nodes. The internal nodes represent the feature tests, the branches of the results of the tests, and the leaf nodes the projected values or class labels. Figure 4 illustrates an example of a decision tree structure, showing how internal nodes split data based on feature tests, with branches leading to leaf nodes that represent class labels or outcomes.

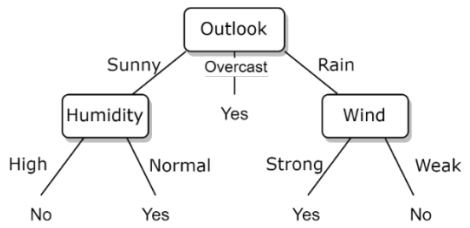

Figure 4. Example decision trees structure

Decision trees can be created using different methods to extract characteristics from the data. The algorithm then learns the most effective divisions on these features, aiming to maximize information gain or reduce entropy at each node. Nevertheless, decision trees have the tendency to overfit when dealing with intricate or noisy data. To tackle this problem, pruning techniques like reduced error pruning and cost-complexity pruning can be utilized. These methods aim to simplify the tree structure by eliminating superfluous nodes or branches that do not significantly contribute to the overall performance. Ensemble methods like random forests and gradient boosting can improve decision tree accuracy and robustness by combining multiple trees.

2.3.1. Random forest classifier

Using random forest in the context of big data provides convenience and consistency in estimating large datasets. It reduces the risk of overfitting and is less likely to suffer from this issue due to the combination of decision trees. However, it also comes with challenges, such as a complex structure formed by multiple decision trees and increased storage requirements.

Another machine learning model, the Extra Trees Classifier, offers faster performance and consumes fewer computational resources by randomly selecting features [11]. However, it performs worse than the Random Forest Classifier. Both models are ensemble methods that combine decision trees and utilize random feature selection, improving prediction accuracy. The Extra Trees Classifier is more efficient and requires fewer resources, while the Random Forest Classifier is more effective but takes longer to train.

Figure 5 shows an example of the Random Forest algorithm's structure and prediction process when applied to huge datasets, which helps to better understand its performance.

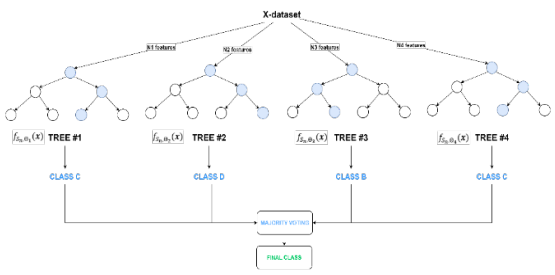

Figure 5. Example random forest classifier

The random forest classifier, $f_m(x)$, aggregates the outputs of m individual randomized trees, $f_{S_n,\Theta_1}(x)$, $f_{S_n,\Theta_2}(x)$, $f_{S_n,\Theta_3}(x)$, $\ldots . f_{S_n,\Theta_m}(x)$ by taking a majority vote. Random Forest Classifier is that;

$$f_m(\mathbf{x}) = \arg\max_{j\in[\tau]} \left\{ \sum_{i=1}^{m} \mathbb{I}\left[f_{S_n,\Theta_i}(\mathbf{x}) = j \right] \right\}$$

The function $f_m(\mathbf{x})$ selects the maximum value j among all possible values in the set $[\tau]$, based on the indicator function that evaluates the condition $f_{S_n,\Theta_i}(\mathbf{x}) = j$, where m and i range from 1 to m value and the ties are broken arbitrarily. The vectors Θ_1, Θ_2,..., Θ_m are randomly distributed and independent of each other, and they define the process of selecting the split leaves, dimensions, and positions when constructing randomized trees. In the following sections, the specific vectors, $\Theta_1, \Theta_2, \ldots \Theta_m$ will be defined for different random forests.

In simpler terms, this formula describes how the Random Forest classifier works by using multiple decision trees to classify data points and aggregating the predictions based on the most common result.

2.4. Support Vector Machine (SVM)

Support Vector Machine (SVM) is a supervised learning technique used for classification and regression [12]. SVM may be used to categorize text as relevant or irrelevant in the context of NLP text detection by considering particular properties.

The fundamental principle behind SVM is to find a decision boundary that maximizes the margin between two classes. The margin is the distance between the decision border and the support vectors, or nearest data points, for each class.

To determine this decision boundary, SVM utilizes an optimization problem-solving approach that aims to maximize the margin while adhering to specific constraints. SVM seeks to minimize the following objective function:

$$(1/2)\left|\left|w\right|\right|^2 + C\sum_i \xi_i$$

In this context, the weight vector is denoted as w, and ξ_i represents the slack variable associated with each data point. The regularization parameter C regulates the trade-off between maximizing the margin and reducing the classification error. The objective function seeks to find the optimal value of w and ξ_i that minimizes the classification error subject to the constraints:

$$y_i(w^T x_i + b) \geq 1 - \xi_i$$

$$\xi_i \geq 0$$

Here, y_i is label of the class for the i-th data point, and the bias term is b. Optimal value of w and b are found, the decision boundary is given by: $w^T x + b = 0$ The classification decision is then made based on the sign of $w^T x + b$ or $k(x, x') = \exp(-\|x - x'\|^2/2\sigma^2)$ may be used to map data into higher dimensions for non-linear classification tasks.

Figure 6 demonstrates an example of SVM decision boundaries, showcasing the optimal margin, support vectors, and separation of two classes in a two-dimensional space.

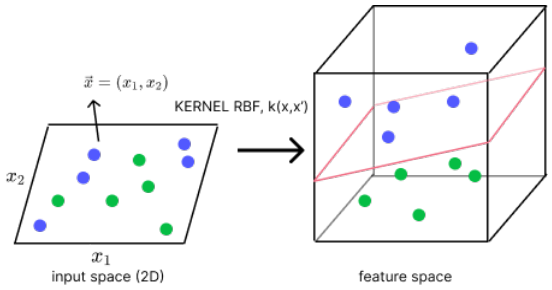

Figure 6. SVM example

2.4.1. Radial Basis Function (RBF)

The SVM-RBF algorithm is a machine learning technique that classifies data by mapping it to a feature space and measuring the distance between points in that space to represent the data in a higher dimensional space. In a Word2vec model with SVM-RBF, the first step is to learn word embeddings and then represent them in the vector space of the feature space. Subsequently, the SVM-RBF algorithm uses these representation of vector in the feature space to classify the data [13]. RBF function is like below;

$$k(x,y) = \exp\left(-\frac{\| x - y \|^2}{2\sigma^2}\right)$$

The performance of the SVM-RBF classifier under varying regularization parameters (C) is demonstrated in Figure 7.

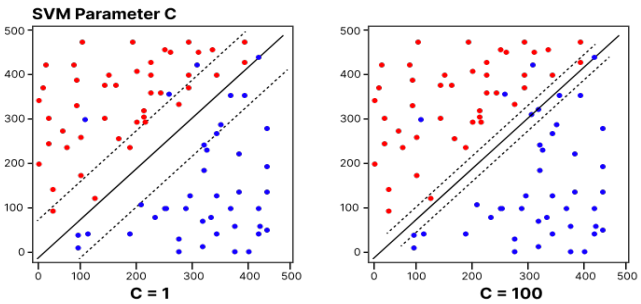

Figure 7. SVM Classifier with different C parameters

2.5. Long Short-Term Memory (LSTM)

LSTM networks are utilized in natural language processing (NLP) applications such as sentiment analysis, language modeling, and machine translation. By considering the prior context, language models may calculate the likelihood of a word sequence in the context of language modeling. Long short-term memory (LSTM) and word2vec have become a common pipeline for jobs in natural language processing [14]. The pipeline has several stages:

2.5.1. Data preprocessing

Preprocessing, lower casing, and punctuating the raw input data into training, validation, and testing sets.

2.5.2. Word embedding

The text is turned into numbers using word embeddings such as word2vec. This makes it easy to use with an LSTM.

2.5.3. LSTM network architecture

The next step is to design an LSTM network architecture, as illustrated in Figure 8, which depicts the integration of one or more LSTM layers, a dropout layer for regularization, and a final dense layer for output classification. This figure provides a schematic representation of how LSTM layers consume word embeddings as input, utilizing memory cells to capture context and long-term dependencies between words in the text. Additionally, the dropout layer, shown in the diagram, mitigates overfitting by selectively deactivating neurons during training. Finally, the dense layer translates the processed information into class probabilities, facilitating output classification.

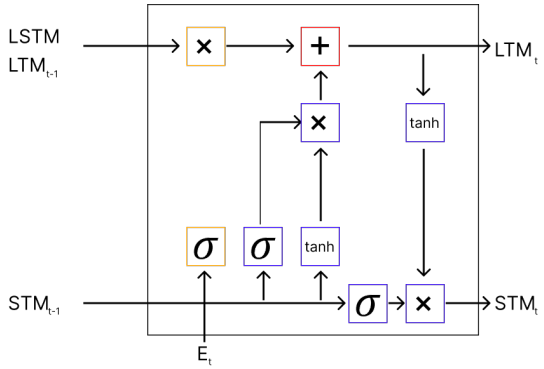

Figure 8. LSTM model working schema

2.5.4 Model training

The LSTM network is trained in cleaned, z-scored data. It has two types of cross-entropy loss functions, one for binary classification and one for multi-class classification.

2.5.5. Model evaluation

After training, the LSTM network is tested on the validation and test sets to see if it works on new data. Its performance is measured by metrics including accuracy, precision, recall, and F1-score.

2.5.6. Model deployment

LSTM can infer user-generated text inputs or real-time data streams after training. This pipeline uses word2vec and LSTM networks for tasks involving natural language, such as named entity identification, text categorization, and sentiment analysis. These components are instrumental in processing and analyzing textual data, facilitating the execution of these language-oriented tasks.

2.5.7. Optimization

Due to the complexity of these models and the requirement for processing huge volumes of textual input, LSTM models in NLP text

classification applications require optimization. By effectively updating the model's parameters and minimizing the loss function, optimization techniques enable the model to learn from the data and enhance its performance and accuracy. Additionally, by modifying the model's weights and biases during training to enhance the prediction performance of minority classes, optimization approaches can assist solve the problem of unbalanced datasets. To achieve high accuracy and performance in text classification tasks using LSTM models in NLP, optimizations are therefore essential [15].

LSTM has optimizations like below;

2.5.7.1. Gradient descent

It is used to minimize loss. Making good predictions is important, so we need to change model parameters. The most common way to do this is "mass gradient descent." This method uses the data set and updates the parameters by computing all the data at each step. This method is faster than other approaches but can produce poorer results if the data is not large enough.

2.5.7.2. Cross-entropy loss

Error measurement is done using the cross-entropy loss. For given review, its predicted sentiment is y and its actual sentiment is y. $L(y,\hat{y}) = -(y\log(\hat{y}) + (1-y)\log(1-\hat{y}))$ The goal of gradient descent is to minimize the average cross-entropy loss over the entire training set and the average loss over the training set as $J(\theta)$. Then the gradient descent rule for θ is:

$$\theta = \theta - \alpha\frac{\partial J(\theta)}{\partial\theta}$$

where α is the learning rate, which controls the step size of each update. The derivative of $J(\theta)$ with respect to θ can be computed using the chain rule of calculus:

$$\frac{\partial J(\theta)}{\partial\theta} = \frac{1}{N}\sum_{i=1}^{N}\frac{\partial L(y_i,\hat{y_i})}{\partial\hat{y_i}}\frac{\partial\hat{y_i}}{\partial\theta}$$

where N is the total number of training instances, and y_i and $\hat{y_i}$ are the actual and predicted sentiments for the i-th training example.

2.5.7.3. Stochastic Gradient Descent (SGD)

Stochastic Gradient Descent (SGD) is a widely using optimization algorithm for updating the parameters $\boldsymbol{\theta}$ of a Deep Neural Network (DNN). In contrast to regular gradient descent, which computes on the entire dataset, SGD randomly selects a small batch of the dataset and performs computations on it. This makes SGD more efficient and capable of producing similar performance as regular gradient descent when the learning rate $\boldsymbol{\eta}$ is low. In LSTM networks, SGD updates the weight vectors iteratively by calculating the gradient from a randomly selected sample.

The goal of SGD is to minimize the loss function $L(\theta, D)$ given the dataset D, where θ is the parameters set. At each step, SGD updates θ with one step towards the negative gradient as follows:

$\theta_{t+1} = \theta_t - \eta\nabla_\theta L(\theta_t, x_i, y_i)$, which is the update formula used by SGD to update the parameters θ at each step.

where $\nabla_\theta L(\theta_t, x_i, y_i)$ corresponds to the gradient of the loss function L with respect to the current parameters θ_t and the randomly selected sample (x_i, y_i).

2.5.7.4. Adaptive Moment Estimation (ADAM)

This can train an LSTM network with parameters $\boldsymbol{\theta}$ using the cross-entropy loss function. $\boldsymbol{\theta} = \boldsymbol{\theta} - \boldsymbol{\alpha}\frac{\hat{\mathbf{m}}}{\sqrt{\hat{\mathbf{v}}}+\boldsymbol{\epsilon}}$ where α,$\hat{m}$ and $\hat{v}$ are learning rate, first and second gradients, and small constant $\boldsymbol{\epsilon}$.

$\hat{m}t = \beta_1\hat{m}t - 1 + (1-\beta_1)g_t$
$\hat{v}t = \beta_2\hat{v}t - 1 + (1-\beta_2)g_t^2$

where t is the current time step, g_t is the loss's gradient with respect to parameters at time step t , and $\beta_1$and β_2 are the first and second moment exponential decay rates.

ADAM combines momentum and adaptive learning rate methods. The momentum term speeds up and stops oscillations, while the adaptive learning rate term adjusts the step size. We do this until the loss is minimal.

The best optimization strategy for LSTM training in NLP depends on the task and dataset. Try different strategies to find the one that works best.

2.6. Gausian naive bayes

Gaussian Naive Bayes is a popular classification technique that employs Bayes theorem to classify data. Bayes' theorem provides a framework for calculating the an event's likelihood depending on the available information about the conditions that influenced the occurrence of the event [16].

This theorem is applied in classification problems to identify the class to which a particular data point belongs. The "Naive" in Gaussian Naive Bayes refers to the assumption that each feature is not dependent on the other features. The "Gaussian" assumption is based on the idea that features follow a normal distribution, making the algorithm effective when data follows this pattern. The algorithm works by calculating the probability of each feature independently and then combining these probabilities to determine the data point's class. Gaussian Naive Bayes is a straightforward and powerful method for classifying data.

$$P(y|x_1, x_2, \dots, x_n) = \frac{P(y)\prod_{i=1}^{n} P(x_i|y)}{\sum_{y'} P(y')\prod_{i=1}^{n} P(x_i|y')}$$

In this equation:

y represents the class. $x_1, x_2, \dots, x_n$ represent the features. $P(y|x_1, x_2, \dots, x_n)$ represents the probability of the class given the features. $P(y)$ indicates the class's previous probability. $P(x_i|y)$ represents the conditional probability of feature x_i in a given class y where

$$f(x|\mu, \sigma^2) = \frac{1}{\sqrt{2\pi\sigma^2}} e^{-\frac{(x-\mu)^2}{2\sigma^2}}$$

x is the random variable. μ represents the mean, σ^2 represents the variance. In other words, the Gaussian probability density function is a way to calculate the probability of x value occurring in a normal distribution with a given mean and variance. It is used in various statistical analyses, including Gaussian Naive Bayes classification.

2.7. Multinominal naive bayes

Multinomial Naive Bayes algorithm is designed to be used in problems such as text classification [17]. This algorithm is used to determine which category a document belongs to. For example, classifying an email as spam or non-spam. This algorithm calculates the frequency of each word in the document and uses these frequencies to make probability calculations. By ignoring the dependencies between words and treating each word separately, the algorithm calculates the probability of each word and multiplies them to determine the class of the document.

$$P(c_j|d) = \frac{\prod_{i=1}^{n} P(t_i|c_j)^{x_i} P(c_j)}{\sum_{k=1}^{K} \prod_{i=1}^{n} P(t_i|c_k)^{x_i} P(c_k)}$$

c_j represents the document class. d represents the document. t_i represents word i. $P(c_j|d)$ represents the probability of document d being of class c_j.

$P(t_i|c_j)$ represents the probability of word t_i occurring in a document of class c_j. x_i represents the frequency of word t_i in the document.

n represents the total number of words. K represents the total number of classes which our case is 2.

This formula is used to determine the class probabilities by calculating the frequency of each word in the document and using these frequencies to make probability calculations, while ignoring dependencies between words and treating each word separately.

2.8. Logistic regression

According to KOLUKISA 2021, Logistic regression is a classification algorithm employed in machine learning. Its main objective is to estimate the probability of a binary outcome, such as a "yes" or "no" response, by considering

input variables. Logistic regression calculates the probability of an event by establishing the connection between a dependent variable and one or multiple independent variables. The logistic regression formula is utilized to model this relationship and make predictions.

$$p(y = 1|x) = 1/\left(1 + \exp\left(-(b0 + b1 * x1 + b2 * x2 + \cdots + bn * xn)\right)\right)$$

Here:

y represents the target variable or class. x represents the independent variables. $b0, b1, b2 \ldots bn$ represent the model parameters. The $\exp(bn * xn)$ function performs the mathematical operation e^x. In Logistic Regression, the correlation between the dependent and independent variables is computed to predict the probability of an event occurrence. This relationship is then utilized to make probabilistic predictions. This algorithm is commonly used in deep learning and was one of the classifiers analyzed in a study on Turkish character usage in text classification.

3. Results

Due to the increase in social media usage, the problem of cyberbullying has become more prominent, and there has been limited research on the issue in the Turkish language. While offensive language on social media is often defended as freedom of speech, this is not a tenable position. Moreover, manually filtering the growing amount of content on social media is becoming increasingly difficult, and developing automated solutions is becoming necessary. Additionally, it has been observed that Turkish uses suffixes rather than prefixes to create word meanings, which may suggest the importance of suffixes in Turkish compared to English.

We aimed to develop a text classification model to detect offensive language in Turkish text data, including posts from various forum sites, such as Twitter and Eksi Sozluk. We started by collecting a total of 11,253 posts and manually labeling them as offensive or non-offensive using a predefined list of offensive words. We then used index-based encoding and word2vec embedding to represent the text data numerically and fed the resulting features into several machine learning models, including LSTM, SVM, Random Forest Classifier, Extra Tree Classifier, Gaussian NB, Multinomial NB, and Logistic Regression. After evaluating the performance of these models. There are several ways to understand the performance of a model. These are confusion matrix, classification report, Receiver Operating Characteristic - ROC, accuracy.

3.1. Confusion matrix

A confusion matrix serves as an assessment tool for evaluating the effectiveness of a classification model. It accomplishes this by comparing the predicted classifications of the model with the actual classifications, enabling the determination of the number of correct and incorrect classifications. The confusion matrix is comprised of four fundamental terms, namely true positives, false positives, true negatives, and false negatives [18].

Table 1 illustrates an example of a confusion matrix, which is commonly used to evaluate the performance of a classification model. In this table, the rows represent the actual classifications, while the columns correspond to the model's predicted classifications. The terms True Positive (TP), False Positive (FP), True Negative (TN), and False Negative (FN) are organized within the matrix to demonstrate how the outcomes are categorized based on the model's predictions and the actual results. This structure provides valuable insights into the model's accuracy and areas where it might require improvement.

Table 1. Confusion matrix example

	Predicted Positive	Predicted Negative
True Positive	TP	FN
True Negative	FP	TN

Within this tabular representation, as outlined by Karimi (2021), the elements TP, FP, TN, and FN illustrate the correspondence between the predicted and actual classifications generated by the model. Specifically, TP denotes the count of true positive predictions, FP denotes the count of false positive predictions, TN denotes the count

of true negative predictions, and FN denotes the count of false negative predictions.

Sensitivity is the ratio of true positive (TP) examples to total positive (TP + FN) examples. Specificity is the ratio of true negative (TN) examples to total negative (TN + FP) examples. When the threshold changes, sensitivity and specificity rates change, and the ROC curve displays different values for these rates.

To gain insights into the performance of a classification model, the confusion matrix, as described by Karimi (2021), is employed to compute performance metrics including accuracy, precision, recall, and F1 score. These metrics serve the purpose of providing a comprehensive understanding of the classification model's performance.

3.2. Classification report

The classification report is a summary report that outlines the performance of a classification model. This report displays performance metrics such as accuracy, precision, recall, and F1 score for each class. These performance metrics are used to determine how well the model performed when classifying data [19].

In the classification report, accuracy represents the ratio of correctly classified examples by the model. Precision represents the ratio of correctly predicted positive examples for a given class. Recall represents the ratio of correctly predicted positive examples over all positive examples for a given class. F1 score represents the balance between precision and recall.

Macro average is the equal-weighted average of the performance metrics for each class. Weighted average is the weighted average of the performance metrics based on the proportion of class examples.

This classification report summarizes the performance of the model for each class and helps analyze the model's performance.

3.3. Receiver Operating Characteristic (ROC)

ROC is a curve and metric used to measure the performance of a classification model. The ROC curve visualizes the sensitivity and specificity rates provided by a model at different thresholds [14].

An ROC curve represents the performance of an ideal classification model, which is determined by how close the curve is to the top-left corner. A curve close to this area represents a model that provides high sensitivity and high specificity.
Additionally, the area under the ROC curve (AUC) is a metric used to measure the performance of the model. As the AUC value approaches 1, the model's performance is better. As the AUC value approaches 0.5, the model is randomly classifying examples.

3.4. Accuracy

Accuracy is a metric that shows the ratio of correctly classified examples by a classification model. The accuracy of a model is calculated by dividing the number of correctly classified examples by the total number of examples [20].

Accuracy rate is an important metric used to measure the performance of a model, but it is not sufficient on its own. Especially in imbalanced datasets, it can mislead the model's performance. For example, if there is a large imbalance between classes in a dataset and one class has much more examples, the model can give a high accuracy result without making correct classifications.
Therefore, other performance metrics should also be used in addition to accuracy. These metrics include confusion matrix, precision, recall, and F1 score, which indicate imbalances between classes and help to evaluate the performance of the model more accurately.

3.5. Model results

We implemented multiple algorithms to achieve the best results. Among the algorithms we tried are Gaussian Naive Bayes, Multinomial Naive Bayes, Logistic Regression, SVM, and LSTM. While obtaining these results, we tried to achieve

the best result by using different parameters for each algorithm.

When we look at the results, with word2Vec Gaussian Naïve bayes and SVM achive better performance. And for the random forest classifier, without word2vec gave us better result. Just after the results, a short summary will be shown in the table in the form of information.

3.5.1. Random forest classifier

When comparing the performance of different models, we evaluated their success based on the Area Under the Curve (AUC) score, a robust measure for assessing classification models. Among these, the random forest classifier stood out, delivering superior results. Specifically, we observed that employing a random forest classifier led to more accurate predictions and higher reliability compared to alternative models such as logistic regression, Gaussian Naive Bayes, SVM, and LSTM.

With an accuracy of 0.82, we surpassed the logistic regression, Gaussian Naive Bayes, SVM, and LSTM models, achieving the best accuracy. Figure 9 demonstrates the confusion matrix for the random forest classifier without the use of Word2Vec, providing insight into the distribution of true positives, false positives, true negatives, and false negatives. Additionally, Figure 10 illustrates the ROC curve for the random forest classifier without Word2Vec, showcasing its performance in terms of the true positive rate (sensitivity) and false positive rate.

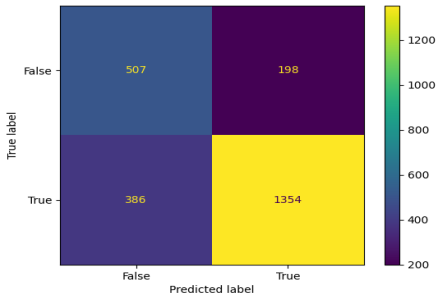

Figure 9. Confusion matrix for random forest classifier without word2vec

In the confusion matrix, there are TP = 507, FP = 198, FN = 386, and TN = 1354. Based on these values, the classifier correctly predicted the true positives (TP) and true negatives (TN). However, it also made some false positives (FP) and false negatives (FN), indicating that the classifier's performance is not ideal.

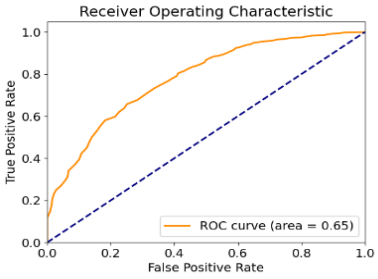

Figure 10. ROC Curve for Random Forest Classifier without Word2vec

Different metrics can be calculated based on this matrix to evaluate the performance of the classifier. For instance, metrics such as precision and recall can show how well the classifier detected true positives and false negatives. Other metrics such as F1-score balance precision and recall evaluating the overall performance of the classifier. The performance evaluation of a binary classifier involves utilizing the AUC (Area Under the Curve) score. This metric assesses the classifier's capability to differentiate between positive and negative classes. A score of 65 signifies that the classifier's performance surpasses that of random guessing.

When the worst result was considered, it was observed that it had an AUC score of 0.59. Regarding the accuracy value, a result of 0.58 was obtained. While it was initially assumed that utilizing Word2Vec would yield better results, it was observed that progressing through vectors led to improved outcomes in this case. Figure 11 presents the confusion matrix for the Random Forest Classifier with Word2Vec, showcasing the classification performance across true positives, false positives, true negatives, and false negatives. Meanwhile, Figure 12 illustrates the ROC curve for the Random Forest Classifier with Word2Vec, highlighting the trade-off between the true positive rate and false positive rate.

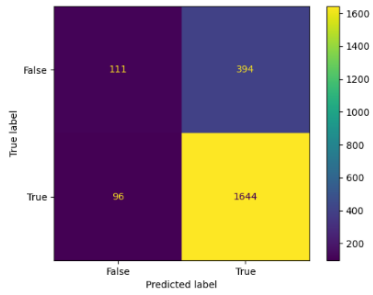

Figure 11. Confusion matrix for random forest classifier with Word2vec

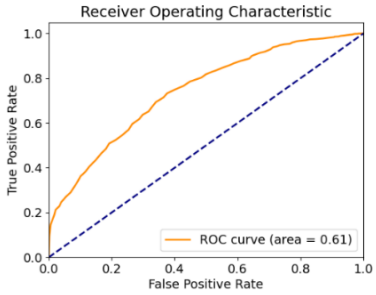

Figure 12. ROC Curve for random forest classifier with Word2vec

When we tested the random forest classifier model using word2vec, it was observed that there was low performance, although it did not differ much from its unused state, as seen in the figure. We can see in Figure 12 that the AUC score has decreased from 0.65 to 0.61.

3.5.2. Gaussian naïve bayes

If we examine a different algorithm, the Gaussian Naive Bayes, we observed that it achieved an accuracy value of 0.79. When we analyzed the AUC score, it resembled the performance of the Random Forest Classifier, yielding a value of 0.53. Notably, this result was obtained without utilizing Word2Vec in the Gaussian Naive Bayes model. Figure 13 illustrates the confusion matrix for Gaussian Naive Bayes without Word2Vec, detailing the distribution of true positives, false positives, true negatives, and false negatives. Additionally, Figure 14 depicts the ROC curve for Gaussian Naive Bayes without Word2Vec, visualizing the relationship between the true positive rate and false positive rate.

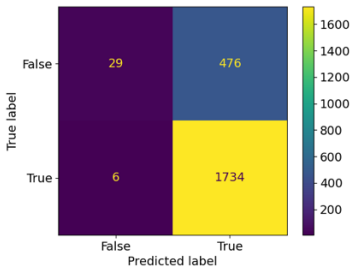

Figure 13. Confusion matrix for gaussian naive bayes without word2vec

Even when considering the highest performance achieved by the Gaussian Naive Bayes model, it fails to deliver the desired outcome or satisfactory results. However, in terms of accuracy, it achieved a respectable value of 0.79.

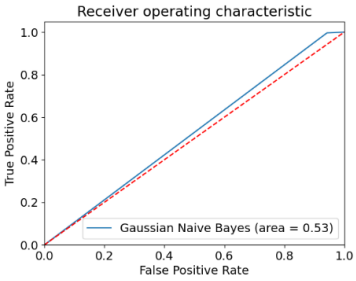

Figure 14. ROC Curve for gaussian naive bayes without word2vec

This result was obtained using Word2Vec as part of the feature representation. Figure 15 illustrates the confusion matrix for Gaussian Naive Bayes with Word2Vec, providing insights into the model's performance across true positives, false positives, true negatives, and false negatives. Moreover, Figure 16 shows the ROC curve for Gaussian Naive Bayes with Word2Vec, highlighting the balance between sensitivity and specificity.

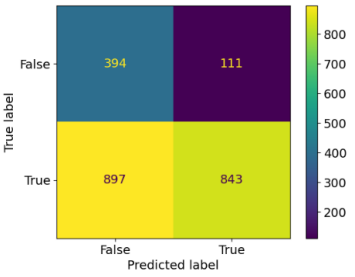

Figure 15. Confusion matrix for gaussian naive bayes with word2vec

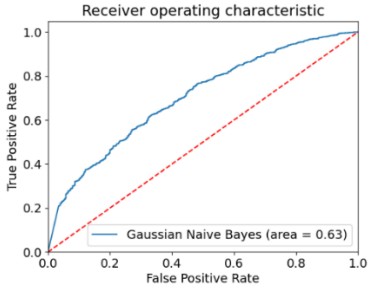

Figure 16. ROC for gaussian naive bayes with word2vec

If we use Word2Vec, it is observed that the AUC score improves significantly. However, the accuracy value drops to 0.55, indicating that the model struggles with correct classifications. Upon examining the confusion matrix in Figure 15, it becomes evident that the model produces a high number of false positives, which affects its overall performance and reliability.

3.5.3. Logistic regression

If we look at another model, namely logistic regression, it is observed that the accuracy value reaches 0.79 when Word2Vec is not used. However, this accuracy drops slightly to 0.77 when Word2Vec is applied. The AUC score and the corresponding confusion matrix for logistic regression without Word2Vec are depicted in Figure 17 and Figure 18, respectively.

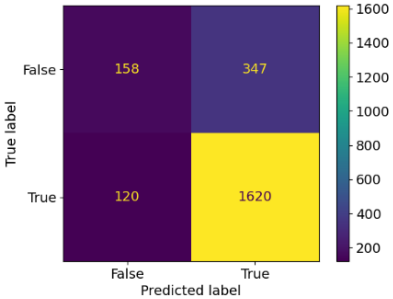

Figure 17. Confusion matrix for logistic regression without Word2vec

Figure 18. ROC for logistic regression without word2vec

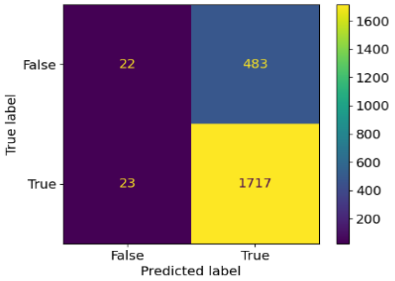

Figure 19. Confusion matrix for logistic regression with word2vec

Although the accuracy value has not changed significantly, it is observed that the number of lines predicted by the model has decreased. Similarly, when examining the ROC curve, a noticeable drop in the score is observed. Specifically, the value decreased from 0.62 to 0.52.

Figure 20. ROC for logistic regression with word2vec

While the use of Word2Vec can be important in certain scenarios, the tests conducted with logistic regression reveal that its impact is not particularly significant. In fact, in the worst-case scenario, the use of Word2Vec leads to a decline in accuracy. These observations are illustrated in Figure 19 and Figure 20, which show the confusion matrix and ROC curve for logistic regression with Word2Vec, respectively.

4.5.4. Support Vector Machine (SVM)

When examining the Support Vector Machine (SVM) algorithm, it is observed that there is an increase in the AUC score when Word2Vec is not used. Specifically, the AUC score, which was 0.62 without Word2Vec, decreased to 0.50 after incorporating Word2Vec. These results suggest that using Word2Vec negatively impacted the model's performance in this case. The confusion matrix and ROC curve for SVM without Word2Vec are shown in Figure 21 and Figure 22, respectively.

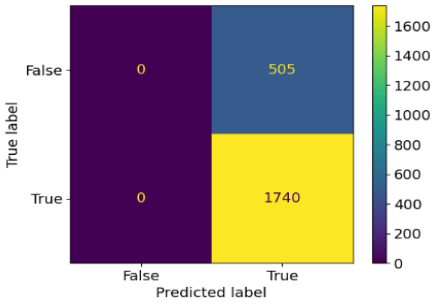

Figure 21. Confusion matrix for SVM without word2vec

Despite the seemingly high AUC score of the model, a closer examination of the confusion matrix reveals that the incorrect predictions are not truly incorrect.

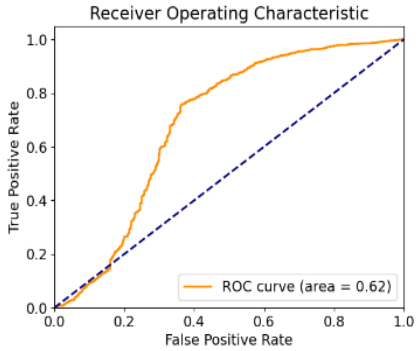

Figure 22. ROC for SVM without word2vec

However, the accuracy value is observed to be 0.77 when Word2Vec is not used. This result is depicted in Figure 23 and Figure 24.

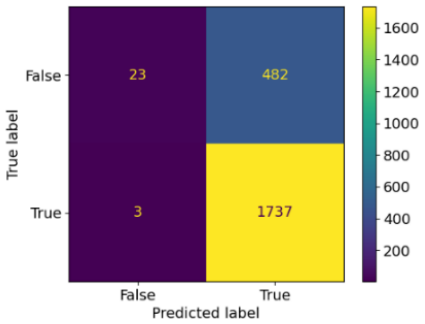

Figure 23. Confusion matrix for SVM with word2vec

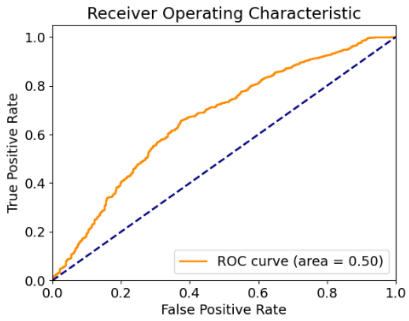

Figure 24. ROC for SVM with word2vec

When Word2Vec is utilized, the AUC score decreases, although the accuracy value remains the same as before. Upon examining the confusion matrix, it becomes evident that while there are a few misclassified instances, the overall number of misclassifications is minimal.

3.5.5. Long Short-Term Memory (LSTM)

When evaluating the performance of LSTM, a leading algorithm in artificial intelligence, its AUC score stands out, showcasing its ability to capture long-term dependencies and complex patterns in sequential data. However, despite this strength, LSTM's accuracy does not surpass that of the Random Forest model, indicating that while LSTM excels in probabilistic differentiation, it may be less consistent in making precise classifications.

As shown in Figure 25, the confusion matrix for the Support Vector Machine (SVM) without using Word2Vec embeddings provides a good classification result when compared to other models.

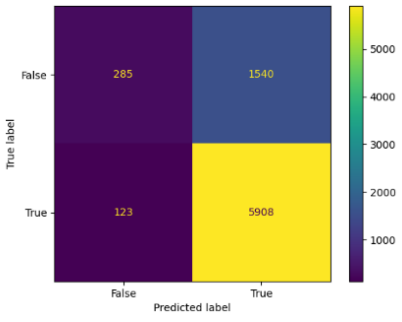

Figure 25. Confusion matrix for SVM without word2vec

Similarly, Figure 26 presents the ROC curve for SVM without Word2Vec, illustrating the model's performance.

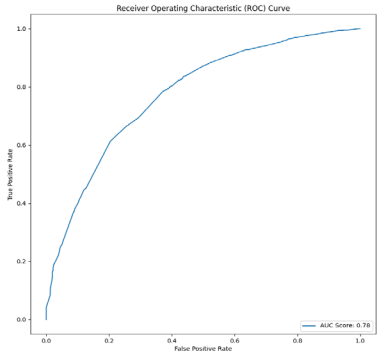

Figure 26. ROC for SVM without word2vec

On the LSTM model, when using only vectors without Word2Vec, the results are impressive, with an accuracy value of 0.78 and an AUC score of 0.79. This result is quite close to the performance of Random Forest. However, a closer look at the confusion matrix (as shown in Figure 25) reveals that while the results are similar, Random Forest achieves a slightly higher accuracy. On the other hand, when comparing AUC scores, Figure 26 clearly demonstrates that LSTM outperforms Random Forest, making it a better choice for distinguishing between classes.

4. Conclusion

In conclusion, this dissertation has conducted an extensive investigation into the identification and analysis of offensive and discriminatory language within the specific context of the Turkish language. Throughout this scholarly inquiry, the dissertation has emphasized the fundamental role of language in facilitating effective communication and its profound impact on human development. It has also underscored the urgent need to address the detrimental consequences of hate speech on individuals and society as a whole.

The study commenced by acknowledging the historical significance of natural language processing (NLP) during World War II, which laid the groundwork for subsequent advancements in this transformative technology. Furthermore, it has shed light on the limited availability of data for studying hate speech in the Turkish language compared to the extensive research conducted in English. This scarcity of data has highlighted the critical importance of generating relevant and contextually appropriate data within the Turkish linguistic domain, particularly in order to understand and mitigate the psychological impacts of inappropriate language use, especially among vulnerable populations such as children.

Moreover, the dissertation has argued that hate speech goes beyond mere violations of freedom of expression, as it has the potential to reinforce biases, perpetuate discrimination, and incite acts of violence. Despite the implementation of community standards and reporting mechanisms on digital platforms, hate speech continues to prevail, necessitating additional measures to ensure the safety and well-being of internet users. To address these challenges, the dissertation has proposed several valuable contributions, including the systematic collection of offensive language data from online sources, the utilization of preprocessing techniques such as stemming, suffix analysis, and censorship to optimize the input data, and the development and evaluation of deep learning models using comprehensive datasets from popular internet platforms. Various classification algorithms have been employed, and the results have been assessed using key performance metrics, such as accuracy, F-1 score, and confusion matrix, with a specific focus on offensive text in the Turkish language.

Through this research, significant insights and tools have been developed to enhance Turkish language processing and facilitate the creation of applications that prioritize child safety. Moreover, this investigation contributes to broader efforts aimed at combating prejudice, discrimination, and intolerance by enabling the detection and analysis of cyberbullying within the Turkish linguistic realm. Ultimately, this dissertation underscores the importance of addressing hate speech, particularly in the Turkish language, and establishes a solid foundation for future research endeavors and practical applications in the field of natural language processing. The ultimate goal remains the protection of individuals, the promotion of tolerance, and the establishment of a secure online environment for all users.

Article Information Form

Acknowledgments
Authors would like to thank Dr. Rüştü Murat Demirer for his contributions.

Funding
Authors has no received any financial support for the research, authorship or publication of this study.

Authors' Contribution
Authors contributed equally to the study.

The Declaration of Conflict of Interest/ Common Interest
No conflict of interest or common interest has been declared by authors.

The Declaration of Ethics Committee Approval
This study does not require ethics committee permission or any special permission.

The Declaration of Research and Publication Ethics
Authors of the paper declare that they comply with the scientific, ethical and quotation rules of SAUJS in all processes of the paper and that they do not make any falsification on the data collected. In addition, they declare that Sakarya University Journal of Science and its editorial board have no responsibility for any ethical violations that may be encountered, and that this study has not been evaluated in any academic publication environment other than Sakarya University Journal of Science.

References

[1] E. Adalı, "Natural Language Processing," Turkish Journal of Electrical Engineering & Computer Sciences, vol. 24, no. 2, pp. 1–17, 2016.

[2] S. Rosenthal, P. Atanasova, G. Karadzhov, M. Zampieri and P. Nakov, "SOLID: A Large-Scale Semi-Supervised Dataset for Offensive Language Identification," arXiv preprint arXiv:2004.14454, 2020.

[3] Ç. Çöltekin, "A Corpus of Turkish Offensive Language on Social Media," Proceedings of the 12th International Conference on Language Resources and Evaluation (LREC 2020), pp. 1–8, 2020.

[4] C. Casula, A. P. Aprosio, S. Menini and S. Tonelli, "FBK-DH at SemEval-2020 Task 12: Using Multi-channel BERT for Multilingual Offensive Language Detection," Proceedings of the 14th International Workshop on Semantic Evaluation (SemEval 2020), pp. 1–10, 2020.

[5] Ö. Anil and R. Yeniterzi, "SU-NLP at SemEval-2020 Task 12: Offensive Language Identification in Turkish Tweets," Proceedings of the 14th International Workshop on Semantic Evaluation (SemEval 2020), pp. 1–8, 2020.

[6] L. Ma, Y. Liu, X. Zhang, Y. Ye, Yin and B. F. G. Johnson, "Deep Learning in Remote Sensing Applications: A Meta-analysis and Review," ISPRS Journal of Photogrammetry and Remote Sensing, vol. 152, pp. 166–177, 2019.

[7] T. Mikolov, K. Chen, G. S. Corrado and J. Dean, "Efficient Estimation of Word Representations in Vector Space," arXiv preprint arXiv:1301.3781, 2013.

[8] K. Potdar, T. S. Pardawala and C. D. Pai, "A Comparative Study of Categorical Variable Encoding Techniques for Neural Network Classifiers," International Journal of Computer Applications, vol. 175, no. 4, pp. 7–9, 2017.

[9] W. Gao and Z. Zhou, "Towards Convergence Rate Analysis of Random Forests for Classification," Artificial Intelligence, vol. 313, p. 103788, 2020.

[10] O. C. Njoku, "Decision Trees and Their Application for Classification and Regression Problems," M.S. thesis,

Missouri State University, 2020. [Online]. Available: https://bearworks.missouristate.edu/theses/3406.

[11] E. K. Ampomah, Z. Qin and G. Nyame, "Evaluation of Tree-Based Ensemble Machine Learning Models in Predicting Stock Price Direction of Movement," Information, vol. 11, no. 6, p. 332, 2020.

[12] X. Lin, "Sentiment Analysis of E-commerce Customer Reviews Based on Natural Language Processing," Proceedings of the 2020 International Conference on Artificial Intelligence and Computer Engineering (ICAICE), pp. 1–5, 2020.

[13] V. Apostolidis-Afentoulis, "SVM Classification with Linear and RBF Kernels," ResearchGate, 2015.

[14] J. I. Razin, A. Karim, M. F. Mridha, S. M. R. Rifat and T. Alam, "A Long Short-Term Memory (LSTM) Model for Business Sentiment Analysis Based on Recurrent Neural Network," in Lecture Notes on Data Engineering and Communications Technologies, Springer, pp. 1–15, 2021.

[15] R. C. Staudemeyer and E. R. Morris, "Understanding LSTM: A Tutorial into Long Short-Term Memory Recurrent Neural Networks," ResearchGate, 2019.

[16] C. Naulak, "A Comparative Study of Naive Bayes Classifiers with Improved Technique on Text Classification," TechRxiv, 2022.

[17] A. A. Kolukisa, "Turkish Character Usage in Text Classification (JAIDA)," ResearchGate, 2021.

[18] Z. Karimi, "Confusion Matrix," ResearchGate, 2021. [Online]. Available: https://www.researchgate.net/publication/355096788_Confusion_Matrix.

[19] S. Akram, "CLASSIFICATION REPORT," ResearchGate, 2021. [Online]. Available: https://www.researchgate.net/publication/357974052_CLASSIFICATION_REPORT.

[20] Q. Kong, W. Wang, D. Zhang and W. Zhang, "Two Kinds of Average Approximation Accuracy," CAAI Transactions on Intelligence Technology, 2023.

Sakarya Üniversitesi Fen Bilimleri Dergisi
Sakarya University Journal of Science

ISSN : 2147-835X
Publisher : Sakarya University

Vol. 29, No. 1, 18-26, 2025
DOI: https://doi.org/10.16984/saufenbilder.1533782

Research Article

Comparison of Integral Equation Formulations for Stokesian Particulate Flow Simulations

Gökberk Kabacaoğlu

Bilkent University, Faculty of Engineering, Department of Mechanical Engineering, Ankara, Türkiye, gkabacaoglu@bilkent.edu.tr

ARTICLE INFO

Keywords:
Stokes Flow
Green's Function
Boundary Integral Equations
Suspensions
Stability

Article History:
Received: 15.08.2024
Revised: 16.12.2024
Accepted: 16.01.2025
Online Available: 12.02.2025

ABSTRACT

Particulate Stokesian flows describe the hydrodynamics of rigid or deformable particles within Stokes flows, where viscous forces dominate over inertial effects. These flows are characterized by highly nonlinear fluid-structure interactions, moving interfaces, and multiple spatial and temporal scales, making numerical simulations both complex and computationally expensive. Accurately capturing these interactions requires sophisticated numerical approaches. The boundary integral equation method (BIEM) is a powerful tool for modeling such flows, as it reduces computational complexity by limiting the discretization to the immersed particle boundaries rather than the entire flow domain. This efficiency makes BIEM particularly suitable for studying systems with many particles or complex boundary geometries. In this work, we explore two fundamental BIEM formulations for Stokesian flows involving rigid particles: the first-kind and second-kind integral equations. These formulations differ in their mathematical structure and computational properties, impacting their stability, accuracy, and overall performance. By comparing these two approaches, we aim to highlight their respective advantages and limitations, providing insights into their applicability to different particulate flow scenarios. This analysis contributes to the broader understanding of numerical methods for Stokesian flows, addressing challenges inherent to fluid-structure interactions and advancing computational techniques in this field.

1. Introduction

Stokesian particulate flows are the flows of a collection of rigid or deformable particles (e.g., drops, capsules, cells, slender bodies, and filaments, possibly elastic or filled by a fluid) that are suspended in a Newtonian fluid and the particle Reynolds number is vanishingly small [1-3]. The hydrodynamics of colloidal suspensions of passive particles is a well-established but still active area of research in soft condensed matter physics and chemical engineering. Recently, there has been growing interest in suspensions of active colloids, which display rich collective behaviors that are quite different from those of passive suspensions [4-7].

The number of computational methods for modeling active suspensions has been increasing, often building on well-established techniques used for passive suspensions in steady Stokes flow, which occurs at zero Reynolds number [8-10]. Since active particles often contain metallic components, they are typically much denser than the solvent, causing them to sediment towards the bottom wall. This necessitates addressing confinement and implementing nonperiodic boundary conditions in any simulation method aimed at experimentally relevant scenarios.

Additionally, because the collective motions observed in active suspensions involve large numbers of particles and hydrodynamic interactions among particles decay slowly with distance, it is essential to develop methods that can capture long-range hydrodynamic effects while still scaling to tens or hundreds of thousands of particles [11].

Cite as: G. Kabacaoğlu (2025). Comparison of Integral Equation Formulations for Stokesian Particulate Flow Simulations, *Sakarya University Journal of Science*, 29(1), 18-26. https://doi.org/10.16984/saufenbilder.1533782

A computational method for colloidal suspensions must incorporate two essential components: long-range hydrodynamic interactions and the correlated Brownian motion of the particles. When active and Brownian motion are not present, accurately describing the hydrodynamics of Stokesian suspensions involves solving mobility problems [12]. This requires calculating the linear and angular velocities of the particles in response to applied external forces and torques. For deterministic Stokes problems, the Boundary Integral Method (BIM) [13] is a highly developed technique that effectively manages complex particle shapes and ensures controlled accuracy, even in dense suspensions. In this approach, the steady Stokes equations are reformulated as an integral equation with unknown densities defined on the boundary, using either a first kind (single-layer densities) or second kind (double-layer densities) formulation, or a combination of both [14-16].

Particles with intricate geometries can be directly discretized using a surface mesh, and with an appropriate choice of surface quadrature, higher-order (or even spectral) accuracy can be attained. The main challenge lies in addressing the singularity of the Green's functions that arise in the boundary integral formulation [17]. Discretizing the boundary integral equation typically results in a dense linear system, necessitating the use of fast algorithms, such as the Fast Multipole Method (FMM) [14], to efficiently perform the dense matrix-vector product and achieve linear scaling. In this study, we aim at comparing the first kind formulation with the second kind formulations. One of such second kind formulations is Power & Miranda's formulation [18]. In addition to that, we suggest another symmetric formulation. The comparison is based on the stability and accuracy of the methods in two dimensions.

2. General Methods

Here we mostly follow the notation in [19]. We consider a suspension of M rigid bodies $\{\mathcal{B}\}_{p=1}^{M}$, with tracking points $\boldsymbol{q}_p$ and orientations θ_p; in compact form $\boldsymbol{x}_p = \{\boldsymbol{q}_p, \theta_p\}$. We denote the linear and angular velocity by $\boldsymbol{u}_p$ and ω_p, respectively. The force and the torque on the body are shown with $\boldsymbol{f}_p$ and τ_p. In compact notation, $\boldsymbol{F}_p = \{\boldsymbol{f}_p, \tau_p\}$ and $\boldsymbol{U}_p = \{\boldsymbol{u}_p, \omega_p\}$. Vectors without scripts refer to the composite vector formed by the variables of all the bodies, i.e., $\boldsymbol{U} = \{\boldsymbol{U}_p\}_{p=1}^{M}$. We define a block diagonal geometric operator, $\mathcal{K} = \{\mathcal{K}_p\}_{p=1}^{M}$, that transforms rigid body velocities into surface velocities

$$\mathcal{K}[\boldsymbol{U}](\boldsymbol{x}) = \boldsymbol{u}_p + \omega_p(\boldsymbol{x} - \boldsymbol{q}_p)^{\perp} \text{ for } \boldsymbol{x} \in \partial\boldsymbol{\mathcal{B}}_p \quad (1)$$

where $\boldsymbol{x}^{\perp} = (x_2, -x_1)$. The adjoint of $\mathcal{K}$ integrates the surface traction of the bodies and yields the total external force and torque on the bodies

$$\mathcal{K}^*\boldsymbol{\lambda} = \boldsymbol{F} = \left\{ \begin{bmatrix} \int \boldsymbol{\lambda}(\boldsymbol{x}) d\mathcal{B}_p \\ \int (\boldsymbol{x} - \boldsymbol{q})^{\perp} \cdot \boldsymbol{\lambda}(\boldsymbol{x}) d\mathcal{B}_p \end{bmatrix}_p \right\}_{p=1}^{M}. \quad (2)$$

The operators $\mathcal{K}$ and $\mathcal{K}^*$ are adjoint. For an arbitrary function defined on the surface of the bodies, $\boldsymbol{g}(\boldsymbol{x})$, and a collection of vectors defined on the bodies, $\boldsymbol{U}$, these operators satisfy

$$(\boldsymbol{g}, \mathcal{K}[\boldsymbol{U}]) = \int \boldsymbol{g}(\boldsymbol{x}) \cdot \mathcal{K}[\boldsymbol{U}](\boldsymbol{x})\, d\mathcal{B} = (\mathcal{K}^*\boldsymbol{g}) \cdot \boldsymbol{U}. \quad (3)$$

Flows of rigid bodies in the limit of vanishing Reynolds numbers (i.e., the ratio of inertial forces to the viscous forces is zero) are governed by the Stokes equations

$$-\nabla p + \eta \nabla^2 \boldsymbol{v} = 0 \quad (4)$$

$$\nabla \cdot \boldsymbol{v} = 0 \quad (5)$$

where p is fluid pressure, η is fluid viscosity and $\boldsymbol{v}$ is fluid velocity. The Green's functions for the Stokes equations are the so-called Stokeslet and stresslet. We consider a two-dimensional problem. The Stokeslet is

$$G_{ij}(\boldsymbol{x}, \boldsymbol{y}) = G_{ij}(\boldsymbol{r}) = \frac{1}{4\pi\eta}\left(-\delta_{ij} \log r + \frac{r_i r_j}{r^2}\right) \quad (6)$$

where $\boldsymbol{r} = \boldsymbol{x} - \boldsymbol{y}$ and $r = |\boldsymbol{r}|_2$. The stresslet is

$$T_{ijk}(\boldsymbol{x},\boldsymbol{y}) = T_{ijk}(\boldsymbol{r}) = -\frac{1}{\pi}\frac{r_i r_j r_k}{r^4} \tag{7}$$

The single layer, the double layer and the adjoint double layer operators acting on an arbitrary function $\boldsymbol{g}(\boldsymbol{x})$ on a body surface are defined as

$$(\mathcal{S}[\boldsymbol{g}])_i(\boldsymbol{x}) = \mathcal{S}_i[\boldsymbol{g}](\boldsymbol{x}) = \int G_{ij}(\boldsymbol{x},\boldsymbol{y}) g_j(\boldsymbol{y}) d\mathcal{B} \tag{8}$$

$$(\mathcal{D}[\boldsymbol{g}])_i(\boldsymbol{x}) = \mathcal{D}[\boldsymbol{g}](\boldsymbol{x}) = \int T_{ijk}(\boldsymbol{x},\boldsymbol{y}) n_k(\boldsymbol{y}) g_j(\boldsymbol{y}) d\mathcal{B} \tag{9}$$

$$(\mathcal{D}^*[\boldsymbol{g}])_i(\boldsymbol{x}) = \mathcal{D}_i^*[\boldsymbol{g}](\boldsymbol{x}) = -n_k(\boldsymbol{x}) \int T_{ijk}(\boldsymbol{x},\boldsymbol{y}) g_j(\boldsymbol{y}) d\mathcal{B} \tag{10}$$

where $\boldsymbol{n}$ is the surface normal pointing into the fluid. The last two double layer operators are adjoint, i.e., for any functions $\boldsymbol{g}$ and $\boldsymbol{h}$

$$(\boldsymbol{g}, \mathcal{D}[\boldsymbol{h}]) = (\mathcal{D}^*[\boldsymbol{g}], \boldsymbol{h}). \tag{11}$$

2.1. First kind formulation

Now, let us complete the continuous formulation for flows rigid particles. As mentioned above, the fluid flow is governed by the Stokes equations. The fluid satisfies the no-slip boundary condition on the bodies

$$\boldsymbol{v}(\boldsymbol{x}) = \mathcal{K}[\boldsymbol{U}](\boldsymbol{x}) \text{ for } \boldsymbol{x} \in \partial\mathcal{B} \tag{12}$$

If $-\boldsymbol{\lambda}$ is the fluid traction on the bodies, the force-torque balance leads to

$$\mathcal{K}^*\boldsymbol{\lambda} = \boldsymbol{F}. \tag{13}$$

Let $\boldsymbol{u}_\infty$ be the background flow moving the particles. With these equations, we can write the first-kind formulation that leads to a symmetric, positive-definite matrix in the linear system to be solved for the traction and rigid body velocity:

$$\begin{bmatrix} \mathcal{S} & -\mathcal{K} \\ -\mathcal{K}^* & 0 \end{bmatrix} \begin{bmatrix} \boldsymbol{\lambda} \\ \boldsymbol{U} \end{bmatrix} = \begin{bmatrix} \boldsymbol{u}_\infty \\ -\boldsymbol{F} \end{bmatrix}. \tag{14}$$

2.2. Second kind formulation

Second kind formulation involves the double layer integral which has better conditioning than the single layer integral. One alternative for the second kind formulation is as follows. According to Pozrikidis [13], the no-slip boundary condition can be written as

$$\frac{1}{2}\mathcal{K}[\boldsymbol{U}] + \mathcal{D}(\mathcal{K}[\boldsymbol{U}]) + \boldsymbol{u}_\infty = \mathcal{S}[\boldsymbol{\lambda}](\boldsymbol{x}) \tag{15}$$

The force-torque balance on the bodies can be written as

$$\frac{1}{2}\mathcal{K}^*\lambda + \mathcal{K}^*\mathcal{D}^*[\boldsymbol{\lambda}] = \boldsymbol{F}. \tag{16}$$

These equations form a linear system for the traction and rigid body velocities

$$\begin{bmatrix} \mathcal{S} & -\frac{1}{2}\mathcal{K} - \mathcal{D}\mathcal{K} \\ -\frac{1}{2}\mathcal{K}^* - \mathcal{K}^*\mathcal{D}^* & 0 \end{bmatrix} \begin{bmatrix} \boldsymbol{\lambda} \\ \boldsymbol{U} \end{bmatrix} = \begin{bmatrix} \boldsymbol{u}_\infty \\ -\boldsymbol{F} \end{bmatrix}. \tag{17}$$

The fact that this first alternative has the single layer operator on the diagonal, its conditioning is determined mostly by the single layer operator. Another alternative can be

$$\begin{bmatrix} \mathcal{S} + \frac{1}{\eta}(-I + \mathcal{D} + \mathcal{D}^*) & -\mathcal{K} \\ -\mathcal{K}^* & 0 \end{bmatrix} \begin{bmatrix} \boldsymbol{\lambda} \\ \boldsymbol{U} \end{bmatrix} = \begin{bmatrix} \boldsymbol{u}_\infty \\ -\boldsymbol{F} \end{bmatrix}. \tag{18}$$

The proof is as follows. An arbitrary flow on a surface $\mathcal{L}$ surrounding a particle $\mathcal{B}$ but far from the particle can be written as [20]

$$\boldsymbol{v}(\boldsymbol{x}) = \left(\mathcal{S} + \frac{1}{\eta}[\mathcal{D} + \mathcal{D}^*]\right)[\boldsymbol{\lambda}](\boldsymbol{x}) \text{ for } \boldsymbol{x} \in \mathcal{L}. \tag{19}$$

When the surface $\mathcal{L}$ approaches to the particle surface, we get

$$\boldsymbol{v}(\boldsymbol{x}) = \left(\mathcal{S} + \frac{1}{\eta}[-I + \mathcal{D}^{P.V.} + (\mathcal{D}^*)^{P.V.}]\right)[\boldsymbol{\lambda}](\boldsymbol{x}) \text{ for } \boldsymbol{x} \in \mathcal{B}. \tag{20}$$

The integrals are in the principal value sense.

2.3. Confined flow

In confined flows, the confining boundary induces flow on the particles. To maintain the symmetry properties of the linear system, we write an integral equation for the outer boundary using the same second kind formulation used for the rigid body. Let us introduce operators for the interaction between the outer boundary (denoted with subscript *o*) and the rigid body (denoted with subscript *b*). $\boldsymbol{S_o}$ and $\boldsymbol{S_b}$ denote the single

layer integral for self-interaction for the outer boundary and the rigid body, respectively. $\boldsymbol{\mathcal{S}_{ob}}$ is the single layer integral due to the sources on the body at the target points on the outer boundary ($\boldsymbol{\mathcal{S}_{bo}}$ is defined similarly). There are double layer integral counterparts of these integrals as well. We can write the following equations

- The no-slip condition on the rigid body is

$$\frac{\mathbf{1}}{\mathbf{2}}\boldsymbol{v}(\boldsymbol{x}) + \boldsymbol{\mathcal{D}}[\boldsymbol{v}](\boldsymbol{x}) = \boldsymbol{\mathcal{S}_b}[\boldsymbol{\lambda_b}](\boldsymbol{x}) + \boldsymbol{\mathcal{S}_{bo}}[\boldsymbol{\lambda_o}](\boldsymbol{x}) \quad (21)$$

- The balance of force and torque on the body is

$$\frac{\mathbf{1}}{\mathbf{2}}\boldsymbol{\mathcal{K}}^*\boldsymbol{\lambda_b} + \boldsymbol{\mathcal{K}}^*(\boldsymbol{\mathcal{D}}_{\boldsymbol{b}}^*[\boldsymbol{\lambda_b}] + \boldsymbol{\mathcal{D}}_{\boldsymbol{bo}}^*[\boldsymbol{\lambda_o}]) = \boldsymbol{F} \quad (22)$$

- The no-slip condition on the outer boundary is

$$\boldsymbol{\mathcal{S}_{ob}}[\boldsymbol{\lambda_b}](\boldsymbol{x}) - \boldsymbol{\mathcal{D}_{ob}}[\boldsymbol{\mathcal{K}U}](\boldsymbol{x}) + \boldsymbol{\mathcal{S}_o}[\boldsymbol{\lambda_o}](\boldsymbol{x}) = \mathbf{0} \quad (23)$$

With this formulation, the linear system becomes

$$\begin{bmatrix} \boldsymbol{\mathcal{S}_b} & -\frac{\mathbf{1}}{\mathbf{2}}\boldsymbol{\mathcal{K}} - \boldsymbol{\mathcal{D}_b}\boldsymbol{\mathcal{K}} & \boldsymbol{\mathcal{S}_{bo}} \\ -\frac{\mathbf{1}}{\mathbf{2}}\boldsymbol{\mathcal{K}}^* - \boldsymbol{\mathcal{K}}^*\boldsymbol{\mathcal{D}}_{\boldsymbol{b}}^* & \mathbf{0} & -\boldsymbol{\mathcal{K}}^*\boldsymbol{\mathcal{D}}_{\boldsymbol{bo}}^* \\ \boldsymbol{\mathcal{S}_{ob}} & -\boldsymbol{\mathcal{D}_{ob}}\boldsymbol{\mathcal{K}} & \boldsymbol{\mathcal{S}_o} \end{bmatrix} \begin{bmatrix} \boldsymbol{\lambda_b} \\ \boldsymbol{U} \\ \boldsymbol{\lambda_o} \end{bmatrix} = \begin{bmatrix} \boldsymbol{u}_\infty \\ -\boldsymbol{F} \\ \mathbf{0} \end{bmatrix}. \quad (24)$$

This is again a symmetric linear system. Note that we implemented the decoupled and coupled formulations which give similar results up to 1E-4 error.

2.4. Suspensions

When there are multiple bodies in a flow, they induce flow on to each other. That adjusts the net flow on the bodies. These changes can be seen below. Let's consider M rigid bodies in a free-space flow $\boldsymbol{u}_\infty(\boldsymbol{x})$. The no-slip condition on the p^{th} body is

$$\begin{aligned} \frac{1}{2}\mathcal{K}[\boldsymbol{U}_p](\boldsymbol{x}) + \mathcal{D}_p\left[\mathcal{K}[\boldsymbol{U}_p]\right](\boldsymbol{x}) &= \boldsymbol{u}_\infty(\boldsymbol{x}) + \mathcal{S}_p[\boldsymbol{\lambda}_p](\boldsymbol{x}) \\ &+ \sum_{\substack{q=1 \\ q\neq p}}^{M}\Big(\mathcal{S}_{pq}[\boldsymbol{\lambda}_q](\boldsymbol{x}) \\ &- \mathcal{D}_{pq}\left[\mathcal{K}[\boldsymbol{U}_q]\right](\boldsymbol{x})\Big). \end{aligned} \quad (25)$$

Here, the subscript *(pq)* denotes the hydrodynamic interaction between the p[th] and q[th] bodies. Then, the force-torque balance on the p[th] body is

$$\frac{1}{2}\mathcal{K}_p^*\boldsymbol{\lambda}_p + \mathcal{K}^*\left(\mathcal{D}_p^*[\boldsymbol{\lambda}_p] + \sum_{\substack{q=1 \\ q\neq p}}^{M}\mathcal{D}_{pq}^*[\boldsymbol{\lambda}_q]\right) = \boldsymbol{F}_p. \quad (26)$$

2.5. Discretization

Since the single layer integral has a logarithmic singularity, we use the hybrid Gauss-trapezoid quadrature rule [21]. The double layer integral has no singularity in two dimensions. Therefore, the trapezoid rule is used. Let H be a diagonal matrix storing the quadrature weights, i.e., $H = \mathrm{diag}(h)$. Hence, the single layer integral can be discretized as

$$\mathcal{S}\boldsymbol{\lambda} \approx SH\boldsymbol{\lambda} = S(H\boldsymbol{\lambda}) \quad (27)$$

Note that the operator SH is not symmetric ($(SH)^T = HS \neq SH$). However, the operator S acting on the discrete traction $H\boldsymbol{\lambda}$ is symmetric. The geometric matrices can be discretized as

$$\mathcal{K}\boldsymbol{U} \approx K\boldsymbol{U} \quad (28)$$

$$\mathcal{K}^*\boldsymbol{\lambda} \approx K^T H\boldsymbol{\lambda} = K^T(\boldsymbol{H\lambda}) \quad (29)$$

Similarly, we can maintain the symmetry by using the discretized traction $\boldsymbol{H\lambda}$ instead of the traction itself. Finally, the double layer operator is discretized as follows

$$\mathcal{D}\mathcal{K}\boldsymbol{U} \approx DHK\boldsymbol{U} \quad (30)$$

$$\mathcal{K}^*\mathcal{D}^*\boldsymbol{\lambda} \approx K^T HD^T H\boldsymbol{\lambda} = K^T HD^T(H\boldsymbol{\lambda}). \quad (31)$$

Let $\boldsymbol{g} = H\boldsymbol{\lambda}$, the linear system for the first alternative of the second kind formulation in the discrete form is

$$\begin{bmatrix} S & -\frac{1}{2}K - DHK \\ -\frac{1}{2}K^T - \frac{1}{2}K^T H D^T & 0 \end{bmatrix} \begin{bmatrix} \boldsymbol{g} \\ \boldsymbol{U} \end{bmatrix} = \begin{bmatrix} \boldsymbol{u}_\infty \\ -\boldsymbol{F} \end{bmatrix}. \quad (32)$$

The discrete form for the confined flow is

$$\begin{bmatrix} S_b & -\frac{1}{2}K - D_b HK & S_{bo} \\ -\frac{1}{2}K^* - K^* H \mathcal{D}_b^* & 0 & -K^* H D_{bo}^* \\ S_{ob} & -D_{ob} HK & S_o \end{bmatrix} \begin{bmatrix} \boldsymbol{g_b} \\ \boldsymbol{U} \\ \boldsymbol{g_o} \end{bmatrix} = \begin{bmatrix} \boldsymbol{u}_\infty \\ -\boldsymbol{F} \\ \boldsymbol{0} \end{bmatrix}. \quad (33)$$

3. Results and Discussion

First, we will present the validation results of the numerical scheme. Then, we will compare the formulations for (i) single disk in a circular confinement, (ii) two disks pushed towards each other, (iii) suspension in a shear flow.

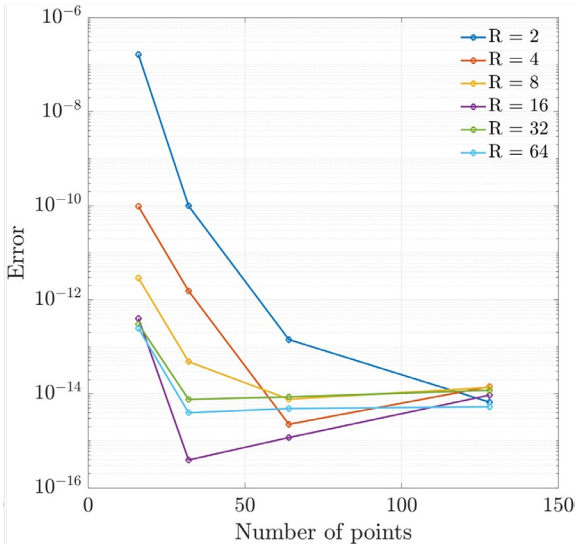

Figure 1. Validation results for the translational mobility test performed with the symmetric Alpert's quadrature implementation. As the number of points increases, the error decreases as expected. Besides, the error is much less for larger confinements since the confinement effects decrease in larger confinements

3.1. Validation

In our first test, we put a circular body of unit radius into a circular confinement of radius R. We set the fluid viscosity to unity as well. We apply a unit force in the x-direction for the translational mobility test and a unit torque for the rotational mobility test. We discretized the body with $N = [16, 32, 64, 128]$ points. We performed simulations for $R = [2, 4, 8, 16, 32, 64]$. For a chosen N, we made sure that the arc-length spacing is the same for the body and the confinement as we changed the confinement radius. We tested our scheme against the analytical results. The analytical translational velocity in the x-direction due to a force f_x in the same direction is

$$u_x = -\frac{f_x}{4\pi\eta h}$$

where the geometry related coefficient h is

$$h = \frac{R_1^2 + R_2^2}{R_1^2(\log R_2 + 1) + R_2^2(\log R_2) - R_2^2 - (R_1^2 + R_2^2)\log R_1}$$

with R_1 is the radius of the disk (it is unity) inside the circular confinement of radius R_2. The results of the translational mobility test are in Figure 1. The analytical rotational velocity ω due to a torque τ is

$$\omega = \frac{\tau}{4\pi\eta}\frac{R_2^2 - R_1^2}{R_1^2 R_2^2}.$$

The validation results of the rotational mobility test are in Figure 2. In both tests, the error is the relative error in the translational (or rotational) velocity given the force (or torque). The results show that the error exponentially decreases to the machine precision as the number of points to discretize the body increases.

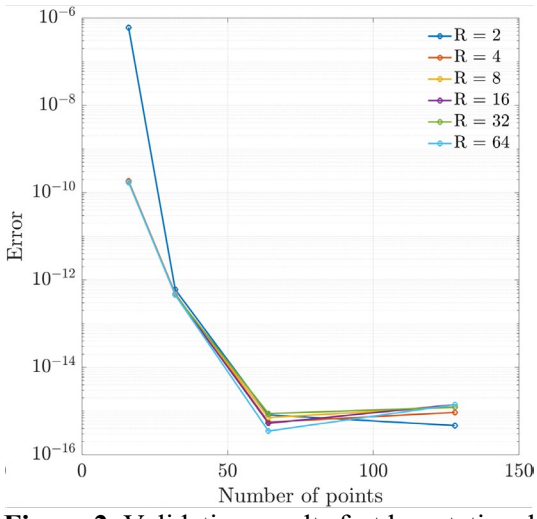

Figure 2. Validation results fort he rotational mobility test

3.2. Comparison: Second kind vs. first kind

Here, we compare the second kind and the first kind formulations in various examples. We test how the number of GMRES iterations differs in the problems where (a) the disk is driven by a vertical force and (b) the disk is driven by the motion defined on a circular confinement.

In the first problem, we consider a disk of radius 0.5 in a circular confinement of radius 5. We ensure that the disk and the confinement have the same minimum arclength spacing while changing the number of points on the disk. The disk is initially off-centered at $x = 0.5$. The GMRES tolerance is set to 1E-10. The results are in Table 1. In this test problem, both formulations lead to the same number of GMRES iterations when solving the linear system.

Table 1. Number of GMRES iterations required when solving the linear system with first and second kind formulations for a disk moving under a constant vertical force in a confinement

Number of points	First kind	Second kind
16	26	26
32	26	26
64	26	26
128	25	25

In the second problem, we consider a disk in a confinement on which a tangential velocity is defined. The results are in Table 2. While both formulations lead to the same number of GMRES iterations, this problem requires a smaller number of GMRES iterations than the case where the disk is moved with a force.

Table 2. Number of GMRES iterations required when solving the linear system with first and second kind formulations for a disk moving in a confinement on which tangential velocity is defined

Number of points	First kind	Second kind
16	19	19
32	19	19
64	20	20
128	21	21

Later, we test problems where there are two disks. In the first problem, we consider two disks driven towards each other by an external force in free space. The disks have the same radius of 0.5. One of them is at [-4, 0] and the other one is at [4, 0]. They are driven towards each other with force [1, 0] and [-1, 0], respectively. The true physics involve two disks staying at a minimum distance in the equilibrium. The GMRES tolerance is 1E-10. The results are in Tables 3 and 4 for the second and first kind formulations, respectively. The results show that the second kind formulation gives the converged solution with 32 points while the first kind formulation requires another step of refinement (convergence in the minimum distance between particles). In terms of the number of GMRES iterations, there are not major differences between both formulations.

Table 3. Number of GMRES iterations for the problem of two disks driven towards each other with external force solved with the second kind formulation

Number of points	Average GMRES	Maximum GMRES	Minimum distance
16	25	34	0.0782
32	29	53	0.0714
64	29	71	0.0714
128	26	88	0.0714

Table 4. Number of GMRES iterations for the problem of two disks driven towards each other with external force solved with the first kind formulation

Number of points	Average GMRES	Maximum GMRES	Minimum distance
16	25	34	0.0788
32	29	53	0.0715
64	29	69	0.0714
128	26	88	0.0714

Table 5. Number of GMRES iterations for the problem of two disks in a free-space shear flow solved with the second kind formulation

Number of points	Average GMRES	Maximum GMRES	Minimum distance
16	29	54	0.1315
32	29	75	0.1316
64	28	101	0.1316
128	27	46	0.1316

In the second problem with multiple disks, we place them in a free-space shear flow. One disk is at [-8, 0.25] and the other one is at [0, 0]. Hence, the disk on the left flows towards the disk at [0, 0] and passes over it. The results are tabulated in Tables 5 and 6 for the first and second kind formulations, respectively. The first

kind formulation requires a smaller number of maximum GMRES iterations at a step however the average GMRES iterations is similar in both cases.

Table 6. Number of GMRES iterations for the problem of two in a free-space shear flow solved with the first kind formulation

Number of points	Average GMRES	Maximum GMRES	Minimum distance
16	28	50	0.1310
32	28	59	0.1316
64	27	78	0.1316
128	27	46	0.1316

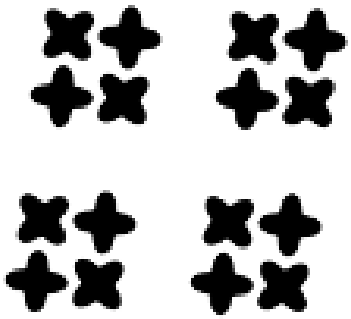

Figure 3. Suspension of 16 star-shaped disks in free-space shear flow

Finally, we put 16 disks in star-shape (Figure 3) in a free-space shear flow. They are discretized with $N = 64$ points. We simulate this case for various values of the GMRES tolerance. Table 7 shows the number of GMRES iterations obtained in both formulations. While for large tolerances both formulations require similar numbers of GMRES iterations, for small GMRES tolerance the first kind formulation requires a smaller number of GMRES iterations, and hence is more preferred.

Table 7. Number of GMRES iterations required when solving the linear system with first and second kind formulations for 16 disks (discretized with 64 points) in free-space shear flow

GMRES tolerance	First kind	Second kind
1E-4	97	97
1E-6	120	120
1E-10	190	269

The second kind formulations are known to have better conditioning than the first kind formulations because of the presence of the double layer operator instead of the single layer operator in the formulation. The question is why the proposed symmetric second kind formulation gives similar numbers of GMRES iterations with the first kind formulation. Youngren & Acrivos [22] distinguishes the two formulations based on whether the double layer integral appears alone or with the single layer integral. If the double layer integral appears by itself, the problem is solved for an unknown (non-physical) density which is then postprocessed to find physical quantities such as traction and velocity. This kind of formulation is called the second kind formulation. If the single layer integral appears in the formulation, that formulation becomes the first kind. Since the single layer operator has unbounded condition number (whereas the double layer operator's condition number is bounded), the appearance of the single layer operator in our proposed formulation makes it first-kind.

To conclude the comparison, we compare the formulations so far with Power & Miranda's second kind formulation [18] in the case of 16 star-shaped disks in free-space shear flow (Figure 3). For the first kind formulation, the number of GMRES iterations is 191 without a preconditioner and 27 with the block-diagonal preconditioner [23]. For the proposed formulation here, the number of GMRES iterations is 269 without the preconditioner and 27 with the preconditioner. Finally, for the Power & Miranda's second kind formulation, the number of GMRES iterations is 111 without a preconditioner and 27 with the block-diagonal preconditioner. Overall, we suggest the first kind formulation for the simulations of Stokesian flows of rigid particles. The formulation is easy to implement and is symmetric. It results in similar stability and convergence properties as the Power & Miranda's second kind formulation and the second kind formulation proposed in this article.

4. Conclusion

In this article, we presented a detailed comparison of the first kind and second kind integral equation formulations for the Stokesian particulate flows in two dimensions in terms of stability, accuracy and performance. To the best of our knowledge, this is one of the first comparative studies of these different formulations. We first aimed at developing a symmetric positive definite second kind formulation that can be used to simulate active particles with Brownian motion. This formulation inherently included the single-layer integral operator that causes the formulation to have similar stability properties as the first kind formulation. Hence, the first kind formulation must still be preferred over the proposed second kind formulation. After comparing these two formulations with the Power & Miranda's second kind formulation, we found out that the first kind formulation does not have much worse stability properties than the second kind formulation. Hence, we conclude that the first kind formulation provides efficient means to simulate active particles in their Stokesian flows.

Article Information Form

Acknowledgments
The author would like to thank Floren Balboa for the idea and help with the analytical calculations.

Funding
The author has no received any financial support for the research, authorship or publication of this study.

Author Contribution
Conceptualization, Methodology, Software, Data curation, Visualization, Investigation, Writing and Editing.

The Declaration of Conflict of Interest/ Common Interest
No conflict of interest or common interest has been declared by the author.

The Declaration of Ethics Committee Approval
This study does not require ethics committee permission or any special permission.

The Declaration of Research and Publication Ethics
The author of the paper declare that they comply with the scientific, ethical and quotation rules of SAUJS in all processes of the paper and that they do not make any falsification on the data collected. In addition, they declare that Sakarya University Journal of Science and its editorial board have no responsibility for any ethical violations that may be encountered, and that this study has not been evaluated in any academic publication environment other than Sakarya University Journal of Science.

References

[1] E. Lauga, T. R. Powers, "The hydrodynamics of swimming microorganisms," Rep. Prog. Phys. 72, 096601, 2009.

[2] J. Happel, H. Brenner, "Low Reynolds Number Hydrodynamics: With Special Applications to Particulate Media," Springer, Berlin, 2012.

[3] D. Barthes-Biesel, "Microhydrodynamics and Complex Fluids," CRC, Boca Raton, FL, 2012.

[4] J. Palacci, S. Sacanna, A. P. Steinberg, D. J. Pine, P. M. Chaikin, "Living crystals of light-activated colloidal surfers," Science 339 (6122), 2013, pp.936-940.

[5] W. F. Paxton, K. C. Kistler, C. C. Olmeda, A. Sen, S. K. St. Angelo, Y. Cao, T. E. Mallouk, P. E. Lammert, V. H. Crespi, "Catalytic Nanomotors: Autonomous Movement of Striped Nanorods," Journal of the American Chemical Society 126(41),2004, pp.13424-13431.

[6] J. R. Howse, R. A. L. Jones, A. J. Ryan, T. Gough, R. Vafabakhsh, R. Golestanian, "Self-Motile Colloidal Particles: From Directed Propulsion to Random Walk,"

Physical Review Letters 99(4), 2007, pp.48102.

[7] S. J. Ebbens, J. R. Howse, “In pursuit of propulsion at the nanoscale,” Soft Matter 6(4), 2010, pp.726-738.

[8] S. Ghose, R. Adhikari, “Irreducible representations of oscillatory and swirling flows in active soft matter,” Physical Review Letters. 112, 2014, pp.118102.

[9] B. Delmotte, E. E. Keaveny, F. Plouraboue, E. Climent, “Large-scale simulation of steady and time-dependent active suspensions with the force-coupling method,” Journal of Computational Physics. 302, 2015, pp.524-547.

[10] A. Pandey, P. B. S. Kumar, R. Adhikari, “Fow-induced nonequilibrium self-assembly in suspensions of stiff, apolar, active filaments,” Soft Matter 12, 2016, pp.9068-9076.

[11] D. Lindbo, A-K. Tornberg, “Spectrally accurate fast summation for periodic Stokes potentials,” Journal of Computational Physics. 229(23), 2010, pp.8994-9010.

[12] S. Kim, S. J. Karrila, “Microhydrodynamics: Principles and selected applications,” Courier Corporation, 2013.

[13] C. Pozrikidis, “Boundary integral and singularity methods for linearized viscous flow,” Cambridge University Press, 1992.

[14] A-K. Tornberg, L. Greengard, “A fast multipole method for the three-dimensional Stokes equations,” Journal of Computational Physics. 227(3), 2008, pp.1613-1619.

[15] M. Rachh, L. Greengards, “Integral equation methods for elastance and mobility problems in two dimensions,” SIAM Journal on Numerical Analysis 54(5), 2016, pp.2889-2909.

[16] E. Corona, L. Greengards, M. Rachh, S. Veerapaneni, “An integral equation formulation for rigid bodies in Stokes flow in three dimensions,” Journal of Computational Physics. 332, 2017, pp.504-519.

[17] D. J. Smith, “A boundary element regularized Stokeslet method applied to cilia-and-flagella-driven flow,” Proceed. of the Royal Society of London A 465(2112), 2009, pp.3605-3626.

[18] H. Power, G. Miranda, “Second Kind Integral Equation Formulation of Stokes’ Flows Past a Particle of Arbitrary Shape,” SIAM Journal on Applied Mathematics 47(4), 1987, pp.689-698.

[19] G. Kabacaoğlu, B. Quaife, G. Biros, “Low-resolution simulations of vesicle suspensions in 2D,” Journal of Computational Physics. 357(43), 2018, pp.43-77.

[20] E. Corona, S. Veerapaneni, “Boundary integral equation analysis for suspension of spheres in Stokes flow,” Journal of Computational Physics. 362, 2018, pp.327-345.

[21] B. K. Alpert, “Hybrid Gauss-trapezoidal quadrature rules,” SIAM Journal of Scientific Computing. 20, 1999, pp.1551-1584.

[22] G. K. Youngren, A. Acrivos, “Stokes flow past a particle of arbitrary shape: a numerical method of solution,” Journal of Fluid Mechanics 69(2), 1975, pp.377-403.

[23] A. Rahimian, S. K. Veerapaneni, G. Biros, “Dynamic simulation of locally inextensible vesicles suspended in an arbitrary two-dimensional domain, a boundary integral method,” Journal of Computational Physics. 229, 2010, pp.6466-6484.

Sakarya Üniversitesi Fen Bilimleri Dergisi
Sakarya University Journal of Science

ISSN : 2147-835X
Publisher : Sakarya University

Vol. 29, No. 1, 27-38, 2025
DOI: https://doi.org/10.16984/saufenbilder.1577506

Research Article

Duplex NiP/NiMo-(h)BN Co-Electroplating: Evaluation of Nanohardness, Room and High Temperature Wear Behaviors

Mert Aydın, Hasan Algül*, Figen Algül, Sezer Tan, Ahmet Alp

Sakarya University, Faculty of Engineering, Department of Metallurgical and Materials Science, Sakarya, Türkiye, mrtaaydin@gmail.com, halgul@sakarya.edu.tr, figenozboz@gmail.com, sezertan@sakarya.edu.tr, alp@sakarya.edu.tr
*Corresponding Author

ARTICLE INFO

Keywords:
Electrodeposition
Pulse reverse current
(h)BN Reinforcement
Duplex coating
Nanohardness
High temperature wear

Article History:
Received: 01.11.2024
Revised: 18.12.2024
Accepted: 29.01.2025
Online Available: 13.02.2024

ABSTRACT

This study explores the fabrication of duplex NiP/NiMo-(h)BN co-electrodeposits on steel substrates utilizing the reverse pulsed current (RPC) deposition method. Duplex electrodeposition offers superior physical and mechanical properties compared to single-layer plating, rendering it highly suitable for applications demanding enhanced wear resistance and adhesion. Here, NiP was selected as the inner layer due to its strong adhesion to steel, while NiMo-(h)BN served as the outer layer to maximize wear resistance. Both NiP and NiP/NiMo-(h)BN electrodeposits were deposited using a reverse pulsed current approach to enhance high temperature wear resistance of the steel substrate. The incorporation of (h)BN nanosheets into the NiMo matrix markedly enhanced the nano-hardness of the deposit, increasing it from 4.26 GPa to 5.23 GPa with the incorporation of 10 g/L (h)BN. Additionally, the solid lubrication properties of (h)BN reduced the friction coefficient of the duplex electrodeposit from 0.7 to 0.4 µ. At 400 °C, the duplex NiP/NiMo-(h)BN co-electrodeposit exhibited a wear rate of 1.77×10^5 mm³/Nm, nearly doubling the wear resistance of the duplex NiP/NiMo alloy deposit.

1. Introduction

Many techniques are used in the production of pure metals and alloys. The most widely recognized and utilized techniques for producing composites and alloys include direct current (DC), pulse current (PC), and pulse-reverse current (PRC) methods. [1, 2].

The most preferred coating type in the production of pure metals, alloys and composite coatings is DC electrodeposition [3]. It provides a wide and easy area of use due to its high physical and chemical properties, reaching high coating thickness quickly. However, irregular and inhomogeneous deposit thicknesses are the disadvantages of the method. Pulse current (PC) and pulse-reverse current (PRC) are a well-known method widely used in the field of alloy and composite depositon. When used instead of direct current, pulse electroplating provides better adhesion strength to the substrate as well as more uniform deposit thickness. It also has several advantages, including improved mechanical properties [4].

Among the transition metal alloys, NiP deposits have attracted much attention due to their functional properties [5, 6]. NiP deposits have attracted much attention due to their good corrosion and wear properties, high hardness, excellent workability and good adhesion strength. NiP deposits are widely used in technological applications, in micro galvanic applications as catalytic coatings for hydrogen evolution reactions, in the automotive industry and in decorative applications [7].

Alloys containing Mo (molybdenum) are highly preferred coating types due to superior hardness, wear, thermal and corrosion resistance. NiMo deposits offer an important alternative to harmful

Cite as: M. Aydın, H. Algul, F. Algul, S. Tan, A. Alp (2025). Duplex NiP/NiMo-(h)BN Co-Electroplating: Evaluation of Nanohardness, Room and High Temperature Wear Behaviors, *Sakarya University Journal of Science*, 29(1), 27-38. https://doi.org/10.16984/saufenbilder.1577506

chrome, especially in the aviation industry [8]. Molybdenum cannot be deposited alone in its pure form [9]. Therefore, it is typically electrodeposition with another iron group metal such as iron, nickel or cobalt by co-deposition [10]. Alloy coatings cannot achieve high hardness, mechanical and tribological properties alone, and in this case, composite deposits can be preferred, and higher deposit performances can be achieved.

Hexagonal boron nitride, BN(h) ceramic particles are a popular reinforcement phase used to obtain composite coatings. BN(h) is preferred due to its chemical inertness, low thermal expansion coefficient, low dielectric constant, good thermal shock resistance, lubricity and high thermal properties [11].

In recent years, metal matrix composite (MMC) deposition have been obtained by reinforcing polymer and ceramic particles into the metal matrix. Composite depositions increase the mechanical, tribological and hardness properties of the metal matrix to very high levels, allowing the deposits to provide high performance even in different environments. In this way, it ensures that the deposits provide high performance at higher operating temperatures [12]. Composite deposition can be produced as a single layer or as duplex.

Duplex depositions leverage the combined structural attributes of two distinct layers, utilizing their synergistic interaction to address potential limitations found in single-layer coatings [13]. Studies have shown that duplex deposits offer superior wear resistance compared to single-layer systems and present the advantage of customizable inner and outer layer combinations. This adaptability enables optimization of coating performance based on specific requirements [13–15].

NiMo-(h)BN composite deposits emerge as next-generation materials providing exceptional wear resistance under high-temperature conditions. These deposits are applied to the surface by the electrodeposition method and combine the hardness and temperature resistance of Ni and Mo with the self-lubricating properties of (h)BN. Thus, friction and wear on surfaces operating at high temperatures are significantly reduced and material life is extended.

This study aims to evaluate the wear resistance and performance characteristics of duplex NiP/NiMo-(h)BN co-electrodeposits designed for high-temperature applications. Within the scope of the study, the mechanical, tribological and structural properties of NiMo-(h)BN co-depositon produced by adding BN(h) to NiMo deposits optimized using different current coating techniques were analyzed and the tribological advantages offered by these coatings under high temperature conditions were evaluated and presented in the study.

2. General Methods

Two-dimensional boron nitride (BN(h)) nanosheets, intended for use as reinforcement elements within electrodeposited Ni-Mo alloy coatings, were synthesized via a metallothermic reduction process. Sodium tetraborate ($Na_2B_4O_7$) and metallic magnesium served as raw materials, while magnesium chloride ($MgCl_2$) was utilized to create the environment necessary for the reaction. Sodium tetraborate and metallic magnesium were mechanically mixed with magnesium chloride powder in stoichiometrically imbalanced ratios using a mortar.

The proportion of magnesium chloride to sodium tetraborate and metallic magnesium was set at 4:1. The resulting mixture was transferred to a crucible and placed in a tube furnace under a nitrogen atmosphere. The mixture was heated to 1200°C with the heating regime of 5°C/min for 3 hours. After the magnesiothermic reduction reaction, two-dimensional BN(h) nanosheets were first reacted with sulfuric acid (2 M) for 12 hours to remove the Na, Mg oxide/chloride impurities and unreacted products formed as reaction products.

Stainless steels are used as a substrate for duplex NiP/NiMo alloy and duplex NiP/NiMo-(h)BN co-electrodeposition. To ensure a uniform surface before coating process, the stainless-steel substrates were cut to 4x4 cm dimensions, ground sequentially with SiC abrasive papers of from 120 to 1200 grit and polished with an

Al_2O_3-containing solution to prepare them for acidic pretreatment. Finally, the samples were etched by immersion in concentrated HCl solution for one minute.

NiP deposits were applied as the inner layer, and NiMo-(h)BN co-electrodeposition were applied as the outer layer. The coating bath components and operating conditions for the electrodeposition NiP (inner layer) are given in Table 1. Before NiMo-(h)BN co-electrodeposition optimization studies for NiMo electrodeposition were conducted using various current modes, including direct current (DC), pulse current (PC), and pulse reverse current (PRC), to determine the optimal current type and conditions for composite coating. Ultrasound homogenization is applied to prevent agglomeration and improve the dispersion of (h)BN nanosheets in the NiMo deposition layer. The bath compositions for NiMo and NiMo-(h)BN co-electrodeposition are provided in Table 2.

Table 1. The coating bath components and operating conditions of NiP electrodeposition

Bath components		**Operating Conditions**	
Nickel Sulphate ($NiSO_4.6H_2O$)	180 g/L	Temperature	60±5 °C
Nickel Chloride ($NiCl_2.6H_2O$)	10 g/L	Current Density	2 A/dm^2
Trisodium citrate ($C_6H_5O_73Na.\ 2H_2O$)	70 g/L	pH	4-5
Phosphorous acid (H_3PO_3)	20 g/L	Magnetic stirring	300 rpm
Phosphoric Acid (H_3PO_4)	10 mL/L	Immersion time	15 min.
		Current type	PC
		Anode	Nickel

Table 2. The coating bath components and operating conditions of NiMo alloy and NiMo-(h)BN co-electrodeposition

,	**NiP/NiMo**	**Ni-P/Ni-Mo-(h)BN**
Nickel Sulphate ($NiSO_4.6H_2O$)	197.2 g/L	197.2 g/L
Sodium Molybdate ($Na_2MoO_4 \cdot 2H_2O$)	7.7 g/L	7.7 g/L
Trisodium citrate ($C_6H_5O_73Na.\ 2H_2O$)	132.3 g/L	132.3 g/L
Saccharin ($C_7H_5NO_3S$)	1 g/L	1 g/L
Sodium Lauryl Sulfate (SLS) ($NaCH_3(CH_2)_{11}OSO_3$)	62.5 mg/L	62.5 mg/L
Hexadecyltrimethylammonium bromide (CTAB ($CH_3(CH_2)_{15}N(Br)(CH_3)_3$	-	62.5 mg/L
BN(h)	-	10 g/L
Temperature	Room temperature	Room temperature
pH	7	7
Immersion time	60 min.	60 min.
Magnetic stirrer	300 rpm	300 rpm
Current Type	DC, PC, PRC	PRC
Average current density	1 A/dm^2	1 A/dm^2
Anode	Nickel	Nickel

The morphologies and elemental compositions of the synthesized (h)BN nanosheets and coatings were analyzed using a scanning electron microscope (JEOL JSM-6060 LV) equipped with energy-dispersive spectrometry (EDS). Additionally, chemical composition and phase analyses of the samples were conducted using X-ray diffraction (XRD). The nano-hardness of the coatings was measured using nanoindentation (Anton Paar, Nano Indentation Tester-NHT3) on cross-sections, following the Oliver and Parr method [16].

Tribological tests were conducted at room temperature and at 400°C using the ball-on-disk method (Anton Paar, High Temperature Tribometer) to evaluate the coatings' operational stability under high-temperature conditions. Alumina balls with a diameter of 6 mm were used as counter material in tribological tests. The sliding speed was maintained at 10 cm/s.

Tribological tests were carried out under a 2N load over a sliding distance of 250 m. After tribological tests, wear tracks were examined by SEM. Additionally, the wear track topography is observed by using 3D profilometer (KLA Tencor P6).

3. Results and Discussion

Figures 1a and 1b present SEM images of the synthesized (h)BN nanosheets at different magnifications. The formation of the two-dimensional (h)BN nanosheets was achieved in four main steps: (i) boron formation via magnesiothermic reduction, (ii) generation of nanoscale boron nitride particles through boron nitridation, (iii) growth of nanoscale boron nitride particles along a specific plane, and (iv) grain coarsening through Ostwald ripening facilitated by a directed bonding mechanism [17]. The reactions involved in BN(h) nanosheet synthesis are shown in Equations (1) and (2):

$$Na_2B_4O_7 + 7Mg \rightarrow Na_2 + 7MgO + 4B \quad (1)$$

$$2B + N_2 \rightarrow 2BN \quad (2)$$

At the synthesis temperature for BN(h) nanosheets, $MgCl_2$ (Tm: 714 °C) and $Na_2B_4O_7$ (Tm: 743 °C) interact to form a melt. In this melt, amorphous boron particles are produced through the reduction of molten $Na_2B_4O_7$ with metallic magnesium as indicated in Reaction (1). Given that magnesium has a vaporization point of 1090 °C, it exhibits a tendency to vaporize at 1200 °C without reacting. To prevent the vaporization of Mg, $MgCl_2$, which melts at this temperature, is added in substantial amounts to function as a slag-forming agent and to reduce the vaporization tendency. During the reaction, the continuous flow of nitrogen gas supplied to the tube furnace promotes the formation of two-dimensional (h)BN nanosheets without the agglomeration of amorphous boron particles, as shown in Reaction (2) [18].

Figure 1c provides EDS analysis results for the BN(h) nanosheets. The EDS results reveal two prominent peaks corresponding to B and N, indicating that the majority of the (h)BN powder structure consists of (h)BN nanosheets. Figure 1d shows the XRD patterns of the (h)BN nanosheets. Analysis of the XRD patterns identifies (h)BN at 2θ of 26.73°, 41.67°, 43.97°, and 55.29° (JCPDS no: 01-073-2095). Feng Liang et al. synthesized (h)BN nanosheets via the magnesiothermic reduction method, reporting the presence of hexagonal BN powder at 26.67°, 41.66°, and 55.16° in their XRD analysis [19] In a similar study, Örnek et al. achieved the synthesis of hexagonal BN powder, with XRD results showing peaks at 2θ of 27.1°, 41.9°, 43.8°, 50.7°, and 55.4° for hexagonal BN powder [20].

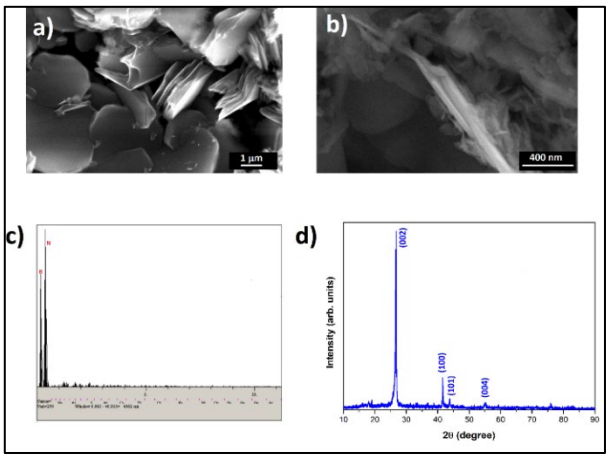

Figure 1. a) and b) The SEM image, c) EDS results and d) X-ray diffraction of (h)BN nano sheets

Figure 2a shows the surface and Figure 2b shows the cross-sectional images of the NiP alloy electrodeposition. From the surface and cross-sectional images, it is evident that the NiP alloy electrodeposition was successfully obtained.

Figure 2c presents the XRD patterns of the NiP alloy electrodeposition displaying a nickel peak at 2θ of 44.42° (JCPDS no: 01-070-1849). A homogeneous cross-sectional view was achieved using the pulsed current of the NiP alloy electrodeposition. Figures 2a and b clearly show the absence of discontinuities or cracks within the coating. Furthermore, the void-free, compact, and crack-free formation between the substrate-coating interface indicates a strong adhesion of the coating layer. The effect of the current type on the electrodeposition of NiMo outer layer.

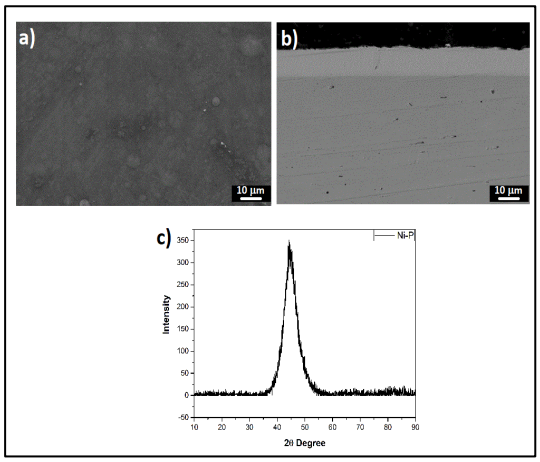

Figure 2. SEM images of a) surface, b) cross-sectional and c) XRD patterns of inner NiP layer

Figures 3a and 3b show the surface and cross-sectional images of electrodeposits produced with direct current (DC), Figures 3c and 3d with pulsed current (PC), and Figures 3e and 3f with reverse pulsed current (PRC). During the coating process, an average current density of 1 A/dm² was maintained constant to examine the effect of DC, PC, and PRC on the coating layer.

In the PRC method, the ton and toff times were kept constant to investigate the effect of the reverse current applied. In the DC-applied plating the growth morphology of the nickel-molybdenum alloy electrodeposition is dendritic and discontinuous. Figure 4c shows the molybdenum content by weight, obtained through EDS analysis of the coatings produced with different current types. The increased molybdenum content causes internal stress, leading to cracking in the coatings; hence, cracks are observed in the DC electrodeposition. Additionally, inhomogeneities are present within the coating layer.

To examine the nickel-molybdenum alloy electrodeposition produced by PC method, it is evident that more rough surface formations appear in the growth morphology of the coating layer, with an irregular surface structure; however, a crack-free structure is observed, likely due to the lower molybdenum content in the PC electrodeposition. In the nickel-molybdenum alloy electrodeposition produced with PRC, peak formations have disappeared, a homogeneous deposition is observed, and the structure contains significantly fewer cracks compared to electrodeposits produced by DC and PC methods. In the PRC method, the application of reverse current (where the anode and cathode alternate at specific intervals) results in poorly adhered and unevenly deposited nickel ions returning to the solution, removing the peaks and creating a more homogeneous and smooth coating layer.

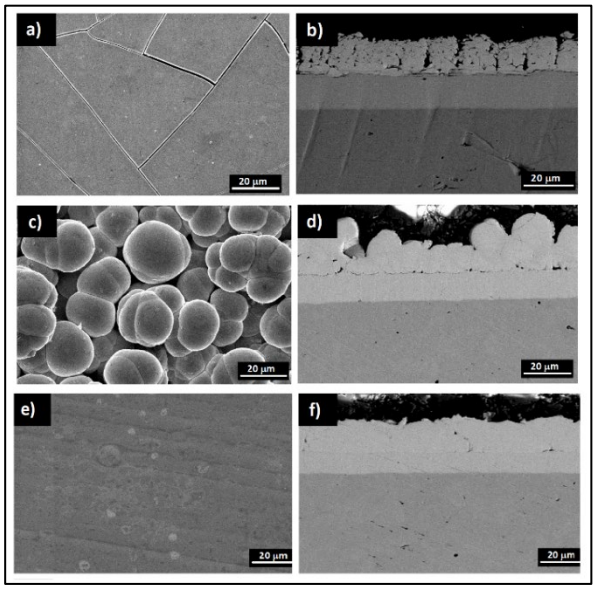

Figure 3. The surface morphology of duplex NiP/NiMo alloy electrodeposition fabricated by different current types of a-b) DC, c-d) PC and e-f) PRC

Chandrasekar et al. reported that the reverse pulsed current technique yields smoother coatings compared to those obtained by DC. They attributed this to the absence of pulsation in DC and the application of short anodic pulses during cathodic pulses in the PRC technique, which preferentially redissolves the dendritic structure formed during the cathodic pulses [1]. Furthermore, in this method, the coarse particles are reduced in size, allowing the subsequent grains to stack more evenly. This improves surface smoothness and reduces internal stress. Haseko et al. reported that coatings produced using the pulsed current (PC) method were superior to those obtained via direct current (DC) technique, and that the reverse pulsed current (PRC) method further improved the coating layer due to the periodic reversal of current direction [21]. Coatings produced using the PC method exhibited lower porosity compared to those achieved with the DC technique [22]. Additionally, they noted that by controlling the current and duration in both the PC and PRC

methods, finer crystal structures could be achieved [21].

The phase structures of duplex NiP/NiMo alloy electrodepositions produced by different current types were characterized using the XRD method. The resulting coatings, which do not contain any Mo-rich or NiMo-based intermetallic phases, exhibit a face-centered cubic NiMo solid solution structure. The effect of different current types on the XRD pattern is presented in Figure 4a. The peak at 2θ of 44.27° corresponds to nickel oriented in the typical (111) plane.

In the NiMo coatings, the peak at 2θ of 51.6° is associated with the (200) plane of nickel, while the peak at 2θ of 75.83° corresponds to nickel grown along the (220) plane (JCPDS no: 01-089-7128). Liu et al. reported that an increase in molybdenum content promotes the amorphization of the coating [23]. The peak observed at 2θ of 51.6° in the DC coating is broader and resembles an amorphous structure. Figure 4b displays the load-penetration depth curves for duplex NiP/NiMo alloy electrodepositions produced with various current types, while Figure 4c presents the corresponding hardness values. An examination of the hardness values shows that the coating produced by the DC method has a hardness of 5.32 GPa, the PC coating has a hardness of 2.676 GPa, and the PRC-produced duplex NiP/NiMo alloy electrdeposit has a hardness of 4.26 GPa.

The hardness values of the duplex NiP/NiMo alloy electrodeposits produced by different current types are consistent with their surface morphologies.

Due to the high molybdenum content, DC coatings are characterized by a brittle and hard nature. Among the coatings compared based on the applied current type, those produced by the PC method, which exhibit the lowest molybdenum content, have the lowest hardness values. Two-dimensional (h)BN nanosheets, produced via the metallothermic reduction method, were incorporated as reinforcement into the NiMo matrix in duplex NiP/NiMo co-electrodeposited. Figure 5a shows the surface image of the duplex NiP/NiMo-(h)BN co-electrodeposited coating.

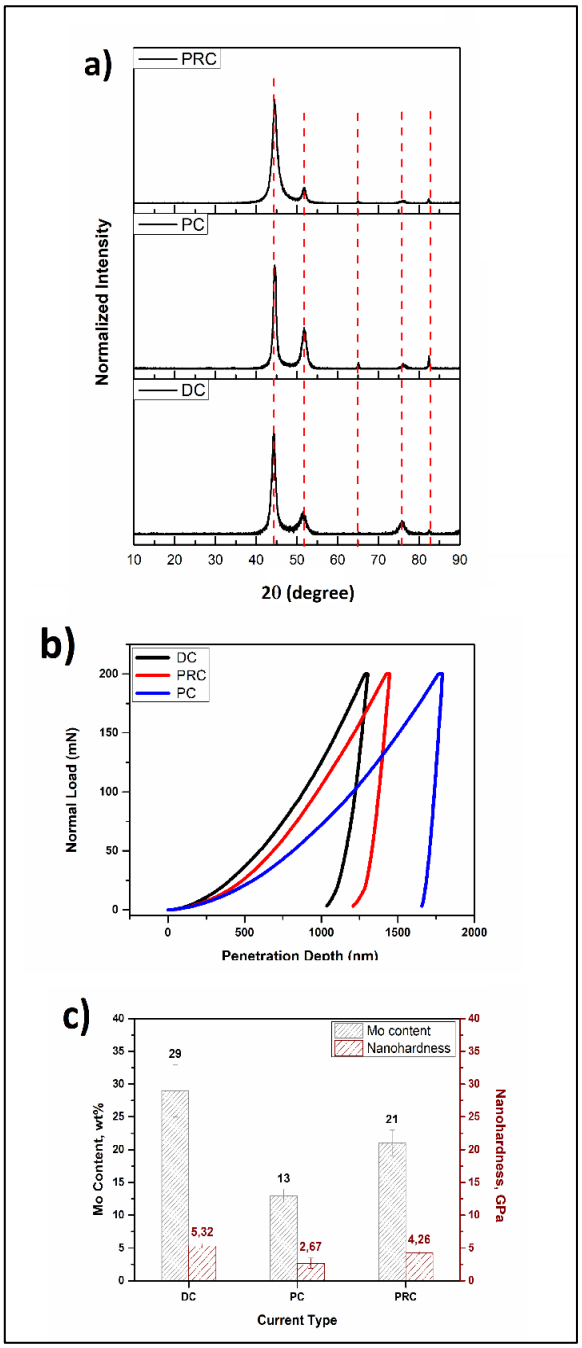

Figure 4. a) XRD patterns, b) nano indentation load vs. displacement curves, c) Mo content (wt.%) and nanohardness values (GPa) of duplex NiP/NiMo alloy electrdepositions produced by different current types of DC, PC and PRC

As seen in Figure 3e, the duplex NiMo alloy electrodeposits produced by the PRC method exhibit a smooth and dense surface structure. (h)BN, reinforced into the coating matrix, plays a significant role in altering the surface morphology. Additionally, due to the high Mo content in the plating capillary cracks have formed. It was previously noted that an increased molybdenum content can lead to cracking within the coating. The (h)BN nanosheets, incorporated

as reinforcement, prevent columnar growth and result in a rougher surface with spherical accumulations in duplex NiP/NiMo-(h)BN co-electrodeposits compared to duplex NiP/NiMo alloy electrodeposits. Dilek et all. reported that TiO_2, reinforced into a NiW matrix, increases surface roughness and creates a spherical growth morphology compared to alloy NiW coatings, attributing the cause of non-uniform grain growth to the preferential growth of nickel atoms on the nickel grains influenced by TiO_2 beneath them [24].

Figure 5b shows the cross-sectional view of the duplex NiP/NiMo-(h)BN co-electrodeposition. It demonstrates the successful deposition of the NiP alloy electrodeposit onto the substrate material. The NiMo-(h)BN layer, deposited onto the NiP alloy electrodeposition was successfully plated, forming a duplex NiP/NiMo-(h)BN structure. Examining Figure 5b, it is evident that the coating exhibits a rougher surface compared to Figure 2f. The presence of mounds and oval shapes, rather than smooth interfaces and outer surfaces, is attributed to the addition of (h)BN has a reinforcement material. Figure 5c displays the XRD patterns for duplex NiP/NiMo alloy electrodeposition and duplex NiP/NiMo-(h)BN co-electrodeposition. Upon examining Figure 5c, it is evident that the addition of (h)BN reinforcement leads to changes in the peaks and variations in crystal growth, particularly with a reduction in the intensity of the Ni (200) plane at 2θ of 75.83°, suggesting an effect on crystal growth.

Figure 6 presents the load-penetration curves and shows the impact of (h)BN reinforcement on the hardness value of the duplex NiP/NiMo alloy and duplex NiP/NiMo-(h)BN co-electrodepositions. With the addition of (h)BN, the coating hardness increased from 4.26 GPa to 5.232 GPa, while the Mo content increased from 18 wt.% to 21 wt.%. This indicates that the weight percent of Mo in composite coatings increases with (h)BN reinforcement, suggesting that the presence of (h)BN nanosheets in the coating bath somewhat facilitates molybdenum accumulation.

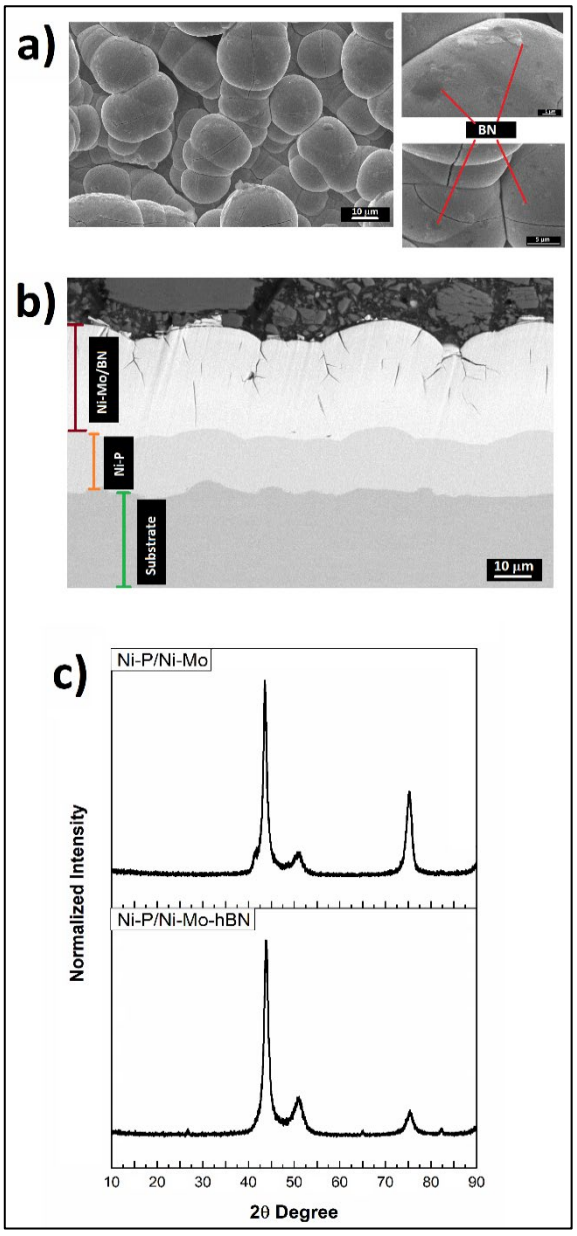

Figure 5. a) Surface morphology, b) cross sectional SEM images and c) XRD patterns of duplex NiP/NiMo-(h)BN co-electrodeposion

Laszczyńska et al. reported in their study that an increase in ZrO_2 in the solution of NiMo-ZrO_2 composite coatings correlates with an increase in Mo content, attributing this effect to the ZrO_2 particles facilitating the reduction of Mo [12].

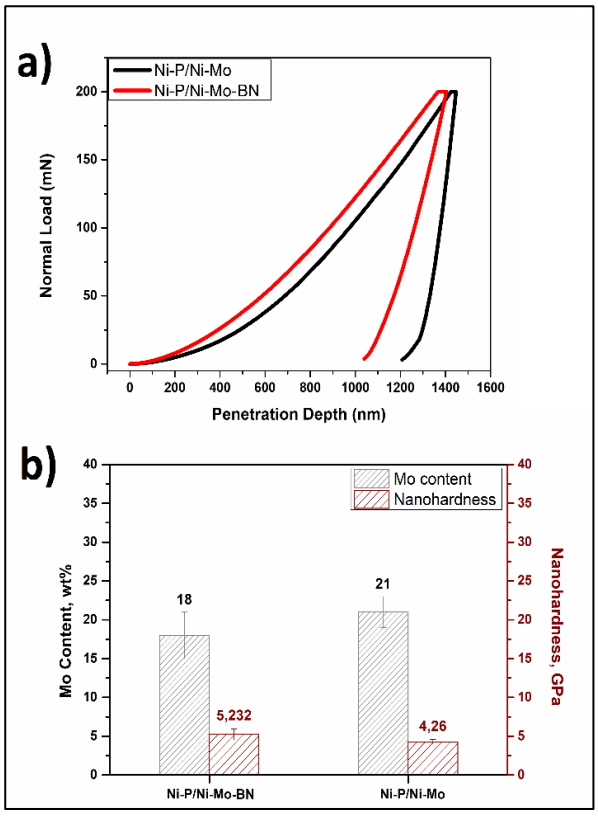

Figure 6. a) Nano indentation load vs. displacement curves, b) Mo content (wt.%) and nanohardness values (GPa) of duplex NiP/NiMo alloy and duplex NiP/NiMo-(h)BN co-electrodepositions

Figure 7 presents friction coefficient graphs for duplex NiP/NiMo alloy and duplex NiP/NiMo-(h)BN co-electrodepositions at room temperature and at 400°C. As observed in the friction coefficient curves in Figure 7a, the (h)BN reinforcement significantly reduces the coating's friction coefficient to approximately 0.4 μ. The wear rates indicate that sliding occurs within the layered lattice structure of the (h)BN particles, which is attributed to the hexagonal structure of (h)BN nanosheets [25]. Due to the non-stick nature of boron nitride particles, the likelihood of adhesion between the two contacting surfaces is reduced.

Figure 7b shows the comparative friction coefficient and wear rates for duplex NiP/NiMo alloy and duplex NiP/NiMo-(h)BN co-electrodepositions subjected to high-temperature wear at 400 °C. As can be seen, an increase in test temperature leads to a rise in the friction coefficient, due to the increased number of interactions between the asperities of the matching surfaces. This is because the contact area between matching surfaces increases exponentially with temperature [26, 27].

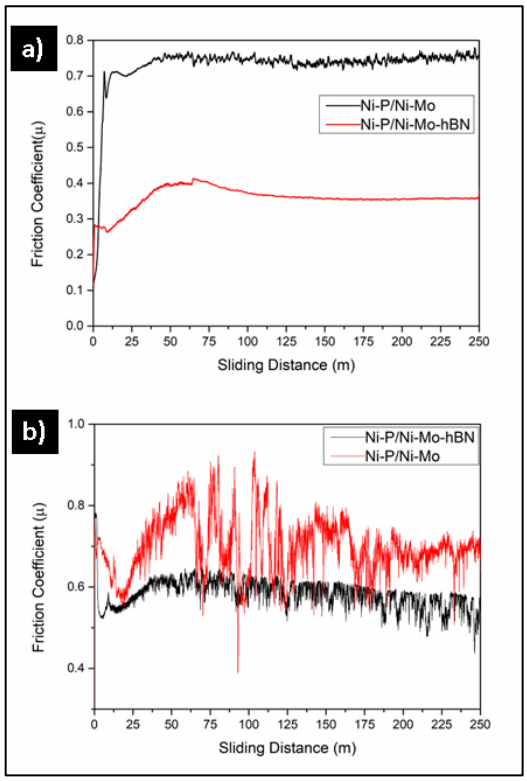

Figure 7. COF curves of duplex NiP/NiMo alloy and duplex NiP/NiMo-(h)BN co-electrodepositions at the a) room temperature and b) 400 °C

At high temperatures, these contacts may form very strong bonds, which subsequently break, often due to failure resulting from plastic flow and creep [26, 28, 29]. The obtained data align with the literature and are characteristic of typical nickel coatings. Comparing friction coefficients reveals that the (h)BN reinforcement reduces the friction coefficient even in the high-temperature wear test.

This result indicates that the (h)BN reinforcement retains its properties at elevated temperatures. The wear rate values also support the observed friction coefficients. With increasing temperature, an increase in adhesive wear components is noted due to the softening of the coatings. An increase in contact area between the abrasive ball and the coating surface is also observed. The shift in wear mechanism to more severe wear, characterized by plastic deformation and increased material transfer to the alumina counter face, is clearly evident in Figure 7.

The wear rate was determined using the following equation [30]:

$$Wear\ rate = \frac{V}{P \times S} \quad (3)$$

where: V represents the wear volume in mm³, P denotes the applied load in N, and S indicates the sliding distance. The wear rate of the duplex NiP/NiMo alloy electrodeposit at room temperature is calculated as $2.432x10^{-5}$ mm^3/Nm, while at 400 °C, the wear rate is $2.498x10^{-5}$ mm^3/Nm. In contrast, the wear rates of the duplex NiP/NiMo-(h)BN co-electrodeposits are calculated as $1.723x10^{-5}$ mm^3/Nm at room temperature and $1.77x10^{-5}$ mm^3/Nm at 400 °C. This indicates that the duplex NiP/NiMo-(h)BN co-electrodepositions are nearly twice as resistant to wear compared to duplex NiP/NiMo alloy electrodeposits, both at room temperature and at elevated temperatures. This improvement is attributed to the (h)BN reinforcement component, which provides a lubricating effect within the structure, thereby protecting it against wear.

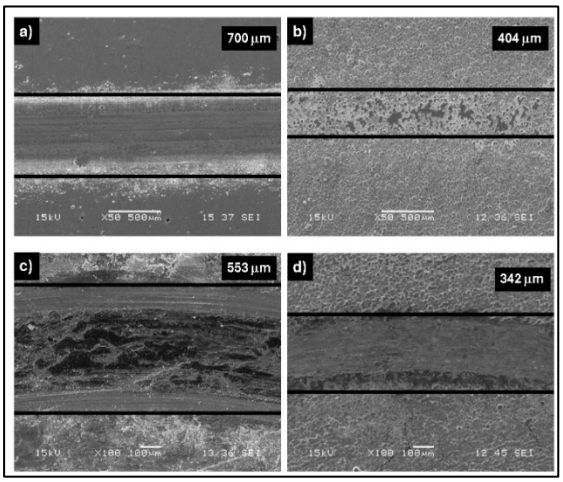

Figure 8. Low magnification SEM morphologies of the wear tracks of a) duplex NiP/NiMo alloy electrodeposits at the room temperature, b) at 400 °C, c) duplex NiP/NiMo-(h)BN co-electrodeposits at the room temperature and d) 400 °C

Figure 8 presents SEM images of the worn surfaces at low magnification, illustrating how (h)BN reinforcement affects the wear behavior of duplex NiP/NiMo alloy electrodeposits at room temperature and 400 °C. At room temperature, the wear track width of duplex NiP/NiMo alloy electrodeposit is found as 700 µm. With addition of (h)BN in the NiMo matrix, track width decreases, likely due to the increased hardness of the composite coatings and the role of (h)BN nanosheets as load-bearing and solid lubricating elements in the structure [31]. The effect of (h)BN at high temperatures becomes more evident with the reduction in wear track width. The high-temperature resistance and self-lubricating properties of (h)BN show that it provides more effective protection against wear at 400 °C

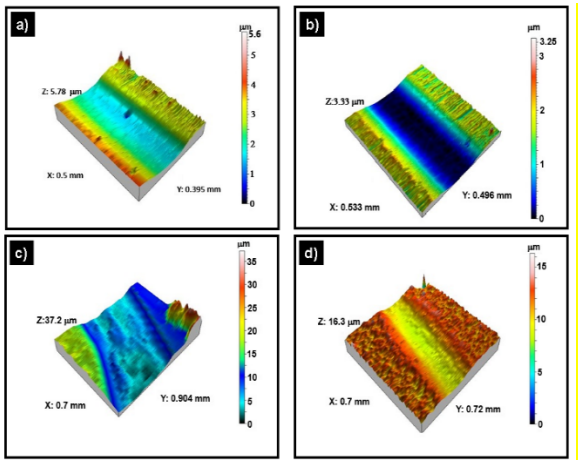

Figure 9. 3D profilometer results from wear tracks for a) duplex NiP/NiMo alloy coating, b) duplex NiP/NiMo-(h)BN co-electrodeposits tested at room temperature and c) duplex NiP/NiMo alloy, d) duplex NiP/NiMo-(h)BN co-electrodeposits tested at 400 °C

Examining the 3D profilometer results of the wear tracks from room temperature wear tests for Ni-Mo coatings in Figure 9a, the characteristics of abrasive wear emerge with an approximate depth of 5.6 µm. With reinforced h(BN) into the Ni-Mo matrix, it is evident from Figure 9b that the wear characteristics change, with the surface exhibiting more homogeneous wear and the wear depth reducing significantly to about 3.25 µm. Figure 9c depicts the surface topography of Ni-Mo after wear tests at 400 °C, while Figure 9d illustrates the corresponding topography for the Ni-Mo-(h)BN composite structure. It is observed that under high-temperature wear conditions, the Ni-Mo matrix is poorly preserved, with a wear depth reaching approximately 36 µm. However, with the addition of h(BN) reinforcement to the Ni-Mo matrix, the wear depth is reduced to around 15 µm. This enhancement is credited to the lubricating characteristics of h(BN), which bolster wear resistance under elevated temperatures.

As shown in Figures 10a and 10b, there is significant material loss and detachment, accompanied by small-scale tearing. The dominant mechanism observed is adhesive wear. It is evident that the smoothness of the wear

surfaces has improved with the addition of (h)BN reinforcement. Due to the lubricating properties provided by the hexagonal structure of (h)BN, material loss has been mitigated, or at least reduced to minimal levels, and no tearing has occurred. Furthermore, the (h)BN reinforcement has effectively decreased the contact area between the abrasive ball and the Ni-Mo base matrix.

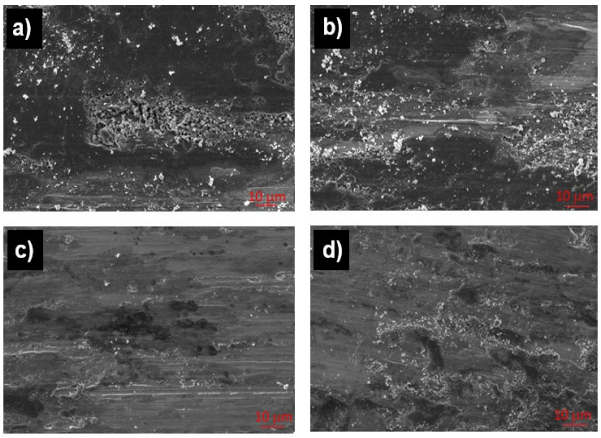

Figure 10. High magnifications SEM images from wear worms a) Ni-Mo at room temperature, b) Ni-Mo at 400°C, c) Ni-Mo-(h)BN at room temperature , d) Ni-Mo-(h)BN at 400°C

4. Conclusion

Two-dimensional (h)BN nanosheets were successfully synthesized using the metallothermic reduction method. The production of the NiP alloy electrodeposit the inner layer of the duplex plating was successfully achieved using the PC (pulsed current) method. In the production of the duplex NiMo alloy electrodeposit which forms the outer layer of the duplex structure, DC (direct current), PC, and PRC (reverse pulsed current) methods were tested, with characterization studies showing that PRC is the optimal current method. Two-dimensional (h)BN nanosheets were reinforced into the NiMo matrix of the outer layer of the duplex NiP/NiMo alloy electrodeposit and characterization studies examined the effects of this reinforcement on the matrix. Wear resistance tests at room temperature and at 400°C indicated that the addition of (h)BN significantly improved the wear resistance of duplex NiP/NiMo-(h)BN co-electrodepositions across high temperatures.

Article Information Form

Acknowledgments
We would like to thank Etimaden A.Ş. for providing us with the sodium tetraborate used in this study.

Funding
This work is supported by Sakarya University Science Research Projects Coordinators under contract number SAU BAP 2020-7-24-86. The authors thank the SAU BAP workers for their financial support.

Authors' Contribution
Authors contributed equally to the study.

The Declaration of Conflict of Interest/ Common Interest
No conflict of interest or common interest has been declared by authors.

The Declaration of Ethics Committee Approval
This study does not require ethics committee permission or any special permission.

The Declaration of Research and Publication Ethics
Authors of the paper declare that they comply with the scientific, ethical and quotation rules of SAUJS in all processes of the paper and that they do not make any falsification on the data collected. In addition, they declare that Sakarya University Journal of Science and its editorial board have no responsibility for any ethical violations that may be encountered, and that this study has not been evaluated in any academic publication environment other than Sakarya University Journal of Science.

References

[1] M. S. Chandrasekar, M. Pushpavanam, “Pulse and pulse reverse plating-Conceptual, advantages and applications,” Electrochimica Acta, vol. 53, pp. 3313–3322, 2008.

[2] S. Tan, H. Algül, E. Kiliçaslan, A. Alp, H. Akbulut, M. Uysal, "The effect of ultrasonic power on high temperature wear and corrosion resistance for Ni based alloy composite coatings," Colloids and Surfaces A: Physicochemical and Engineering Aspects, vol. 656, pp.130345, 2023.

[3] B. Pan, Y. Yao, L. Peng, Q. Zhang, Y. Yang, "Ultrasound-assisted pulse electrodeposition of cobalt films," Materials Chemistry and Physics, vol. 241, pp. 122395, 2020.

[4] S. I. Ghazanlou, S. Ahmadiyeh, R. Yavari, "Investigation of pulse electrodeposited Ni–Co/SiO2 nanocomposite plating" Surface Engineering, vol. 33, pp. 337-347, 2017.

[5] Y. Wang, L. Guan, Z. He, S. Zhang, H. Singh, M.D. Hayat, C. Yao, "Influence of pretreatments on physicochemical properties of Ni-P coatings electrodeposited on aluminum alloy," Materials and Design, vol. 197, pp. 109233, 2021.

[6] A. A. Wronkowska, A. Wronkowski, "Optical properties of polycrystalline and amorphous Nil-xPx layers by ellipsometry," Journal of Materials Science vol. 27, pp. 1842-1848, 1992.

[7] F. E. T. Heakal, M. A. Shoeib, M. A. Maanoum, "Optimizing parameters affecting electroless Ni-P coatings on AZ91D magnesium alloy as corrosion protection barriers," Protection of Metals and Physical Chemistry of Surfaces, vol. 53, pp. 177-187, 2017.

[8] E. W. Brooman, "Corrosion behavior of environmentally acceptable alternatives to cadmium and chromium coatings: Cadmium. Part I," Metal Finishing, vol. 98, pp.42-50, 2000.

[9] V. Torabinejad, M. Aliofkhazraei, A.S. Rouhaghdam, M. H. Allahyarzadeh, "Electrodeposition of Ni–Fe–Mn/Al2O3 functionally graded nanocomposite coatings," Surface Engineering, vol. 33, pp.122-130,2017.

[10] P. Kedzierzawski, D. Oleszak, M. Janik-Czachor, "Hydrogen evolution on hot and cold consolidated Ni-Mo alloys produced by mechanical alloying," Materials Science and Engineering: A, vol. 300, pp. 105-112, 2001.

[11] E. Ünal, H. Karahan, "Production and characterization of electrodeposited Ni-B/hBN composite coatings", Surface and Coatings Technology, vol. 333, pp.125-137, 2018.

[12] A. Laszczyńska, J. Winiarski, B. Szczygieł, I. Szczygieł, "Electrodeposition and characterization of Ni-Mo-ZrO2 composite coatings," Applied Surface Science., vol. 369, pp. 224-231,2016.

[13] Y. Xu, B. Liang, Y. Gao, J. Zou, R. Hua, Y. Z. Sun, Y. Chen, Q. Zhao, "Pulse electrodeposition of a duplex-layer structured composite nickel-based coating with improved corrosion and abrasion resistance," Ceramic International, vol. 50, pp. 10515-10524, 2024.

[14] B. Li, W. Zhang, D. Li, Y. Huan, J. Dong, "Microstructural, surface and electrochemical properties of a novel Ni–B/Ni–W–BN duplex composite coating by co-electrodeposition," Applied Surface Science, vol. 458, pp. 305-318, 2018.

[15] M. S. Safavi, A. Rasooli, F. A. Sorkhabi, "Electrodeposition of Ni-P/Ni-Co-Al2O3 duplex nanocomposite coatings: towards improved mechanical and corrosion properties," Transactions of the Institute of Metal Finishing, vol. 98, pp. 320-327, 2020.

[16] H. Algul, M. Uysal, A. Alp, "A comparative study on morphological, mechanical and tribological properties of electroless NiP, NiB and NiBP coatings," Applied Surface Science Advances, vol. 4, pp. 100089, 2021.

[17] K. Bao, F. Yu, L. Shi, S. Liu, X. Hu, J. Cao, Y. Qian, "Synthesis of highly crystalline rhombohedral BN triangular nanoplates via a convenient solid state reaction," Journal of Solid State Chemistry, vol. 182, pp.925-931, 2009.

[18] L. Ye, L. Zhao, F. Liang, X. He, W. Fang, H. Chen, S. Zhang, S. An, "Facile synthesis of hexagonal boron nitride nanoplates via molten-salt-mediated magnesiothermic reduction," Ceramic International, vol. 41, pp. 14941–14948, 2015.

[19] Q. Li, C. Lee, R. W. Carpick, J. Hone, "Substrate effect on thickness-dependent friction on graphene," Physica Status Solidi (B) – Basic Solid State Physics, vol. 247, pp. 2909-2914, 2010.

[20] M. Örnek, K. Wang, S. Xiang, C. Hwang, K. Y. Xie, R. A. Haber, "Molten salt synthesis of highly ordered and nanostructured hexagonal boron nitride," Diamond and Related Materials, vol. 93, pp. 179–186 ,2019.

[21] Y. Haseko, N. K. Shrestha, S. Teruyama, T. Saji, "Reversal pulsing electrodeposition of Ni/polypyrrole composite film," Electrochimica Acta, vol. 51, pp. 3652–3657, 2006.

[22] C. Guo, Y. Zuo, X. Zhao, J. Zhao, J. Xiong, "The effects of pulse-reverse parameters on the properties of Ni-carbon nanotubes composite coatings," Surface and Coating Technology, vol. 201, pp. 9491-9496, 2007.

[23] J. H. Liu, J. X. Yan, Z. L. Pei, J. Gong, C. Sun, "Effects of Mo content on the grain size, hardness and anti–wear performance of electrodeposited nanocrystalline and amorphous Ni–Mo alloys," Surface and Coating Technology, vol. 404, pp. 126476, 2020.

[24] S. Dilek, H. Algül, A. Akyol, A. Alp, H. Akbulut, M. Uysal, "Pulse electro co-deposition of submicron-sized TiC reinforced Ni–W coatings: tribological and corrosion properties," Journal of Asian Ceramic Societies, vol. 9, pp. 673–685, 2021.

[25] C. Baldwin, T. E. Such, "The Plating Rates and Physical Properties of Electroless Nickel/Phosphorus Alloy Deposits," Transactions of the IMF, vol. 46, pp. 73-80, 1968.

[26] O. A. León, M. H. Staia, H. E. Hintermann, "Wear mechanism of Ni-P-BN(h) composite autocatalytic coatings," Surface and Coating Technology, vol. 200, pp. 1825-1829, 2005.

[27] M. H. Staia, H. E. Hintermann, O. A. Leon, "Influence of the heat treatment on the tribological behavior of a Ni – P – BN (h) autocatalytic composite plating" Surface and Coating Technology, vol. 121, pp. 641-645, 1999.

[28] F. Kiliç, H. Gül, S. Aslan, A. Alp, H. Akbulut, "Effect of CTAB concentration in the electrolyte on the tribological properties of nanoparticle SiC reinforced Ni metal matrix composite (MMC) coatings produced by electrodeposition," Colloids and Surfaces A: Physicochemical and Engineering Aspects, vol. 419, pp. 53-60, 2013.

[29] H. Algul, H. Gul, M. Uysal, A. Alp, H. Akbulut, "Tribological Properties of TiO2 Reinforced Nickel Based MMCs Produced by Pulse Electrodeposition Technique," Transactions of the Indian Institute of Metals, vol. 68, pp.79-87, 2014.

[30] H. Akbulut, G. Hatipoglu, H. Algul, M. Tokur, M. Kartal, M. Uysal, T. Cetinkaya, "Co-deposition of Cu/WC/graphene hybrid nanocomposites produced by electrophoretic deposition," Surface and Coating Technology, vol. 284, pp. 344-352, 2015.

[31] O. A. León, M. H. Staia, H. E. Hintermann, "High temperature wear of an electroless Ni-P-BN (h) composite plating" Surface and Coating Technology, vol. 163–164, pp. 578-584, 2003.

Sakarya Üniversitesi Fen Bilimleri Dergisi
Sakarya University Journal of Science

ISSN : 2147-835X
Publisher : Sakarya University

Vol. 29, No. 1, 39-49, 2025
DOI: https://doi.org/10.16984/saufenbilder.1492476

Research Article

Characterization of C/C Composites Produced Using 3D-preforms by CVD/CVI Method for Biomedical Applications

Cemalettin Çamyurdu[1,3], Şahin Ateş[1*], Kerim Emre Öksüz[2], Ayşe Şükran Demirkıran[3,4]

[1] TUBITAK Marmara Research Center, Kocaeli, Türkiye, cemalettin.camyurdu@tubitak.gov.tr, sahin.ates@tubitak.gov.tr
[2] Sivas Cumhuriyet University, Department of Metallurgical and Materials Engineering, Sivas, Türkiye, emre.oksuz@cumhuriyet.edu.tr
[3] Sakarya University, Engineering Faculty, Department of Metallurgy and Materials Engineering, Sakarya, Türkiye, dkiran@sakarya.edu.tr
[4] Sakarya University, Research, Development and Application Center (SARGEM), Sakarya, Türkiye
[*]Corresponding Author

ARTICLE INFO

Keywords:
Carbon/Carbon composites
3D Carbon fibers
Chemical vapor infiltration
Pyrolitic Carbon (PyC)
Biodegradation

Article History:
Received: 31.05.2024
Revised: 19.12.2024
Accepted: 29.01.2025
Online Available: 13.02.2025

ABSTRACT

In this study, carbon/carbon (C/C) composite structures were produced by depositing a pyrolytic carbon matrix around carbon fibers found in a three-dimensional (3D) preform using the Chemical Vapor Infiltration (CVI) method. The preforms used as starting materials were in orthogonal fiber geometry and 3D carbon fiber knitting structure. The CVI process performed in the CVD (Chemical Vapor Deposition) device was carried out at 1250 °C, under 2 mbar pressure, with a methane gas flow rate of 2.0 lt/min, for a total period of 312 hours gradually applied in an inert atmosphere consisting of argon and nitrogen gases. The produced block piece was processed to obtain small test samples; tensile and three-point bending tests were applied to the pieces, and their densities were measured. Samples were subjected to in-vitro biodegradation tests in 0.9 % isotonic sodium chloride solution by weight at 37 °C for a total of 21 days. The density and apparent porosity of the produced samples were measured to be 1.395 g/cm³ and 13.424%, respectively. The tensile strength and bending strength of the produced C/C composites were determined to be 252.5±6.20 MPa and 236.6±25.7 MPa, respectively. At the end of 21 days, the biodegradation ratio of C/C composites was calculated as 0.0095%.

1. Introduction

Carbon fiber is a material of great interest in various applications in the industry due to its extraordinary properties. This material, characterized by its high carbon content and fibrous structure, boasts a low density and outstanding mechanical characteristics, making it a highly desirable choice for a wide range of applications [1].

Carbon fiber fabrics are versatile materials that vary based on their application areas, manufacturing methods, and mechanical properties. In addition, they are characterized by weave types, weight per square meter, product manufacturing techniques, fiber orientation, and the polymer materials used. These fabrics are made into preforms on weaving machines using methods such as braiding, stitching, and pinning, depending on the weave type. Preforms for composite materials can be fabricated using various textile technologies, including weaving, knitting, and braiding, to produce one-dimensional (1D), two- dimensional (2D), or three-dimensional (3D) structures [2].

1D carbon fiber fabrics consist of fibers aligned in a single direction and are typically used in applications requiring high tensile strength. These fabrics provide maximum durability in the direction of fiber orientation, making them suitable for biomedical applications where localized load-bearing and high tensile strength

Cite as: C. Çamyurdu, Ş. Ateş, K. E. Öksüz, A. Ş. Demirkıran (2025). Characterization of C/C Composites Produced Using 3D-preforms by CVD/CVI Method for Biomedical Applications, *Sakarya University Journal of Science*, 29(1), 39-49. https://doi.org/10.16984/saufenbilder.1492476

are critical, such as in tendon or ligament repair materials. 2D carbon fiber fabrics, with fibers aligned in two directions (warp and weft), are produced using weaving or braiding techniques. These fabrics deliver high strength and stiffness in two-dimensional planes, which makes them applicable for prosthetics or load-bearing implants requiring planar strength and flexibility [3]. Among carbon fiber fabrics, 3D woven preforms offer distinct advantages over traditional 2D fabrics. 3D carbon fiber fabrics, composed of fibers aligned in three directions (warp, weft, and z-axis), are produced using advanced 3D weaving techniques [4]. Furthermore, novel 3D weaving techniques have been developed to continuously and rapidly produce 3D woven fabric preforms, addressing common issues such as delamination and fiber buckling found in 2D laminated composites [5]. These fabrics provide multidirectional load-bearing capacity, superior mechanical properties, enhanced durability, and structural integrity. In biomedical applications, their ability to evenly distribute mechanical stresses while maintaining biocompatibility makes them ideal for complex implants, bone scaffolds, artificial ribs, and surgical tools [6].

In the selection and design of carbon fiber preforms, not only physical, chemical, and mechanical properties but also biocompatibility, which is crucial in biomedical applications, must be considered. For instance, scaffolds must support cell adhesion, proliferation, and tissue integration in implants designed for bone replacement while withstanding mechanical loads [7]. With their exceptional strength, durability, and structural integrity, 3D woven carbon fiber fabrics meet all these requirements specified. Their capacity to accommodate multidirectional forces without compromising biocompatibility ensures they meet the rigorous demands of applications where compatibility with biological tissues is as critical as mechanical performance [8].

Pyrolytic carbon is a synthetic biomaterial first introduced in the 1960s and known for its outstanding biocompatibility and mechanical properties [9]. These unique properties have made it a fundamental material for many medical applications, especially implantable devices such as heart valve prostheses, orthopedic implants, and vascular grafts [10]. The biocompatibility of pyrolytic carbon stems from its ability to resist immune rejection and support tissue integration, making it a reliable choice for long-term implantation [11]. One of the key factors contributing to its widespread adoption in the medical field is its ability to endure harsh physiological conditions within the human body. Pyrolytic carbon exhibits excellent corrosion, wear, and fatigue resistance, even under continuous mechanical stress and exposure to bodily fluids [12].

Its surface properties, including smoothness and hydrophobicity, also minimize platelet adhesion and thrombus formation, making it particularly suitable for cardiovascular devices [13]. Pyrolytic carbon is typically produced through the CVI process, a technique wherein amorphous carbon is deposited from solid or gaseous hydrocarbons onto the surface of a substrate, such as graphite or carbon fiber woven preforms [14]. This process not only ensures precise control over material thickness, density, and microstructure but also enables the production of materials with enhanced durability and performance. Layered structures in pyrolytic carbon can be fabricated via the CVI process, allowing the material to exhibit anisotropic mechanical properties. This tailored anisotropy, characterized by high strength and flexibility, renders pyrolytic carbon particularly advantageous for specialized applications, including those in the biomedical field [15, 16].

C/C composites having the capacity to withstand temperatures up to 3000 °C without melting are materials known for their thermal stability and resistance to high temperatures. Their non-flammability, high corrosion resistance, and oxidation stability ensure durability and reliability, even in chemically aggressive or high-stress environments [17]. In addition to these excellent properties, C/C composites have unique physical and mechanical properties that enable their use as biomaterials [18]. These composite materials can absorb and convey magnetic and electrical energy with high efficiency, exhibiting greater mechanical strength than steel, all while being considerably lighter and maintaining a strong strength-to-

weight ratio. Their superior fatigue and wear resistance further enhance their suitability for biomedical applications, particularly in load-bearing or high-friction environments [19].

CVI, Polymer Impregnation and Pyrolysis (PIP), which are the basic production methods of C/C composites, differ in infiltration mechanisms and lead to dissimilar material properties. CVI utilizes gaseous precursors for adequate densification, while PIP uses liquid polymer precursors to offer a more scalable yet less homogeneous process [20]. In the CVI process, a gaseous hydrocarbon precursor is introduced into a heated chamber containing a porous carbon preform. At high temperatures, the precursor decomposes and deposits pyrolytic carbon on the internal surfaces of the preform. This controlled, layer-by-layer densification minimizes voids and creates a high-purity carbon matrix with superior mechanical strength, thermal stability, and uniformity [14]. With its ability to produce defect-free, structurally reliable materials, the CVI method is especially valuable for biomedical applications. These methods enable precise control over the material's microstructure and properties, ensuring biocompatibility, structural integrity, and longevity in biomedical settings [21, 22]. Figure 1 presents the manufacturing flowchart of C/C composites by the CVD/CVI method.

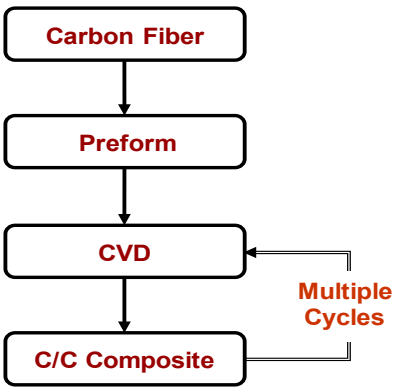

Figure 1. The manufacturing flowchart of C/C composites by the CVD/CVI method [3]

This study aimed to produce C/C composites using 3D carbon fiber preforms via the isothermal CVI method, to characterize the produced composites and reveal their potential for use in biomedical applications through in-vitro biodegradation tests. There is not enough information in the literature regarding using these composites in biomedical applications. The applied biodegradation tests will reveal the potential of the produced composites to maintain stability and structural integrity over extended periods in biological environments, thereby making a significant contribution to the literature.

2. Experimental

2.1. Production of C/C composite samples

In this study, the preform, having a 3D carbon fiber weave structure with orthogonal fiber geometry supplied by a domestic institution (3DWovens Composite Ltd.), was used. The first step applied before the CVI process is removing the polymeric sizing coating on the carbon fiber filaments. Subsequently, the initial weight of the preform was measured and subjected to a total of six CVD/CVI processes, varying in duration between 24, 48, and 72 hours each, at 1250 °C and 2 mbar pressure in a CVD system on an industrial scale (Figure 2). CVI processes were carried out with a methane gas (purity: 99.5%) flow rate of 2.0 lt/min in an inert atmosphere consisting of a combination of argon (purity: 99.999%) and nitrogen (purity: 99.999%) gases.

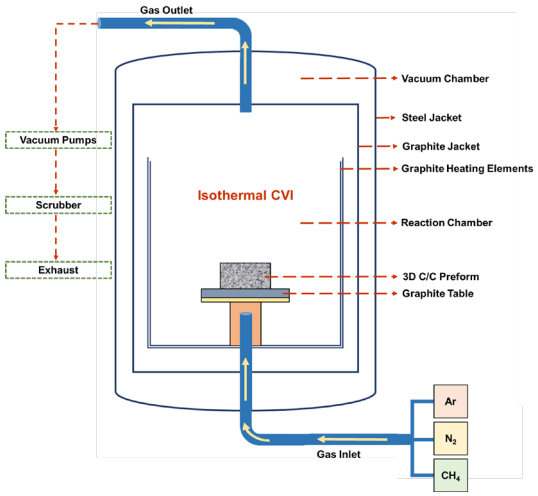

Figure 2. Schematically illustration of the CVD system utilized to perform CVI processes

At the end of each cycle, the CVD apparatus was turned on, and the preform was removed to note the weight increase resulting from pyrolytic carbon matrix deposition. At the end of 6 cycles, a total of 312 hours of CVD/CVI process was applied to the preform.

After a certain period in CVI processes, the fringes on the sample were trimmed and removed from the sample surface to increase the efficiency of subsequent CVI processes. Therefore, the change in weight ratio was revised by calculating the new initial weights. The CVI processes applied to the preform and the weight changes occurring in the preform are presented in Table 1.

Table 1. The CVI processes applied to the preform and the weight changes occurring in the preform

Process	Process Cycle Number	CVI Process Time (h)	Preform	
			Weight (gr)	Weight Change (%)
Initial weight		---	198.5	---
Initial weight after sizing*		---	191.5	---
	1	48	243.5	27
	2	72	290.9	52
Removal of fringers**		---	288.5	---
Initial weight (Revision – 1)*		---	189.9	---
	3	24	298.8	57
	4	72	320.1	69
Trimming***		---	305.3	---
Initial weight (Revision – 2)***		---	182.7	---
	5	48	319.7	75
	6	48	324.1	77
Trimming ****		---	144.7	---
Total:		**312**		

NOTES:

Sizing* : The weight values measured after removing of the polymeric coating on the raw fibers were taken as the initial weight in the calculations.

Removal of Fringes** : To increase the CVI efficiency, the fringes on the sample were cut with scissors. The proportional decrease in weight was applied to the initial weight to find the revised initial weight.

Trimming*** : Cutting from the edges with a milling machine to obtain a smooth prismatic structure. The proportional decrease in weight was applied to the initial weight to find the revised initial weight.

Trimming**** : Giving the samples their final shape by cutting with a milling machine.

As seen in Table 1, a 77% weight increase, indicating carbon accumulation, occurred in the 3D preform densified using the CVI method. The visual presentation of the C/C composite block obtained from the studies is presented in Figure 3. The test pieces required for characterization studies were extracted from this block.

2.2. Characterization of C/C composites

The phase composition of samples was determined using a PANalytical X'Pert PRO MPD model diffractometer operating with Cu-Kα (λ = 1.54056 Å) radiation. The XRD patterns of samples were obtained at 45 kV and 40 mA. The measurements were carried out in the 2–70° 2θ scanning range, with a measurement step of 0.03° 2θ and a duration of 10 minutes.

The morphologies of samples were examined by scanning electron microscopy with energy dispersive X-ray spectroscopy (SEM-EDS) (JEOL-JSM 6510 LV). The density and apparent porosity of samples were measured using the Archimedes method in distilled water.

Tensile tests of C/C composites prepared with a CNC lathe was carried out using a ZWICK Z250 Universal tensile device by ASTM C1275 standards at room temperature and a 2 mm/min speed. The initial gauge length (L_0) for strain measurement was 10 mm, measured using an extensometer. Test results were determined by calculating the arithmetic mean of the results of tests applied to three different samples.

Three-point bending tests of C/C composite samples prepared with a CNC lathe, with dimensions of 4x3x40 mm, were performed by ASTM C1161 standards, using a 5 kN load cell on a ZWICK Z250 Universal tensile device at a test speed of 1 mm/min at room temperature. The

distance between the supports and the diameter of the supports was 30 mm and 10 mm, respectively. Test results are determined by calculating the arithmetic average of the experiments.

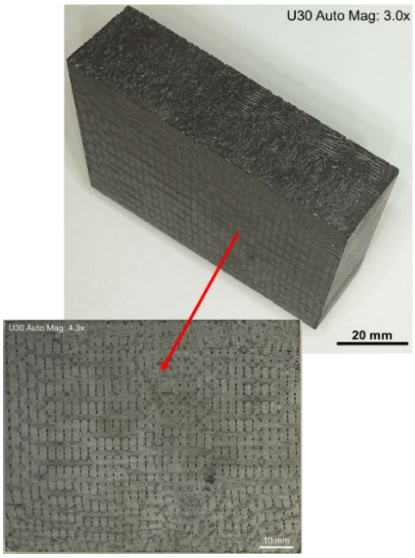

Figure 3. The visual presentation of the C/C composite block produced by CVD/CVI method

Hydrogels, biocomposites, and biodegradable implant materials used in biomedical applications are commonly subjected to in vitro biodegradation testing to evaluate their biocompatibility or biodegradability. Accordingly, biodegradation tests were conducted on C/C composite samples as well. Each sample was divided into pieces and weighed using an electronic balance with an accuracy of 0.0001 g. Subsequently, the samples were immersed in a 0.9 wt% isotonic sodium chloride solution (NaCl, I.V. Infusion) at 37 °C for 1, 3, 5, 7, 14, and 21 days [23-25].

At the end of each period, the samples were removed from the prepared solution, washed with distilled water, cleaned ultrasonically, dried for 30 minutes, and then their weights were measured again. A fresh solution was used during each incubation period, and the experiment was conducted on three samples. Weight loss was calculated according to the weight recorded before and after the incubation period [26], and the results were determined by the arithmetic mean. The biodegradation ratio was calculated using Equation 1:

$$\text{Biodegradation ratio (\%)} = \frac{w_0 - w_f}{w_0} x100 \qquad (1)$$

where; w_0 and w_f are the weights of C/C composite samples before and after in vitro biodegradation test, respectively.

3. Results and Discussion

X-ray diffractometry (XRD) analysis was conducted to identify the phases in the C/C composite densified using the CVI process, and the obtained XRD pattern is presented in Figure 4. According to the analysis result obtained from the sample surface, it was seen that the present phase was only carbon within the detection limits of XRD.

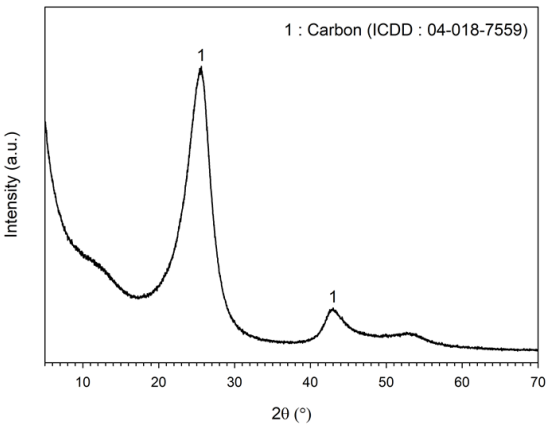

Figure 4. XRD pattern of the sample after the CVD/CVI process

Figure 5 shows the regional EDS analysis results obtained from two different regions. The presence of 100% carbon in both regions indicates that pyrolytic carbon accumulated both on the surface of the carbon fibers and between the fibers using the CVI method. Additionally, the EDS analysis results are consistent with and support the XRD analysis results.

The microstructure and morphology from both the surface and the cross-sectional of C/C composites densified using the CVI process were thoroughly examined using SEM, and the obtained images were presented in Figures 6, Figure 7 and Figure 8.

The x-y-z fiber bundles, individual carbon fibers, and macro-pores created by the orthogonal weave texture were clearly visible in the images. It was observed that the pyrolytic carbon layer deposited via the CVD/CVI method formed on

both the fiber bundles and individual fibers (Figure 6).

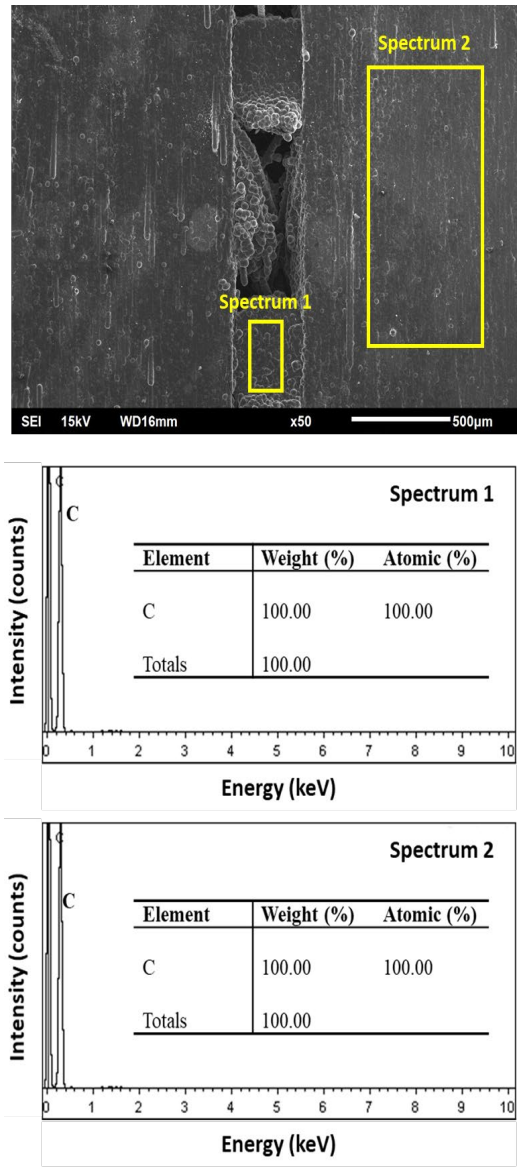

Figure 5. Regional EDS analysis results after the CVD/CVI process

The average fiber diameter was measured at 5–6 µm, while the thickness of the pyrolytic carbon layer on the fibers averaged 0.6 µm (Figure 7). Additionally, the average size of the macro voids along the y-axis of the preforms was determined to be 230 µm (Figure 8).

The orientation of carbon fiber strands, the type of weave, and the manufacturing method applied directly affect the density of the C/C composite. For example, a composite made with densely woven fibers provides higher density and mechanical properties [27]. The density of the C/C composite produced in this study, measured by the Archimedes principle, was 1.395±0.0065 g/cm³, and the amount of apparent porosity was calculated as 13.424±0.572%. These values are also presented graphically in Figure 9. E. Fitzer and M. Manocha reported that the density of C/C composites produced by various methods varies between 1.4 and 1.9 g/cm³, while H. O.

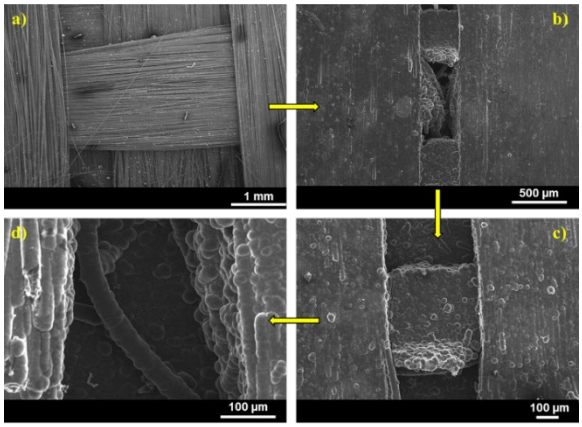

Figure 6. SEM micrographs of the C/C composites showing a) fiber bundles in the x-y axes, b) fiber bundles in the x-axis, c) fiber bundles in the y-axis, and d) pyrolytic carbon deposits on the fibers

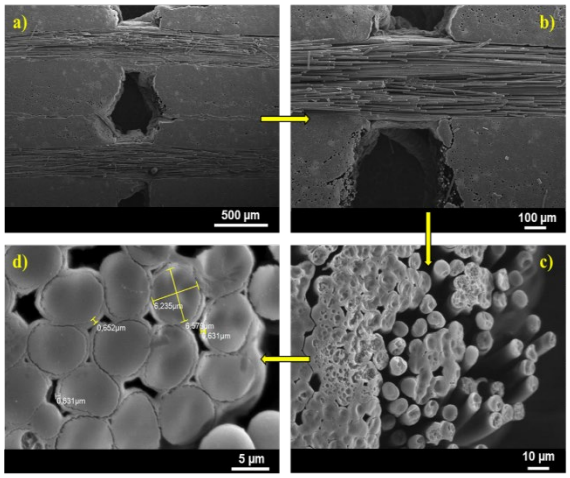

Figure 7. SEM micrographs of the C/C composites showing a) fiber bundles along the y-axis, b) enlarged view of the fiber bundles along the y-axis, c) cross-section of carbon fibers along the y-axis, d) fibers and the pyrolytic carbon layer along the y-axis

Pierson expressed the density of C/C composites as 1.7 and 1.84 g/cm³ [28, 29]. As seen, the determined density value is close to and compatible with the density value ranges reported in the literature for C/C composites.

Tensile and three-point bending tests were conducted on the C/C composites produced by the CVD/CVI method. The data for the mechanical properties obtained from these tests

are presented in Table 2. Example results from both tests are shown in Figure 10.

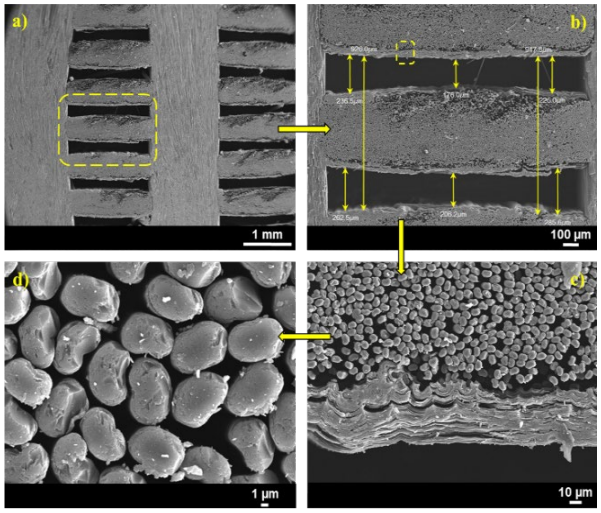

Figure 8. SEM micrographs of the C/C composites showing a) the cross-section of fiber bundles in the z-y axes, b) the cross-section of a fiber bundle in the y-axis, c) carbon fibers in the y-axis, and d) a magnified view of carbon fibers in the y-axis

E. Fitzer and M. Manocha [29] reported that the tensile strengths of C/C composites produced by various methods vary between 349 MPa and 1350 MPa, while their bending strengths range from 88 MPa to 450 MPa. H. O. Pierson [28] stated that the tensile strength of C/C composites is 270 MPa, while the bending strength is 303 MPa. As seen in Table 2, the tensile and bending strengths we found are within the ranges of values stated in the literature.

According to the results obtained from the in vitro biodegradation tests performed by immersing the samples in 0.9 wt% isotonic sodium chloride solution (NaCl, I.V. Infusion) at 37 °C for 1, 3, 5, 7, 14, and 21 days, C/C composites maintained their stability for 14 days and underwent minimal degradation in subsequent periods. The graph depicting the biodegradation ratio plotted depending on incubation time was presented in Figure 11. It is seen that the curve drawn by applying regression changes exponentially.

At the end of 21 days, the biodegradation rate of C/C composites was determined as 0.0095%. The results obtained suggest that the samples produced by the CVD/CVI process can be used in the implanted area without deformation, maintaining its integrity and stability for a long time.

In recent studies, C/C composites have been described for their exceptional mechanical, chemical, and biological properties, as well as their stability. For example, it was stated in studies by various researchers [30-32] that the pyrolytic carbon matrix and carbon fibers enhance the composite's resistance to chemical and thermal degradation, contributing to its long-term stability in different environments.

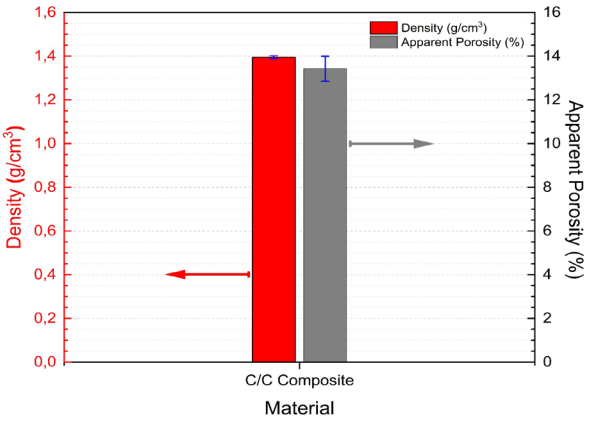

Figure 9. The density and apparent porosity graph of the C/C composites produced by CVI method

Table 2. The mechanical property data obtained from the tensile and three-point bending tests

Tests	Mechanical Properties	Value
Tensile Test	Tensile Strength (MPa)	252.5±6.20
	Elastic Modulus (GPa)	56.879±4.05
	Strain (%)	0.82±0.01
Bending Test	Bending Strength (MPa)	236.6±25.7
	Elastic Modulus (GPa)	20.318±3.39
	Strain (mm)	0.8±0.2

Wan et al. [33] studied carbon fiber-reinforced polylactide (C/PLA) composites to determine the influence of interfacial adhesion strength (IAS) on their in vitro degradation behavior in phosphate-buffered saline (PBS; pH 7.4, 37 ± 0.5 °C). They found that the PLA matrix in treated composites with nitric acid-oxidized carbon fibers absorbed less water and experienced lower mass and molecular weight loss compared to untreated composites. All samples (pure PLA and C/PLA) showed a reduced mass loss rate after 15 days of degradation. From day 16 to 25, the degradation rates were 0.51% for pure PLA and 0.27% for C/PLA composites, respectively.

Díaz et al. [34] studied the in vitro degradation of PCL and PCL/nHA composite scaffolds. They found that the polymer structures, molecular

weight, and other characteristics influenced the degradation rates. PCL, derived from fossil carbon, is hydrophobic, highly crystalline, degraded slowly, and shows only a 0.2% weight loss after 16 weeks. However, PCL/nHA composites with high oxide phase content exhibited more significant weight loss.

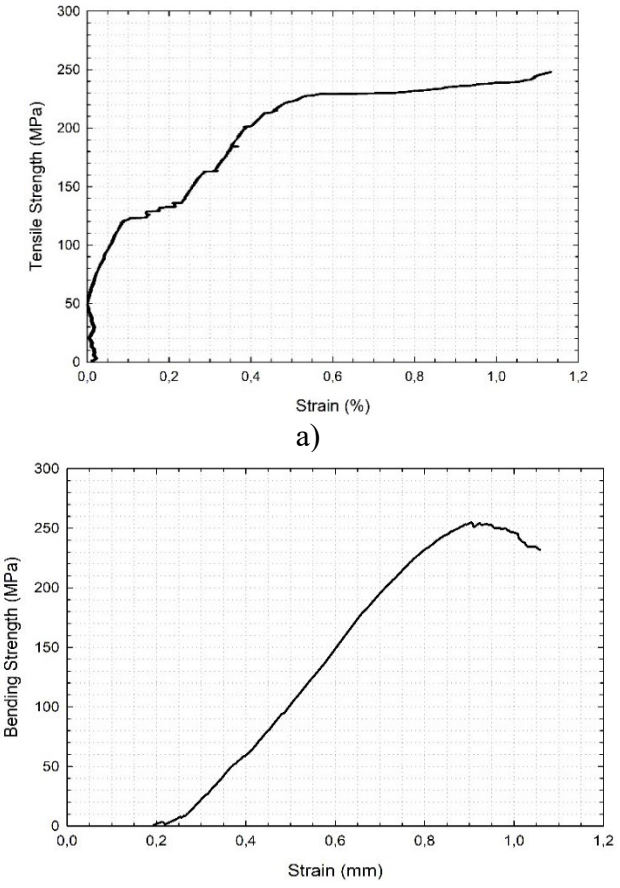

Figure 10. An example of the results from each of the two tests: a) tensile strength-strain curve, b) bending-strain curve

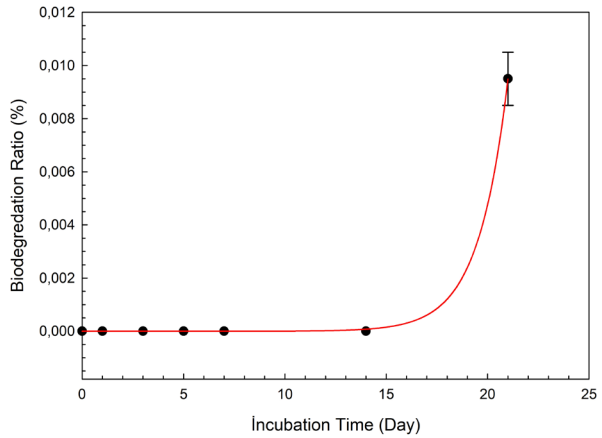

Figure 11. The biodegradation ratio graph plotted depending on incubation time

Similarly, Krishnakumar et al. [35] reported the biodegradation behavior of as-fabricated and annealed polylactic acid composites reinforced with varying carbon fiber (CF) volumes. They found that annealed carbon fiber composites exhibited improved mechanical properties and better degradation resistance than as-fabricated ones. Carbon fiber reinforcement accelerated degradation, resulting in significant changes in weight, pH, and mechanical properties of the composites immersed in simulated body fluid (SBF).

As seen, the degradation behavior in our study aligns with findings reported in the literature, where C/C composites exhibit minimal biodegradation over extended periods, even under physiological conditions.

4. Conclusion

In this study, the structural and mechanical properties of a carbon/carbon composite produced by consolidating a 3D preform woven from carbon fibers using the CVI method were examined. Additionally, the biodegradation of the produced C/C composite was investigated in 0.9 wt% isotonic sodium chloride solution (NaCl, I.V. Infusion) at 37 °C for different incubation periods. The obtained results are summarized below.

A 77% weight increase, which is an indicator of carbon accumulation in the preform, occurred in the 3D preform densified with the CVI method.

The final density of the produced samples reached the targeted level. The density and apparent porosity amount of the samples were calculated as 1.395±0.0065 g/cm³ and 13.424±0.572%, respectively.

The XRD analysis revealed that the present phase consisted solely of carbon, and EDS analyses supported this result.

SEM examinations revealed that the structure consists of a carbon matrix, fiber bundles, and pores, consistent with the structure expected from carbon/carbon composites.

Tensile and three-point bending tests applied to the samples showed that the tensile strength and bending strength of the samples were 252.5±6.20 and 236.6±25.7 MPa, respectively. Thus, applied mechanical tests revealed that the produced samples exhibited mechanical properties similar to those expected from biomaterials to be used as bone or hard tissue implants.

The in vitro biodegradation tests have shown that C/C composites maintained their stability for 14 days and underwent minimal degradation in subsequent periods. At the end of 21 days, the biodegradation rate of C/C composites was determined as 0.0095%.

Even though the biodegradation results are positive, it is necessary to perform more advanced in vitro and in vivo tests to confidently assert that these produced materials can be used as biomaterials.

Article Information Form

Funding
Authors have not received any financial support for the research, authorship, or publication of this study.

Authors' Contribution
Authors contributed equally to the study.

The Declaration of Conflict of Interest/ Common Interest
No conflict of interest or common interest has been declared by authors.

The Declaration of Ethics Committee Approval
This study does not require ethics committee permission or any special permission.

The Declaration of Research and Publication Ethics
Authors of the paper declare that they comply with the scientific, ethical, and quotation rules of SAUJS in all processes of the paper and that they do not make any falsification of the data collected. In addition, they declare that Sakarya University Journal of Science and its editorial board have no responsibility for any ethical violations that may be encountered and that this study has not been evaluated in any academic.

References

[1] S. Chand, "Review carbon fibers for composites," Journal of Materials Science, vol. 35, pp. 1303-1313, 2000.

[2] P. Wambua, R. Anandjiwala, "A review of preforms for the composites industry," Journal of Industrial Textiles, vol. 40(4), pp. 310-333, 2011.

[3] G. Rohini Devi, K. Rama Rao, "Carbon-carbon composites," Defence Science Journal, vol. 43(4), pp. 369-383, 1993.

[4] R. Mishra, V. Baheti, B.K. Behera, J. Militký, "Novelties of 3-D woven composites and nanocomposites," The Journal of The Textile Institute, vol. 105(1), pp. 84-92, 2014.

[5] H. J. Yang, D. Kim, K. M. Kang, W. R. Yu., "Manufacturing seamless three-dimensional woven preforms withcomplex shapes based on a new weaving technology," Heliyon, Cellpress, vol. 10, 2024.

[6] Z. Tan, X. Zhang, J. Ruan, "Synthesis, structure and properties of carbon/carbon composites artificial rib for chest wall reconstruction," Scientific Reports, vol. 11(1), 11285, 2021.

[7] C. Y. X. Chua, H. C. Liu, A. Susnjar, J. Rudy, G. Scorrano, M. Frerrari, J. Ho, R. Cicalo, A. Grattoni, N. Hernandez, "Carbon fiber reinforced polymers for implantable medical devices," Biomaterials, vol. 271, 120719, 2021.

[8] W. Krenkel, Ceramic Matrix Composites: Fiber Reinforced Ceramics and Their Applications, Germany, 2008.

[9] J. C. Bokros, Chemistry and Physics of Carbon, vol. 5, Dekker, New York, 1969.

[10] R. B. More, A. D. Haubold, J. C. Bokros, Biomaterials Science, 3rd. Edition, Elsevier, Book, USA, 2013.

[11] S. L. Salkeld, L. P. Patron, J. C. Lien, "Biological and functional evaluation of a novel pyrolytic carbon implant for the treatment of focal osteochondral defects in the medial femoral condyle: Assessment in a canine model," Journal of Orthopaedic Surgery and Research, vol. 11(155), pp. 1-12, 2016.

[12] J. C. Bokros, "Carbon Biomedical Devices," Carbon, vol. 15(6), pp. 353-371 1977.

[13] W. Ze, T. Wen-sheng, Ye-Xia, "Preparation of anticoagulant PyC biomaterials with super-hydrophobic surface," Journal of Applied Biomaterials & Functional Materials, vol. 16(1S), pp. 125-131, 2018.

[14] R. Naslain, F. Langlais, G. Vignoles, R. Pailler, ''The CVI-process: State of the art and perspective. In: Mechanical Properties and Performance of Engineering Ceramics II'' Ceramic Engineering and Science Proceedings, Wiley, pp. 373–386, 2008.

[15] M. Wang, L. Guo, H. Sun, ''Manufacture of Biomaterials", Encyclopedia of Biomedical Engineering, Elsevier, Book, 2019.

[16] M. Ross, C. James, J. Klawitter, "Pyrocarbon small joint arthroplasty of the extremities", Joint Replacement Technology, 2nd Edition, Elsevier, Book, 2014.

[17] N. Agarwal, A. Rangamani, K. Bhavsar, S. S. Virnodkar, A. A. Fernandes, U. Chadha, D. Srivastava, A. E. Patterson, V. Rajasekharan, "An overview of carbon-carbon composite materials and their applications," Frontiers in Materials, vol. 11:1374034, 2024.

[18] C. H. Kim, S. Y. Lee, K. Y. Rhee, S. J Park, "Carbon-based composites in biomedical applications: A comprehensive review of properties, applications, and future directions," Advanced Composites and Hybrid Materials, vol. 7:55, 2024.

[19] W. Murphy, J. Black, G. Hastings, Handbook of Biomaterial Properties, 2nd Edition, Springer, Book, 2016.

[20] F. Li, Y. Ma, W. Xu, W. Zhu, G. Wang, Y. Xu, H. Guo, Y. Li, "Study on the mechanical and tribological properties of C/C composites by CVI and PIP," Emerging Materials Research, vol. 11(4), pp. 438-446, 2022.

[21] L. Zhang, H. Li, S. Zhang, J. Lu, Y. Zhang, X. Zhao, C. Gu, X. Zeng, "Characterization of wear particles from biomedical carbon/carbon composites with different preforms in hip joint simulator". Transactions of Nonferrous Metals Society of China, vol. 22(10), pp. 2562-2568, 2012.

[22] P. Christel, A. D. Meunier, S. Leclercq, P. Bouquet, B. Buttazzoni, "Development of a carbon-carbon hip prosthesis," Journal of Biomedical Materials Research, vol. 21(A2 Suppl), pp. 191-218, 1987.

[23] V. S. S. H. Vardhan, A. Sharma, S. Tiruveedhula, R. S. Buradagunta, "Comparative study on the biodegradation behavior of pure Mg in NaCl solution and simulated body fluids", Advances in Science and Technology, vol. 120, pp. 69-73, 2022.

[24] H. Wang, Z. Shi, "In vitro Biodegradation Behavior of Magnesium and Magnesium Alloy", Journal of Biomedical Materials Research Part B: Applied Biomaterials, vol. 98(2), pp. 203–209, 2011.

[25] X. Liu, H. Yang, P. Xiong, W. Li, Huang, H. H. Y. Zheng, "Comparative studies of Tris-HCl, HEPES and $NaHCO_3/CO_2$ buffer systems on the biodegradation behaviour of pure Zn in NaCl and SBF solutions," Corrosion Science, vol. 157, pp. 205–219, 2019.

[26] C. D. Bohorquez-Moreno, K. E. Öksüz, E. Dinçer, "Porous polymer scaffolds derived from bioresources for biomedical applications," Cellulose Chemistry and Technology, vol. 57(1-2), pp. 107-116, 2023.

[27] N. P. Bansal, J. Lamon, Ceramic matrix composites: Materials, Modeling and Technology, Wiley, The American Ceramic Society, Book, 2014.

[28] H. O. Pierson, Handbook of Carbon, Graphite, Diamond and Fullerenes-Processing, Properties and Applications, 1st edition, Elsevier, eBook, 1994.

[29] E. Fitzer, L. M. Manocha, ''Carbon Reinforcements and Carbon/Carbon Composites", Springer, Book, Germany, 1998.

[30] S. Zhang, Y. Ma, L. Suresh, A. Hao, M. Bick, S. C. Tan, J. Chen, "Carbon nanotube reinforced strong carbon matrix composites," ACS Nano, vol. 14(8), pp. 9282-9319, 2020.

[31] A. B. Perumal, R. B. Nambiar, P. S. Sellamuthu, E. R. Sadiku, "Carbon Fiber Composites'', In Springer eBooks, pp. 85–115, 2021.

[32] A. Ateş, B. Aydemir, K. E. Öksüz, "Investigation of physicochemical and biological properties of boron-doped biochar," Biomass Conversion and Biorefinery, vol. 14(20), pp. 26355-26369, 2023.

[33] Y. Z. Wan, Y.L. Wang, X. H. Xu, Q. Y. Li, "In vitro degradation behavior of carbon fiber-reinforced PLA composites and influence of interfacial adhesion strength," Journal of Applied Polymer Science, vol. 82(1), pp. 150–158, 2001.

[34] E. Díaz, I. Sandonis, M. B. Valle, "In Vitro degradation of Poly(caprolactone)/nHA composites," Journal of Nanomaterials, vol. 2014(1), 802435, 2014.

[35] S. Krishnakumar, S. Thiyagarajan, "In vitro degradation analysis and mechanical characterization of PLA-CF composites prepared by fused filament fabrication technique for bio-medical applications," Journal of Thermoplastic Composite Materials, vol. 37(8), pp. 2702-2722, 2023.

Sakarya Üniversitesi Fen Bilimleri Dergisi
Sakarya University Journal of Science

ISSN : 2147-835X
Publisher : Sakarya University

Vol. 29, No. 1, 50-70, 2025
DOI: https://doi.org/10.16984/saufenbilder.1572662

Research Article

Can Waste Heat of a Thermal Power Plant Be a Key for Absorption Cooling Systems?

Erdal Kacan[1], Erkan Kacan[2*]

[1] PamukkaleUniversity, Denizli Vocational School of Technical Sciences, Department of Chemistry and Chemical Processes Technology, Denizli, Türkiye, ekacan@pau.edu.tr
[2] Mugla Sıtkı Kocman University, Mugla Sıtkı Kocman Vocational School, Department of Electric and Energy, Muğla, Türkiye, erkankacan@mu.edu.tr
[*] Corresponding Author

ARTICLE INFO

Keywords:
Energy and exergy analysis
Absorption cooling
Waste heat
Thermal power plant
Optimization
Engineering equation solver (EES)

Article History:
Received: 24.10.2024
Revised: 27.01.2025
Accepted: 30.01.2025
Online Available: 20.02.2025

ABSTRACT

Waste Heat Driven Absorption Cooling Systems (WHDACS) can be simply defined as a cooling system which uses thermal fluid couples such as LiBr-H_2O or NH_3-H_2O to decrease the temperature of selected space via waste heat usage in generator. This study focuses on the use waste heat that is discharged from thermal power plants in order to meet heat load of generator used in absorption cooling systems. Yatagan thermal power plant that has 3 discharged waste heat units with 145 MWt per unit. 172°C steam temperature and 1.18bar steam pressure is examined as a case study. LiBr-H_2O ACS is designed and optimum working parameters of system elements are determined by both considering single effect of the parameter and interacted effect of the temperature and concentration ratio parameters on Coefficient of Performance (COP) and Exergetic Coefficient of Performance (EPC) of the system. Optimum values of T_1, T_2, T_4. T_5, X_w, X_s for single effect are found as; T_1=100°C. T_2=40°C. T_4=10°C for max COP 4°C for max EPC. T_5=70°C. X_w=45% and X_s=63.41%. Optimum values for interacted independent parameters are found as 100°C for T_1. 46.86°C for T_2. 9.996°C for T_4 and 70°C for T_5. 45% for X_w. 60% for X_s by using Nelder-Mead Method. It is observed that the waste heat discharged from Yatagan Thermal Power Plant is convenient to establish an absorption cooling system. Cooling potential of WHDACS is calculated 84MWt approximately for each waste heat unit.

1. Introduction

Absorption cooling system (ACS) is based on the idea of absorbing heat from a selected area (space) by using cooling fluid such as water (H_2O), ammonia (NH_3), methylamine (CH_3NH_2), methyl chloride (CH_2Cl_2). The materials which are used to transfer the absorbed heat to an absorber are lithium bromide (LiBr), water (H_2O), calcium chloride ($CaCl_2$), strontium chloride ($SrCl_2$), lithium nitrate ($LiNO_3$). Drawing heat from a selected area decreases the temperature in that space so the cooling process can achieve its main goal.

There are different types of absorption cooling systems such as, Single Staged ACS, Double and Triple Staged ACS, Triple Staged Hybrid ACS, Generator-Absorber Heat Exc. Cycles (GAX), Regenerative Absorption Cycles (RA), etc [1]. Each kind of ACS has its own goal to achieve can be used effectively in different conditions for different purposes. For instance, single staged ACSs are preferable in the market because of their quiet, low cost and no maintenance required cycle structure [2, 3].

On the other hand, energetic and exergetic analysis showed that their COP (coefficient of performance) is around 0,7. Double staged or triple staged ACSs can be more efficient than single staged ACSs with COP values more than 2 and 3 [4]. But some disadvantages follow the increase of COP values such as large installation

Cite as: E. Kacan, E. Kacan (2025). Can Waste Heat of a Thermal Power Plant Be a Key for Absorption Cooling Systems?, *Sakarya University Journal of Science*, 29(1), 50-70. https://doi.org/10.16984/saufenbilder.1572662

area, high input temperature requirements. Therefore, numerous studies are carried on to discuss system efficiencies, requirements, different thermal fluid couples, energetic and exergetic efficiencies of entire systems or individual system elements. Lately, vast majority of studies focused on the heat source of generator and tried to answer "which energy source should drive the generator system?"

Solar energy driven ABSs are examined in literature and max. cooling loads, max COP values are calculated as well as exergetic efficiencies of system components. Results showed that most significant design parameter is outlet temperature of the solar collector, in other words inlet temperature of generator [5-15]. Some studies aimed to form a general irreversible cycle model for absorption refrigerators and endoreversible absorption refrigeration cycle model with the irreversibility of heat transfer between the working fluid and the heat reservoir [16, 17].

Also, single staged absorption cooling systems are examined in order to determine the exergy loss and driving force values in each sub system. According to the results exergetic loss in premixing process in the absorber is higher than other system components and it is suggested that reducing the flow ratio increases the premixing exergy loss in the absorber [18]. As mentioned above, high heat emission values are detected in thermodynamic processes of ACS and it is underlined that entropy, enthalpy, temperature and flow rate values should be defined as significant variables for system design [19].

ACSs can be driven by many different energy sources such as electricity, combustion tanks, some waste heat discharged from different energy sources. These systems can be designed for meeting the cooling loads of ships or big fishing vehicles [20-22]. Some studies used exhaust gas as a primary energy source for ACSs which discharge from vehicles or combustion engines with high temperature. According to the results exhaust gas driven absorption cooling systems can be a good alternative to classic compressed air-cooling systems [23, 24].

As ACS can be defined as green cooling systems there should be a measurable/quantitative scientific indicator. Therefore, Üst 2005, defined an ecological performance criterion for different energy source driven ACSs such as Carnot heat engine, gas tribunes, heat pumps and calculated optimum design parameters of system components [25, 26]. Absorption systems can be used for dehumidification, heating and cooling by driving industrial waste heat and it is presented that these systems are usable according to the energy efficiencies [27]. As seen above, numerous studies are carried on about different energy source driven ACS lately because main energy input is HEAT in generator in order to gain COOLING energy. This reverse relation highly enables the usage of solar energy as an energy source regarding high cooling load means high solar energy [6, 8-10, 12, 28].

When all studies are taken into consideration, it can be seen that there are numerous studies deal with ACSs which are triggered by various energy sources such as waste heat of a combustion engine, solar energy, boiler with auxiliary energy input etc. On the other hand, there are numerous studies deal with the reuse or recovery of waste heat discharged from energy power plants such as space heating, domestic water heating, greenhouse heating etc. In the Literature, there is a lack of studies discuss the ACSs which use waste heat of a power plant as an input energy source. In this study, it is aimed to prove that if waste heat energy discharged from power plants would be usable to trigger ACSs as an input energy source or not. In advance, the major target of this paper is to determine the optimum working/design parameters of single stage ACS triggered by waste heat energy of a power plant in order to gain max energetic and exergetic efficiencies.

2. General methods

In this study, waste heat driven absorption cooling systems (WHDACS) are examined and waste heat discharged from Yatagan Thermal Power Plant is used as a primary energy source in generator. It is aimed to draw energy between medium pressure and low-pressure turbines for cooling demand. This will also improve the energy performance of power plant [29]. The

main goal is to determine whether waste heat discharged from the power plant is usable or not for ACSs. As mentioned above, different type of energy driven ACSs have some troubles such as crystallization problem or insufficient temperature level. So, there will be a discussion part including solution suggestions about probable problems in the recommended system.

2.1. System description

Waste heat driven absorption cooling system (WHDACS) used in this study is a single stage LiBr-H_2O ACS with cooling tower due to being most common system in the market. Cooling water flows through the direction of absorber in-absorber out-condenser in-condenser out-cooling tower with the temperatures 32-35 °C in absorber and 35-37.5 °C in condenser. Yatagan Thermal Power Plant of which waste heat is used to drive generator to produce superheated steam and to separate cooling fluid (water) from LiBr-H_2O solution is in Muğla. Muğla is located in the south-west district of Türkiye where the average

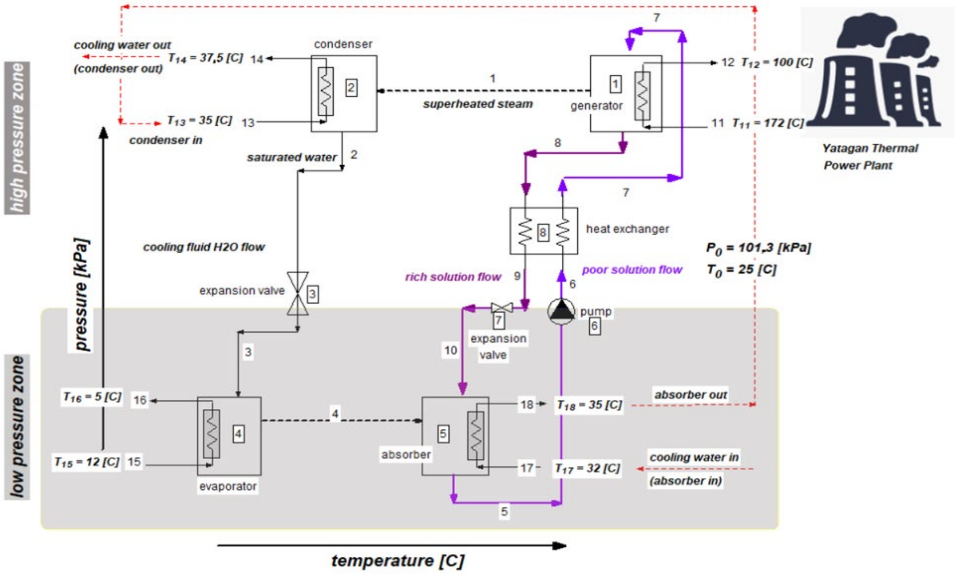

Figure 1. Schematic design of WHDACS and flow diagram

external temperature is relatively high. Thus, the external temperature and pressure values are considered as 25°C and 101.325kPa (1atm) which are used to calculate the dead state exergetic thermophysical properties such as dead state enthalpy (h_0), dead state entropy (s_0) etc. There are two pressure zones in the system which are created by the expansion valves and a pump used in cooling fluid strong solution and weak solution flow line numbered as 3-6-7 in Figure 1. Creating different pressure zones by these system elements, thermodynamic properties of the cooling fluid is getting capable of driving heat from the space.

Therefore, system element of compressor used in typical cooling/refrigeration systems which is known as high energy consumer is not needed in absorption cooling systems. That is why absorption cooling systems are much more preferable than classic compressor refrigeration systems.

1-2 First, when the LiBr-H_2O solution in the generator is heated by the inlet heat from the Yatağan Thermal Power Plant, H_2O separates from the solution and becomes superheated vapor in flow line 1 due to its lower evaporation point than the LiBr brine. Then, the superheated vapor enters the condenser to condense into saturated water with the help of cooling water.

T_1 and T_2 are the temperature values of superheated steam and saturated water in flow line number 1-2 which has a significant impact on coefficient of performance (COP) and exergetic coefficient of performance (EPC). Therefore, T_1 and T_2 values which are set as input parameters in Engineering Equation Solver (EES) software are one of the focal points of this study. In order to provide most efficient system

conditions, T_1 and T_2 values are defined as independent variable that allows design engineer to set boundary conditions in different set values. 2-3 Saturated water which condensed to liquid state in condenser passes through expansion valve in order to decrease its pressure by isenthalpic transformation in system element 3.

3-4 Saturated water in P_{min} conditions enters to evaporator in order to absorb heat from cooling fluid that follows the flow line number 15-16 and become saturated steam due to heat transfer in evaporator. Heat transfer in evaporator decides cooling conditions. Therefore, T_4 and cooling power of evaporator (Q_{eva}) is set to be an independent parameter in the software.

4-5 Saturated steam transfers its heat loaded in evaporator to the absorber fluid that comes from generator as in the state of strong solution. All the energy drained from space passes to LiBr via H_2O. The strong solution coming from generator dilutes by mixing with water comes from evaporator and weak solution occurs in absorber. Energy and exergy flows are strictly depending on the temperature of absorber (T_5) and concentration of LiBr in weak (X_w) and strong (X_s) solution. Therefore, T_5, (X_w) and (X_s) values are set to be independent parameters in the software. In the literature, generally concentration values are considered as a specific constant value such as X_w=0.56 and X_s=0.64 [30].

5-6 After the absorber, weak solution passes through pump to increase pressure. However, power of the pump is negligible as compared to the power of other system elements, it is also set to be independent parameter in order to make accurate solutions for energetic and exergetic flow in this study. In simulations, it is observed that 3kW pump power is preferable.

6-7 After getting into high pressure zone, weak solution enters to the heat exchanger before entering generator for pre-heating in order to increase the efficiency of the system.

7-8 Weak solution concentration ratio increases due to water vaporization in generator and become strong solution after the removal of some water in superheated steam state in flow line 1.

8-9-10 Strong solution passes through heat exchanger in order to transfer its heat to weak solution and increase absorption potential. After that, strong solution enters to the expansion valve to decrease pressure and become efficient absorbent for the system in low pressure zone.

T_1-T_2-T_4-T_5 and X_w-X_s values are set to be independent parameters, simulated and iterated in order to determine the optimum values for each individual effect and simultaneous effect on COP-EPC values of the system.

2.2. Methodology

2.2.1. Thermodynamic analysis

It is assumed that, all system elements' temperature distribution is homogenous and all outlet temperature and pressure values are assumed to be same value of the system element. Pressure losses are neglected inside the system and pipeline circle.

There are 4 major system elements called generator, condenser, evaporator and absorber with pressure control elements called expansion valve and pump. All major elements are in closed loop and have energetic interaction with following flow lines. Inlet and outlet flow temperatures and pressure values are as shown in Figure 1. Environmental properties of death state conditions are taken as 101,3 kPa and 25 °C in accordance with the literature.

Also, system elements are assumed to be in adiabatic conditions. Thermodynamic analysis needs enthalpy, entropy, mass-fraction, pressure and mass-flow-rate values of the fluid in each flow point which are calculated by ESS software by using following functions;

Pressure functions;

$$P_{max}=p\_{sat}(\text{water};\ T=T_2) \quad (1)$$

$$P_{min}=p\_{sat}(\text{water};\ T=T_4) \quad (2)$$

Enthalpy functions in each flow point; fluid type expresses the state of fluid such as steam, water, saturated water/steam etc. and *i* presents the flow points shown in Figure.1.

h_i=enthalpy (fluid type; T=T_i; P=P_i) (3)

$(1 \leq i \leq 4 \ \& \ 11 \leq i \leq 18)$

h_i=h_LiBrH_2O (T=T_i; X=X_w) $(5 \leq i \leq 7)$ (4)

h_i=h_LiBrH_2O (T=T_i; X=X_s) $(8 \leq i \leq 10)$ (5)

specific heat at constant pressure functions;

$c_{p\text{-}w}$= cp_LiBrH_2O(T=T_i; X=X_w) (6)

$c_{p\text{-}s}$= cp_LiBrH_2O(T=T_i; X=X_s) (7)

Entropy functions in each flow point;

s_i=entropy (fluid type; T=T_i; P=P_i)

$(1 \leq i \leq 4 \ \& \ 11 \leq i \leq 18)$ (8)

s_i=s_LiBrH_2O (T=T_i; X=X_w) $(5 \leq i \leq 7)$ (9)

s_i=s_LiBrH_2O (T=T_i; X=X_s) $(8 \leq i \leq 10)$ (10)

In each flow line, exergetic flow rates that are interacted inside the system are calculated as shown in Table 1 as well as exergetic flow rates in each system elements interacted with outside flow such as cooling water or space cooling system. All system elements are interacted with both inside and outside flow which makes Exergy in and Exergy out values up. Therefore, each system elements Exergy in and out flows are calculated as;

$$\mathrm{Ex_{in-gen}} = \mathrm{Ex_{11}} - \mathrm{Ex_{12}} \quad (11)$$

$$\mathrm{Ex_{out-gen}} = (\mathrm{Ex_1} + \mathrm{Ex_8}) - \mathrm{Ex_7} \quad (12)$$

$$\mathrm{Ex_{in-con}} = \mathrm{Ex_1} - \mathrm{Ex_2} \quad (13)$$

$$\mathrm{Ex_{out-con}} = \mathrm{Ex_{14}} - \mathrm{Ex_{13}} \quad (14)$$

$$\mathrm{Ex_{in-eva}} = \mathrm{Ex_3} - \mathrm{Ex_4} \quad (15)$$

$$\mathrm{Ex_{out-eva}} = \mathrm{Ex_{16}} - \mathrm{Ex_{15}} \quad (16)$$

$$\mathrm{Ex_{in-abs}} = \mathrm{Ex_5} - (\mathrm{Ex_{10}} + \mathrm{Ex_4}) \quad (17)$$

$$\mathrm{Ex_{out-abs}} = \mathrm{Ex_{18}} - \mathrm{Ex_{17}} \quad (18)$$

Exergy destruction can be defined as the difference between inlet exergy, work ect. and outlet exergy, work etc. As it is assumed that all system elements are in adiabatic conditions and no heat loss occurs through the flow line borders, all system elements' exergy destruction values are calculated as;

$$\mathrm{Ex_{des-gen}} = \mathrm{Ex_{in-gen}} - \mathrm{Ex_{out-gen}} \quad (19)$$

$$\mathrm{Ex_{des-con}} = \mathrm{Ex_{in-con}} - \mathrm{Ex_{out-con}} \quad (20)$$

$$\mathrm{Ex_{des-eva}} = \mathrm{Ex_{in-eva}} - \mathrm{Ex_{out-eva}} \quad (21)$$

$$\mathrm{Ex_{des-abs}} = \mathrm{Ex_{in-abs}} - \mathrm{Ex_{out-abs}} \quad (22)$$

It is expected that Ex_{des} values display the development potential of system elements

2.2.2. Optimization principle

Optimization of system elements for different purposes is the major topic of energy engineering process. In the literature, generally studies are focused on a single and instant situation of a system flow and all system parameters are calculated according to the specified-chosen values.

Optimization procedure of EES is used to determine the optimum values of independent parameters which can be listed as Conjugate Directions Method, Direct Method, Genetic Method, Variable Metric Method, Nelder Mead Method.

Conjugate Direction Method (CDM); mostly known as Direct Search or Powell's Method which is based on to determine the max-min points of a function in series that depend on one-dimension independent variable.

Direct Method (DM); is based on to determine local max-min points in small intervals. After all local max-min points are determined in all defined intervals, the max value among all max points are set to be absolute max point and the min value among all min points are set to be absolute min point.

Genetic Method (GM); is the optimization algorithm that gives the most stable results. However, it works rather slow than other

optimization methods because of having too many iterations. Genetic Method Algorithm calculates the possibility of local max-min points obtained from local small intervals to be the absolute max-min point of all defined intervals.

Variable Metric Method (VMM); is multi-dimensional state of Quadratic Approximation method. The main idea is to equate the partial differential of second order independent parameter objective function to zero.

Nelder Mead Method (NMM); is found in 1965 by himself and based on to depend objective function to multi independent parameter without considering deviations in these parameters. In this algorithm (n+1) test points are used for n-dimensional space.

3. Results and Discussions

3.1. Flow inside the system

EES software calculates flow parameters of the system including mass flow rate. Temperature, enthalpy and energy of system elements in each flow points in accordance with the set values of independents parameters. Independent parameters are defined as input parameters in EES program in order to allow design engineer to set suitable values for different cases which is seen in blue brackets in Figure 2.

Table 1. Mathematical model of energetic and exergetic analysis

System elements & flow lines	Diagram	Mass balance	Energy balance	Exergy flow
Generator (1)	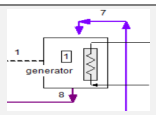	$\dot{m}_7 = \dot{m}_1 + \dot{m}_8$ $\dot{m_{gen}} = \frac{\dot{Q}_{gen}}{h_{11} - h_{12}}$	$\dot{m}_7 . h_7 = \dot{m}_1 . h_1 + \dot{m}_8 . h_8$ $\dot{q_{gen}} = F . h_8 + h_1 - (F+1) . h_7$ $\dot{Q}_{gen} = \dot{q_{gen}} . \dot{m}_1$	$\psi_1 = (h_1 - h_{01}) - T_0 . (s_1 - s_{01})$ $Ex_1 = \dot{m}_1 . \psi_1$
Condenser (2)	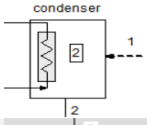	$\dot{m}_1 = \dot{m}_2$ $\dot{m_{con}} = \frac{\dot{Q}_{con}}{h_{13} - h_{14}}$	$\dot{q_{con}} = h_2 - h_1$ $\dot{Q}_{con} = \dot{q_{con}} . \dot{m}_2$	$\psi_2 = (h_2 - h_{02}) - T_0 . (s_2 - s_{02})$ $Ex_2 = \dot{m}_2 . \psi_2$
Evaporator (4)	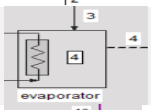	$\dot{m}_3 = \dot{m}_4$ $\dot{m_{eva}} = \frac{\dot{Q}_{eva}}{h_{15} - h_{16}}$	$\dot{q_{eva}} = h_4 - h_3$ $\dot{Q}_{eva} = \dot{q_{eva}} . \dot{m}_4$	$\psi_4 = (h_4 - h_{04}) - T_0 . (s_4 - s_{04})$ $Ex_4 = \dot{m}_4 . \psi_4$
Absorber (5)	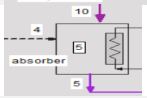	$\dot{m}_5 = \dot{m}_4 + \dot{m}_{10}$ $\dot{m_{abs}} = \frac{\dot{Q}_{abs}}{h_{17} - h_{18}}$	$\dot{m}_5 . h_5 = \dot{m}_4 . h_4 + \dot{m}_{10} . h_{10}$ $\dot{q_{abs}} = (F+1) . h_5 - h_4 - F . h_{10}$ $\dot{Q}_{abs} = \dot{q_{abs}} . \dot{m}_4$	$\psi_5 = (h_5 - h_{05}) - T_0 . (s_5 - s_{05})$ $Ex_5 = \dot{m}_5 . \psi_5$
Expansion valve (3-7)	ISENTHALPIC FLOW	$\dot{m}_2 = \dot{m}_3$ $\dot{m}_9 = \dot{m}_{10}$	$h_2 = h_3$ $h_9 = h_{10}$	$\psi_3 = (h_3 - h_{03}) - T_0 . (s_3 - s_{03})$ $Ex_3 = \dot{m}_3 . \psi_3$
Pump (6)	$W_{in} = W_{pump}$		$\dot{m}_6 . h_6 = \dot{m}_5 . h_5 + W_{pump}$	
Heat exchanger (8)	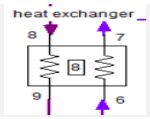	$\eta_{ex}; efficiency$ $(independent$ $parameter)$	$\eta_{ex} = \frac{T_8 - T_9}{T_8 - T_6}$ $\eta_{ex} = \frac{\dot{m}_6 . cp_w . (T_7 - T_6)}{\dot{m}_{10} . cp_s . (T_8 - T_9)}$	
Fow lines i=1 to 10			$\psi_i = (h_i - h_{0i}) - T_0 . (s_i - s_{0i})$ $Ex_i = \dot{m}_i . \psi_i$	
Flow lines i=11 to 18	$i = 11\ to\ 12$ $Ex_i = \dot{m_{gen}} . \psi_i$	$i = 13\ to\ 14$ $Ex_i = \dot{m_{con}} . \psi_i$	$i = 15\ to\ 16$ $Ex_i = \dot{m_{eva}} . \psi_i$	$i = 17\ to\ 18$ $Ex_i = \dot{m_{abs}} . \psi_i$
F - COP - EPC	$F = \frac{x_w}{x_s - x_w} = \frac{\dot{m}_{10}}{\dot{m}_1}$	$COP = \frac{\dot{Q}_{eva}}{\dot{Q}_{gen}}$	$EPC = \frac{\dot{m_{eva}} . (\psi_{16} - \psi_{15})}{\dot{m_{gen}} . (\psi_{11} - \psi_{12})}$	

The output of the software is compared with studies in the literature at constant values selected as

T_1=120°C, T_2=40°C, T_4=6°C and T_5=50°C as well as Q_{eva}=1500kW, X_s=64% and X_w=56% in Ref. 30.
T_1=100°C. T_2=45,8°C. T_4=5°C and T_5=40°C as well as Q_{eva}=174kW. X_s=64% and X_w=58% in Ref. 31

T_1=81,4°C T_2=37,4°C. T_4=4,7°C and T_5=37,4°C as well as Q_{eva}=35kW. X_s=63.51% and X_w=56.68% in Ref. 32.
T_1=85°C. T_2=40°C. T_4=10°C and T_5=40°C as well as Q_{eva}=50kW. X_s=59.91% and X_w=54.91% in Ref. 33. [30-33]

As seen in Table 2, most thermodynamic variables are the same or very close to be

neglected the deviation but physical exergy values deviate critically at some points.

The physical exergy value is calculated by multiplying the enthalpy difference between the flow point and the dead state thermal conditions and the entropy difference between the flow point and the dead state thermal conditions by the dead state temperature in K.

It is considered that the deviation in the physical exergy values at some points is due to different dead state conditions

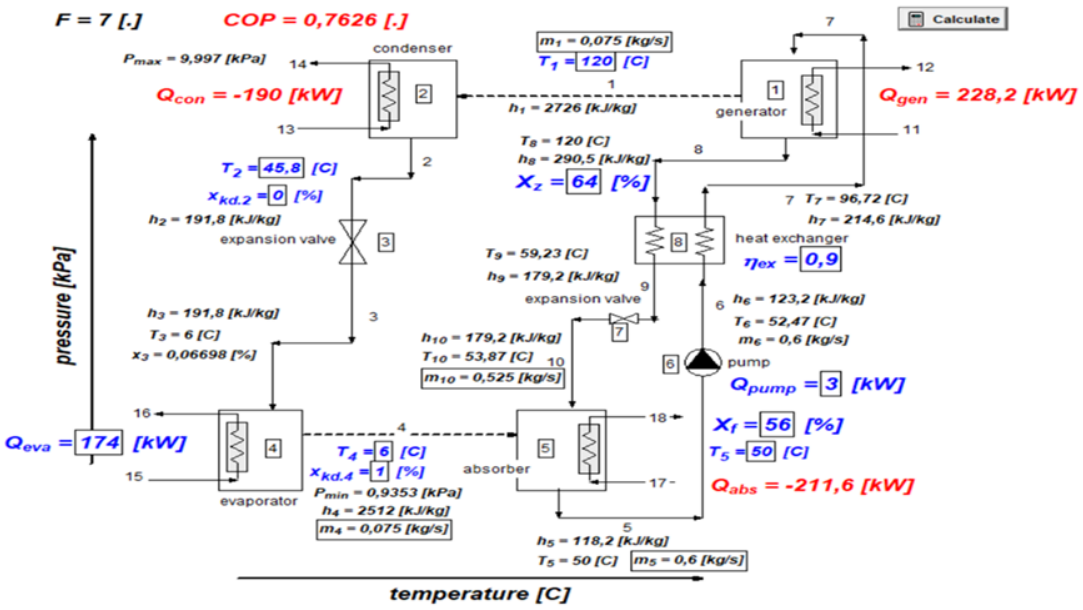

Figure 2. Energetic results and mass flow rates output of EES

Table 2. Comparison of Thermophysical Properties in each flow points calculated by EES with other studies – Validation crosscheck

Flow Points (i)		T_i [°C]	$\dot{m}_i$ [kg/s]	X_i [%]	h_i [kJ/kg]	s_i [kJ/kgK]	ψ_i [kJ/kg]
1	**EES vs Ref.30**	120	0.6398		2726		
		120	0.6399		2725		
	EES vs Ref.31	100	0.075		2687	8.449	173
		100	0.08		2687.5	8.4479	174.62
	EES vs Ref.32	81.4	0.0149		2653	8.557	105.9
		81.4	0.0149		2652	8.556	105.8
	EES vs Ref.33	85	0.0212		2659	8.511	126.2
		85	0.0212		2659	8.51	-
2	**EES vs Ref.30**	40	0.6398		167.5		
		40	0.6399		167.5		
	EES vs Ref.31	45.8	0.075		191.8	0.6491	2.903
		45.8	0.08		191.83	0.6493	2.93
	EES vs Ref.32	37.4	0.0149		156.7	0.5376	1.05
		37.4	0.0149		156.6	0.5374	0.9558
	EES vs Ref.33	40	0.0212		167.5	0.5724	1.528
		40	0.0212		167.5	0.5723	-
3	**EES vs Ref.30**	6	0.6398		167.5		
		6	0.6399		167.5		
	EES vs Ref.31	5	0.075		191.8	0.6902	-9.335
		5	0.08		191.83	0.6903	-9.28
	EES vs Ref.32	4.7	0.0149		156.7	0.5645	-6.968
		4.7	0.0149		156.6	0.5643	-7.066
	EES vs Ref.33	10	0.0212		167.5	0.5944	-5.015
		10	0.0212		167.5	0.5942	-

Table 2. Comparison of Thermophysical Properties in each flow points calculated by EES with other studies – Validation crosscheck (Continue)

	Flow Points (i)	T_i [°C]	$\dot{m}_i$ [kg/s]	X_i [%]	h_i [kJ/kg]	s_i [kJ/kgK]	ψ_i [kJ/kg]
4	**EES vs Ref.30**	6	0.6398		2512		
		6	0.6399		2512		
	EES vs Ref.31	5	0.075		2510	9.025	-176
		5	0.08		2510.6	9.0254	-174.37
	EES vs Ref.32	4.7	0.0149		2510	9.033	-178.9
		4.7	0.0149		2509	9.031	-178.9
	EES vs Ref.33	10	0.0212		2519	8.9	-129.6
		10	0.0212		2519	8.899	-
5	**EES vs Ref.30**	50	5.119	56	118.2		
		50	5.119	56	117.7		
	EES vs Ref.31	40	0.801	58	107	0.2299	0.6626
		40	0.8	58	105.71	0.2395	1.58
	EES vs Ref.32	37.4	0.1383	56.68	95.77	0.2196	0.4513
		37.4	0.1384	56.68	95.76	0.2195	34.87
	EES vs Ref.33	40	0.2548	54.91	94.08	0.2461	0.6638
		40	0.2547	54.91	94.05	0.2461	-
6	**EES vs Ref.30**	50.29	5.119	56	118.8		
		50	4.479	56	117.7		
	EES vs Ref.31	41.93	0.801	58	110.8	0.2419	0.8448
		42	0.8	58	109.68	0.2518	1.88
	EES vs Ref.32	48.34	0.1383	56.68	117.5	0.2884	1.62
		37.4	0.1384	56.68	95.77	0.2195	34.87
	EES vs Ref.33	45.79	0.2548	54.91	105.9	0.2835	1.3
		40	0.2547	54.91	94.06	0.2461	-
7	**EES vs Ref.30**	96.05	5.119	56	213.1		
		-	-	-	-		
	EES vs Ref.31	82.46	0.801	58	191	0.4815	9.656
		85	0.8	58	195.13	0.5027	12.57
	EES vs Ref.32	70.44	0.1383	56.68	162	0.4226	6.201
		63.12	0.1384	56.68	147.2	0.3788	38.78
	EES vs Ref.33	73.67	0.2548	54.91	163.6	0.4569	7.343
		63.31	0.2547	54.91	141.9	0.3937	-
8	**EES vs Ref.30**	120 120	4.479	64	290.5		
			4.479	64	284.7		
	EES vs Ref.31	100	0.7255	64	253.3	0.5299	13.3
		100	0.73	64	248.38	0.5302	16.67
	EES vs Ref.32	81.4	0.1234	63.51	216.2	0.4388	7.559
		90	0.1236	63.51	232	0.4829	92.55
	EES vs Ref.33	85	0.2335	59.91	203.9	0.4809	10.12
		85	0.2334	59.91	203.8	0.4808	-
9	**EES vs Ref.30**	57.26	4.479	64	175.7		
		-	-	-	-		
	EES vs Ref.31	47.74	0.7255	64	158.7	0.2564	0.2708
		51	0.73	64	159.35	0.2765	3.24
	EES vs Ref.32	51.64	0.1234	63.51	162.2	0.2794	1.079
		58.44	0.1236	63.51	174.4	0.3168	84.5
	EES vs Ref.33	49.71	0.2335	59.91	135.8	0.2806	1.731
		58	0.2334	59.91	151.6	0.3291	-

Table 2. Comparison of Thermophysical Properties in each flow points calculated by EES with other studies – Validation crosscheck (Continue)

	Flow Points (i)	T_i [°C]	$\dot{m}_i$ [kg/s]	X_i [%]	h_i [kJ/kg]	s_i [kJ/kgK]	ψ_i [kJ/kg]
10	**EES vs Ref.30**	53.87	4.479	64	175.7		
		52.68	4.479	64	284.7		
	EES vs Ref.31	47.68	0.7255	64	158.7	0.2561	3.596
		49	0.73	64	159.35	0.2655	6.52
	EES vs Ref.32	46.33	0.1234	63.51	162.2	0.2498	9.917
		51.79	0.1236	63.51	174.4	0.329	80.87
	EES vs Ref.33	45.11	0.2335	59.91	135.8	0.2534	9.863
		58	0.2334	59.91	151.6	0.3291	-

3.2. Optimization of system parameters

EES software has its embedded optimization procedure. Once the flow and energy-mass balances are coded correctly, parameter which will be optimized, set as an independent parameter. All iterations are done according to the boundary conditions of independent parameters as seen in Table 3.

Table 3. Boundary conditions of independent parameters

	Boundaries	Thermophysical State
T_1 [°C]	$100 \leq T_1 \leq 160$	Superheated steam in generator
T_2 [°C]	$40 \leq T_2 \leq 55$	Saturated water in condenser
T_4 [°C]	$4 \leq T_4 \leq 10$	Saturated steam in evaporator
T_5 [°C]	$50 \leq T_5 \leq 70$	Weak $LiBrH_2O$ solution in absorber
X_w [%]	$45 \leq X_w \leq 60$	Weak $LiBrH_2O$ solution in flow line 5-6-7
X_s [%]	$60 \leq X_s \leq 75$	Strong $LiBrH_2O$ solution in flow line 8-9-10

3.2.1. Optimization of T_1, T_2, T_4, T_5 for maximum COP and EPC

The abbreviation of T_1 which presents the temperature of generator is set as an independent variable in order to determine all thermodynamic properties of inner flow of the system. Other independent parameters T_2, T_4, T_5, X_w and X_s are set as constant values of 40°C, 6°C, 70°C, 56%, 64 % respectively. EES software run 26 iterations according to Quadratic Approximation Method and found optimum T_1 value as 100°C for maximum COP value as 0.821 and EPC value as 0.2181 shown in Figure 3.

After determining the optimum value of T_1, T_2 which presents the temperature of condenser is set as an independent parameter. T_2 oscillates in its boundary conditions between 40°C and 55°C while T_1, T_4, T_5, X_w and X_s are set as constant values of 100°C, 6°C, 70°C, 56%, 64% respectively. The optimum value of condenser temperature is found as 40°C according to Quadratic Approximation Method with 25 iterations for maximum COP value as 0.821 and EPC value as 0.2181 shown in Figure 4.

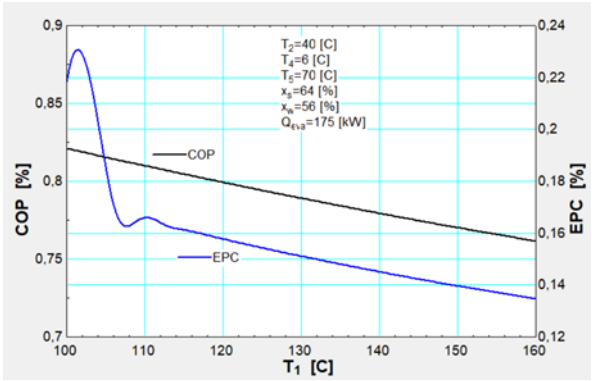

Figure 3. COP and EPC change for T_1

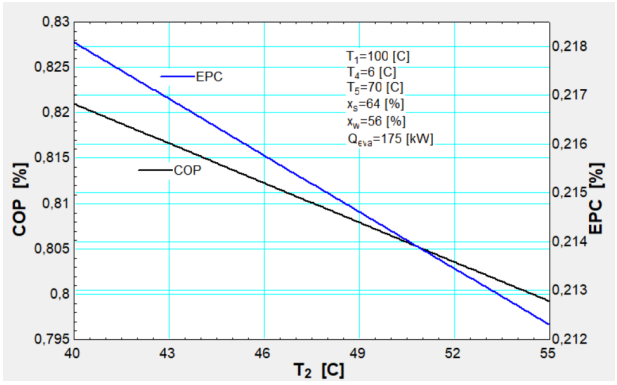

Figure 4. COP and EPC change for T_2

T_4 the value of evaporator temperature is the most significant and complicated variable that determines energetic and energetic efficiency values of the system. As seen in Figure 5. while COP is directly proportional with T_4, EPC has reverse proportion. Therefore, different optimum T_4 values are found for both maximizing COP and EPC as 10°C and 4°C. Single independent variable test which is used as Quadratic Optimization Method is not enough for maximizing both COP and EPC values because optimum T_4 value is found 10°C with max COP 0.8236 by 34 iterations and 4°C with max EPC 0.2323 by 28 iterations. So optimum value of evaporator temperature would be determined by defining all values as independent variable with two objective functions.

T_5 temperature of absorber has positive effect on both COP and EPC of the system as seen in Figure 6. Optimum value of T_5 is found 70 °C according to Quadratic Approximation Method with 0.821 COP value by making 32 iterations. The same optimum value is valid for maximum EPC of 0.2181 that is achieved by 32 iterations with same optimization method.

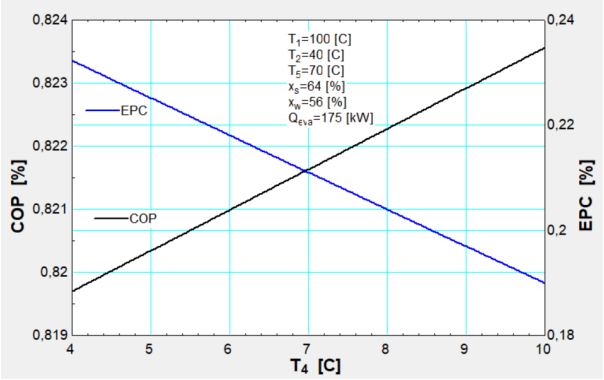

Figure 5. COP and EPC change for T_4

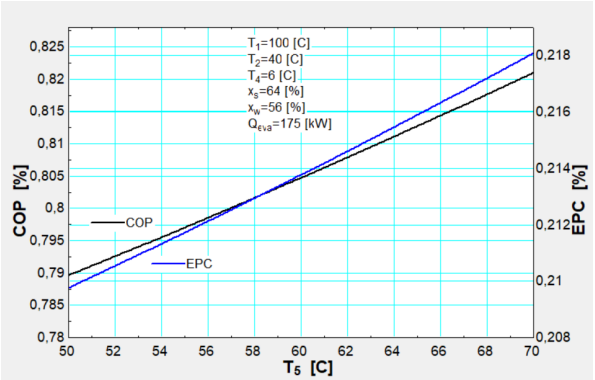

Figure 6. COP and EPC change for T_5

The boundary conditions of T_1. T_2. T_4 and T_5 has a major part for determining the optimum values. So, it is recommended that design engineer should consider the working principles and boundary conditions by absolute match with cooling purposes such as which products will be used in cooling prosses, time period of cold storage and required minimum temperature.

3.2.2. Optimization of X_w. X_s for maximum COP and EPC

Weak and strong concentration ratio values are the most significant values that creates the flow rate of system. Because it depends on the ratio of weak solution concentration to difference between strong and weak solution concentration values. Nonetheless, concentration values are very effective on determining efficiencies of the system.

Weak solution follows the flow line between 5 to 7 and once it enters into generator H_2O leaves the solution due to low vaporization point as superheated steam. Therefore, weak solution turns into strong solution due to increment in concentration value and follows flow line 8-10. While ratio of H_2O in LiBr derives between weak and strong solution ratios mass flow rates and heat transfer values change along with all thermodynamic properties. Although, Xw and Xs values are depended to temperature, pressure, composition of solution, concentration ratios are independent parameters which effects COP and EPC values of the system. T_1, T_2, T_4, T_5, X_s values are set as constant variables at 100°C, 40°C, 6°C, 70°C and 64% respectively. In the optimization proses, it is not considered how concentration ratios occur but only how they affect the COP and EPC of the system.

As seen in Figure 7, both COP and EPC values are reverse proportional with weak solution concentration value.

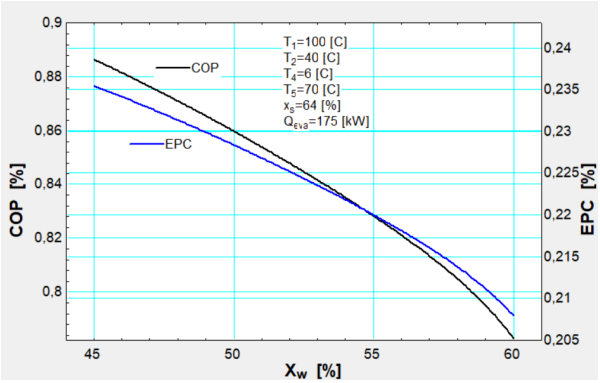

Figure 7. COP and EPC change for X_w

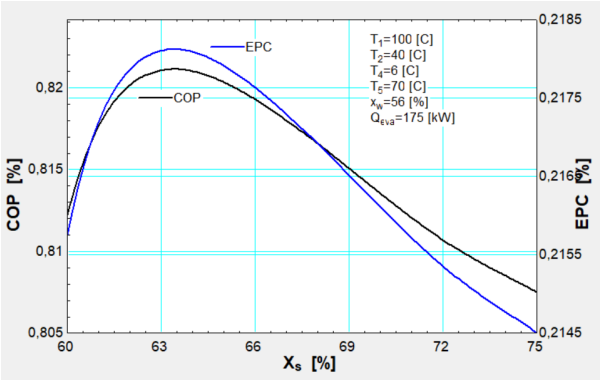

Figure 8. COP and EPC change for X_s

Weaker solution concentration means higher system efficiency. Quadratic Approximation Method calculated the optimum X_w value as 45% with 0.8863 COP and 0.2354 EPC values by making 25 iterations. As expressed above, X_w value is the most significant parameter that determines the efficiency of system and COP value reached to 0.8863 even higher than COP of the system that has optimum value of T_4 as 0.8236. Also. same results showed up for EPC value of the system even higher than EPC of the system that has optimum value of T_4 as 0.2323. The optimum X_s value is found 63.41% with 0.8211 max COP and 0.2181 max EPC by making 16 iterations as seen in Figure 8.

3.2.3. Independent variable interaction in optimization process

All temperature values are set as an independent variable that varies between its boundary conditions in order to observe the effect of all interacted independent variable on system efficiencies. Figure 9 shows the effect of independent temperature variables on COP of the system.

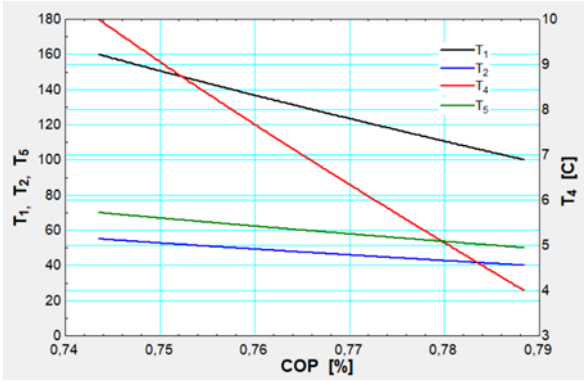

Figure 9. The effect of all independent temperature variables on COP

Figure 10 shows the correlation between EPC and independent temperature values.

After 4 independent temperature values are defined to the software and single objective function is set for both maximizing COP and EPC individually; Conjugate Directions Method (CDM) run 311 iterations for maximizing COP. Optimum T_1, T_2, T_4 and T_5 values are found as 100°C, 40°C, 10°C and 70°C respectively for max COP value of 0.8236. CDM run 123 iterations for maximizing EPC and found optimum T_1, T_2, T_4 and T_5 values as 100°C. 40°C. 4°C and 70°C with max EPC 0.2323.

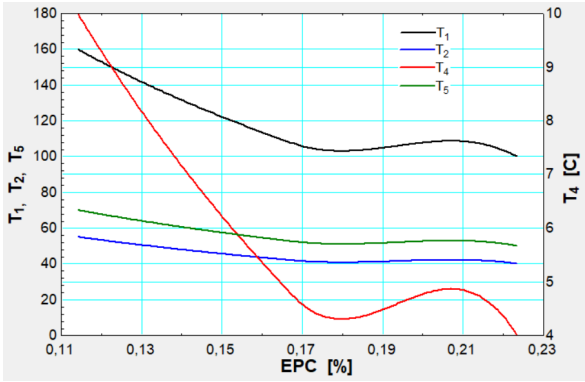

Figure 10. The effect of all independent temperature variables on EPC

According to the Variable Metric Method (VMM) optimum values of T_1, T_2, T_4 and T_5 are found as 100°C. 40°C. 4°C and 50°C respectively for maximum COP value of 0.7884 by making 36 iterations. VMM run 47 iterations for maximizing EPC and found optimum T_1, T_2, T_4 and T_5 values as 100°C, 40°C, 4°C and 50°C with max EPC 0.2234.

Nelder-Mead Method (NMM) gives more sensitive results for optimum values of T_1, T_2, T_4 and T_5 as 100°C, 40°C, 4°C and 55.77C

respectively. The maximum COP value is found as 0.7969 by making 197 iterations. According to NMM for max EPC objective function optimum values of T_1, T_2, T_4 and T_5 are found as 100°C. 46.89°C, 4°C and 69.88°C respectively with max EPC 0.2294.

According to Direct Method (DM) optimum values are found as 100°C for T_1, 40.01°C for T_2, 9.996°C for T_4 and 70°C for T_5 with max COP 0.8235 by making over 1000 iterations. DM found the optimum values of T_1, T_2, T_4 and T_5 as 100°C, 40°C, 4.01°C and 70°C respectively when objective function is set for max EPC. Max EPC value is found as 0.2323.

Genetic Method (GM) run over 1100 iterations and found 100°C for optimum T_1, 40.26°C for optimum T_2, 9.764°C for optimum T_4 and 70°C for optimum T_5 with max COP value of 0.823. When objective function is set for maximizing EPC optimum values of T_1, T_2, T_4 and T_5 are found as 102.6°C, 40.33°C, 4.026°C and 69.96°C respectively with max EPC 0.2311.
Weak solution and strong solution concentration ratios are reverse proportional with both energetic and exergetic efficiency of the system as seen on Figure 11 and Figure 12. The lower concentration ratio means higher efficiency.

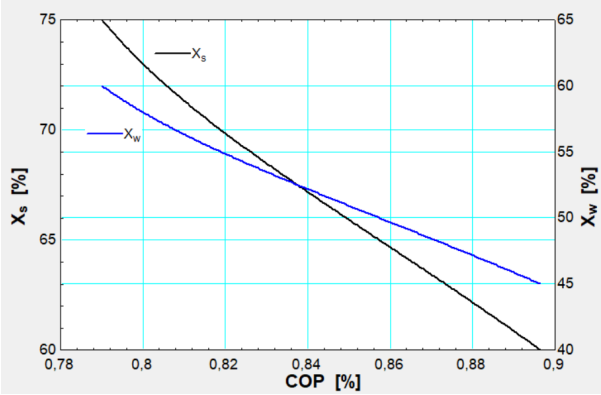

Figure 11. The effect of all independent concentration variables on COP

However, it must be mentioned that if X_w or X_s values keep decreasing at some critical point, absorption prosses fails due to low concentration ratio. The absorbent material is LiBr in the system, the more concentration ratio means higher absorption of heat that is absorbed from cooling space in evaporator. In addition to the fact, flow ratio "F" decreases by difference between X_s and X_w. Concentration ratios can be decreased to some critical point in order maximize energetic and exergetic efficiencies without failing the absorption prosses and causing low flow ratio. Therefore, boundary conditions are crucial to determine the optimum value.

The optimum weak and strong solution concentration ratios are calculated by defining both ratio as an independent parameter and two single objective functions are used one for maximizing COP and the other for maximizing EPC. Five different optimization methods are used same as temperature values as shown in Table 4.

Optimum values of concentration values are found much more rigid and stable than temperature values in each optimization method.

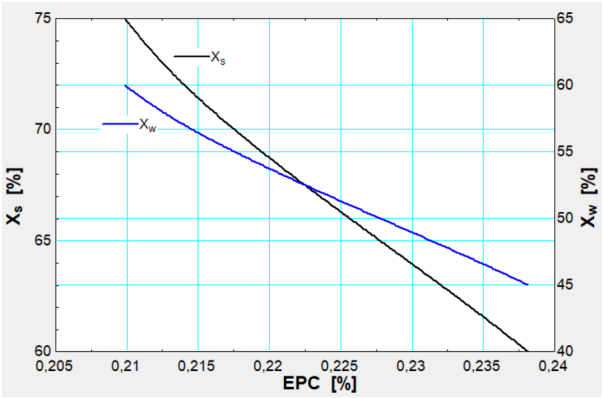

Figure 12. The effect of all independent concentration variables on EPC

Table 4. Optimum concentration ratios (X_w-X_s) with different optimization methods

		X_w	X_s
Conjugate Directions Method	**Value**	45 %	60 %
	COP	0.8964	0.8964
	EPC	0.2381	0.2381
	Iterations	156	69
Variable Metric Method	**Value**	45%	60%
	COP	0.8964	0.8964
	EPC	0.2381	0.2381
	Iterations	15	15
Nelder-Mead Method	**Value**	45%	60%
	COP	0.8964	0.8964
	EPC	0.2381	0.2381
	Iterations	12	12
Direct Method	**Value**	45%	60%
	COP	0.8961	0.8964
	EPC	0.2381	0.238
	Iterations	550	550
Genetic Method	**Value**	45%	60%
	COP	0.8964	0.8964
	EPC	0.2381	0.2381
	Iterations	1111	1111

3.3. Energy and exergy flow in the system

WHDACS used in this study feeds by the waste heat discharged from Yatagan Thermal Power Plant. Thus, superheated waste steam should be drawn between the flow lines mid-pressure line and low-pressure line at staged turbines.

Superheated steam flow between mid-pressure and low-pressure flow line is 1.18Bar, 172°C and 145MWt total thermal energy [34]

All independent parameters are set as an independent parameter in the software and iterated 10 steps in boundary conditions. While T_1 oscillates between 100-160°C, T_2 between 40-55°C, T_4 between 4-10°C, T_5 between 50-70°C, X_w between 45-60%, X_s between 60-75% and Q_{eva} is set to constant value of 175kW, power of entire system elements, mass flow rates and system efficiencies are as shown in Table 5.

For instance, while all independent parameters are in their lowest level, system efficiencies are at the highest level and it is vice versa for the highest level of independent parameters. The most dramatic and interesting fall is in EPC value in Run-2 from 0.245 to 0.1827 just one step further from the optimum values of the independent parameters.

Therefore, it is observed that optimum values of generator temperature, condenser temperature, evaporator temperature, absorber temperature, weak and strong solution concentration ratios are significant over system efficiencies.

Also, these are significant over mass flow rate in weak solution flow line and strong solution flow line which can be describe as absorbent flow line. On the other hand, in cooling flow line which is followed by cooling fluid H_2O from 1 to 4 till mixing with the absorbent LiBr, mass flow rate is relatively constant, small changes occur while independent parameters oscillate between their boundary values.

That's why evaporator power is set to a constant value which is considered as 175W in order to make it easy to compare with the results found in literature. However, power of evaporator is the main output of the system and should be considered according to cooling requirements.
So, power of evaporator is set to be independent parameter between 50 to 500 kW while other independent parameters are set to their optimum values in order to see how mass flow rate and power of system elements such as absorber and condenser changes.

As seen in Figure 13. mass flow rates except $\dot{m}_1$ and power of condenser and absorber increases dramatically. It should be expressed that negative value in power of absorber and condenser shows the direction of energy flow not the quantitative value.

Table 5. Mass flow rate and power of system elements in different values of independent parameters (10 iterations in boundary conditions)

	COP	EPC	$\dot{m}_1$	$\dot{m}_5$	$\dot{m}_{10}$	Q_{abs}	Q_{con}	Q_{gen}	T_1	T_2	T_4	T_5	X_w	X_s
Run-1	0.865	0.245	0.0748	0.2243	0.2991	-190.6	-188.4	202.4	**100**	**40**	**4**	**50**	**45**	**60**
Run-2	0.848	0.183	0.0750	0.2332	0.3081	-193.6	-189.3	206.4	**106.7**	**41.67**	**4.667**	**52.22**	**46.67**	**61.67**
Run-3	0.831	0.171	0.0751	0.2421	0.3172	-196.9	-190.2	210.5	**113.3**	**43.33**	**5.333**	**54.44**	**48.33**	**63.33**
Run-4	0.815	0.161	0.0753	0.2511	0.3264	-200.2	-191.1	214.8	**120**	**45**	**6**	**56.67**	**50**	**65**
Run-5	0.798	0.151	0.0755	0.2601	0.3356	-203.7	-192	219.2	**126.7**	**46.67**	**6.667**	**58.89**	**51.67**	**66.67**
Run-6	0.783	0.142	0.0757	0.2691	0.3448	-207.1	-192.9	223.6	**133.3**	**48.33**	**7.333**	**61.11**	**53.33**	**68.33**
Run-7	0.768	0.134	0.0759	0.2782	0.3541	-210.4	-193.8	227.9	**140**	**50**	**8**	**63.33**	**55**	**70**
Run-8	0.754	0.126	0.0761	0.2874	0.3635	-213.3	-194.7	232.2	**146.7**	**51.67**	**8.667**	**65.56**	**56.67**	**71.67**
Run-9	0.741	0.119	0.0763	0.2966	0.3728	-215.8	-195.7	236.3	**153.3**	**53.33**	**9.333**	**67.78**	**58.33**	**73.33**
Run-10	0.728	0.112	0.0765	0.3058	0.3823	-217.6	-196.6	240.5	**160**	**55**	**10**	**70**	**60**	**75**

Mass flow rate is critical parameter while designing and sizing system elements. High mass flow rates are undesirable because of the difficulties to control the flow and high-power requirements in the circulation-flow line. It should be examined that how power of evaporator effects the power of generator which is the energy input system element and COP and EPC before determining the optimum evaporator power.

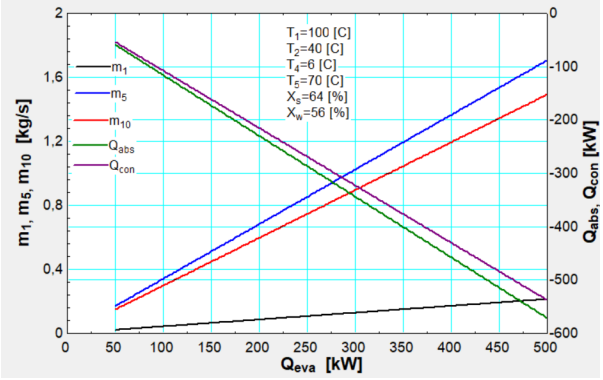

Figure 13. The effect of Q_{eva} on mass flow rate and Q_{abs}-Q_{con}

Figure 14 shows that power of the evaporator has significant effect on power of generator but not on system efficiencies.

Therefore, while determining the optimum value of evaporator power, the main determinant should be mass flow rates. Waste heat discharged from Yatagan Thermal Power Plant is quite high enough to feed all generator requirements but mass flow rates are getting above the critical point of 1kg/s when Q_{eva} exceeds over 300kW.

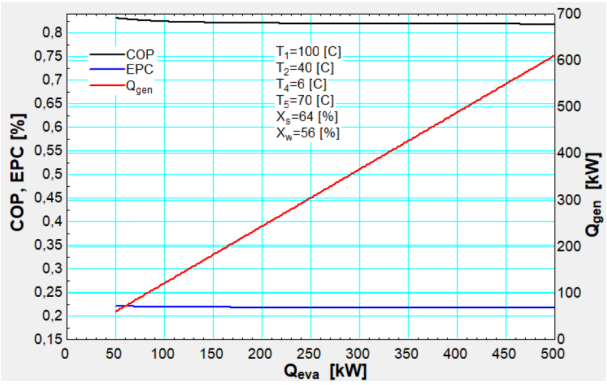

Figure 14. The effect of Q_{eva} on COP-EPC and Q_{gen}

Thus, optimum evaporator power should be considered around 300 kW in this case scenario. Figure 15 shows the effect of generator temperature on exergy flows in flow lines 1-7-8-9-10 and exergy destruction in system elements. The exergy flow in the flow lines increases depending on the generator temperature. While the exergy destruction values in the condenser, evaporator and absorber system elements remain relatively constant, exergy destruction in the generator increases significantly. Especially, between 100-110°C exergy destruction in generator increases exponentially and linear rise follows after 110°C. Therefore, selection of T_1 close to 100°C helps to reduce exergy destruction in generator.

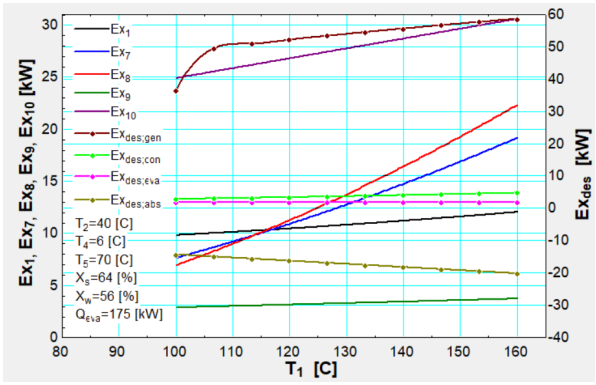

Figure 15. The effect of T_1 on exergy flow in related flow lines and exergy destruction in system elements.

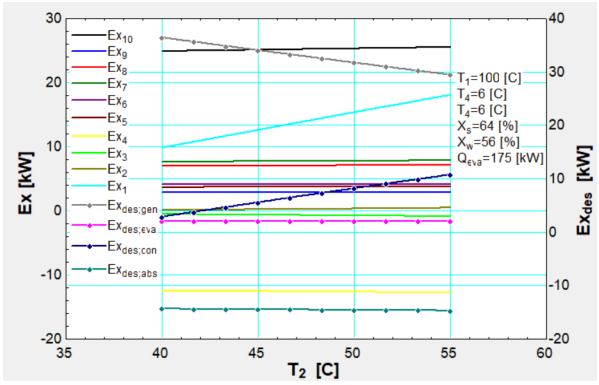

Figure 16. The effect of T_2 on exergy flow in related flow lines and exergy destruction in system elements.

Exergy flows in flow lines 2-3-4-5-6-7-8-9 increases slightly by condenser temperature while exergy flow in flow line 1 and 10 increases at high rate as seen in Figure 16. Exergy destruction in condenser is reversely proportional with condenser temperature. Exergy destruction decreases in generator by temperature of condenser increases.

Temperature of evaporator decreases the exergy flow in flow line 10 and increases exergy flow in

flow line 4 and exergy destruction in absorber while it slightly decreases exergy destruction in evaporator as seen in Figure 17.

It is observed that energetic change in exergy flow in flow lines except 4 and exergy destruction except absorber is not significant. Temperature of absorber is significant for both exergy flow in flow lines of absorbent flow and exergy destruction of system elements as seen in Figure 18. engineer while designing or sizing absorber unit in particular.

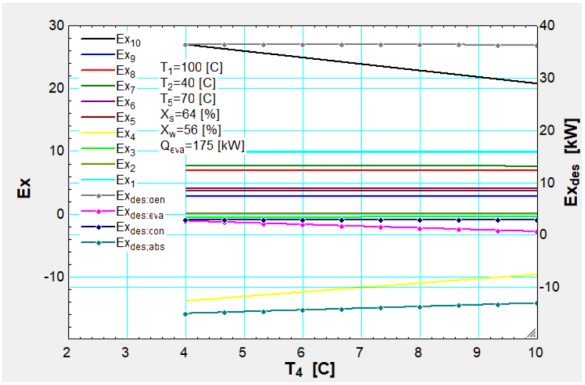

Figure 17. The effect of T_4 on exergy flow in related flow lines and exergy destruction in system elements.

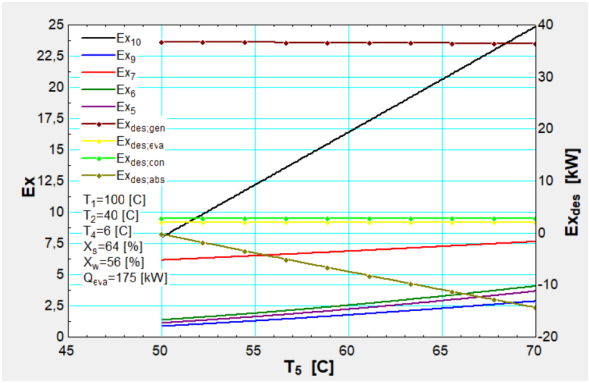

Figure 18. The effect of T5 on exergy flow in related flow lines and exergy destruction in system elements

Concentration ratio of weak solution is significant over exergy flow in flow lines especially 7-8-10 and exergy destruction in absorber. As seen in Figure 19 exergy destruction in absorber is exponentially reverse proportional with the concentration ratio of weak solution while exergy flow in flow line 7-8-10 are exponentially increasing by the weak solution concentration ratio.

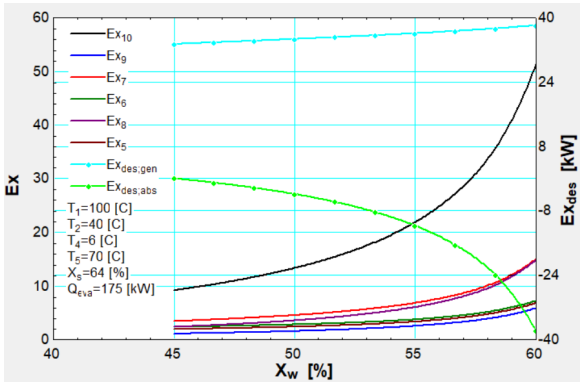

Figure 19. The effect of X_w on exergy flow in related flow lines and exergy destruction in system elements

Exergy flow in flow lines 5 to 10 is reversely proportional by concentration ratio of strong solution and it is observed that decrement is getting higher after 68%. Also, exergy destruction in absorber and generator exponentially increases after 68%. Therefore 68% of strong solution concentration ratio is critical point for both max exergy flow in flow lines and min exergy destruction in system elements as seen in Figure 20.

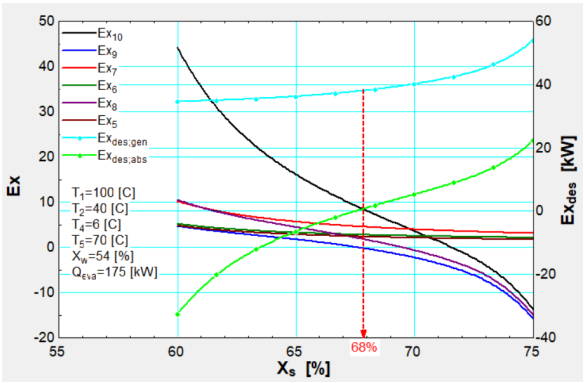

Figure 20. The effect of X_s on exergy flow in related flow lines and exergy destruction in system elements

Exergy destruction values in each system element, physical and total exergy values in each flow line and mass flow rate values at optimum conditions of system elements can be seen in Figure 21.

3.4. Potential of WHDACS fed by Yatagan thermal power plant

Thermal power of flow line between mid-pressure and low-pressure turbine flow line is 145 MWt and mass flow rate is much greater than mass flow rate of superheated steam needed by

generator. Therefore, steam flow from power plant to ACS should be divided to parallel flow lines which can be arranged by distribution center as seen in Figure. 22. Each flow line is designed to feed an individual ACS by the help of appropriate pumps to ensure the proper circulation.

WHDACSs COP values are around 0.7 and in some particular conditions it can be reached to 0.82 and all optimum conditions are discussed earlier.

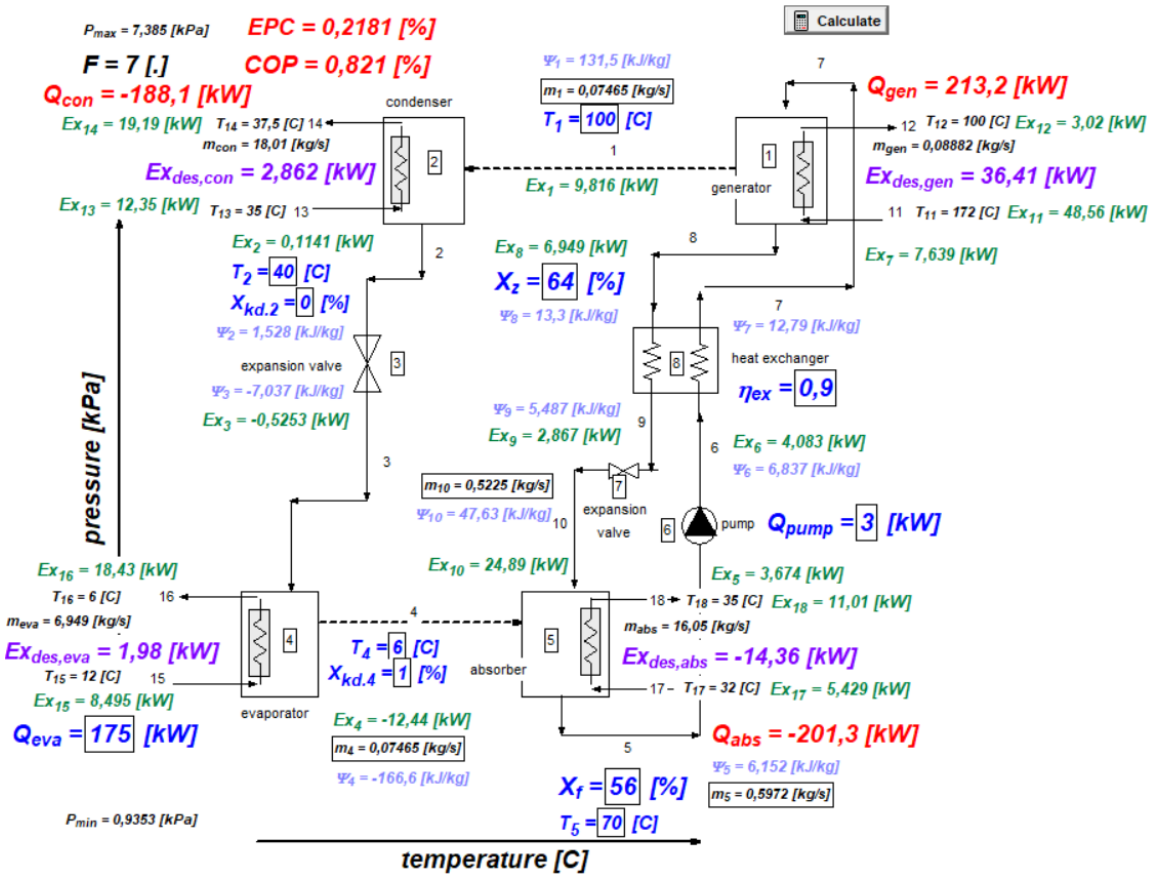

Figure 21. Exergy destruction in system elements and flow lines

It is necessary to add distribution center as shown in Figure 22, between Yatagan Thermal Power Plant and each ACS which means more energy loss will occur due to distribution flow lines, plumbing components and even means more pressure loss due to plumbing corners, valves, turbulent flow and pumps. All energy loss is assumed to be 15%. These mentioned losses depend on distribution line position, length, material, number and properties of plumbing elements [34, 35]. Since, the optimum ACS is 300 kW, the number of parallel flow lines would reach 280. If the power of evaporator considered as 400kW number of parallel flow lines would reach 210, parallel flow

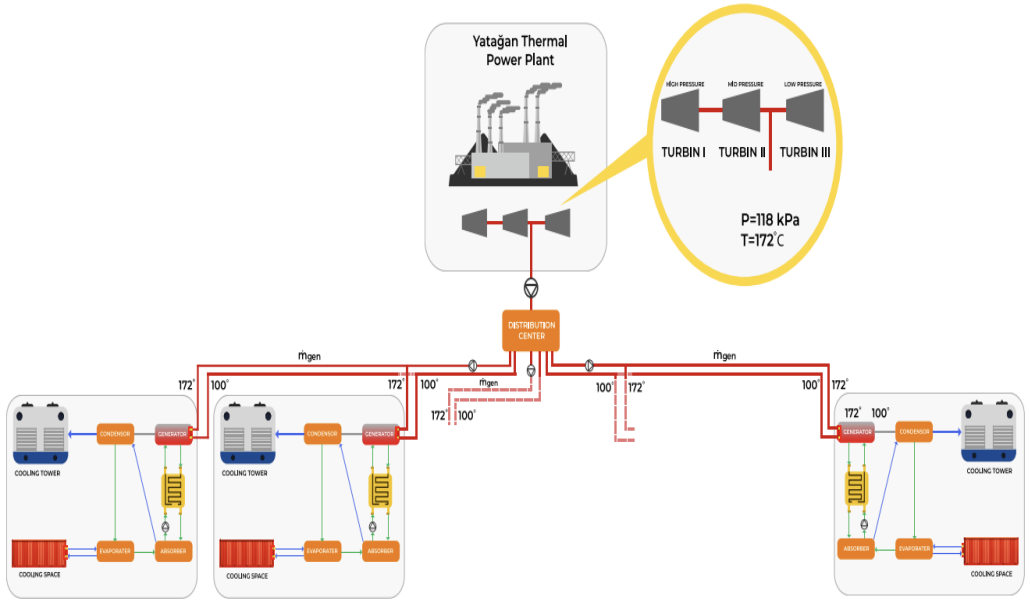

Figure 22. Schematic presentation of superheated steam distribution taken from Yatagan Thermal Power Plant

lines would reach 340 if power of the evaporator designed as 250kW. Either way cooling potential reaches 84MWt approximately.

It can be defined that total exergy flow in ACS applications is composed of kinetic, potential, physical and chemical exergy due to lack of any other energy input source such as electrical, nuclear etc. Kinetic and potential exergy is neglectable in ACS because work against gravity or kinetic exergy change is quite small when it is compared with other exergy flow values [36, 37].

It is same for chemical exergy flow in both cooling cycle and absorption cycle [38, 39]. In fact, chemical exergy potential $\mu_i$calculation method is coded to the software and the results are examined, It is observed that chemical exergy flow can be neglected, even "0" in cooling cycle. Therefore, the main component for exergy flow in ACS is physical exergy which is dependent to enthalpy and entropy difference between flow point conditions and dead state thermophysical properties.

The key part is to determine the dead state conditions in order to find exact exergy in flow lines or system elements. As it is discussed in the study made by [36]. There are different approaches for determining the dead state conditions. It is underlined that in most studies, dead state conditions are taken as the conditions of surrounding environment. But in the mentioned study, this generalization is criticized for being some system elements are not interacted directly to the surrounding environment which the fluid cannot be in equilibrium with. Therefore, it is suggested that system elements should be divided into subsystems considering different surrounding environment. In this study, dead state conditions are taken as ambient conditions for Mugla city regarding cooling cycle flows though evaporator, condenser and absorber with cooling tower. Only few system elements are surrounded by other system elements and this is not significant over the total energy and exergy flow between flow lines.

To avoid the conflict, it is best recommended that exergy destruction parameters provide more precise outputs for exergetic cycle of system than exergy values of flow line and system elements. Exergy destruction in generator is greater than exergy destruction in absorber, condenser and evaporator respectively as seen in Figure 21. This course is same as the exergy destruction values in the Literature [36, 40, 41]. If exergy destruction defined as improvement potential of system element, it is certain that generator is the most developable system element in this case.

4. Conclusion

In this paper, energy and exergy analyses are carried out for single stage LiBr-H_2O ACS with

cooling tower by using EES program. Energetic and exergetic performance of single stage LiBr-H_2O ACS is analyzed in order to determine whether waste heat of Yatagan Thermal Power Plant is convenient to drive selected absorption cooling system or not. It is seen that T_1, T_2, T_4, T_5, X_w, X_s parameters are the most important parameters determining the system efficiency.

At first, T_1, T_2, T_4, T_5, X_w, X_s are set as independent parameters and single effect of each independent parameter on COP and EPC is found while other independent parameters are set to a constant (optimum) value.
Optimum values of T_1, T_2, T_4, T_5, X_w, X_s are found as; T_1=100°C. T_2=40°C. T_4=10°C for max COP 4°C for max EPC. T_5=70°C. X_w=45% and X_s=63.41 %.

Then, all independent temperature parameters and concentration ratios are interacted with each other in order to find more accurate optimum parameters. Five different optimization processes are used and found; 100°C for T_1, 46.86°C for T_2, 9.996°C for T_4 and 70°C for T_5, 45% for X_w,60% for X_s by using Nelder-Mead Method.

Evaporator power is examined as an independent parameter to observe the effect on other system elements and mass flow rates. 300kW evaporator power is the optimum power for ACS driven by waste heat discharged from Yatagan Thermal Power Plant.

If analysis redone by changing the prospect for min exergy destruction perspective, selection of T_1 close to 100°C helps to reduce exergy destruction in generator.
Also, 68% of strong solution concentration ratio (X_s) is a critical point for max exergy flow and min exergy destruction in system elements.
Exergy destruction in generator is greater than exergy destruction in absorber, condenser and evaporator.

WHDACS would be preferable for cold storage especially for local products.
As a result, waste heat of Yatagan Thermal Power Plant is a convenient source for ACS especially for the kind that uses LiBr-H_2O. All results showed that ACS driven by waste heat of Yatagan Thermal Power Plant has similar efficiency, mass flow rate and power values with the system results presented in the literature which are driven by other energy sources. This means Yatagan Thermal Power Plant carries out sufficient thermodynamic properties to drive ACS. It is observed that WHDACS are preferable for cold storage especially for local products that need cold storage.

For further motivation, there are so many questions waiting to be answered such as if ACS which uses different fluid couples are more congruent with waste heat of Thermal Power Plants or not. What is the potential of countries for WHDACS? How does WHDACS contribute to eliminate the foreign dependency in energy for especially developing countries?

Article Information Form

Funding
Authors have no received any financial support for the research, authorship or publication of this study.

Authors' Contribution
In the study carried out, Author 1 under the headings of evaluation of the results obtained, arrangement of the text and examination of the results, the author 2 under the titles of forming the idea, making the design, performing the numerical analysis and literature review.

The Declaration of Conflict of Interest/ Common Interest
No conflict of interest or common interest has been declared by authors.

The Declaration of Ethics Committee Approval
This study does not require ethics committee permission or any special permission.

The Declaration of Research and Publication Ethics
Authors of the paper declare that they comply with the scientific, ethical and quotation rules of SAUJS in all processes of the paper and that they do not make any falsification on the data collected. In addition, they declare that Sakarya University Journal of Science and its editorial board have no responsibility for any ethical violations that may be encountered, and that this

study has not been evaluated in any academic publication environment other than Sakarya University Journal of Science.

References

[1] O. Akdemir, A. Güngör, "Cycles Developed to Increase Efficiency of Absorption Cooling Systems" V National Plumbing Engineering Congress and Exhibition, İzmir, 2001,

[2] A. J. Elsafty, Al-Daini, "Economical comparison between a solar-powered vapour absorption air-conditioning system and a vapour compression system in the Middle East," Renewable Energy, 25, 569-583, 2002.

[3] G.G. Maidment, R.M., Tozer, "Combined cooling heat and power in supermarkets." Applied Thermal Engineering, 22, 2002.

[4] A. Kaya, "Performance Analysis and Optimization of Absorption Cooling Systems", Master Thesis, Yıldız Teknik University, İstanbul, Türkiye, 2011.

[5] C. Wu, L. Chen, F. Sun, "Optimization of Solar Absorption Refrigerator." Applied Thermal Engineering, 17, 1997.

[6] T.S. Ravikumar, L. Suganthi, A.S. Anand, "Exergy analysis of solar assisted double effect absorption refrigeration system." Renewable Energy, 14, 1998.

[7] A. Şencan, "Absorbsiyonlu Soğutma Sisteminin Tasarımı ve S.D.Ü. Oditoryumunda Uygulanabilirliğinin Araştırılması", Master Thesis, Süleyman Demirel University, Isparta, Türkiye, 1999.

[8] Z.F. Li, K. Sumathy "Simulation of a Solar Absorption Air Conditioning System." Energy Conversion and Management, 42, 313-327, 2001.

[9] Z.F. Li, K. Sumathy "Technology Development in the Solar Absorption Air-Conditioning Systems." Renewable and Sustainable Energy Reviews, 4, 267-293, 2000.

[10] N. Kurtdere, "Thermodynamic Investigation of Absorption Cooling Systems Working with Solar Energy System Simulation and Analysis" Master Thesis, Yıldız Technical University, Istanbul, Turkey, 2010.

[11] R. Fathi, C. Guemimi, S. Ouaskit, "An Irreversible Thermodynamic Model for Solar Absorption Refrigerator" Renewable Energy, 29, 1349-1365, 2004.

[12] M. Balghouthi, M.H. Chahbani, M. Guizani, "Feasibility of Solar Absorption Air Conditioning in Tunisia" Building and Enviroment, 43, 1459-1470, 2008.

[13] İ. Atmaca, A. Yiğit, "Simulation of Solar Energy Sourced Absorption Cooling System". Dokuz Eylül University Faculty of Engineering Journal of Science and Engineering, 3, 125-136, 2002.

[14] F. Assilzadeh, S.A. Kalogirou, Y. Ali, K. Sopian "Simulation and Optimization of a LiBr Solar Absorption Cooling System with Evacuated Tube Collectors". Renewable Energy, 30, 1143-1159, 2005.

[15] K.C.A. Alam, B.B. Saha, A. Akisawa, T. Kashiwagi, "Optimization of a Solar Driven Absorption Refrigeration System" Energy Conversion and Management, 42, 741-753, 2001.

[16] J. Chen, J.A. Schouten, "Optimum Performance Characteristics of an Irreversible Absorption Refrigeration System" Energy Conversion and Management, 39, 999-1007, 1998.

[17] L. Chen, Y. Li, F. Sun, C. Wu, "Optimal Performance of an Irreversible Absorption Refrigerator" Exergy, an International Journal, 2, 167-172, 2002.

[18] M. Ishida, J. Ji, “Graphical Exergy Study on Single Stage Absorption Heat Transformer” Applied Thermal Engineering, 19, 1191-1206, 1999.

[19] M.M. Talbi, B. Agnew, “Exergy Analysis: an Absorption Refrigerator Using Lithium Bromide and Water as the Working Fluids” Applied Thermal Engineering, 20, 619-630, 2000.

[20] T. Cao, H. Lee, Y. Hwang, Radermacher R, Chun HH “Performance investigation of engine waste heat powered absorption cycle cooling system for shipboard applications” Applied Thermal Engineering, 90, 820-830, 2015.

[21] J. Fernandez-Seara, A. Vales, M. Vazquez, “Heat recovery system to power an onboard NH3-H2O absorption refrigeration plant in trawler chiller fishing vessels” Applied Thermal Engineering, 18, 1189-1205, 1998.

[22] C. Ezgi “Design and thermodynamic analysis of an H2O-LiBr AHP system for naval surface ship application” International Journal of Refrigeration, 48, 153-165, 2014.

[23] A.A. Menzela, S.M. Hanriot, L. Cabezas-Gomez, J.R. Sodre, “Using engine exhaust gas as an energy source for an absorption refrigeration system” Applied Energy, 87, 1141-1148, 2010.

[24] A.K. Kavaklı, “Egzoz Gazı ile Çalışan Absorbsiyonlu Soğutma Sisteminin Otobüslerde Kullanımı” Master Thesis, Balıkesir University, Balıkesir, Türkiye, 2005.

[25] Y. Üst, “Ecological Performance Analysis and Optimization of Energy Production Systems” Ph.D. Thesis, Yıldız Technical University, Graduate School of Natural and Applied Sciences, İstanbul, Turkey, 2005.

[26] Y. Üst, B. Şahin, T. Yılmaz, “Optimization of Regenerative Gas-turbine Cogeneration System Based on A New Exergetic Performance Criterion Exergetic Performance Coefficient” Journal of Power and Energy, 221, 447-456, 2007.

[27] M.K. Shahzad, Y. Ding, Y. Xuan, N. Gao, G. Chen “Energy efficiency analysis of a multifunctional hybrid open absorption system for dehumidification. heating. and cooling: An industrial waste heat recovery application” Energy Conversion and Management, 243, 2021.

[28] E. Kaçan, K. Ülgen “Theoretical Analysis of Solar Assisted Heating and Absorption Cooling Systems” Renewable Energy Syposium, Girne, Cypus, 2013.

[29] H. Erdem, A. Dagdas, S. Sevilgen, “Thermodynamic analysis of an existing coal-fired power plant for district heating/cooling application” Applied Thermal Engineering, 30, 181-187, 2010.

[30] E. Turhan, “Comparative Thermodynamic Analysis For An Absorption Refrigeration System On An Aluminum Profile Factory” Msc. Thesis, Istanbul, Technical University, İstanbul, Turkey, 2018.

[31] M.Z. Yılmazoğlu, “Thermodynamic Analysis Of A Single Effect Absorption Cooling System” Gazi University Journal of Science, 25, 397-404, 2010.

[32] B.H. Bavul, “Design And Construction Of An Optimum Libr-Water Absorption Refrigeration Machine For Air Conditioning” Phd. Thesis. Uludağ University Graduate School of Natural and Applied Sciences, Bursa, Turkey, 2017.

[33] A.H. Gündüz, C. Cimşit, “Thermodynamic Analysis Of Solar Sourced Absorption Refrigeration System With Different Working Pairs” Engineer and Machinery, 63, 201-221, 2022.

[34] M. Kahraman, H.M. Bağ, “Feasibility Report Greenhouse Project Heated by waste heat of Afşin Elbistan Thermal Power Plant” Eastern Mediterrian Development Agency, Osmaniye, Turkey, 2020.

[35] Resistant Structures Technologies Engineering, “Feasibility Report to Heat Greenhouses via Waste Heat Driven form Thermal Power Plant”. Ministry of Industry and Technology of Turkish Republic, 2020.

[36] A.M. Blanco-Marigorta, C.J. Marcos, “Key issues on the exergetic analysis of H2O/LiBr absorption cooling systems. Case studies” Case Studies in Thermal Engineering, 28, 101568, 2021.

[37] D.M. Paulus, R.A. Gaggioli, “The Dead State According to the Available Energy of Gibbs” New York, USA, AES. vol. 40 ASME, 2000.

[38] Z. Yuan, K.E. Herold, “Thermodynamic properties of aqueous lithium bromide using a multiproperty free energy correlation” Heating, ventilation, air conditioning and refrigeration Research, 11, 377–393, 2005.

[39] D.S. Kim, C.A.I.A. Ferreira, “Gibbs energy equation for LiBr aqueous solutions” International Journal of Refrigeration, 29, 36–46, 2006.

[40] K.A. Sencan, S.A. Yakut, S. Kalogirou, “Exergy analysis of lithium bromide/water absorption systems” Renewable Energy, 30, 645-657, 2005.

[41] R. Palacios-Bereche, R. Gonzales, S.A. Nebra, “Exergy calculation of lithium bromide–water solution and its application in the exergetic evaluation of absorption refrigeration systems LiBr-H2O” International Journal of Energy Research, 36, 166-181, 2012.

Sakarya Üniversitesi Fen Bilimleri Dergisi
Sakarya University Journal of Science

ISSN : 2147-835X
Publisher : Sakarya University

Vol. 29, No. 1, 71-82, 2025
DOI: https://doi.org/10.16984/saufenbilder.1589003

Research Article

Characterization of Olive Seed Powder Incorporated Low Density Polyethylene Composites

Sibel Tuna, İbrahim Şen*

Bursa Technical University, Central Research Laboratory, Bursa, Türkiye, sibel.tuna@btu.edu.tr, ibrahim.sen@btu.edu.tr
*Corresponding Author

ARTICLE INFO

Keywords:
Olive seeds
Natural fillers
Plant based fillers
Green composites
LDPE composites with Natural based fillers

Article History:
Received: 21.11.2024
Revied: 29.01.2025
Accepted: 13.02.2025
Online Available: 20.02.2025

ABSTRACT

Global warming, increasing production and consumption rates, environmental concerns have revealed the need for some innovative material studies, and studies on the use of polymeric composites prepared with natural based fillers have become widespread to increase environmental awareness and ensure sustainable production. Composite materials prepared by using easily accessible, affordable, lightweight, high-strength plant based fillers can be used in many areas. In this study, composites of low density polyethylene (LDPE), which is one of the most widely used thermoplastics, were prepared by injection moulding process using the waste seeds of olives (OS), which have an important place in Turkey's agriculture and economy, and the density, hardness (Shore D), spectroscopic (Fourier transform infrared (FTIR) spectroscopy), morphological (Scanning electron microscopy (SEM)), mechanical, thermal (Differential Scanning Calorimetry (DSC), Heat Deflection Temperature (HDT) and Vicat softening temperature) analyses of OS filled LDPE composites were performed. As a result of the study, an increase in hardness and elastic modulus values of OS filled LDPE composites was observed, while no noticeable decrease in thermal properties was seen.

1. Introduction

Environmental and ecological awareness, which has emerged as a result of increasing concerns about sustainability and environmental issues, has led to efforts to develop innovative materials in various sectors. Increasing environmental sensitivity and the enforcement of environmental regulations with greater seriousness, coupled with competitive cost concerns, bio based composite materials produced from environmentally friendly and renewable materials have become increasingly widely used to replace composite materials obtained from synthetic materials in this context [1–3].

When it comes to bio based composite materials, the first thing that comes to mind is composite materials reinforced with natural based fillers. In this context, plant based additives, which are considered as natural based fillers, are cost-effective and environmentally friendly materials that have come to the agenda as an alternative to the use of synthetic additives, suitable for many industrial applications, and can be used as reinforcement in the composite structures [4–6]. Their environmental impact is remarkable in that they do not cause chemical emissions in production and processing processes such as synthetic additives and minimise both fuel consumption and greenhouse gas emissions due to their light weight [7].

In addition to being environmentally friendly, one of the biggest advantages of composites containing plant based fillers is that they have lower density compared to synthetic additives. They have significant advantages over synthetic additives such as favourable cost, easy accessibility, high strength, high hardness, low density, fatigue and corrosion resistance, easy processability, high thermal and acoustic insulation performance [8–12].

Cite as: S. Tuna, İ. Şen (2025). Characterization of Olive Seed Powder Incorporated Low Density Polyethylene Composites, *Sakarya University Journal of Science*, 29(1), 71-82. https://doi.org/10.16984/saufenbilder.1589003

Studies have shown that plant based fillers can strengthen polymeric composites in general due to their low density, elongation tendency and high strength. In particular, fillers with higher surface area can be distributed more homogeneously, enabling a more compatible interface between the matrix and the reinforcement phase [13]. Plant based fillers are recognised as an alternative to synthetic fillers in various industries due to their comparable physical and mechanical performance [7, 14].

The automotive, construction, energy, sports, electronics, aerospace and aeronautics industries are the main areas of use of plant based composites [15]. Automotive companies such as Ford, Volkswagen, General Motors, Honda have started to use plant based fillers in parts such as trunk lids, floor coverings, ceilings, dashboard coverings, seat backs [16]. It is possible to witness the use of plant based composites in a wide variety of sectors and parts such as insulation boards, roof panels, door frames in the construction field [17], turbine blades in the energy field [18], rackets, golf clubs, surfboards in the sports field [15], telephone and computer cases and bodies in the electronics field [15, 19], interior panels and outer bodies in the aerospace field [15]. Commonly used plant based fillers can be listed as jute, kenaf, hemp, flax, bamboo, sisal, muaz bark, sugar cane [20–24]. These fillers have been studied with various thermoplastics and thermosets and are generally known to provide high toughness, acoustic absorption, improved thermal properties and corrosion resistance [7, 25, 26].

Polyethylene (PE), one of the most widely used thermoplastic materials in many sectors today, has various subclasses including low density PE (LDPE), linear low density PE (LLDPE), high density PE (HDPE) and ultra high molecular weight PE (UHMWPE) [27–29]. PE types, which have many features such as high processability, low cost, durability, chemical resistance, recyclability, can be used in many sectors such as packaging, construction, furniture, biomedical applications and industrial products by shaping with processes such as injection and extrusion [15, 30–33].

LDPE, is widely used in many industrial applications due to its versatile properties, usefulness and easy processability [34]. However, as a result of the insufficient properties of LDPE used alone in some applications and the increasing interest in the development of sustainable materials, studies have started to improve the properties of LDPE with various reinforcement phases. When the studies in the literature are examined, it is reported that the stiffness and tensile strength values of LDPE were improved in the study conducted by Rodriguez- Fabia et al. [35] by adding pulp fibre to the LDPE matrix, and in a study conducted by Taşdemir et al. [36], increases in the elastic modules and hardness properties of LDPE were observed in the use of wood fibre. In another study conducted by Gomes et al. [37] in which amazon palm fibre was used as the reinforcement phase, a decrease in strength was observed while an increase in the modulus of elasticity was reported.

Olive, which has an important place in the agriculture of Mediterranean countries, is widely used both with its fruit and oil and always stands out with its nutritional and economic value. While 90% of the world's olive cultivation is carried out in the Mediterranean basin, Turkey, with its approximately 170 million olive trees, ranks high in the world in terms of both the number of olive trees and olive production [38, 39]. Olives can be consumed as table olives after being harvested through various processes, or they can be obtained in the form of olive oil by separating the juice from the olive fruit. In high production and consumption cycles, olive seeds remain as plant waste without any added value. When the studies are evaluated, it is seen that olive seeds can be considered as biowaste and can be used especially in environmental studies such as water adsorption and heavy metal removal [40–43].

In this study, studies were carried out to evaluate olive seeds, a plant based filler, as a reinforcing phase and to prepare OS filled LDPE composites with OS concentrations ranging from 2.5% to 10% by injection moulding. In order to develop OS filled LDPE composites, the particle size and morphology of OS were first determined and its effect on the density, hardness, FTIR, SEM,

mechanical, DSC, HDT and Vicat temperature properties of OS filled LDPE composites were investigated. The aim of this study is to evaluate the use of OS waste from the agricultural sector as a reinforcing material for potential applications such as automotive, construction, sports and energy by producing LDPE based composites by injection moulding.

2. Experimental Details

2.1 Materials

Low density polyethylene (LDPE) polymer in powder form was supplied from the A+Plus Polimer in Izmir. Olive seeds (OS) were separated from olives collected from olive trees in the Marmara Region, dried and ground naturally and used.

1.1. Preparation of OS filled LDPE composites

Table 1 shows the sample codes and composite ratios used for OS filled LDPE composites. LDPE and OS powders were dried at 70 °C for 12 hours and after the moisture was removed, they were weighed in the specified proportions and blended in a ziplock bag until uniform according to the ratios given in Table 1. The OS filled LDPE composites were then injection moulded using a BOY/22A Pro Lab injection moulding machine at 205-210-205-200-200-200 ºC zone temperatures and 160 bar injection pressure. Samples were prepared according to the following standards: ISO 527-2 (Type 1A) for tensile test, ISO180 for impact test and ISO 75-2 for heat deflection temperature (HDT) tests.

1.2. Characterizations of OS, LDPE and OS filled LDPE composites

1.2.1. Density measurements

Density measurements of the LDPE and OS filled LDPE composites were calculated by taking into account the weights of the samples in air and water environments according to the Archimedes principle. Weight measurements were measured using Shimadzu-AUX321 brand/model precision balance. Three repetitions were performed for each sample.

Table 1. The ratios and sample codes of OS filled LDPE composites

Sample Code	LDPE, wt. %	OS, wt. %
LDPE	100	0
2.5OS	97.5	2.5
5OS	95	5
7.5OS	92.5	7.5
10OS	90	10

1.2.2. Hardness (Shore D) analysis

Shore D hardness tests of LDPE and OS filled LDPE Composites were carried out using the AMITTARI-HSM-SD-ST device at 23 °C temperature and 55% humidity in accordance with the ASTM D2240 standard, with 5 measurements for each sample.

1.2.3. Fourier transform infrared (FTIR) spectroscopy analysis

FTIR analyses, which were carried out to observe the existing functional groups and their changes in LDPE and OS filled LDPE composite structures, were performed with a Thermo Scientific Nicolet iS50 brand model FTIR spectrophotometer device. Spectra were recorded in the wavenumber range of 4000–600 cm^{-1} with 32 scan numbers and 4 cm^{-1} spectral resolution.

1.2.4. Particle size analysis

Particle size distributions of OS powders were characterized using a Malvern/Mastersizer 3000E brand/model laser particle size analyzer in the water phase as dispersant, and D10, D50 and D90 values representing 10%, 50% and 90% distributions of particle amounts were determined.

1.2.5. Scanning Electron Microscopy (SEM)

The morphological structures of LDPE and OS filled LDPE composites were examined with a Carl Zeiss/Gemini 300 brand/model scanning electron microscope and for this purpose, the fracture surfaces formed after the impact test were analyzed under 1000× magnification and 5 kV acceleration voltage. In order to provide conductivity to the samples, a thin gold/palladium layer coating process was performed before the analysis.

1.2.6. Mechanical tests

Tensile tests of the LDPE and OS filled LDPE composites were carried out at a speed of 100 mm/min according to the ISO 527-2 (Type 1A) standard. As a result of the tensile tests performed using the Shimadzu AGS-X universal testing machine, tensile strength (TS), elongation at break (EB) and modulus of elasticity (EM) values were analyzed. Impact tests were carried out using the Instron Ceast 9050 brand/model testing machine and a 5.5 J Izod hammer in accordance with the ISO 180/A standard, and as a result of the test, the Notched Impact Strength (NIS) values were evaluated.

1.2.7. Differential Scanning Calorimetry (DSC) analysis

DSC analyses of OS powder, LDPE sample and OS filled LDPE composites were carried out using TA Instruments/DSC250 brand/model device to investigate melting and crystallization behaviors and crystallinity ratios (Equation 1). Tests were carried out in the temperature range of -80 °C to 150 °C with a heating rate of 10 °C/min.

$$X_c = \frac{\Delta H_m}{\Delta H^\circ_m (1-w)} \quad (1)$$

While the ΔHm value in Equation 1 represents the melting enthalpy of LDPE, the ΔHom value represents the melting enthalpy of the completely crystalline form of the polymer, and this value is accepted as 285 J/g in the literature [44]. The *w* in the equation represents the weight ratio of the polymer in the mixture.

1.2.8. Heat Deflection Temperature (HDT) and Vicat softening temperature measurements

HDT tests of LDPE and OS filled LDPE composites were conducted according to the B method of the ISO 75-2 standard with a flexural stress of 0.45 MPa and a heating rate of 120 °C/h, and the Vicat softening temperature tests were carried out according to the A50 method of the ISO 306 standard with a force of 10 N and a heating rate of 50 °C/h using an Instron/Ceast HV3 brand/model testing device.

2. Results and Discussion

2.1. Characterization of OS powders

Particle size distribution and SEM image results of OS powder used in the composites are presented in Figure 1.(a-b), respectively. A single peak is seen in the particle distribution graph of OS powder in Figure 1.a. The D10, D50 and D90 values of OS powder were found to be 15.4 µm, 53.4 µm and 125 µm, respectively. In the SEM image given in Figure 1.b, it is seen that OS powder particles have an irregular shape and consist of particles of different sizes.

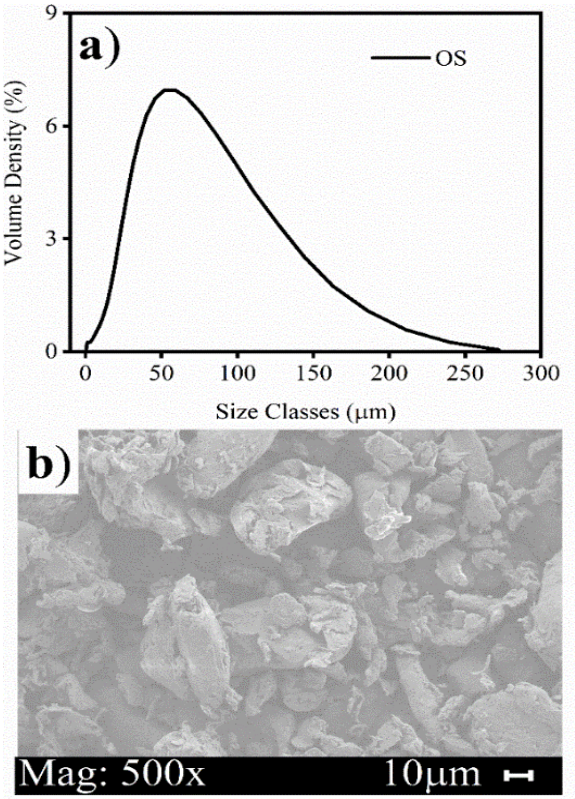

Figure 1. a) Particle size distribution and b) SEM image under 500× magnification of OS powder

2.2. Characterization of LDPE and OS filled LDPE composites

2.2.1. Physical properties

Density and hardness (Shore D) values of LDPE and OS filled LPDE composites are given in Table 2. It is observed that density values increase as OS amount increases in composites. Since the densities of plant based additives are generally in the range of 1.10-1.60 g/cm^3, the increase obtained in the study was found to be consistent with the literature [45, 46]. When the

hardness values in Table 2 are examined, although a small increase was observed with the addition of 2.5% OS, no significant change was observed in the other filled composites. This small increase is associated with an increase in the surface hardness of the composite when the surface hardness of the natural fibre is harder than that of the matrix [36, 47].

Table 2. Density and hardness test results of LDPE and OS filled LDPE composites

Analysis	LDPE	2.5OS	5OS	7.5OS	10OS
Density (g/cm^3)	0.9161±0.0005	0.9243±0.0005	0.9329±0.0002	0.9421±0.0010	0.9493±0.0016
Hardness (Shore D)	42.8±0.6	45.2±0.9	45.0±1.2	45.6±1.1	46.0±0.6

2.2.2. Fourier transform infrared (FTIR) spectroscopy analysis

FTIR spectra of LDPE and OS filled LDPE composites are given in Figure 2. When the spectra are examined, the characteristic peaks of the LDPE polymer are clearly observed. Among these peaks, the most characteristic one is the peak at 2918 cm^{-1} which represents the asymmetric stretching vibration of the CH2 molecule and the peak at 2851 cm^{-1} which represents the symmetric stretching vibration of the CH_2 molecule. Apart from this, the bending deformation at the wave number 1468 cm^{-1}, the symmetric deformation at the wave number 1370 cm^{-1} and the rocking deformation peaks at the wave number 716 cm^{-1} are also related to the functional groups in the LDPE structure [48, 49].

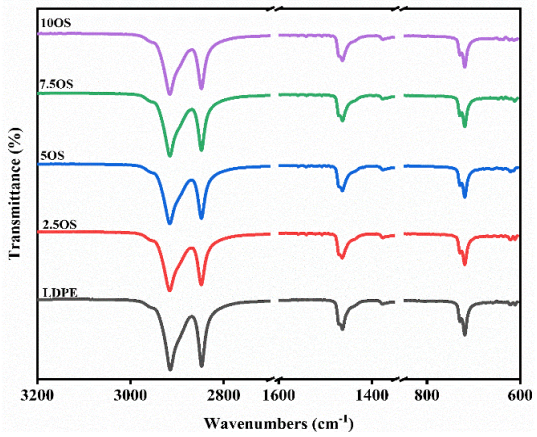

Figure 2. FTIR spectra of LDPE and OS filled LDPE composites

It can be mentioned that the addition of OS powder into the LDPE matrix does not cause a significant change in the FTIR spectrum. This situation shows that there is no chemical interaction between LDPE and OS powders. The absence of significant differences in the peaks and peak intensities supports the existence of physical intermolecular interactions such as hydrogen bonding and Van der Waals between LDPE and OS powders [50, 51].

2.2.3. Scanning electron microscopy (SEM)

SEM images of the LDPE and OS filled LDPE composites under 500× magnification are presented in Figure 3.

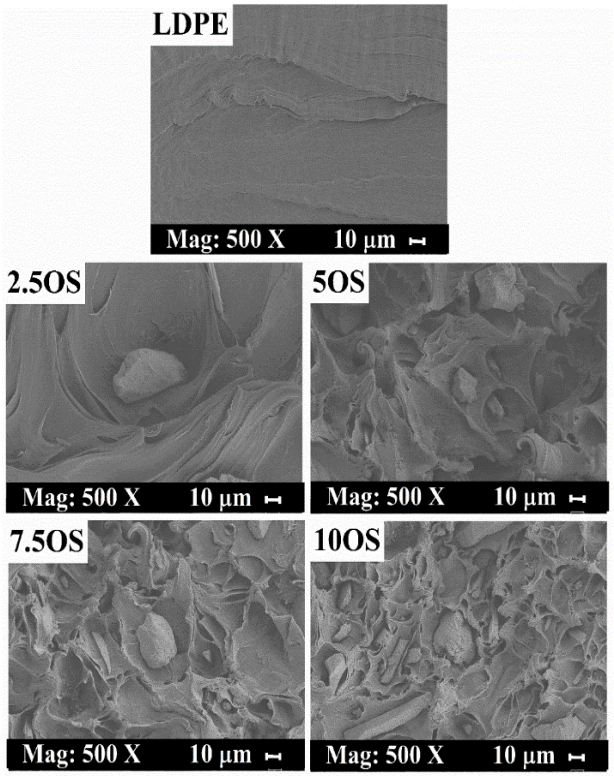

Figure 3. SEM micrograms of LDPE and OS filled LDPE composites at 500× magnification

When the SEM images in Figure 3 are examined, the fracture surface of LDPE exhibited a flatter fracture performance, while the addition of OS powder to the composite structure made the surface rougher. The SEM images of the

composites with OS powders show that there are large gaps between the OS particles and the matrix. In addition, the absence of LDPE matrix residues on the OS powder particles indicates that the surface interaction between LDPE and OS powders is low [52]. In composites containing higher amounts of OS powder, the increase in the amount of OS on the fracture surface caused these gaps to increase. This situation supports the decrease in TS, EB and NIS values from the mechanical test results in Table 3 and Figure 4 [52, 53].

2.2.4. Mechanical properties

The results of tensile and impact mechanical tests of LDPE and OS filled LDPE composites are given in Figure 4.(a-b) and Table 3.

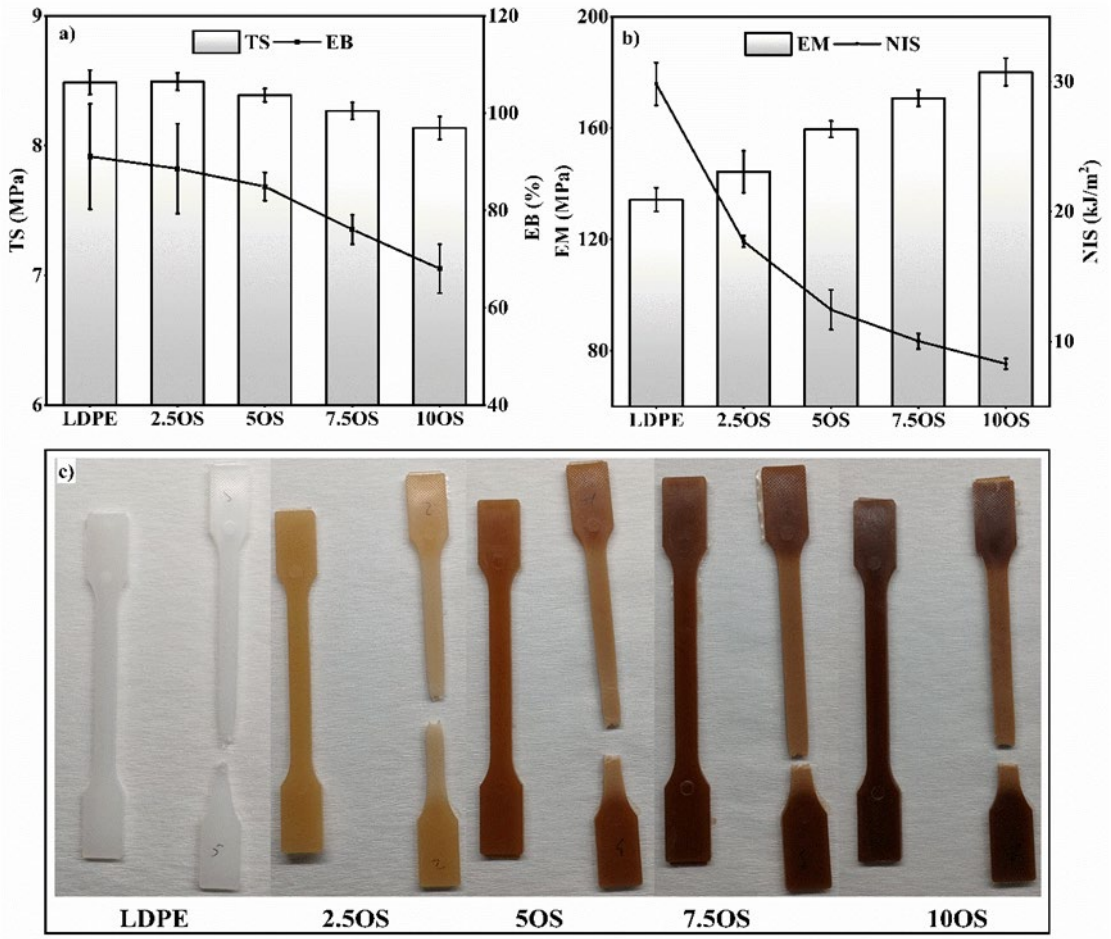

Figure 4. Changes in a) TS-EB, b) EM-NIS values according to varying OS ratios in LDPE composites and c) images of the tensile test bars

As shown in Figure 4.c, the colour of the composites changed from mustard to dark brown as the amount of OS increased. In addition, the test bars showed a homogeneous distribution in colour. Examining the EM values of the composites, it can be seen that the EM value of LDPE is 134 MPa, while it increases to 180 MPa in the 10% OS filled material, an increase of approximately 50%. A regular increase was observed as a function of the amount of OS in the composites containing 2.5, 5 and 7.5% OS powder. Tronc et al. [54] reported in their study that significant EM increases occurred. Arrakhiz et al. [55] also found in their study that the EM value of pure PP material increased from 1034 MPa to 1541 MPa with the addition of 25% pinecone dust. It was found that the reason for these increases obtained in both studies was due to the use of a harder filler material than the matrix. On the other hand, as the amount of OS in the LDPE matrix increases, the TS, EB and NIS values decrease. The decrease in these values is associated with the negative effect of the matrix on the force distribution under stress,

as seen in the SEM images of OS powders (see Figure 1 and Figure 3) [56]. In addition, the brittle structure of natural fibers also supports the decrease in EB values [54, 57]. When the rupture end points in Figure 4.c are carefully examined, it can be seen that while ductile rupture is observed in LDPE, more brittle rupture occurs as the amount of OS increases.

2.2.5. Differential Scanning Calorimetry (DSC) analysis

DSC analyses were performed to examine the temperature dependent heat transfer performances of the composites, DSC thermograms are presented in Figure 5 and the analysis results obtained from DSC thermograms are presented in Table 4.

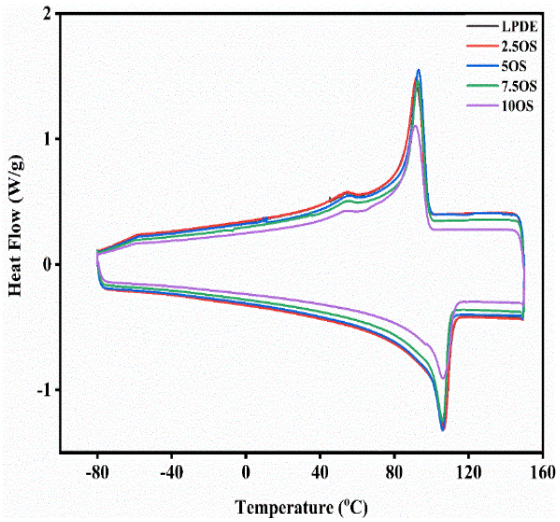

Figure 5. DSC thermograms of LDPE and OS filled LDPE composites with heating and cooling curves

As the amount of OS in the LDPE matrix increases, fluctuations are observed in both Tc and Tm temperature values. When we examined the Xc values, there were no significant changes in the Xc value in OS filled materials with a ratio of 2.5-5%, while decreases were observed in materials with a ratio of 7.5-10%. This can be explained by the fact that the use of OS filler at 2.5-5% has no significant effect on crystal formation in LDPE polymer, while the use of OS filler at 7.5 and 10% has an inhibitory effect on crystal formation [58]. Furthermore, the cellulose content of the plant based filler impedes heat transfer and diffusion between the LDPE molecular chains within the composite [59].

3.2.6. Heat Deflection Temperature (HDT) and Vicat softening temperature analysis

Graphical representation of HDT and Vicat softening temperature is given in Figure 6. In both values, no significant change was observed due to the increase in the amount of OS. Especially since it is known that the HDT temperature change depends on the thermal transition temperature of the matrix material and the change in the crystal structure, it can be interpreted that results are obtained in parallel with the Xc values obtained as a result of DSC analysis [60].

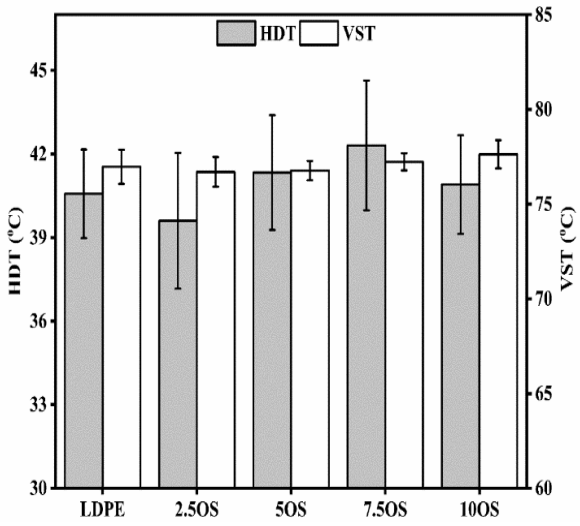

Figure 6. Changes in HDT and Vicat softening temperature according to varying OS ratios in LDPE composites

Table 3. Mechanical test results of LDPE and OS filled LDPE composites

Analysis	Parameter	LDPE	2.5OS	5OS	7.5OS	10OS
Tensile	TS (MPa)	8.490 ± 0.09	8.490 ± 0.07	8.390 ± 0.05	8.270 ± 0.07	8.140 ± 0.09
	EM (MPa)	134.3 ± 4.26	144.3 ± 7.53	159.6 ± 2.95	170.7 ± 2.93	180.1 ± 4.95
	EB (%)	91.10 ± 10.8	88.60 ± 9.22	84.91 ± 2.9	76.09 ± 3.03	68.02 ± 5.02
Impact	NIS (kJ/m^2)	29.82 ± 1.64	17.70 ± 0.44	12.45 ± 1.53	10.03 ± 0.59	8.290 ± 0.4

Table 4. DSC analysis results of LDPE and OS filled LDPE composites

Parameter	LDPE	2.5OS	5OS	7.5OS	10OS
Tc (°C)	92.10	91.91	93.000	92.60	91.50
ΔHc (J/g)	108.0	108.5	106.3	98.61	94.12
Tm (°C)	106.7	106.5	106.1	105.9	106.1
ΔHm (J/g)	108.9	108.3	105.9	100.0	84.20
Xc (%)	38.20	39.00	39.10	37.90	32.80

4. Conclusion

LDPE is one of the most widely used thermoplastic matrices worldwide. In some application areas, the production of composite materials with natural fillers added LDPE composites has gained importance when its properties are insufficient and the need for improvement is combined with both environmental pollution and cost reduction concerns.

In this study, in order to reduce the unit cost and to obtain more environmentally friendly material, OS was added into the LDPE matrix and characterisations were carried out. It was observed that as the amount of OS in LDPE increased, the density increased slightly in line with the densities of natural based fillers. While the hardness changes of LDPE composites filled with OS at varying ratios were close to each other, an increase was obtained compared to LDPE polymer. No chemical interactions were observed in the FTIR spectra, indicating that there are intermolecular physical interactions between OS powder and LDPE. In the SEM images, the gaps between the OS particles and the LDPE matrix interface supported the decrease in TS, EB and NIS values. In order to increase the weak interfacial interactions between the matrix and the filler material, it has been observed in the literature that binding agents are used and the interactions are increased.

There is a requirement for the use of a binding agent to achieve improved mechanical performance. When the EM values were analysed, it was observed that while the EM value of LDPE polymer was 134.3 MPa, this value increased up to 180.1 MPa with the use of 10% OS. When the thermal properties were analysed, small changes were observed in both Tc and Tm values. However, while there was no significant change in Xc values up to 7.5% filled OS, a decrease was observed in 10% OS composite. No significant change was observed in HDT and Vicat softening temperature values. Once the materials have been characterised, it will be possible to determine the areas in which such composites can be used, depending on their performance, their intended use and their cost. For example, if impact resistance is not desired, but instead cost-effectiveness is desired, the 4.2% decrease in TS value of 10OS material compared to LDPE polymer can be ignored. At the same rate, the EM value was also found to be maximum. In the future studies, it will be possible to obtain higher mechanical performance at higher OS ratios, taking into account the cost with the use of the necessary binding agents.

Article Information Form

Acknowledgments
Authors thank the Central Research Laboratory management for their support.

Funding
Authors has no received any financial support for the research, authorship or publication of this study.

Authors' Contribution
Sibel TUNA: Conceptualization, Investigation, Methodology, Formal analysis, Writing, Review & editing.
İbrahim ŞEN: Conceptualization, Investigation, Methodology, Resources, Review & editing.

The Declaration of Conflict of Interest/ Common Interest
No conflict of interest or common interest has been declared by authors.

The Declaration of Ethics Committee Approval
This study does not require ethics committee permission or any special permission.

The Declaration of Research and Publication Ethics
Authors of the paper declare that they comply with the scientific, ethical and quotation rules of SAUJS in all processes of the paper and that they do not make any falsification on the data collected. In addition, they declare that Sakarya University Journal of Science and its editorial board have no responsibility for any ethical violations that may be encountered, and that this study has not been evaluated in any academic publication environment other than Sakarya University Journal of Science.

References

[1] T. Väisänen, O. Das, L. Tomppo, "A review on new bio-based constituents for natural fiber-polymer composites.," Journal of Cleaner Production, vol. 149, pp. 582–596, 2017.

[2] I. I. Qamhia, S. S. Shams, R. F. El-Hajjar, "Quasi-isotropic triaxially braided cellulose-reinforced composites.," Mechanics of Advanced Materials and Structures, vol. 22, no. 12, pp. 988–995, 2015.

[3] V. K. Thakur, M. K. Thakur, "Processing and characterization of natural cellulose fibers/thermoset polymer composites.," Carbohydrate polymers, vol. 109, pp. 102–117, 2014.

[4] S. Siengchin, "Editorial corner–a personal view Potential use of'green'composites in automotive applications,." Express Polymer Letters, vol. 11, no. 8, p. 600, 2017.

[5] I. K. Neelamana, S. Thomas, J. Parameswaranpillai, "Characteristics of banana fibers and banana fiber reinforced phenol formaldehyde composites-macroscale to nanoscale.," Journal of Applied Polymer Science, vol. 130, no. 2, pp. 1239–1246, 2013.

[6] B. Karacor, M. Özcanlı, "Characterization of jute/aramid hybrid composite materials with using different resins.," Sakarya University Journal of Science, vol. 26, no. 5, pp. 915–930, 2022.

[7] E. Omrani, P. L. Menezes, P. K. Rohatgi, "State of the art on tribological behavior of polymer matrix composites reinforced with natural fibers in the green materials world.," Engineering Science and Technology, an International Journal, vol. 19, no. 2, pp. 717–736, 2016.

[8] A. K. Rana, A. Mandal, S. Bandyopadhyay, "Short jute fiber reinforced polypropylene composites: effect of compatibiliser, impact modifier and fiber loading.," Composites Science and Technology, vol. 63, no. 6, pp. 801–806, 2003.

[9] A. K. Bledzki, J. Gassan, "Composites reinforced with cellulose based fibres.," Progress in polymer science, vol. 24, no. 2, pp. 221–274, 1999.

[10] M. Jawaid, H. P. S. A. Khalil, "Cellulosic/synthetic fibre reinforced polymer hybrid composites: A review.," Carbohydrate polymers, vol. 86, no. 1, pp. 1–18, 2011.

[11] P. L. Menezes, P. K. Rohatgi, M. R. Lovell, "Studies on the tribological behavior of natural fiber reinforced polymer composite.," Green tribology: Biomimetics, energy conservation and sustainability, pp. 329–345, 2012.

[12] D. B. Dittenber, H. V. S. GangaRao, "Critical review of recent publications on use of natural composites in infrastructure.," Composites Part A: Applied science and manufacturing, vol. 43, no. 8, pp. 1419–1429, 2012.

[13] P. Dey, S. Ray, "An overview of the recent trends in manufacturing of green composites–considerations and

challenges.," Materials Today: Proceedings, vol. 5, no. 9, pp. 19783–19789, 2018.

[14] E. Zini, M. Scandola, "Green composites: an overview.," Polymer composites, vol. 32, no. 12, pp. 1905–1915, 2011.

[15] R. Potluri, N. C. Krishna, "Potential and applications of green composites in industrial space.," Materials Today: Proceedings, vol. 22, pp. 2041–2048, 2020.

[16] T. dos Santos Pegoretti, F. Mathieux, D. Evrard, D. Brissaud, J. R. de França Arruda, "Use of recycled natural fibres in industrial products: a comparative LCA case study on acoustic components in the Brazilian automotive sector.," Resources, conservation and recycling, vol. 84, pp. 1–14, 2014.

[17] M. Fan, F. Fu, "Introduction: A perspective–natural fibre composites in construction.," In: Advanced high strength natural fibre composites in construction. pp. 1–20. Elsevier (2017).

[18] R. Potluri, "Natural fiber-based hybrid bio-composites: processing, characterization, and applications.," In: Green composites: processing, characterisation and applications for textiles. pp. 1–46. Springer (2018).

[19] B. Lucintel, "Opportunities in Natural Fiber Composites.," Texas Lucintel: Dallas, TX, USA, p. 2011.

[20] M. J. John, S. Thomas, "Biofibres and biocomposites.," Carbohydrate polymers, vol. 71, no. 3, pp. 343–364, 2008.

[21] P. Madhu, M. R. Sanjay, P. Senthamaraikannan, S. Pradeep, S. S. Saravanakumar, B. Yogesha, "A review on synthesis and characterization of commercially available natural fibers: Part II.," Journal of Natural Fibers, vol. 16, no. 1, pp. 25–36, 2019.

[22] A. Al Rashid, M. Y. Khalid, R. Imran, U. Ali, M. Koc, "Utilization of banana fiber-reinforced hybrid composites in the sports industry.," Materials, vol. 13, no. 14, p. 3167, 2020.

[23] D. G. Devadiga, K. S. Bhat, G. T. Mahesha, "Sugarcane bagasse fiber reinforced composites: Recent advances and applications.," Cogent Engineering, vol. 7, no. 1, p. 1823159, 2020.

[24] S. Jothibasu, S. Mohanamurugan, R. Vijay, D. Lenin Singaravelu, A. Vinod, M. R. Sanjay, "Investigation on the mechanical behavior of areca sheath fibers/jute fibers/glass fabrics reinforced hybrid composite for light weight applications.," Journal of Industrial Textiles, vol. 49, no. 8, pp. 1036–1060, 2020.

[25] E. Roumeli, Z. Terzopoulou, E. Pavlidou, K. Chrissafis, E.Papadopoulou, E. Athanasiadou, K. Triantafyllidis, D. N. Bikiaris, "Effect of maleic anhydride on the mechanical and thermal properties of hemp/high-density polyethylene green composites.," Journal of Thermal Analysis and Calorimetry, vol. 121, pp. 93–105, 2015.

[26] P. Russo, G. Simeoli, D. Acierno, V. Lopresto, "Mechanical properties of virgin and recycled polyolefin-based composite laminates reinforced with jute fabric.," Polymer Composites, vol. 36, no. 11, pp. 2022–2029, 2015.

[27] E. Saldivar-Guerra, E. Vivaldo-Lima, Handbook of polymer synthesis, characterization, and processing. John Wiley & Sons, 2013.

[28] L. A. Utracki, C. A. Wilkie, Polymer blends handbook. Kluwer academic publishers Dordrecht, 2002.

[29] H. Yetgin, "Otomotiv sektörü için polimer köpük malzeme üretimi ve karakterizasyonu. Sakarya Üniversitesi.," Fen Bilimleri Enstitüsü, Metal Eğitimi Bölümü, Yüksek Lisans Tezi, p. 2012.

[30] B. Manjula , A. B. Reddy , E.R. Sadiku , V. Sivanjineyulu , G.F. Molelekwa 3, J.

Jayaramudu , K. R. Kumar., “Use of polyolefins in hygienic applications.,” In: Polyolefin Fibres. pp. 539–560. Elsevier (2017).

[31] S. Lüftl, P. Visakh, “Polyethylene-based Biocomposites and Bionanocomposites: State-of-the-Art, New Challenges and Opportunities.,” Polyethylene-Based Biocomposites and Bionanocomposites, pp. 1–41, 2016.

[32] N. C. Paxton, M. C. Allenby, P. M. Lewis, M. A. Woodruff, “Biomedical applications of polyethylene.,” European Polymer Journal, vol. 118, pp. 412–428, 2019.

[33] Y. Behjat, J. J. Cheng, M. A. Polak, A. Penlidis, “Effect of molecular structure on the short-term and long-term mechanical behavior of high-density polyethylene.,” Journal of materials in civil engineering, vol. 26, no. 5, pp. 795–802, 2014.

[34] P. K. Roy, S. Titus, P. Surekha, E. Tulsi, C. Deshmukh, C. Rajagopal, “Degradation of abiotically aged LDPE films containing pro-oxidant by bacterial consortium.,” Polymer degradation and stability, vol. 93, no. 10, pp. 1917–1922, 2008.

[35] S. Rodríguez-Fabià, C. Zarna, G. Chinga-Carrasco, “A comparative study of kraft pulp fibres and the corresponding fibrillated materials as reinforcement of LDPE-and HDPE-biocomposites.,” Composites Part A: Applied Science and Manufacturing, vol. 173, p. 107678, 2023.

[36] M. Taşdemır, H. Biltekin, G. T. Caneba, “Preparation and characterization of LDPE and PP—wood fiber composites.,” Journal of applied polymer science, vol. 112, no. 5, pp. 3095–3102, 2009.

[37] D. A. C. Gomes , E. H. de Novais Miranda, M. C. R. de Araújo Veloso , M. G. da Silva , G. C. Ferreira , L. M. Mendes , J. B. G. Júnio, “Production and characterization of recycled low-density polyethylene/amazon palm fiber composites.,” Industrial Crops and Products, vol. 201, p. 116833, 2023.

[38] E. Sakar, H. Ünver, “Türkiye’de zeytin yetiştiriciliğinin durumu ve ülkemizde yapılan bazı seleksiyon ve adaptasyon çalışmaları.,” Harran Tarım ve Gıda Bilimleri Dergisi, vol. 15, no. 2, pp. 19–25, 2011.

[39] M. K. Savran, Z. Y. Ü. K. MÜH, “Dünyada ve Türkiye’de Zeytincilik,” (2017).

[40] A. Abd Mohammed, A. L. M. E. Depart, “Study the Thermal Properties and Water Absorption of Composite Materials Rrinforced With Data and Olive Seeds.,” Iraqi J. Mech. Mater. Eng, vol. 15, no. 2, pp. 138–152, 2015.

[41] M. R. El-Aassar, F. M. Mohamed, I. H. Alsohaimi, R. E. Khalifa, “Fabrication of novel valorized ecofriendly olive seed residue/anthracite/chitosan composite for removal of Cr (VI): kinetics, isotherms and thermodynamics modeling.,” Cellulose, vol. 28, no. 11, pp. 7165–7183, 2021.

[42] S. Valvez, A. Maceiras, P. Santos, P. N. B. Reis, “Olive stones as filler for polymer-based composites: a review.,” Materials, vol. 14, no. 4, p. 845, 2021.

[43] N. Pardalis, E. Xanthopoulou, A. Zamboulis, D.N. Bikiaris, “Olive stone as a filler for recycled high-density polyethylene: A promising valorization of solid wastes from olive oil industry.,” Sustainable Chemistry for the Environment, vol. 6, p. 100090, 2024.

[44] W. Marzouk, F. Bettaieb, R. Khiari, H. Majdoub, “Composite materials based on low-density polyethylene loaded with date pits.,” Journal of Thermoplastic Composite Materials, vol. 30, no. 9, pp. 1200–1216, 2017.

[45] K. tak Lau, P. yan Hung, M. H. Zhu, D. Hui, “Properties of natural fibre composites for structural engineering applications.,” Composites Part B: Engineering, vol. 136, no. October 2017, pp. 222–233, 2018.

[46] V. K. Balla, K. H. Kate, J. Satyavolu, P. Singh, J. G. D. Tadimeti, “Additive

manufacturing of natural fiber reinforced polymer composites: Processing and prospects.," Composites Part B: Engineering, vol. 174, no. May, p. 2019.

[47] M. Valente, F. Sarasini, F. Marra, J. Tirillo, G. Pulci, "Hybrid recycled glass fiber/wood flour thermoplastic composites: Manufacturing and mechanical characterization.," Composites Part A: Applied Science and Manufacturing, vol. 42, no. 6, pp. 649–657, 2011.

[48] N. M. Stark, L. M. Matuana, "Surface chemistry changes of weathered HDPE/wood-flour composites studied by XPS and FTIR spectroscopy.," Polymer degradation and stability, vol. 86, no. 1, pp. 1–9, 2004.

[49] S. S. Ndlovu, A. J. Van Reenen, A. S. Luyt, "LDPE–wood composites utilizing degraded LDPE as compatibilizer.," Composites Part A: Applied Science and Manufacturing, vol. 51, pp. 80–88, 2013.

[50] Z. Sydow, K. Bieńczak, "The overview on the use of natural fibers reinforced composites for food packaging.," Journal of Natural Fibers, p. 2018.

[51] C. Swaroop, M. Shukla, "Development of blown polylactic acid-MgO nanocomposite films for food packaging.," Composites Part A: Applied Science and Manufacturing, vol. 124, p. 105482, 2019.

[52] M Atagür, N Kaya, T Uysalman, C Durmuşkahya, M Sarikanat, K Sever, Y Seki., "A detailed characterization of sandalwood-filled high-density polyethylene composites.," Journal of Thermoplastic Composite Materials, vol. 35, no. 11, pp. 1903–1920, 2022.

[53] L Altay, M Atagür, K Sever, Y Sekİ, H Yilmazkarasu, A Oruç, H Toprak, Y Seki, M Sarikanat, E. Bozacı, "The Effect of Wastes of Nettle Fiber on Mechanical and Thermal Properties of Polypropylene Composite.," Journal of Natural Fibers, vol. 20, no. 1, p. 2172641, 2023.

[54] E. Tronc, C. A. Hernández-Escobar, R. Ibarra-Gómez, A. Estrada-Monje, J. Navarrete-Bolaños, E. A. Zaragoza-Contreras, "Blue agave fiber esterification for the reinforcement of thermoplastic composites.," Carbohydrate Polymers, vol. 67, no. 2, pp. 245–255, 2007.

[55] F. Z. Arrakhiz, M. El Achaby, K. Benmoussa, R. Bouhfid, E. M. Essassi, A. Qaiss, "Evaluation of mechanical and thermal properties of Pine cone fibers reinforced compatibilized polypropylene.," Materials & Design, vol. 40, pp. 528–535, 2012.

[56] Ü. Tayfun, Y. Kanbur, "Mechanical, physical and morphological properties of acidic and basic pumice containing polypropylene composites.," Sakarya University Journal of Science, vol. 22, no. 2, pp. 333–339, 2018.

[57] F.Z. Arrakhiz, M. El Achaby , M. Malha , M.O. Bensalah , O. Fassi-Fehri , R. Bouhfid , K. Benmoussa , A. Qaiss, "Mechanical and thermal properties of natural fibers reinforced polymer composites: Doum/low density polyethylene.," Materials & Design, vol. 43, pp. 200–205, 2013.

[58] A. Faisal, H. Salmah, "Mechanical and thermal properties of compatibilized waste office white paper-filled low-density polyethylene composites.," Journal of Thermoplastic Composite Materials, vol. 25, no. 2, pp. 193–207, 2012.

[59] H. Salmah, A. Faisal, "The effect of waste office white paper content and size on the mechanical and thermal properties of low-density polyethylene (LDPE) composites.," Polymer-Plastics Technology and Engineering, vol. 49, no. 7, pp. 672–677, 2010.

[60] S. Singh, A. K. Mohanty, "Wood fiber reinforced bacterial bioplastic composites: Fabrication and performance evaluation.," Composites Science and Technology, vol. 67, no. 9, pp. 1753–1763, 2007.

Sakarya Üniversitesi Fen Bilimleri Dergisi
Sakarya University Journal of Science

ISSN : 2147-835X
Publisher : Sakarya University

Vol. 29, No. 1, 83-99, 2025
DOI: https://doi.org/10.16984/saufenbilder.1560385

Research Article

Urban Quality of Life from the Perspective of Industrial Migration: Bursa Inegol Huzur Neighbourhood

Miray Gür*, Ezgi Koyun

Bursa Uludag University, Faculty of Architecture, Department of Architecture, Bursa, Türkiye, miraygur@uludag.edu.tr, 502212004@ogr.uludag.edu.tr
*Corresponding Author

ARTICLE INFO

Keywords:
Industrial migration
Urban quality of life
Quality of life
Environmental health
Unplanned urbanization

Article History:
Received: 05.10.2024
Revised: 07.02.2025
Accepted: 17.02.2025
Online Available: 27.02.2025

ABSTRACT

Aside from its numerous beneficial impacts, the Industrial Revolution has also resulted in environmental issues and the unchecked expansion of urban populations. The allure of enhanced employment prospects, educational opportunities, and improved access to healthcare facilities, particularly in urban areas, has emerged as a compelling incentive for individuals residing in rural regions, prompting a surge in migration towards cities. The influx of people moving to metropolitan areas has resulted in the unchecked expansion of cities and the emergence of detrimental urban settings. Slums and haphazard urbanization are tangible illustrations of detrimental urban environments. Urban planners, architects, and researchers in related fields are studying the urban quality of life to address the problems caused by migration and unplanned urbanization. They aim to identify and improve these issues, as well as to prepare for potential future threats. The study's objective is to assess the urban quality of life in the Huzur Neighborhood. This area has experienced distorted urbanization due to migration in the outskirts of the Inegöl district of Bursa. The neighbourhood has developed primarily due to the furniture industry. The evaluation will be based on the opinions of residents living in the Huzur Neighborhood and on-site observations of the physical environment. Physical environment observation pertains to examining the living environment and public amenities in the local community. The in-depth interview consisted of 18 questions categorized under demographic structure, accessibility and transportation, satisfaction and feeling of belonging, security, expectation, and environment.

1. Introduction

Founded in the 18th century in England, the Industrial Revolution laid the foundations of an economic, social and political transformation, especially in developing countries. With industrialisation, a dissolution occurred in the social structure and this situation triggered population mobility from rural to urban, from agriculture to industry and from less developed regions to more developed regions [1]. Different lines of work in cities, together with advanced education and health services, have become attractive factors in terms of employment opportunities for individuals in rural or deprived regions [2]. The migration movement from rural to urban areas has affected both the people and urban life in the city and the migrant population. The inability of the mass migrating to the city to adapt to urban life has brought about the further interlocking of people who have migrated from the same region. In the cities, neighbourhoods where fellow citizens who migrated from nearby regions lived together were formed and individuals tried to meet their housing needs in a fast and practical way in the neighbourhoods they formed mostly on the periphery of the city. However, these practical solutions have led to the emergence of the concept of squatter settlements, which lack infrastructure and bring unhealthy housing conditions [3].

Cite as: M. Gür, E. Koyun (2025). Urban Quality of Life from the Perspective of Industrial Migration: Bursa Inegol Huzur Neighbourhood, *Sakarya University Journal of Science*, 29(1), 83-99. https://doi.org/10.16984/saufenbilder.1560385

In these settlements, housing structures with adjoining layouts, without ventilation and daylight, water puddles, etc., are some of the unhealthy living and environmental conditions. In addition, crowded households where 4-6 people live in one room make the use of interior space problematic. The interiors of dwellings where there is no or insufficient furniture, damp, dark and broken Windows, health and quality cannot be mentioned, and bring about lifestyles that lack comfort conditions [4]. It can be stated that the negative living conditions emphasised by Engels in the mid-19th century overlap with the environmental conditions in neighbourhoods with similar Dynamics in Turkey in the 21st century. Especially the intensive migration movement to industrialised cities in rural areas of the country leads to settlements far from healthy living conditions. The shanty settlements produced in parallel with the industrial migration for the solution of the need for shelter, which is the most basic right of the person, led to questioning the way of life in the neighbourhoods within the framework of urban quality of life.

In the literature, there are many studies on quality of life and improving urban quality of life in studies with different topics carried out at different environmental scales [5-8]. However, while there are urban quality of life studies conducted in slum settlements in cities [9-11], there are not many studies on the quality of urban life in slum neighbourhoods formed in regions receiving industrial migration. In this context, the study aims to discuss the concept of urban quality of life by associating it with migration from the perspective of industrialisation. In the evaluation of the relationship between industrial migration and urban quality of life, Bursa İnegöl district, which has an important potential in terms of furniture exports in Turkey and where blue-collar workers working in this sector migrate intensively, is taken into consideration. Huzur neighbourhood, which is located on the periphery of the region in the İnegöl district close to the city scale, is a shanty settlement area developed as a result of industrial migration, where the unhealthy infrastructure and housing conditions mentioned in the previous paragraphs are seen. In this framework, the main problem determined in the research is to determine the perception of urban quality of life in Huzur Neighbourhood, where blue-collar workers mainly working in the furniture sector migrate intensively, and the factors that are effective in shaping the perception.

In this context, the aim of the research is to evaluate the urban quality of life in the region with the opinions of the users living in İnegöl Huzur Neighbourhood, which is determined as the study area, and on-site examination of the physical environment. In line with this purpose, in-depth interview method was applied in order to determine the life styles of the users living in Huzur Neighbourhood and their perceptions and satisfaction levels regarding the living environment where unhealthy conditions are observed. Thus, in addition to the urban quality of life studies in the literature, it is aimed to contribute to the literature by addressing the issue from the perspective of industrial migration and to develop suggestions for areas with similar dynamics with the study area.

2. Individual, Social and Urban Quality of Life in Relation to the Environment

Today, regardless of where we live in the world, there is a continuous migration from rural to urban areas in many countries. According to the United Nations (UN) report, as of 2008, more than half of the world's population now lives in cities [12]. However, it is expected that one out of every three people born in the next 30 years will live in the city [5]. Despite the problems associated with increasing population growth, cities continue to receive migration rapidly as they offer higher education, healthcare and employment opportunities. While it is certain that the size of cities will grow it remains unclear how urban amenities will be distributed and how conditions, especially in large cities, and the quality of life of city dwellers will be affected. The current situation has led researchers interested in the subject to research on "urban quality of life", an area where the multidimensional nature of cities can be monitored [13]. Before discussing the concept of urban quality of life, the concept of quality of life, which includes many disciplines related to life, should be mentioned to create a background.

The concept of quality of life is used worldwide to describe the well-being of societies and people [13]. The concept covers the conditions of the environment in which people live (air and water pollution or poor housing) or some qualities of people themselves and their lives (health, educational achievement, etc.) [8]. It is accepted that the concept of quality of life, which is related to individuals' perception of their position in life in the context of the culture and value systems in which they live, including both environmental and psychological components, depends on internal and external factors [14, 6]. However, quality of life, which expresses the judgement made by the individual, is a whole that is also shaped by society [15].

Quality of life has many dimensions, including family, work life, economic situation and most importantly health. In the case of the environment, the different environmental scales at which we live have an important role to play in characterising quality of life. From individual dwellings to the local neighbourhood scale, to the city, to the wider region and even to the national scale, the effects of where people live on their quality of life are at the centre of research. In the literature, there are different studieson residential environment, neighbourhood relations and quality of life. For example, Greenberg (1999), focusing on the relationship between neighbourhood units and various characteristics of residents, found that crime, physical obsolescence and distrust of government are higher in settlements with low levels of living [16].

Lovejoy et al. (2010), who compared the satisfaction levels of those living in traditional settlements and suburbs, stated that the satisfaction levels of those living in suburbs were lower [17]. Türkoğlu (1997), who investigated the satisfaction of people living in different residential areas in Istanbul, found that the of physical comfort, building quality, housing plan, size of the housing and proximity to the city centre interacted with the satisfaction levels of the users [18]. However, the basic assumption underlying many planning, design and research approaches is that spaces can be designed to improve people's quality of life [5]. As stated in the previous statements, it is predicted that the current volume of cities will increase further in the future and more people will live in cities and metropolitan areas. The relationship between urban areas and the quality of life of urban dwellers and the researches focussing on urban quality of life always maintains its relevance and importance with the changing times and life style.

Urban quality of life is a concept formed by all the factors that make a city a city, together with physical and intangible (belonging, spirit of place, justice, equality, etc.) factors. Therefore, in terms of social, economic and spatial elements, urban infrastructure; facilities such as communication, transport, housing are above the standards determined in proportion to the dynamics of the country, and the individuals living in the city can also be defined as the state of benefiting equally from these facilities and opportunities offered by the city [19]. In other words, urban quality of life is the complete fulfilment of the urban needs of city dwellers, the conformity of urban services to certain criteria, the objective positive development of living conditions and accordingly the complete well-being and prosperity of city dwellers [20]. Urban quality of life is directly related to the provision of environmental standards and the equal provision of urban rights to everyone [21].

Drawing on work on human ecosystems and sustainable communities, Shafer et al. (2000) developed a model in an attempt to describe the fundamental relationships between the components of a place: physical, social and economic (Figure 1) [22]. The model also shows that quality of life is generated by an ongoing interaction between community, environmental and economic attributes.

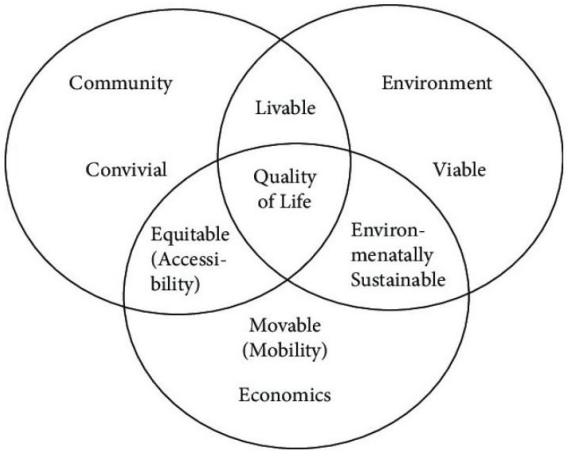

Figure 1. Quality of life components [22]

Veenhoven (2000), who analysed quality of life researches through individual life, stated that the concept of quality of life affects the quality of society in some conditions, while in some cases it expresses the happiness of the community [23]. As can be seen in Schafer's model (Figure 1), another important component considered together with the concept of community is the environment. Human being, who is a whole with the environment, is affected by the conditions of the environment while changing and transforming the environment [24].

Over time, the positive or negative reflections of this interaction are observed within the society. With this situation, measuring and evaluating the quality of urban life and investigating its effects on human behaviour are becoming increasingly important in social sciences. Research on the concept of urban quality of life is important not only because it affects people's behaviour, but also because it affects their lives, living standards and happiness. In order to understand the quality of life in a particular environment, such as urban settlements, it is necessary to measure the conditions in that area with the help of indicators [5].

When we look at the research on measuring urban quality of life, Marans' studies stand out in the literature for being comprehensive and adaptable to different fields. In his research, Marans argues that model frameworks should be used to make sense of different dimensions of quality of life and data should be collected to make these frameworks functional in a specific context. According to the research model he developed, Marans' approaches;

a) The first is objective, in the form of monitoring of Quality of Life / Quality of Urban Life through a set of indicators derived from aggregated spatial data using official sources such as census. (household income, crime rates, pollution levels, housing costs, etc.).

b) The second involves modelling relationships based on subjective, evaluative measures of the characteristics of the urban environment and people's satisfaction with life. This approach typically involves data collected through survey research methods and analysed using techniques such as regression analysis or structural equation models [25].

Monitoring the indicators over time generates data on the increase or decrease in people's quality of life and provides feedback to urban policies. In addition, survey data can provide information on individual and social perceptions, behaviours, subjective evaluations and satisfaction levels regarding various aspects of urban life [25]. However, it is within the scope of the discussions on the subject that indicators constitute a limited data source and are helpful. Even if residents are asked to rank the list of data on quality of life in order of importance, the information obtained in this way may not be sufficient to estimate the proportion of satisfaction level explained by any factor.

It is, therefore, important to analyse data and develop research models to test hypotheses about these links, using methods to identify the relative importance of different aspects of urban life in improving the quality of life of various user groups [5]. Marans and Rodgers (1975) developed a broad conceptual model of environment-based quality of life in which objective factors related to the environment and subjective perception related to them are addressed within the conceptual framework (Figure 2) [26].

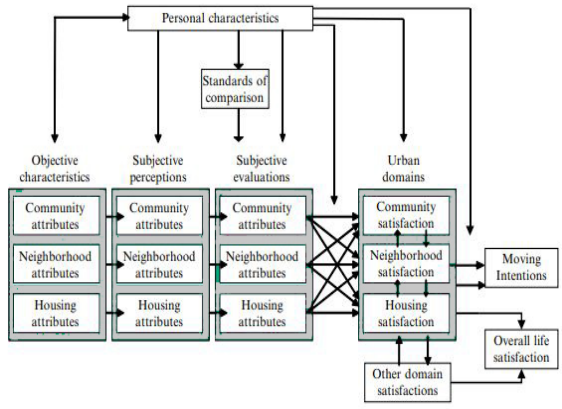

Figure 2. Model of determinants of satisfaction around housing [26, 27]

The model is basically based on four principles: individuals' experiences emerge from interactions with their environment, subjective experiences are different from the objective environment, individuals react to their experiences with the environment, and the level of satisfaction in various life domains contributes to the overall quality of life. It is suggested that the approach model put forward by Campbell, Converse, Rodgers, and Marans can be evaluated for different living spaces in life satisfaction research. For example, satisfaction with the environment can be examined at different levels such as satisfaction with housing, satisfaction with the neighbourhood, satisfaction with wider communities or satisfaction with wider regions.

This model has contributed to the analysis of the relationships between various quality of life domains and geographical levels of the urban scale [27]. In the model, it is seen that arrows extending in one direction express causal relationships, and double-sided arrows express an association. To the model, objective characteristics of the environment and subjective evaluations of the urban environment directly affect life satisfaction. For example, heavy traffic perceived by a user through senses is subjectively evaluated as noisy. Through a series of subjective evaluations of a user's neighbourhood, satisfaction in that urban area (neighbourhood satisfaction) is estimated, as well as satisfaction in other urban areas (such as housing and community satisfaction). With the satisfaction scale in these three urban areas, overall life satisfaction is also predicted (employment, relationships, health, etc.).

Neighbourhood satisfaction in an urban area also predicts mobility intentions and subjective quality of life can be associated with broader implications for regions as well as the objective urban environment [28]. In quality of life research, objective indicators are generally used to estimate objective quality of life data, while subjective measures are used to estimate quality of life in relation to perceptual variables. Thus, quality of life is determined with two separate sets of indicators, objective and subjective measurements [29]. While objective quality of life studies in urban areas generally focus on objectively ranking different places in urban quality of life, quality of life studies aim to reveal the importance of various subjective evaluations of the urban environment in determining the subjective urban quality of life.

Urban quality of life studies may focus only on objective or subjective indicators for specific purposes. When both objective and subjective indicators are included in a study, they are conceptualised as separate indicators of objective and subjective urban quality of life, respectively. The evaluation of the two indicator models separately at independent levels has been identified as a research gap in the literatüre (Figure 3) [28].

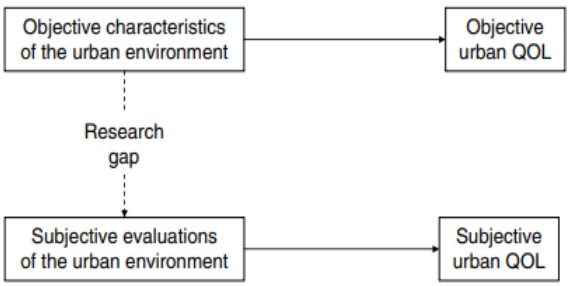

Figure 3. Literature gap model in urban quality of life research

In social indicator research, much of which has focussed on objective or subjective measures, one type of indicator has contributed to the interpretation of another [26, 27]. Many factors, including personal and social characteristics such as age, income and education, stand between the objective world and the individual's perception of it. Individual perceptions translate what is initially seen as a universal objective situation into a personal interpretation of behaviour. Individual experience is also an important factor that will influence the perception of a particular

domain. For example, the experience of being a victim of crime, regardless of the level of crime measured by objective indices, has a profound and lasting effect on the individual's perception of security in his/her home or neighbourhood.

Another factor that may be important in the objective-subjective relationship is the level of desire or expectations of the individual. This helps to understand a statement in which objective data are weak but which has a high satisfaction value according to the individual [30]. The concept of adaptation to the environment is another variable that can affect the relationship between objective and subjective conditions. This helps to explain why, in a fixed situation, an individual's satisfaction with a situation can increase over time with adaptation to that situation, and why people who are semi-permanently trapped in poor objective conditions express higher levels of satisfaction in their own conditions.

Other factors that intervene between objective and subjective assessments of quality of life include the cultural background of the individual producing the standard of comparison against which objective conditions are measured. This factor, which is of obvious importance on an international scale, can also affect different ethnic or social groups within a city [30]. Another factor to be considered is scale mismatch. Accordingly, when collecting objective social indicators for well-defined territorial units, it is recognised that the territorial base of an individual's perception is unlikely to coincide exactly with the boundaries of the administrative unit used to collect the objective data. Scale mismatch can affect all aspects of perceived well-being that include a territorial component, including notions of overall neighbourhood satisfaction [30].

Urban environment is a relative term related to urban liveability, time, purpose and the value system of the user, as opposed to the objective definition of quality that is evoked in the mind. This view suggests that quality is not an attribute specific to the environment, but a behavioural function of the interaction of environmental and personal characteristics. In this case, both objective and subjective data should be used in order to understand urban environmental quality correctly. In other words, the city on the ground and the city in the mind should be considered together [30]. With reference to the research argument, Pacione (2003) proposed a five-dimensional framework that combines the various dimensions of quality of life research through a set of key concepts: objective, subjective, time, site specificity, geographical scale and social group dimensions (Figure 4)[30].

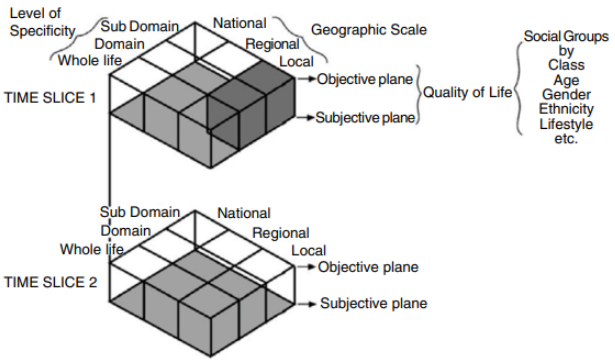

Figure 4. Five-dimensional model on quality of life research

The level of specificity defined in the framework refers to which areas of quality of life are the subject of research. These can range from the whole-life view of well-being to individual domains and sub-domains. The first contribution in the framework was the introduction of a spatial dimension to strengthen the previous two-dimensional assessments of social conditions over time. At the second level, just as individual quality of life can be assessed at different levels, society can be assessed at different geographical scales, from the individual to the group or local, city, regional, etc. scale.

The third plane represents the type of quality of life indicator used. It states that any definition of quality of life should include two basic elements and that two different types of social indicators are appropriate for measuring social and individual well-being. The first are objective indicators that describe the environments in which people live and work, while the second are subjective indicators that aim to describe the ways in which people perceive and evaluate the conditions around them. The fourth plane of the framework is used to measure quality of life at different times and to track the impact of policies designed to improve quality of life for specific

people and places. The fifth dimension reflects the socio-spatial structure of the city and refers to the need to measure the quality of life of individual social communities in the city, which differ along various dimensions such as class, lifestyle, ethnicity, gender and age [8].

In summary, under the title of quality of life, it has been tried to define the subject with the findings of researchers who have made significant contributions to the literature on urban quality of life. In addition to the indicators that are important in defining urban quality of life, different research models have been analysed. In general, it is understood that a research model that will blend the common data of two disciplines together, rather than the distinction between objective and subjective indicators, is one of the healthiest methods to reach accurate data. The results of the observations and surveys carried out in Huzur District will be thoroughly explained below, taking into account the theoretical framework that was previously reviewed.

3. Workspace

The area examined within the scope of this study is Huzur Neighbourhood in İnegöl district of Bursa, which is one of the largest provinces of trade and industry volume of the Marmara Region, which hosts Turkey's significant volume in terms of industry. In the examination of the study area where industrial migration is addressed in order to associate with urban quality of life, firstly, the geographical and strategic location of İnegöl and its industrial volume should be mentioned. İnegöl district is located on a fertile plain within the borders of Bursa, between Mezit Bogaz in the east and Ümitalan in the west. In the west of İnegöl, there is Kestel district of Bursa, Yenişehir district in the north and Keles district in the southwest [31]. (Figure 5). İnegöl is an area bounded by Domaniç district of Kütahya from the south and Pazaryeri and Merkez districts of Bilecik province from the east [32].

Surrounded by Uludağ and its extensions Domaniç and Ahi Mountains, İnegöl has a large forest cover and the people living in the region have provided their livelihood from these forests throughout history [33]. The district stands out with its proximity to raw materials and furniture making activities [34].

Figure 5. Location of İnegöl in relation to Bursa province

Furniture production, which started in small workshops, has grown over time and with the effect of industrialisation and has created different employment branches in the city. In particular, İnegöl Organised Industrial Zone, the first of which was established with the state incentive in 1977, attracted many investors to the city, accelerated mass production and triggered the emergence of more need for labour in the district [35]. In the following years, the Inegol furniture industry, where chipboard material started to be used, started to switch from traditional workshop type production to fabricated production [36]. With the increasing technological developments, advertising activities and the search for new markets, especially in Istanbul, have rapidly increased furniture production.

In the 2000s, furniture enterprises that increased and accelerated their production volume started to give importance to design and branding. In the same year, with the Furniture Decoration Fair (MODEF) organised for the first time in İnegöl, İnegöl furniture started to gain a place in the world market [35]. In the following years, with the expanding market network, proximity to raw materials, logistical advantages and export potential, industrialisation in İnegöl increased rapidly, and new industrial sites were established in the city. According to the 2021 Furniture Sector Report data, İnegöl, which ranks third after Istanbul and Kayseri in the distribution of Turkey's furniture exports by region [37], has become a preferred place to migrate with its developed industry and business lines.

Especially since the beginning of the 2000s, the migration movement to İnegöl and the population increase in the city have been observed in a remarkable way. In order to develop the city in a planned way, a housing area implemented by TOKİ was established in 2007 in the north of Bursa-İnegöl highway [35]. The buffer zone between the TOKİ zoning area outside the city centre and the city centre has been inhabited by immigrant families who could not afford the houses whose prices increased in the city over time.

The houses in the area where many houses were built illegally were included in the zoning plan in time. The buffer zone named Huzur Neighbourhood is far from healthy living conditions with adverse housing conditions, security problems, lack of recreation and social areas and has the characteristics of "unplanned urbanisation" and "shanty settlement" which are widely used today. The neighbourhood is located outside of İnegöl city centre, close to İnegöl entrance on Bursa highway (Figure 6-7).

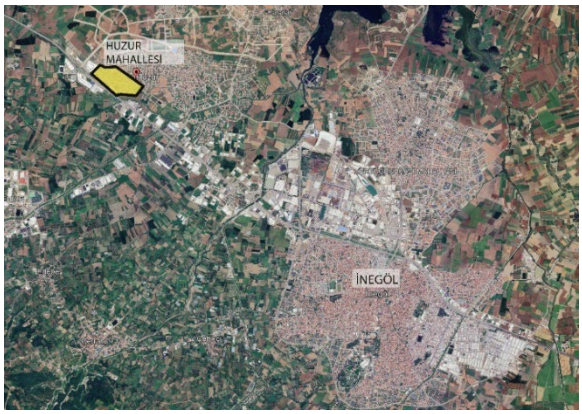

Figure 6. Location of Huzur Neighbourhood on aerial photograph

In line with the defined problem and the determined location, the aims and objectives of this study are, to evaluate the urban quality of life of the users in Huzur Neighbourhood within the scope of interviews with the residents and observations in the field to determine the determinant factors in the quality of urban life, to create preliminary data for future urban quality of life researches through the results obtained, and to develop suggestions to improve the quality of urban life for areas with similar problems related to industrial migration.

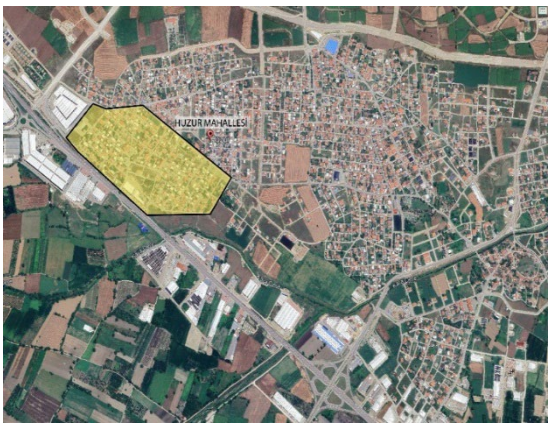

Figure 7. Aerial photograph of Huzur Neighbourhood and its surroundings

4. Methodology

Within the scope of the objective, in-depth interview methods are utilised together with on-site observations and questionnaires conducted in the physical environment to investigate the quality of urban life. Residents' satisfaction and perceptions about the environment are questioned through survey questions measuring different parameters, observations and in-depth interviews focusing on the casual relationship of survey data. The observation of the physical environment concerns the investigation of existing residential buildings, services and circulation elements in the neighbourhood. These are categorised according to diversity, architectural features, accessibility and landscape characteristics.

The results obtained in this pilot study, which was conducted in preparation for future studies, are discussed through visuals expressing the physical characteristics of the neighbourhood. In the in-depth interview, data on the perception and satisfaction levels of the users of the neighbourhood are obtained through 18 semi-structured questions created under the headings of demographic structure, accessibility and transportation, satisfaction and feeling of belonging, security, expectation and environment.

5. Results and Discussion

The research was carried out in the form of a questionnaire and in-depth interviews with 20 different people residing in the region, aged between 18 and 53, belonging to different

occupational groups, not working or students, together with on-site observations made in, Huzur Neighbourhood. The combination of questionnaire and in-depth interviews provides a better explanation of the interaction of individuals' perceptions of life.

When the number of individuals living in the household was questioned in relation to demographic factors, 30% of the participants stated that there were six people living in the dwelling, 40% stated that there were five people, 25% stated that there were four people and 5% stated that there were three people. In line with factors such as crowded households, inability to provide personal privacy and hygiene, and lack of sufficient space for people to perform their activities, as stated by Clark and Onaka (1983), the quality of life and housing satisfaction in Huzur Neighbourhood are negatively affected, thus is a factor that reduces the quality of life [38].

Accordingly, the fact that the rate of households consisting of five or more people in the neighbourhood is 70% is interpreted as a factor that can directly affect the urban quality of life of the neighbourhood residents. When the length of residence of the research group in the neighbourhood was questioned, it was learnt that four people have been living in the neighbourhood since they were born, while the others have lived in the neighbourhood for at least 11 years and at most 33 years. The sense of belonging to a place is shaped by the interactions with the people in the place as well as the emotional and social relationships that take place in the place over time [39].

In Crete, where Potter et al. (2005) investigated the effects of migration on small cities, it was concluded that the satisfaction level of immigrants living in the region for a long time decreased, while the conditions were perceived better for new immigrants shows that life expectancy also changes the perception for immigrants, supporting the findings obtained in the research [40]. Within the quality of life studies, the belonging factor has an important place as a life component that is shaped by time as well as the physical and emotional conditions in which immigrants are. In this framework, in a comprehensive urban quality of life research to be carried out in the future for Huzur Neighbourhood, the sense of belonging and the concept of time should be addressed and the satisfaction levels of people with their environment should be addressed.

When the accessibility factor is evaluated, it should be taken into consideration that access to İnegöl is provided by various road routes. The first of the road networks connecting the city to the surrounding provinces and districts is the state highways network; Bursa-İnegöl-Ankara TCK State Highways, İnegöl-Yenişehir-İznik TCK State Highways and İnegöl-Tahtaköprü and Domaniç TCK State Highways. The second is the network of provincial and village roads; Inegol-Hasanpaşa-Kursunlu-Pazarcık roads, Inegol-Gündüzlü-Oylat roads and Inegol-Tekke village and Bilecik road. The last one is stated as three different transport routes, including roads with different characteristics (levelling, raw and village roads) [41].

Urban transport in İnegöl is provided by the personal vehicles of the users and by buses, which are public transport vehicles. Huzur Quarter, which is approximately 10 kilometres outside the city centre, can be reached by personal vehicle or public transport. When 20 people living in the region and participating in the survey study were asked how they evaluated the access and transportation opportunities to the neighbourhood, 15 of them stated that they could reach the neighbourhood easily. It was noted that these people do not need to use public transport much in daily life and generally try to solve their long-distance work with their personal vehicles.

On the other hand, 5 interviewees described the access to the neighbourhood as inadequate, difficult and a waste of time. It should be emphasised that the people who expressed negative opinions generally have to use public transport. In order to directly experience the access opportunities to the region, the authors reached the region by both personal vehicle and public transport and determined how long it took to reach the region by different methods. While it takes approximately 15 minutes to reach Huzur Quarter from the city centre by private car, this time varies between 1-1.5 hours on average by

public transport, depending on the bus waiting time. Due to its distance from the İnegöl city center, the Huzur neighborhood is situated in a spatially disadvantaged area when viewed through the lens of the spatial dimension concept, which is one of the components of quality of life models, particularly those by Pacione and Marrans. [26, 27, 30].

The research data show that public transport facilities and services in İnegöl Huzur Neighbourhood, where transportation, which is accepted as one of the main components of quality of life [42] is provided by public transport, personal vehicles and taxis, are not sufficient and cause loss of time. The efficiency of public transport in terms of accessibility is an important criterion in terms of urban quality of life [43], and it can be stated that public transport in İnegöl is not efficient, which is compulsorily preferred by a small number of users and has a negative impact on urban quality of life.

The intention was to get empirical data through neighborhood observations, while subjective data was gathered via surveys, as illustrated by Marans and Rodgers' Environment-Based Quality of Life Model, which integrates both objective and subjective components. Observational data from the region concerning transportation and accessibility indicate insufficient green spaces and recreational facilities, as well as inadequate sidewalks for safe pedestrian movement. This circumstance presents a possible hazard for people sharing the roadway with automobiles. Furthermore, there are no appropriate alternative choices for transportation vehicles, such as bicycles or seagulls. In the survey study assessing the region's walkability, 15 individuals deemed the neighborhood unsuitable for walking, whilst 5 individuals asserted that it was walkable. Individuals who deemed the area unwalkable cited the shared use of the roadway by walkers and vehicles, leading to hazardous conditions and the absence of sidewalks. The responses provided by the users align with empirical observations.

Walkability is an important criterion in terms of livability and urban quality of life [44, 45] and the lack of safe and pleasant walking opportunities has a negative impact on the urban quality of life of the users living in Huzur Neighbourhood. When the accessibility to units such as health centres and pharmacies that should be easliy and quickly accessible for daily needs was questioned, everyone interviewed stated that these units are located in easily accessible areas. As stated by Dumbaugh (2005), easy accessibility to daily needs has a positive effect on urban quality of life [46]. In this context, it can be stated that Huzur Neighbourhood is not attractive in terms of walkability or recreational activities and this aspect is negative in terms of urban quality of life, but the QOUL is supported in terms of easy accessibility to daily necessities.

Another topic that covers the physical environmental features where objective and subjective data are evaluated together is the houses and the environment they are located in. The observational study revealed that the buildings have a minimum of one storey and a maximum of four floors, based on their structural characteristics. It was observed that most of the buildings do not comply with the regulations as required by the building standards, as well as the high density of idle buildings. It was even found that the columns and rebar of the last floor of many buildings were left open against the possibility of building the next floor. In most of the buildings built in reinforced concrete, the brick walls, which are generally used as building material, are visible, and the buildings are left without exterior insulation and exterior cladding during the application phase.

The fact that the buildings in Huzur Neighbourhood are constructed without the basic insulation materials required for the winter months has been determined as a factor that negatively affects the quality of life directly, as it negatively affects the comfort conditions and may lead to various health problems. Provision of comfort conditions and construction quality are highly effective on quality of life [47-49].

In a research study where similar conditions were observed in the Manila region within the borders of the Philippines, which has similar qualities in terms of illegal construction and environmental infrastructure with some deprivations with the research area, it was mentioned that the slum

settlements built with low-quality construction materials were damaged by natural disasters and high number of casualties [50]. Uncontrolled urbanisation, unhealthy construction, negligence and failure to take necessary precautions, especially in rapidly growing urban areas such as İnegöl, not only reduce the quality of urban life of people in possible disaster scenarios but also endanger their lives. The continuation of the construction of unhealthy buildings that preserve their current existence negatively affects not only the quality of life of the people living in the area but also the environmental quality of the neighbourhood and the quality of urban life of all urbanites who are in a visual or physical relationship with the environment.

In the questionnaire study conducted within the scope of satisfaction with the dwelling and its surroundings (Figure 8) together with the observations, 12 people stated that they were not satisfied with the physical characteristics of the dwelling and its surroundings, while eight people stated that they were satisfied with the dwelling and its surroundings. When the data obtained as a result of the questionnaire and in-depth interviews were questioned as to why the respondents were dissatisfied, the lack of asphalt roads in some regions and damage to vehicle tyres due to this reason, the lack of sufficient garbage collection areas in the vicinity, environmental pollution, disorder, unhealthy living conditions came to the fore as the reasons that triggered dissatisfaction.

In line with the model of Marans and Rodgers, deficiencies in building quality and data obtained regarding the building environment reduced both objective and subjective satisfaction. When the participants' attitude towards municipal services is analysed, half of the users are satisfied, and half are not. Compared to other neighbourhoods the delay in services in Huzur Neighbourhood is at the top of the disturbances stated by those who are not satisfied with municipal services.

The lack of sufficient parking space for vehicles in the neighbourhood is also observed as a different problem in the other housing environment. Users who cannot find a defined parking area for their vehicles park their vehicles directly on the road, in front of their houses or on idle lands in front of their houses. The idle plots and lands in the area are also used as areas where garbage and rubble are accumulated. In this context, it should be noted that the poorly maintained physical environment is also an environmental factor that negatively affects the quality of life of the users.

Figure 8. Visuals from the residential neighbourhood in Huzur Neighbourhood

The existence of green areas around the neighbourhood has been identified, but it has been observed that they are not used for their intended purpose. As a result of the satisfaction survey on environmental cleanliness and green areas, feedback was received that 18 people were not satisfied with this situation. When the dissatisfied people were asked about the reasons for their dissatisfaction, they stated that there are not enough garbage containers around, people throw their garbage haphazardly at the base of trees or in vacant lots, and that this creates serious cleanliness and health problems in the neighbourhood as well as visual pollution.

As stated in the Declaration of European Urban Rights in the European Urban Charter adopted by the Council of Europe in 1992, the right to live in an unpolluted and healthy environment is one of the fundamental rights of urban residents living in European settlements [51]. When it was questioned whether the green areas in the neighbourhood were sufficient, 18 users stated that they found them insufficient in terms of quantity and quality. The presence of green and recreational areas such as parks and gardens in cities helps to protect urban ecology and contributes to the improvement of physical and mental health [52]. The residential environment, which is described as the part of the space that directs the life experience, emotions and thoughts in the city the most, together with the observations and user opinions, is an important

factor that reduces the quality of urban life by not adequately meeting and satisfying the need of its users to live in a clean, healthy and green environment [53].

Similar to the parking areas, the fact that playgrounds are not spatially defined is another negative situation observed in the neighbourhood. In Huzur Neighbourhood, where the houses are located along the street axis in adjacent or separated order, the existence of defined playgrounds built by the municipality for children was observed only in one area. Young children usually play in front of their houses on roads that are vehicle routes. Although this situation is stated as safe by some users in terms of being at a distance where the child can be seen from the window, it is among the conditions stated as very dangerous and unhealthy by many users.

When asked whether the area is safe for raising children, seven people stated that the environment and neighbours generally know each other and that it is safe, while the other thirteen people expressed negative opinions. Within the scope of the problems defined as insecurity, comments such as the aggressive behaviour of stray animals and wandering around, the fact that the areas where children want to play are also vehicle routes and the presence of unknown people in the area were encountered.

When a separate security assessment was made for day and night, all participants in the research stated that free movement during the day is not a problem for people, but they do not prefer to stay out after a certain hour in the neighbourhood at night because they find it unsafe. As accepted and observed by most of the users interviewed in the region, the title of security within the components of quality of life has been noted as a factor that negatively affects the urban quality of life in Huzur neighbourhood, which is unsuitable for raising children, has a stray dog problem and fear of attack, has dangerous children's playgrounds, and unsafe environments at night.
It has been observed that the areas where people can spend time for sportive and social activities are not numerous in the neighbourhood, as well as being at distances that are not easily accessible to every residence. When the users of the neighbourhood were asked whether these areas are sufficient or not, all of the users stated that they found the areas inadequate and inefficient and that the existing areas, which are not efficient, have become environments that pose a security risk by being used for purposes other than their purpose. The lack of safe and clean social facilities where families and children can spend time together and where friends can meet was also emphasised.

Urban infrastructure elements, social facilities and sufficient green areas, which are among the physical components of urban quality of life, stand out as factors that directly affect the quality of life, productivity and efficiency of individuals [54]. In Huzur Neighbourhood, the fact that people cannot benefit from social facilities that are not adequate and efficient enough and the use of existing areas for purposes other than their purpose is noted as another factor that negatively affects the quality of urban life in the region.

Finally, the expectations of the interviewees for the region in general terms can be stated as improving the structures in terms of strength and aesthetics and creating more favourable environmental conditions, providing more qualified municipal services to the region, pouring asphalt for unpaved vehicle roads, defining vehicle and pedestrian roads separately from each other for certain areas, installing a camera tracking system for security, widening roads and creating suitable, safe walking route alternatives for pedestrians, improving environmental cleanliness and creating more green recreation areas.

6. Conclusion

Inegöl, one of the 17 districts of Bursa province, is a settlement that stands out with its developed furniture sector, which has grown and continues to grow thanks to various dynamics such as logistics, raw materials and industrial investments. Employment opportunities in parallel with the developing industry have made the region a settlement that receives continuous migration. The rapid migration towards the city as of the point the city has reached today has brought unhealthy living conditions and

unhealthy urbanisation problems together with the shanty settlements formed on the periphery of the city. Within the scope of this study, Huzur Neighbourhood, which is a shanty settlement area formed on the periphery of the city due to industrial migration, has been analysed from the perspective of urban quality of life.

As a result of the questionnaire survey, in-depth interviews with users and socio-physical observations, the data obtained on environmental parameters and user satisfaction and the problems identified are evaluated in detail in the discussion of the findings. To summarise the data in question; transportation, inadequate and delayed municipal services (lack of pavements, landscaping, inadequacy in parks and sports facilities, etc.), infrastructure deficiencies, idle building density and housing in unhealthy conditions, environmental pollution, inadequate car parking, undefined and unsafe playgrounds for children, conflicting pedestrian-vehicle circulations, neighbourhood-wide security problems and stray street animals are the prominent problems in the region.

Although the Huzur Neighbourhood and the slum settlements with similar conditions have different dynamics, they basically host people who are in search of better living conditions due to economic and social reasons. When the interaction of the built environment in Huzur Neighbourhood with the urban quality of life is evaluated, it is predicted that if the necessary measures are not taken and the deficiencies are not eliminated, the quality of life of the people living in the region will continue to negatively affect the quality of life in individual and social terms. Houses built with inadequate facilities and building materials through unhealthy zoning plans transform the need for shelter, which is the most fundamental right of people, into an unhealthy situation with economic, social and physical barriers.

These places that meet the need for shelter are not resistant to disasters such as earthquakes and floods that we have witnessed in recent years and may cause loss of life. In addition, crime rates in these regions may increase at the same rate as a result of rapidly increasing uncontrolled migration towards these regions over time. The increase in the need for a labour force in İnegöl is directly proportional to the increase in population and unhealthy buildings in the region. Unless measures are taken, unhealthy construction and uncontrolled growth have the capacity to negatively affect not only the quality of life of individuals but also the urban quality of life of the neighbourhood and the district.

The fact that the region is close to the entrance of İnegöl also creates a different negative impact on the region in terms of urban aesthetics. The city of İnegöl, which continues to receive rapid migration, is increasing its urban and housing development activities towards Bursa. Huzur neighbourhood, located in the direction of Bursa and at the exit of İnegöl, is surrounded by new settlements and state-built housing areas. These areas indicate how the Huzur neighbourhood may evolve in the future.

Although the Huzur neighbourhood, which is located in a rapidly changing and developing environment with insufficient opportunities, may be addressed within the scope of the Urban Transformation Project in the future, it is aimed that the urban life quality studies carried out now will help in creating projects that produce solutions for the demands and needs of the neighbourhood users. The livability and quality of life in cities must be considered, as numerous Turkish settlements have seen structural transformations due to industrial migration or external migration, similar to the Huzur neighborhood. It is essential to evaluate user interactions with their environments in different neighborhoods and to analyze the quality of life over time, considering the changes in user and administrative organizations.

Consequently, novel research domains and proposed solutions will emerge in the future as user requirements and environmental advancements are better comprehended within the framework of urban quality of life. As long as industrial structures remain unevenly dispersed, many cities in Turkey will experience population influxes due to their growing industries and the associated job prospects. Unplanned population migration to urban areas leads to slums and unregulated urbanization, resulting in issues related to urban quality of life.

Upon examining the enhancement studies conducted specifically for slum settlements in Turkey, it is evident that while there exists the potential to generate beneficial solutions through urban transformation that make these areas more habitable, there are also large-scale housing developments that prioritize rental income and fail to align with the identity, culture, and needs of the local populace. In analogous areas facing urban deprivation, the first objective should be to comprehensively comprehend the demands of the territory and its inhabitants, and to formulate solution options that are appropriate for the city and its surrounding socio-economic context. In this context, potential topics for future studies include the effects of internal and external migration on urban centers and peripheral settlements, the relationship between these settlements and their immediate environment, the quality of life for users and urban inhabitants, and the influence of fragmented transformations on overall urban cohesion and settlement integration.

Article Information Form

Funding
Authors has no received any financial support for the research, authorship or publication of this study.

Authors' Contribution
Authors contributed equally to the study.

The Declaration of Conflict of Interest/ Common Interest
No conflict of interest or common interest has been declared by authors.

The Declaration of Ethics Committee Approval
This study does not require ethics committee permission or any special permission.

The Declaration of Research and Publication Ethics
Authors of the paper declare that they comply with the scientific, ethical and quotation rules of SAUJS in all processes of the paper and that they do not make any falsification on the data collected. In addition, they declare that Sakarya University Journal of Science and its editorial board have no responsibility for any ethical violations that may be encountered, and that this study has not been evaluated in any academic publication environment other than Sakarya University Journal of Science.

References

[1] E. Güreşçi, “Reflections of Migration from Village to City in Village and City: An Evaluation on Akpınar Village”, Journal of Social and Human Sciences, vol. 2, pp. 47-55, 2010.

[2] H. Candan, E. Oktay, İ. Sürmeli, “The Effect of Industrialisation and Migration on Urban Plans: The Case of Karaman”, International Journal of Social Research, vol. 11, issue 60, 2018.

[3] C. Kaymal, “Cultural Consequences of Rural to Urban Migration: Squatting and Arabesque”, Ulakbilge Journal of Social Sciences, vol. 5, pp. 1499-1519, 2017.

[4] F. Engels, “The Condition of the English Working Class”, Moscow: Progress Publishers, 1975.

[5] R. Marans, R. J. Stimson, “Investigating Quality of Urban Life: Theory, Methods, and Empirical Research”, Springer, 2011.

[6] J. C. Dissart, S. C. Deller, “Quality of Life in the Planning Litterature”, Journal of Planning Literature, pp. 135-161, 2000.

[7] Ö. Yakın İnan, N. Özdemir Söznmez, “Development of Urban Quality of Life Measurement Methods”, International Journal of Economics, Politics, Humanities & Social Sciences, vol. 2, issue 3, 2019.

[8] M. Pacione, “Quality of Life Research in Urban Geography”, Urban Geography, pp. 314-339, 2013.

[9] M. Çoban, Quality of Life in Slums in Turkey (Hatay Example), MA dissertation, Dept. Social Sci., Mersin Univ., Mersin, 2018.

[10] E. Saleh, H. Gomaa, “Community Development Within Slums' Illumination: A Post Occupancy Evaluation Study of Al-Asmarat Project Inhabitants”, Journal of Al-Azhar University Engineering Sector, vol. 17, issue 67, pp. 684-697, 2022.

[11] N. Zainal, G. Kaur, J. Khalili, “Housing Conditions and Quality of Life of the Urban Poor in Malaysia”, Procedia - Social and Behavioural Sciences, vol. 50, pp. 827-838, 2012.

[12] United Nations. (2018, May 16). 2018 Revision of World Urbanization Prospects. [Online]. Available: https://esa.un.org/unpd/wup/

[13] E. Psatha, A. Deffner, Y. Psycharis, “Defining the quality of urban life: Which factors should be considered?”, European Regional Science Association 51st European Congress, Barcelona, Spain, 2011.

[14] The WHOQOL Group, “The World Health Organisation quality of life assessment (WHOQOL): Position paper from the World Health Organisation”, Social Science & Medicine, vol. 41, pp. 1403-1409, 1995.

[15] E. J. Randall, A. M. Williams, “Urban Quality of Life: An Overview”, Canadian Journal of Urban Research, vol. 10, pp. 167-173, 2001.

[16] M. R. Greenberg, “Improving Neighbourhood Quality: A Hierarchy of Needs”, Housing Policy Debate, vol. 10, pp. 601-624, 1999.

[17] K. Lovejoy, S. Handy, P. Mokhtarian, “Neighbourhood Satisfaction in Suburban Versus Traditional Environments: An Evaluation of Contributing Characteristics in Eight California Neighbourhoods”, Landscape and Urban Planning, vol. 97, pp. 37-48, 2010.

[18] H. D. Türkoğlu, “Resident's Satisfaction of Housing Environments: The Case of Istanbul, Turkey”, Landscape and Urban Planning, vol. 39, pp. 55-67, 1997.

[19] C. Geray, “Urban Quality of Life and Municipalities”, Turkish Administrative Journal, iss. 421, pp. 323-345, 1998.

[20] F. Sapancalı, Urban Quality of Life from a Social Perspective, Izmir: Altın Nokta Press and Publication, 2009.

[21] E. Torunoğlu, “Urbanisation, Environmental Problems and Urban Life Quality” in Ve Kirlendi Dünya, Ankara: Öteki Press, 1997.

[22] C. S. Shafer, B. K. Lee, S. Turner, “A tale of three greenway trails: user perceptions related to quality of life”, Landscape and Urban Planning, vol. 49, pp. 163-178, 2000.

[23] R. Veenhoven, “The Four Qualities of Life: Ordering Concepts and Measures of the Good Life”, Journal of Happiness Studies, vol. 1, pp. 1-39, 2000.

[24] J. N. Erzen, Environmental Aesthetics, Ankara: METU Publishing, 2006.

[25] R. W. Marans, “Quality of Urban Life Studies: An Overview and Implications for Environment-Behaviour Research”, in Asia Pacific International Conference on Environment-Behaviour Studies, North Cyprus: Famagusta, 2011, pp. 9-22.

[26] R. W. Marans, W. Rodgers, Towards an Understanding of Community Satisfaction, New York: Halsted Press, 1975.

[27] A. Campbell, P. E. Converse, W. L. Rodgers, The quality of American life: Perceptions, evaluations and satisfactions, New York: Russel Sage, 1976.

[28] R. McCrea, "Urban Quality of Life: Linking Objective Dimensions and Subjective Evaluations of the Urban Environment", Ph.D. Dissertation, Dept. Planning and Architecture, Univ. of Queensland, Australia, 2007.

[29] R. Andelman, R. Board, L. Carman, B. Cummins, A. Ferris, P. Friedman, A. Michalos, J. Samli, S. Shapiro, J. Sirgy, J. Vitterso, R. Veenhoven, Quality of life definition and terminology: A discussion document from the International Society of Quality of Life Studies, The International Society for Quality-of-Life Studies (ISQOLS), 1998.

[30] M. Pacione, "Urban Environmental Quality and Human Wellbeing - A Social Geographical Perspective", Landscape and Urban Planning, vol. 65, pp. 19-30, 2003.

[31] M. Polat, "Socio-Cultural and Economic Life in İnegöl in the XIXth Century According to Archival Records", Ph.D. dissertation, Dept. of Islamic History and Arts, Uludag Univ., Bursa, 2017.

[32] M. M. Yüceşahin, "Urban Settlements of İnegöl District in terms of Urbanisation Process", Journal of Geographical Sciences, vol. 1, pp. 75-95, 2003.

[33] E. H. Peker, "A Nostalgic Stroll in Inegol, this is Our Story", Bursa İnegöl: İnegöl Municipality Culture and Art Services, 2017.

[34] Inegöl Wood Industry Museum (2014, Dec. 14), Inegol Municipality Woodworking Museum Archive Records [Online]. Available: https://www.inegolmobilyamuzesi.gov.tr/tr/Home/

[35] Inegöl City Museum, Inegol Municipality City Museum Introduction Book, Bursa İnegöl, 2009.

[36] S. Coşkun, "Increasing Export Potential in the Furniture Industry: The İnegöl Example", MA Dissertation, Dept. of International Business and Trade, Uludag Univ., Bursa, 2019.

[37] Turkey Ministry of Trade (2021), Republic of Turkey Ministry of Trade Furniture Sector Report, General Directorate of Export, Department of Mining, Metal and Forest Products [Online]. Available: https://ticaret.gov.tr/data/5b87000813b8761450e18d7b/Mobilya%20Sekt%C3%B6r%20Raporu%202021.pdf

[38] W. A. Clark & J. L. Onaka, "Life Cycle and Housing Adjustment as Explanations of Residental Mobility", Urban Studies, vol. 20, pp. 47-57, 1983.

[39] S. K. Erdoğan, G. Birol, "Home" and Place Attachment in the Novel of Cevdet Bey ve Oğulları", Afyon Kocatepe University Journal of Social Sciences, vol. 23, pp. 1567-1580, 2021.

[40] J. J. Potter, R. Cantarero, X. W. Yan, S. Larrick, H. Keele, B. E. Ramirez, "How Does Immigration Impact on the Quality of Life in a Small Town?" in Housing, Space and Quality of Life, R. García-Mira, D. L. Uzzell, J. E. Real, and J. Romay, Aldershot, UK: Ashgate, 2005, pp. 85-91.

[41] Inegol Municipality (2020, July 10), Inegol Municipality. Transportation to Inegol [Online]. Available: https://www.inegol.bel.tr/inegol/inegole-ulasim/

[42] H. Türkoğlu, F. Bölen, P. K. Baran, R. W. Marans, "Measuring Quality of Life in Istanbul", ITU Journal of Architecture Planning Design, vol. 7, pp. 103-113, 2008.

[43] A. L. Alvarez & D. Müller-Eie, "Neighbourhood Conditions and Quality of Life Among Local and Immigrant

Population in Norway", International Journal of Community Well-Being, vol. 5, pp. 753-776, 2022.

[44] B. Nafizoğlu, "Urban Quality of Life and Walkability Experience on Alanya", MA Dissertation, Inst. of Sci. and Techn. Dept. of Architecture, İstanbul Kültür University, İstanbul, 2016.

[45] L. G. N. Orozco, D. Deritei, A. Vancso, O. Vasarhelyi, "Quantifying Life Quality as Walkability on Urban Networks: The Case of Budapest", in Complex Networks and Their Applications VIII, H. Cherifi, S. Gaito, J. Mendes, E. Moro, L. Rocha, Springer, Cham, 2019, pp. 905-918.

[46] E. Dumbaugh, "Safe Streets, Livable Streets", Journal of the American Planning Association, vol. 71, pp. 283-300, 2005.

[47] N. R. Kapoor, J. Tegar, "Human Comfort Indicators Pertaining to Indoor Environmental Quality Parameters of Residental Buildings in Bhopal", International Research Journal of Engineering and Technology (IRJET), vol. 5, pp. 1744-1750, 2018.

[48] M. Frontczak, R. V. Andersen & P. Wargocki, "Construction and Analysis of a Composite Quality of Life Index for a Region of South Africa", Social Indicator Research, vol. 50, pp.887-930, 2012.

[49] T. Greying, F. Tregenna, "Construction and Analysis of a Composite Quality of Life Index for a Region of South Africa", Social Indicator Research, vol. 131, pp. 887-930, 2017

[50] A. Yulu, "Slum Areas of South East Asia: The Case of Manila, Philippines", Turkish Geographical Review, vol. 77, pp. 171-182, 2021.

[51] Z. Yener, K. Arapkirlioğlu, "European Urban Charter (Translation), Ministry of Internal Affairs, General Directorate of Local Administrations Publication, Ankara, 1996.

[52] C. Ambrey, C. Fleming, "Public Greenspace and Life Satisfaction in Urban Australia", Urban Studies, vol. 51, pp. 1290-1321, 2014.

[53] T. Salihoğlu, H. Türkoğlu, "Housing Environment and Urban Quality of Life", Megaron, vol. 14, pp. 203-217, 2019.

[54] S. Öztürk, Z. Özdemir, "The Effect of Urban Open and Green Spaces on Quality of Life; Kastamonu Example", Kastamonu University Journal of Faculty of Forestry, vol. 13, pp. 109-116, 2013.

Sakarya Üniversitesi Fen Bilimleri Dergisi
Sakarya University Journal of Science

ISSN : 2147-835X
Publisher : Sakarya University

Vol. 29, No. 1, 100-112, 2025
DOI: https://doi.org/10.16984/saufenbilder.1440619

Research Article

The Impact of *Hypericum perforatum L.* as an Organic Free-Radical Scavenger in Biodiesel-Diesel Blends

Nalan Türköz Karakullukçu

Karadeniz Advanced Technology Research and Application Center, Ondokuz Mayis University, Samsun, Türkiye, nturkoz@omu.edu.tr

ARTICLE INFO

Keywords:
Hypericum perforatum L.
Biodiesel
Free-radical scavenger
Oxidative stability
BHT

Article History:
Received: 20.02.2024
Revised: 11.02.2025
Accepted: 15.02.2025
Online Available: 28.02.2025

ABSTRACT

The extraction of *Hypericum perforatum* L. (HP) was performed using the Soxhlet extraction method to evaluate its potential as an organic free-radical scavenger in biodiesel-diesel blends. Experimental blends—B100, B20D80, B20D80BHT, and B20D80HP—were prepared, incorporating *Hypericum perforatum* L. extract at a concentration of 3000 ppm, and compared with butylhydroxytoluene (BHT). The antioxidant properties were assessed using differential scanning calorimetry (DSC), thermogravimetric analysis (TGA), Fourier-transform infrared spectroscopy (FT-IR), high-performance liquid chromatography (HPLC), and the 2,2-diphenyl-1-picrylhydrazyl (DPPH) assay. DSC analysis ranked the antioxidant efficiency as D100 < B20D80 < B20D80BHT < B20D80HP, demonstrating the superior stabilization effect of *Hypericum perforatum* L. extract. TGA and FT-IR results confirmed enhanced thermal stability, while HPLC identified key phenolic compounds such as rutin, ellagic acid, and kaempferol, which contribute to antioxidant activity. DPPH assays further confirmed the extract's superior free-radical scavenging efficiency compared to BHT. These findings highlight *Hypericum perforatum* L. as a promising natural antioxidant for improving biodiesel oxidative stability.

1. Introduction

The proportion of energy requirements that are now being covered by fossil fuels is expected to grow. Due to the detrimental impact of fossil resource utilization on environmental contamination, there has been a growing body of research focused on exploring alternate fuel sources [1]. Biodiesel, a sustainable energy source, is widely considered essential for maintaining a healthy ecosystem [2]. The use of biodiesel has several advantages. One noteworthy advantage of this specific feature lies in its non-toxic nature, which guarantees safety and cost-effectiveness [3].

The biodiesel production process entails a sequential progression of chemical reactions, resulting in the formation of free radicals that are prone to oxidation within the surrounding atmosphere [4]. This oxidation process has been shown to reduce fuel efficiency and engine performance [5]. The maintenance of storage stability is a crucial aspect of assessing the quality of biodiesel. Consequently, the significance of standards and fuel quality assurance in Europe cannot be overstated [6].

Free-radical scavengers are a class of molecules that play a crucial role in terminating the oxidation process. They achieve this by either inhibiting the formation of free radicals or scavenging existing radicals, thereby effectively managing the oxidation of biodiesel even at low concentrations [7]. Typically, free-radical scavengers possess phenolic functional groups within their chemical structure [8]. Antioxidant defenses in organisms depend on the intricate interaction between tiny molecules and enzymes to control the levels of potentially hazardous oxidizing species within physiological

Cite as: N. Türköz Karakullukçu (2025). The Impact of *Hypericum perforatum* L. as an Organic Free-Radical Scavenger in Biodiesel-Diesel Blends, *Sakarya University Journal of Science*, 29(1), 100-112. https://doi.org/10.16984/saufenbilder.1440619

boundaries. Chain reactions fueled by peroxyl radicals (ROO·) from uncontrolled oxygen and nitrogen centered radicals lead to enhanced toxic effects [9].

Recent research has shown that organic and synthetic free-radical scavengers must be included in biodiesel in order to improve and optimize its oxidative stability. The prominence of lowering the quantity of free radicals in biodiesel and prolonging oxidation is underscored by the use of free-radical scavengers [10]. This study investigates the phenolic compounds acquired by the extraction process from readily accessible, ecologically sustainable sources [11]. Plant-based biodiesel-diesel fuel blends involving radical reactions were quenched using the *Hypericum perforatum L.* plant from soxhlet extraction.

The free-radical scavenger capacity of the phenolic compounds employed has been validated by a comparative analysis with butylhydroxytoluene (BHT). 3,5-di-tert-butyl-4-hydroxybenzoic acid is a significant metabolite of BHT that can be produced from the corresponding alcohol and aldehyde (BHT-CHO) [12]. This synthetic free-radical scavenger variant is believed to possess hazardous and carcinogenic properties. BHT is a derivative of toluene utilized as an antioxidant. BHT has been found to have both positive and negative effects on cancer growth in many tissues and organs, suggesting that it can serve as either a prooxidant or an antioxidant [13].
However, the specific antioxidant activity kinetics of BHT remain uncertain [14]. Table 1 lists the properties of BHT antioxidation. To achieve the desired objective, blends of biodiesel and diesel were created in certain proportions, namely B100, B20D80, B20D80BHT, and B20D80HP.

The extraction of *Hypericum perforatum L.* plant extract was performed using soxhlet equipment. After adding extract, the mixtures were supplemented with a concentration of 3000 parts per million (ppm) [15].

Table 1. Properties of BHT antioxidation

Property	**Butyl hydroxytoluene (BHT)**
Molecular formula	$C_{15}H_{24}O$
Molecular mass (g/mol)	220.35
Density (g/cm^3)	1.05
Boiling temperature (°C)	265
Flash point temperature (°C)	127

An evaluation was carried out on the plant extract from *Hypericum perforatum L.* to determine its free-radical scavenger activity. Various characterization techniques were utilized, such as thermogravimetric analysis (TGA), differential scanning calorimetry (DSC), fourier-transform infrared spectroscopy (FT-IR), high-performance liquid chromatography (HPLC), and the 2,2-diphenyl-1-picrylhydrazyl (DPPH·) assay. This study's results suggest that incorporating phenolic chemicals, which are recognized for their ability to scavenge free radicals organically, led to a significant reduction in the oxidation of biodiesel-diesel blends [16].

Phenolic free-radical scavengers (AH) are compounds found in plant extracts that can terminate free radicals. These options are typically favored due to their ecologically conscious nature, efficacy, natural composition, affordability, and widespread accessibility [17]. Resonance delocalization in phenolic free-radical scavengers prevents the formation of reactive oxygen species (ROS) and allows for the formation of stable radical intermediates [18]. Phenolic free-radical scavengers demonstrate advantageous attributes in their capacity as hydrogen donors. The stability of the phenoxy radical is attained by the mechanism of electron delocalization across the aromatic ring, as indicated by the presence of valence bond isomers [19].

Oxidation is the most prevalent reaction that produces hydroperoxides as the primary by-product. The rate of the hydroperoxide formation reaction determines the rate of the oxidation reaction. The degree of autooxidation sensitivity is determined by the ease with which allylic hydrogens and peroxyl radicals (ROO·) react with oil production chain forces with weak ties [9]. The hybrid radical is produced when the peroxide radical reacts with the allylic system.

Oxygen attack at both extremities of the allylic system generates a combination of 1- and 3-hydroperoxides [20].

Hypericum perforatum L. is a plant species characterized by its yellow blossoms. Originally indigenous to Europe, this botanical specimen has also been seen to thrive in natural habitat throughout several regions, including North America, Asia, India, Australia, South Africa, and several islands [21] and [22]. The plant in issue is a member of *the Hypericaceae family*, formerly included in the *Clusiaceae family*. The spread of this phenomenon spans across the globe [23]. The pharmacological properties of *Hypericum perforatum L.* have been proven to include its potential for reducing depression and its antiviral and antibacterial activity. These findings support the traditional usage of this plant The potential therapeutic implications of the antidepressant effect within the framework of diabetes have been demonstrated in animal studies [24].

2. General Methods

All compounds were utilized in their as-received state without additional purification and were procured from reputable suppliers such as Merck, Sigma, or Aldrich Chemical Company. The solvent employed in the experiment was of spectroscopic quality. Aves Energy Oil and Food Industry provided Aspire biodiesel, while OPET supplied diesel fuel in Turkiye. The *Hypericum perforatum L.* plant specimens were hand-gathered from the Nebiyan district of Atakum, Samsun, Turkiye. Surface contaminants were removed using distilled water.
Subsequently, the sample was subjected to a drying process in an oven set at a temperature of 60 °C for 72 hours, resulting in the production of a final powdered substance. A grinding apparatus was employed to compact and separate the desiccated substances. The sample was appropriately preserved by being stored at a temperature of 4 °C while ensuring it was shielded from light and humidity until the following extraction protocols were carried out [25-26].

2.1. Soxhlet extraction

Hypericum perforatum L. plant powder (30 g) was put in a filter paper cellulose cartridge and then extracted using 300 mL of analytical grade n-hexane over 8 hours on a soxhlet system. After the completion of the extraction procedure, the residual solvent was efficiently isolated from the solid sample using a rotary evaporator. Following this, the materials within the glass flask with a round bottom were securely centrifuged at 2000 rpm for 7 minute and stored at a temperature of 4 °C, anticipating the upcoming experimental steps [27].

2.2. Preparations of biodiesel-diesel blends

Diesel and biodiesel blends were typically formulated with a biodiesel-to-diesel ratio ranging from 20% to 80%. The B20D80 formula provided the composition information. The plant extracts were combined at a concentration of 3000 ppm [28].

2.3. Differential scanning calorimetry (DSC)

DSC methods can be employed to characterize, quantify, and infer. The present study aimed to examine the initiation temperatures of crystallization for the materials D100, B20D80, B20D80BHT, and B20D80HP. This investigation was conducted using a TA Q-2000 model calorimeter with an RCS90 fitted with a cooling system. Aluminum pans were employed to conduct the analysis. In this experimental procedure, a sample weighing 5 ± 0.5 mg was meticulously placed into the pan. Within the temperature range of 25 °C to -90 °C, the cooling rate was established at 10 °C, accompanied by a nitrogen flow of 50 mL per minute [28].

2.4. Thermogravimetric analysis (TGA)

TGA is mainly utilized for the purpose of ascertaining the relationship between mass loss and increasing or constant temperature under regulated atmospheric conditions. This analytical technique is employed to measure vapors, assess combustion reactions, evaluate degradation processes, and determine leftover substances in products. The breakdown points of numerous organic compounds and the enhancement of their

components may be seen using the TGA [29]. TGA was conducted with the help of an SDT Q-600 (TA Instrument-Waters, USA). The samples were obtained by heating five 5 ± 0.5 mg powder samples to a temperature of 10 °C/min in an alumina pan with an oxygen gas flow of 50 mL/min up to 400 °C [30].

2.5. Fourier transform infrared spectroscopy (FT- IR)

The chemical functional groups present in the plant extract of *Hypericum perforatum L.* were examined using FT-IR spectroscopy with a Perkin Elmer Spectrum-Two equipment from the USA. The spectral range of 650 to 4000 cm^{-1} was utilized for analyzing the surface of the sample. The ATR FT-IR spectra were collected at a consistent temperature under normal environmental conditions. Background subtraction methods, baseline correction, and data fine-tuning were applied as described in reference [31-32].

2.6. High performance liquid chromatography (HPLC)

HPLC is a separation method that involves the transfer of mass between stationary and mobile phases. The primary usage of this is for analytical purposes, where a liquid mobile phase is mechanically pushed through a column holding a stationary phase This setup is illustrated in Figure 1 of an HPLC equipment.

HPLC analysis was performed on the samples using a Shimadzu LC20-A Prominence device. A mass of 0.1 mg was taken from the model and subsequently dissolved in 10 mL of methyl alcohol. 100 µL of extractant was acquired from a filter with a pore diameter of 0.45 µm. The extractant was then combined with 900 µL of methanol and subsequently analyzed [33].

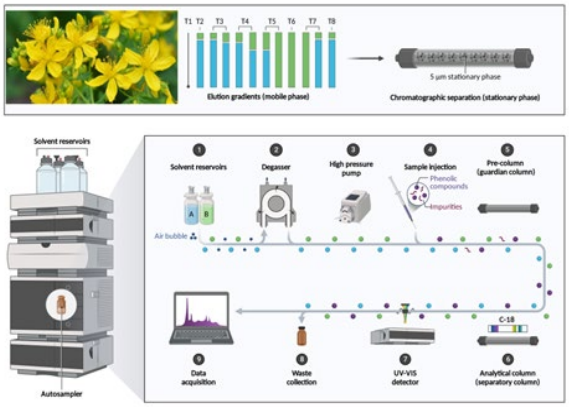

Figure 1. Components and steps of HPLC analysis

2.7. Free-radical scavenger activity

DPPH· is a stable radical with an unpaired electron. It reacts with antioxidant chemicals to produce 1,1-diphenyl-2-picrylhydrazine, leading to discoloration. DPPH· was dissolved in ethanol at 100 mM. The novel compounds were dissolved in dimethyl sulfoxide (DMSO) to create stock solutions at a concentration of 1024 µg/mL. A uniform mixture was created by mixing 150 µL of material with quantities varying from 2 to 1024 µg/mL, along with a reference component (BHT). The mixture was uniformly combined with 50 µL of 0.1 mM DPPH· and dissolved in ethanol. The combination was prepared on a 96-well plate. The combinations were kept in a dark area at room temperature for 30 minutes. Absorbance measurements were taken for each combination at a wavelength of 517 nm, with a blank used as the reference point. The IC50 value in grams per milliliter was determined using the calibration curve. The IC50 value is calculated by measuring the concentration of chemicals needed to cause a 50% inhibition, where a lower IC50 value signifies a higher level of free-radical scavenging activity [34- 35].

2.8. Statistical analysis

Information was examined using SPSS 20.0, an application developed by IBM for the Statistical Package for the Social Sciences. Because the data were normally distributed and the two independent groups' means were similar, an analysis of variance (ANOVA) was used in the study. Using the data gathered, the Tukey honestly significant difference (HSD) test was used for multiple comparisons. The significance

threshold of the values was set at $p < 0.05$, and their statistical significance was ascertained by comparing them to the set of results from the activity analysis. Statistical significance was determined for these values [36-37].

3. Results and Discussion

3.1. Differential scanning calorimetry (DSC)

DSC readings of mixed fuel with organic free-radical scavengers and unbleached fuel were obtained in a nitrogen environment, as shown in Figure 2. The crystallization temperature of the organic free-radical scavenger mix fuel rose from -8.06 °C to -12.67 °C upon comparison of the samples, as indicated in Table 2.

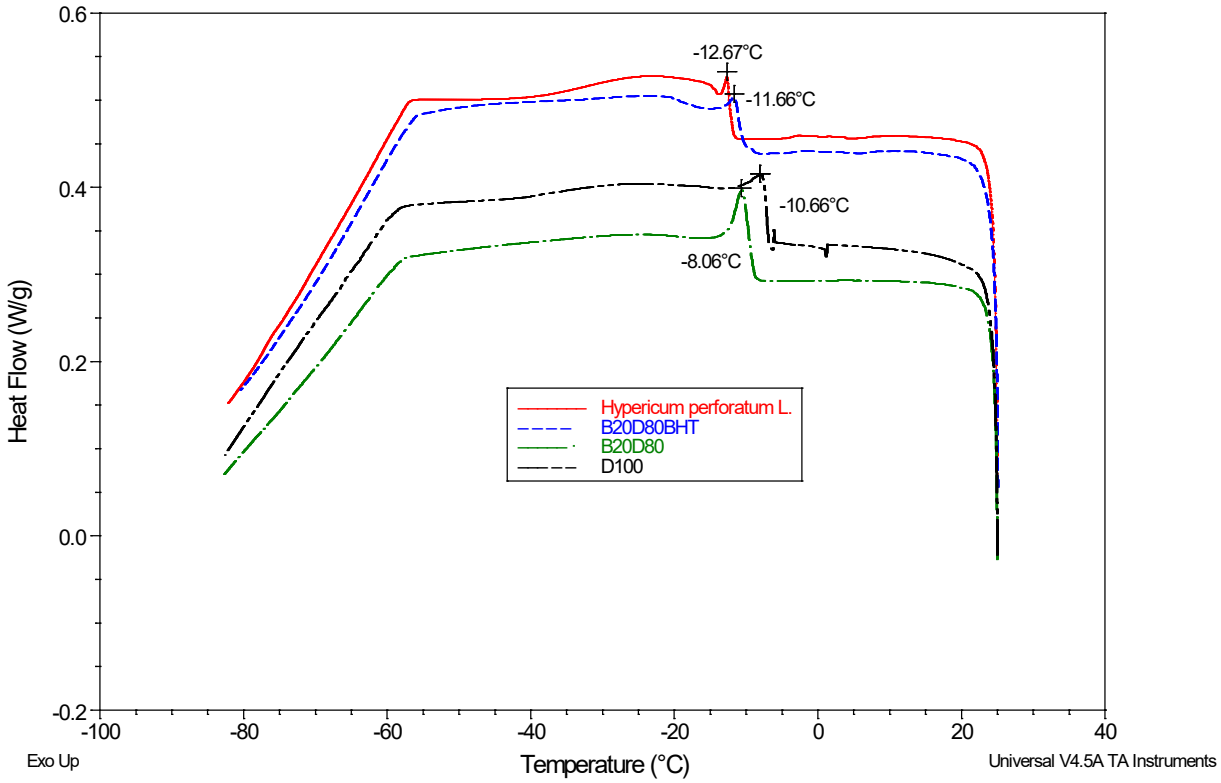

Figure 2. DSC thermograms of D100, B20D80, B20D80BHT, B20D80HP under N_2 atmosphere

Table 2. D100, B20D80, B20D80BHT, and B20D80HP crystallization onset temperatures (°C) in a N2 atmosphere and biodiesel-diesel mix amounts

Sample	Crystallization onset temperature (°C)	Biodiesel (%)	Diesel (%)
D100	|-8.06|	-	100
B20D80	|-10.66|	20	80
B20D80 BHT	|-11.66|	20	80
B20D80 HP	|-12.67|	20	80

When comparing the regular solution model's predictions to the data from the DSC, it is evident that the amount of precipitated crystal is rather close to what was seen in the experiment.

The objective of this research was to determine the critical sites of crystallization for biodiesel-diesel blends, including extracts from the herb *Hypericum perforatum L.*, which neutralize toxic free radicals. A higher crystallization point was found in the *Hypericum perforatum L.* extract, according to the study's results [36].

The temperatures at which the crystallization process begins for D100, B20D80, B20D80BHT, and B20D80HP are different from one another. The experimental findings indicate that the crystallization starting temperatures for the samples labeled as D100, B20D80, B20D80BHT, and B20D80HP were determined to be $|-8.06|$ °C, $|-10.66|$ °C, $|-11.66|$ °C, and $|-12.67|$ °C, respectively.

Due to the fact that the incorporation of organic free-radical scavengers improves oxidation stability in the same sequence, B20D80, B20D80BHT, and B20D80HP would all crystallize at a temperature that is lower than that of D100.
Considering all these factors, it can be concluded that the chemical exhibits traits like quick oxidation, premature crystallization, and a heightened susceptibility to oxidation. This decline results in decreased stability of the properties. The items are B20D80HP, B20D80BHT, B20D80, and D100.

3.2.Thermogravimetric analysis (TGA)

In TGA, the mass of a sample is measured against time and a temperature that is linearly changing in a certain environment. TG is carried out with the use of a thermobalance or a thermogravimetric analyzer. Monitoring the change in weight while maintaining a steady heating rate is how this is accomplished. The outcome is a graph that shows the relationship between mass and either time or temperature. TGA has developed as an alternative technology in the biofuels business that is less costly, faster, and easier to manage [37].

There is just one deterioration degree vs. temperature when all TGA-DTG graphs of the mixes are compared to one another. The onset temperature, which represents the early deterioration temperature, provides insight into the thermal stability and the first boiling point [38].

There is a positive correlation between the stability of the samples and the Tonset values, indicating that as the stability of the samples increases, the Tonset values also increase [39].

The curves depicting the TGA and derivative thermogravimetric analysis (DrTGA) are presented in Figure 3.

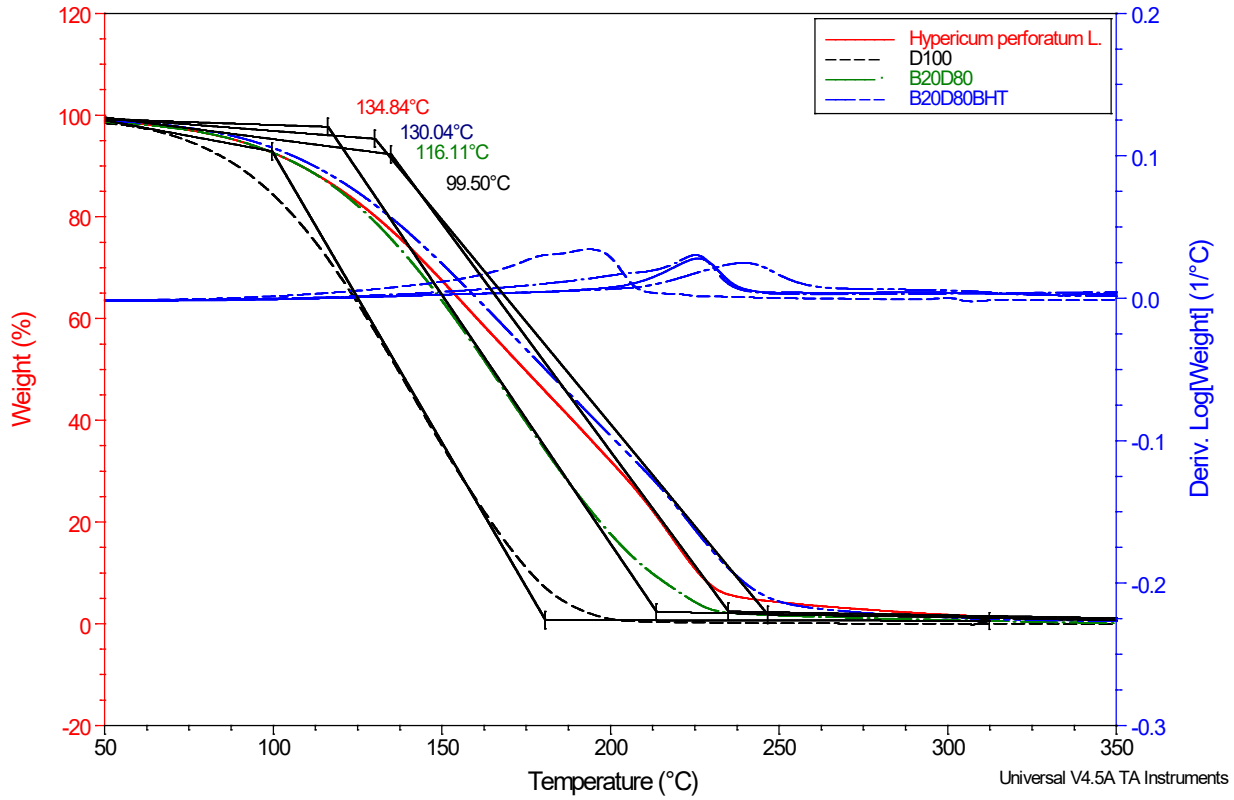

Figure 3. TGA and DrTGA curves of D100, B20D80, B20D80BHT, B20D80HP under O_2 atmosphere

The curves show a significant similarity when observed. Between these temperatures, there is a sample mass loss ranging from 99.28% to 99.59%. The thermometer values obtained from the thermograms are outlined in Table 3.

Table 3. Thermogravimetric analysis (TGA) of samples

Sample name	Temp. range (°C) (From 25 °C)	Max, degradation temp. (°C) (Tonset)	Mass loss (%)
D100	180.55	99.50	99.42
B20D80	213.58	116.11	99.28
B20D80BHT	246.64	130.04	99.33
B20D80HP	234.94	134.84	99.59

3.3. Fourier transform infrared spectroscopy (FT-IR)

The FTIR spectra of a material can be analyzed to determine the presence of ether or ester functional groups by looking for the characteristic ν(CO) and ν(C=O) vibrations. The valence-stretching vibration of an unbounded hydroxyl group, denoted as ν(O−H), is reported to have a frequency of 3392 cm^{-1}. Furthermore, the infrared spectra of the functional biodiesel samples demonstrate a reduction in the magnitude of the vibrations at ν(C−H) (2700−3000 cm^{-1}). Esters exhibit two distinct absorptions resulting from the ν(C=O) and ν(C−O) functional groups.

The presence of an adjacent oxygen atom significantly elevates the carbonyl frequency compared to typical ketones, hence facilitating the distinction between the two. Nevertheless, there exists a degree of overlap among unsaturated esters, resulting in a reduction in the CO frequency [40].

The spectra as a whole exhibit significant absorption bands that are characteristic of the important ester carbonyl functional group ν(CO–O). Because of this, the absence of any neighboring bands indicates the absence of carboxylic acids. The durability of the examined biodiesel samples during storage and oxidation is a result of the extremely low oxidation levels across the board [41]. The FT-IR spectra of D100, B20D80, B20D80BHT, and B20D80HP are depicted in Figures 4, 5 and 6. The impact of including both organic and synthetic free-radical scavengers in biodiesel samples at a concentration of 3000 ppm is documented in Table 4.

Table 4. Frequencies of the functional groups for the fuel samples

Wavenumber, cm^{-1}	Types of vibration	Functional Groups
3392	Stretching	O−H of alcohols functional group
2955	Asymmetrical stretching	=C−H of alkenes functional group
2923	Asymmetrical stretching	C−H of alkanes functional group
2850	Symmetrical stretching	C−H of methylene functional group
1748	Stretching	C=O of ester carbonyl functional group
1462−1380	Stretching	C−O of alkoxy esters, ethers and C−O−C functional groups
725	Bending of alkenes and overlapping of rocking vibration of methylene	=C−H and $-(CH_2)_n$ methylene functional groups of cis disubstituted alkenes and aromatic functional groups

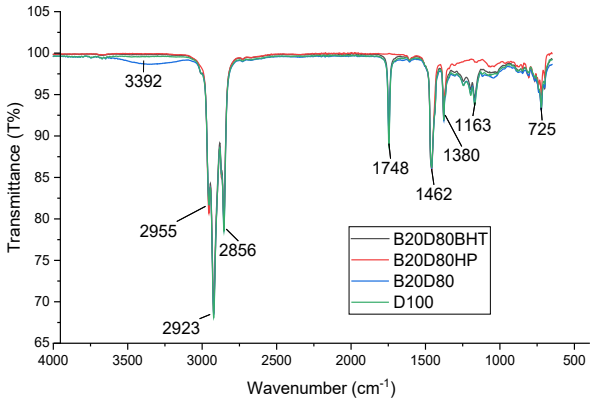

Figure 4. FT-IR spectra of D100, B20D80, B20D80BHT, and B20D80HP at 4000-500 cm^{-1}

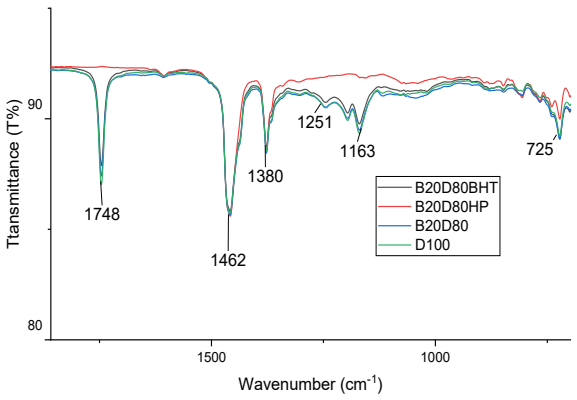

Figure 5. FT-IR spectra of D100, B20D80, B20D80BHT, and B20D80HP at 1875-750 cm^{-1}

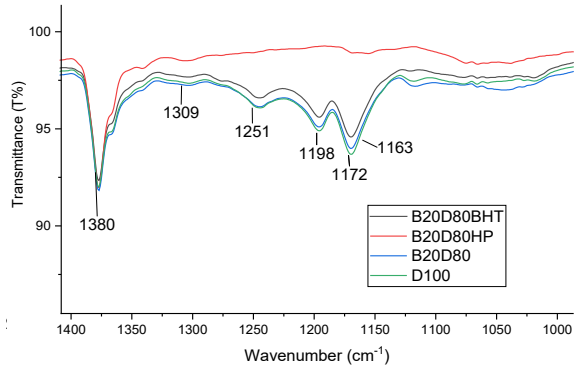

Figure 6. FT-IR spectra of D100, B20D80, B20D80BHT, and B20D80HP at 1400-1000 cm^{-1}

3.4. High performance liquid chromatography (HPLC)

Research has related the ability to scavenge free radicals to the concentration of phenolic components. Phenolic chemicals generated from plants are commonly found in nature and have been noted for their ability to scavenge free radicals. Therefore, it is crucial to identify the phenolic compounds found in plant extracts [42].

Hypericum perforatum L. is known to possess a diverse array of chemical constituents, encompassing volatile oils, flavonoids, anthraquinone derivatives (such as naphthodianthrones), prenylated phloroglucinols, tannins, xanthones, and several other odd substances. The medicinal chemicals found in *Hypericum perforatum L.* species are of significant importance. These compounds include phloroglucinols, including hyperforin, naphthodianthrones like hypericin and pseudohypericin, and flavonoids such as quercetin, quercitrin, rutin, and hyperoside [43].

The HPLC examination of extracts obtained from *Hypericum perforatum L.* revealed that rutin was present at a concentration of 195.243 mg/L, while ellagic acid was shown to be the major component among the phenolic compounds, with a concentration of 173.492 mg/L. The findings of the study indicate that the secondary metabolites present in the *Hypericum perforatum L.* extract are butein (45.989 mg/L), 2,5-dihydroxy benzoic acid (36.902 mg/L), kaempherol (31.050 mg/L), catechin (20.693 mg/L), and myricetin (18.325 mg/L). Naringenin (11.629 mg/L), ferulic acid (5.817 mg/L), chrysin (3.572 mg/L), taxifolin (2.059 mg/L), and coumaric acid (0.576 mg/L) are small components found in the extract as well.

Table 5 shows the findings from high-performance liquid chromatography (HPLC) tests on certain phenolic parts of *Hypericum perforatum L.* extracts. When it comes to the existence of phenolic and flavonoid compounds, our study's results are in line with previous studies [46-48]

3.5. Antioxidant activity evaluation with DPPH· free radical scavenger effect

As seen in Table 6, in comparison to BHT, it was observed that the *Hypericum perforatum L.* extract exhibited a greater numerical value. This finding suggests that the phenolic compounds included in the composition of *Hypericum perforatum L.* extracts exhibit greater efficacy compared to BHT. This implies that the biological activity and free radical-scavenging capabilities of *Hypericum perforatum L.* extracts are superior to those of BHT.

Table 5. HPLC determination of particular phenolic compounds in *Hypericum perforatum L.* extracts

Phenolic Compound	***Hypericum perforatum L.***		
	t_R (min.)	**Conc. (mg/L)**	**λ (nm)**
Catechin	26.688	20.693	280
Taxifolin	47.664	2.059	280
Ellagic acid	71.227	173.492	280
Caffeic acid	0.000	0.000	320
Coumaric acid	43.125	0.576	320
Myricetin	75.086	18.325	360
Kaempherol	79.744	31.050	360
Naringenin	67.671	11.629	280
Chrysin	81.456	3.572	280
Triacetin	0.000	0.000	280
2,5-Dihydroxy Benzoic acid	26.654	36.902	320
Ferulic acid	48.487	5.817	320
Rutin	70.595	195.243	360
Butein	77.534	45.989	360

Table 6. DPPH· free radical scavenging activity of compounds

Sample	**IC50**
Hypericum perforatum L.	15.63±0.95a
BHT	24.42±0.39a

4. Conclusion

In order to carry out this investigation, four samples were created, namely D100, B20D80, B20D80BHT, and B20D80HP. The samples underwent characterization by the utilization of several analytical methods, including DSC, TGA, FT-IR, HPLC, and assessment of the DPPH· free radical scavenging action. The subsequent section presents a concise overview of the outcomes that were obtained.

The use of organic or synthetic antioxidants leads to an elevation in the crystallization temperature (Tc). As a result of contrasting several samples, the crystallization temperatures were found to range from |-8.06| °C to |-12.67| °C, with lower temperatures indicating more purity. The relative ranking of antioxidant potency was determined to be as follows: D100 < B20D80 < B20D80BHT < B20D80HP. The findings derived from the DSC research revealed that the biodiesel samples B100, B20D80, B20D80BHT, and B20D80HP exhibited crystallization onset temperatures of |-8.06| °C, |-10.66| °C, |-11.66| °C, and |-12.67| °C, respectively.

The thermal stability of the samples is observed to increase with the addition of organic free-radical scavengers, as indicated by the TGA and DrTGA curves [44].

The TGA method accurately evaluates the thermal and oxidative stability of fuels. We utilized the DSC technique to precisely identify the initiation of crystallization in the fuel samples [45]. The rationale behind this argument is that depositing foreign material, such as salt or sand, onto snowy roadways functions as a means of impeding the process of crystallization and averting frostbite. Based on the concept, the freezing point exhibits a drop, and the lower the temperature, the later the crystallization occurs. The delayed solidification of matter implies that it may maintain its characteristics for an extended duration, directly correlated with its stability. Thus, a product that has undergone late crystallization has the ability to be stored for a long duration. Late crystallization refers to a situation when the freezing point is low and oxidation occurs slowly.

The FT-IR diagrams show that the oxidative stability of the biodiesel-diesel blend with 3000 ppm of *Hypericum perforatum L.* oil extract (designated B20D80D) was improved because the blend contained fewer functional groups than other simples, such as B20D80BHT.

HPLC analysis of *Hypericum perforatum L.* extracts from Turkiye demonstrated a comprehensive profile of its phenolic constituents. The notable presence of rutin and the significant concentration of ellagic acid underscore their importance in the chemical composition of this plant extract. Especially, rutin is a flavonoid with free-radical scavenger properties. It has been studied for its potential to improve blood vessel health, reduce inflammation, and protect against oxidative stress, which would be beneficial in managing conditions such as cardiovascular disease, diabetes, and arthritis. Rutin-rich plants like buckwheat have been used in traditional medicine for their potential to strengthen blood vessels and reduce bleeding. Rutin-containing herbs have also been employed to treat conditions like hemorrhoids and varicose veins.

The second dominant compound, ellagic acid is a polyphenol with potent free-radical scavenger properties. It has been investigated for its potential in cancer prevention, as it may help inhibit the growth of cancer cells and reduce oxidative damage. Ellagic acid is found in various fruits like strawberries, raspberries, and pomegranates. Traditional herbal medicine has used these fruits to treat diarrhoea, inflammation, and wounds. It has also been considered for its potential anticancer properties.

Similarly to rutin and ellagic acid may also have anti-inflammatory and antimicrobial effects. Moreover, our study has identified and quantified a range of secondary metabolites, including butein, 2,5-dihydroxy benzoic acid, kaempherol, catechin, and myricetin. Naringenin, ferulic acid, chrysin, taxifolin, and coumaric acid also have various health-promoting properties. Naringenin, for example, is found in citrus fruits and has been studied for its potential role in reducing cholesterol levels. Overall, our findings align with previous research, confirming the presence of various flavonoid and phenolic compounds in

this extract. This knowledge is crucial for understanding the potential therapeutic benefits associated with *Hypericum perforatum L.* It may pave the way for further investigations into its applications in pharmaceuticals, nutraceuticals, and natural product-based therapies. The detailed composition data provided in this study will serve as a valuable resource for future research endeavors in the fields of phytochemistry and plant-based medicine.

The assessment of in vitro free-radical scavenger activity was conducted using the free radical scavenging approach, employing the DPPH· molecule. The results were presented in relation to IC50 values, which were denoted in micrograms per milliliter (µg/mL). The samples that included free-radical scavengers showed a decrease in values in comparison to the biodiesel sample lacking free-radical scavengers (D100).

The ranking was primarily established by DSC, TGA, FT-IR, and HPLC tests, illustrating the contribution of *Hypericum perforatum L.* extract to improved oxidative stability. The IC50 values from the DPPH study corroborated this ranking, so validating the effectiveness of the organic free radical scavenger.

Mixed samples of Aspire biodiesel and diesel mix benefit from organic free-radical scavengers. Organic free-radical scavengers improve the oxidative stability of diesel and Aspire biodiesel blends at all concentrations.

Incorporating *Hypericum perforatum L.* plant extract as an organic free-radical scavenger improved biodiesel's oxidative stability, especially at a concentration of 3000 ppm. An extract of the plant *Hypericum perforatum L.* has free-radical scavenger properties that are equivalent to those of the synthetic drug BHT.

Article Information Form

Acknowledgments
The author thanks Prof. Dr. İkbal Agah İnce from the University Medical Center Groningen, Netherlands, for conducting the systematic characterization of the *Hypericum perforatum L.* type and providing support with the literature research.

Funding
The author has no received any financial support for the research, authorship or publication of this study.

Author Contribution
Conceptualization, methodology, software, validation, formal analysis, investigation, resources, data curation, writing—original draft preparation, writing—review and editing, visualization, supervision, project administration and funding acquisition performed by N.T.K. Author has read and agreed to the published version of the manuscript.

The Declaration of Conflict of Interest/ Common Interest
No conflict of interest or common interest has been declared by the author.

The Declaration of Ethics Committee Approval
This study does not require ethics committee permission or any special permission.

The Declaration of Research and Publication Ethics
The author of the paper declares that she complies with the scientific, ethical and quotation rules of SAUJS in all processes of the paper and that she does not make any falsification on the data collected. In addition, she declares that Sakarya University Journal of Science and its editorial board have no responsibility for any ethical violations that may be encountered, and that this study has not been evaluated in any academic publication environment other than Sakarya University Journal of Science.

References

[1] M. M. Ali, S. A. Gheni, S. M. R. Ahmed, H. M. Hmood, A. A. Hassan, H. R. Mohammed, S. T. Mohammed, N. T. Karakullukcu, "Catalytic production of biodiesel from waste cooking oil in a two-phase oscillatory baffled reactor:

Deactivation kinetics and ANN modeling study," Energy Conversion and Management: X, vol. 19, p. 100383, 2023.

[2] A. Srivastava, R. Prasad, "Triglycerides-based diesel fuels," Renewable & Sustainable Energy Reviews, vol. 4, pp. 111–133, 2000.

[3] N. Khan, M. A. Warith, G. Luk, "A comparison of acute toxicity of biodiesel, biodiesel blends, and diesel on aquatic organisms," Journal of the Air and Waste Management Association, vol. 57, pp. 286–296, 2007.

[4] H. Hosseinzadeh-Bandbafha, D. Kumar, B. Singh, H. Shahbeig, "Biodiesel antioxidants and their impact on the behavior of diesel engines: A comprehensive review," Fuel Processing Technology, vol. 232, p. 107264, 2022.

[5] I. M. Rizwanul Fattah, H. H. Masjuki, M. A. Kalam, M. Mofijur, "Effect of antioxidant on the performance and emission characteristics of a diesel engine fueled with palm biodiesel blends," Energy Conversion and Management, vol. 79, pp. 265–272, 2014.

[6] K. Varatharajan, D. S. Pushparani, "Screening of antioxidant additives for biodiesel fuels," Renewable and Sustainable Energy Reviews, vol. 82, pp. 2017–2028, 2018.

[7] L. S. De Sousa, C. V. R. De Moura, J. E. De Oliveira, E. M. De Moura, "Use of natural antioxidants in soybean biodiesel," Fuel, vol. 134, pp. 420–428, 2014.

[8] A. Kurek-Górecka, A. Rzepecka-Stojko, M. Górecki, J. Stojko, M. Sosada, G. Swierczek-Zieba, "Structure and antioxidant activity of polyphenols derived from propolis," Molecules, vol. 19, pp. 78–101, 2014.

[9] M. C. Foti, R. Amorati, "Non-phenolic radical-trapping antioxidants," Journal of Pharmacy and Pharmacology, vol. 61, pp. 1435–1448, 2009.

[10] I. M. Rizwanul Fattah, H. H. Masjuki, M. A. Kalam, M. A. Hazrat, B. M. Masum, S. Imtenan, A. M. Ashraful, "Effect of antioxidants on oxidation stability of biodiesel derived from vegetable and animal based feedstocks," Renewable and Sustainable Energy Reviews, vol. 30, pp. 356–370, 2014.

[11] X. Pan, F. Sun, M. Wang, H. Sun, R. Zhang, M. Feng, X. Zhang, "Fe (VI) oxidation of synthetic phenolic antioxidants: Kinetics, influencing factors, transformation mechanism and toxicity," Chemical Engineering Journal, vol. 480, 2024.

[12] G. Kumar, D. Kumar, Poonam, R. Johari, C. P. Singh, "Enzymatic transesterification of *Jatropha curcas* oil assisted by ultrasonication," Ultrasonics Sonochemistry, vol. 18, pp. 923–927, 2011.

[13] V. Sindhi, V. Gupta, K. Sharma, S. Bhatnagar, R. Kumari, N. Dhaka, "Potential applications of antioxidants – A review," Journal of Pharmacy Research, vol. 7, pp. 828–835, 2013.

[14] R. S. Lanigan, T. A. Yamarik, F. A. Andersen, "Final report on the safety assessment of BHT," vol. 21, 2002.

[15] A. A. Hamid, Z. M. Shah, R. Muse, S. Mohamed, "Characterisation of antioxidative activities of various extracts of *Centella asiatica* (L.) urban," Food Chemistry, vol. 77, pp. 465–469, 2002.

[16] S. N. Nichenametla, T. G. Taruscio, D. L. Barney, J. H. Exon, "A review of the effects and mechanisms of polyphenolics in cancer," Critical Reviews in Food Science and Nutrition, vol. 46, pp. 161–183, 2006.

[17] R. E. Mutha, A. U. Tatiya, S. J. Surana, "Flavonoids as natural phenolic

compounds and their role in therapeutics: An overview," Future Journal of Pharmaceutical Sciences, vol. 7, 2021.

[18] J. Zhu, W. J. Johnson, C. L. Sevilla, J. W. Herrington, M. D. Sevilla, "An electron spin resonance study of the reactions of lipid peroxyl radicals with antioxidants," Journal of Physical Chemistry, vol. 94, pp. 7185–7190, 1990.

[19] J. Gu, J. Ma, J. Jiang, L. Yang, J. Yang, J. Zhang, H. Chi, Y. Song, S. Sun, W. Q. Tian, "Hydrated electron (*eaq*−) generation from phenol/UV: Efficiency, influencing factors, and mechanism," Applied Catalysis B: Environmental, vol. 200, pp. 585–593, 2017.

[20] T. Dugmore, "The autoxidation of biodiesel and its effects on engine lubricants," PhD dissertation, 2011.

[21] É. Signori, D. Borsato, L. Ramazzoti, C. Silva, T. L. Gomes, E. Antônio, "Kinetic parameters of the oxidation reaction of commercial biodiesel with natural antioxidant additives," Industrial Crops & Products, vol. 125, pp. 59–64, 2018.

[22] J. M. C. Gutteridge, B. Halliwell, "Free radicals and antioxidants in the year 2000: A historical look to the future," Annals of the New York Academy of Sciences, vol. 899, pp. 136–147, 2000.

[23] Y. Zou, Y. Lu, D. Wei, "Antioxidant activity of a flavonoid-rich extract of *Hypericum perforatum* L. in vitro," Journal of Agricultural and Food Chemistry, vol. 52, pp. 5032–5039, 2004.

[24] A. Mullaicharam, N. Halligudi, "St John's Wort (*Hypericum perforatum* L.): A review of its chemistry, pharmacology and clinical properties," International Journal of Research In Phytochemical And Pharmacological Sciences, vol. 1, pp. 5–11, 2018.

[25] S. Z. Nobakht, M. Akaberi, A. H. Mohammadpour, A. T. Moghadam, S. A. Emami, "Hypericum perforatum: Traditional uses, clinical trials, and drug interactions," Iranian Journal of Basic Medical Sciences, vol. 26, pp. 1045–1058, 2022.

[26] A. Alahmad, I. Alghoraibi, R. Zein, S. Kraft, G. Dräger, J. G. Walter, T. Scheper, "Identification of major constituents of *Hypericum perforatum* L. extracts in Syria by development of a rapid, simple, and reproducible HPLC-ESI-Q-TOF MS analysis and their antioxidant activities," ACS Omega, vol. 7, pp. 13475–13493, 2022.

[27] E. Burgaz, M. G. Sezener, Ç. Dikbas, A. K. Ceylan, M. Andac, A. Çiftci, "Determination of antibacterial properties of silver nanoparticles with aqueous extracts of *Brassica oleracea* L. var. *Acephala* D.C. in cotton textiles," Journal of Elementology, vol. 26, pp. 447–462, 2021.

[28] X. Wang, M. Dai, Y. Xie, J. Han, Y. Ma, C. Chen, "Experimental investigation of evaporation characteristics of biodiesel-diesel blend droplets with carbon nanotubes and nanoceria as nanoadditives," Applied Surface Science, vol. 505, p. 144186, 2020.

[29] E. Meyvaci, E. Catiker, T. Ozturk, "Synthesis and characterization of poly(β-propiolactone) b-poly(methyl methacrylate) tri-arm block copolymer using atom transfer radical polymerization," Karadeniz Fen Bilimleri Dergisi, vol. 13, pp. 882–893, 2023.

[30] S. Bento, "The effects of the addition of dill oil (*Anethum graveolens*) into biodiesel-diesel blends," Fuel, vol. 5, pp. 203–212, 2022.

[31] V. A. Huck-Pezzei, J. D. Pallua, C. Pezzei, L. K. Bittner, S. A. Schönbichler, G. Abel, M. Popp, G. K. Bonn, C. W. Huck, "Fourier transform infrared imaging analysis in discrimination studies of *St. John's Wort* (*Hypericum perforatum*),"

Analytical and Bioanalytical Chemistry, vol. 404, pp. 1771–1778, 2012.

[32] H. Bouzmane, S. Tirkeş, V. M. Yılmaz, Ü. Tayfun, S. Tirkeş, "Contribution of surface silanization process on mechanical characteristics of TPU-based composites involving feldspar and quartz minerals," Journal of Vinyl and Additive Technology, vol. 29, pp. 109–119, 2023.

[33] M. R. Jung, F. D. Horgen, S. V. Orski, C. V. Rodriguez, K. L. Beers, G. H. Balazs, T. T. Jones, T. M. Work, K. C. Brignac, S. J. Royer, "Validation of ATR FT-IR to identify polymers of plastic marine debris, including those ingested by marine organisms," Marine Pollution Bulletin, vol. 127, pp. 704–716, 2018.

[34] H. Yakan, "Novel Schiff bases derived from isothiocyanates: Synthesis, characterization, and antioxidant activity," Research on Chemical Intermediates, vol. 46, pp. 3979–3995, 2020.

[35] P. de M. Cândido-Bacani, M. B. dos Reis, J. M. Serpeloni, T. R. Calvo, W. Vilegas, E. A. Varanda, I. M. de S. Cólus, "Mutagenicity and genotoxicity of isatin in mammalian cells in vivo," Mutation Research - Genetic Toxicology and Environmental Mutagenesis, vol. 719, pp. 47–51, 2011.

[36] M. Y. Mir, A. N. Kamili, Q. P. Hassan, S. Rafi, J. A. Parray, S. Jan, "In vitro regeneration and free radical scavenging assay of *Hypericum perforatum* L.," National Academy Science Letters, vol. 42, pp. 161–167, 2019.

[37] L. Ivanova, P. Vassileva, A. Detcheva, "Characterization and adsorption properties of *Hypericum perforatum* L. for the removal of Cu^{2+} ions from aqueous solutions," Cellulose Chemistry and Technology, vol. 54, pp. 1023–1030, 2020.

[38] V. M. Yılmaz, T. Tunç Parlak, K. Yıldız, "Dehydroxylation of high-energy ball-milled diasporic bauxite," Journal of Thermal Analysis and Calorimetry, vol. 134, pp. 135–141, 2018.

[39] S. Jain, M. P. Sharma, "Thermal stability of biodiesel and its blends: A review," Renewable and Sustainable Energy Reviews, vol. 15, pp. 438–448, 2011.

[40] A. Oyerinde, E. Bello, "Use of Fourier transformation infrared (FTIR) spectroscopy for analysis of functional groups in peanut oil biodiesel and its blends," British Journal of Applied Science & Technology, vol. 13, pp. 1–14, 2016.

[41] Z. Movasaghi, S. Rehman, I. U. Rehman, "Fourier transform infrared (FTIR) spectroscopy of biological tissues," Applied Spectroscopy Reviews, vol. 43, pp. 134–179, 2008.

[42] B. Taşcı, H. Kütük, İ. Koca, "Antioxidant activity of *Allium scorodoprasum L.* subsp. *Rotundum* (L.) Stearn plant grown in Turkey," Turkish Journal of Agriculture - Food Science and Technology, vol. 7, pp. 1561–1567, 2019.

[43] C. Rice-Evans, "Plant polyphenols: Free radical scavengers or chain-breaking antioxidants?" Biochemical Society Symposium, vol. 61, pp. 103–116, 1995.

[44] R. R. Al-Samaraae, A. E. Atabani, G. Uguz, G. Kumar, O. Arpa, A. Ayanoglu, M. N. Mohammed, H. Farouk, "Perspective of safflower (*Carthamus tinctorius*) as a potential biodiesel feedstock in Turkey: Characterization, engine performance and emissions analyses of butanol–biodiesel–diesel blends," Biofuels, vol. 11, pp. 715–731, 2020.

[45] G. Uğuz, A. E. Atabani, M. N. Mohammed, S. Shobana, S. Uğuz, G. Kumar, A. H. Al-Muhtaseb, "Fuel stability of biodiesel from waste cooking oil: A comparative evaluation with various antioxidants using FT-IR and DSC techniques," Biocatalysis and Agricultural Biotechnology, vol. 21, 2019.

Sakarya Üniversitesi Fen Bilimleri Dergisi
Sakarya University Journal of Science

ISSN : 2147-835X
Publisher : Sakarya University

Vol. 29, No. 1, 113-124, 2025
DOI: https://doi.org/10.16984/saufenbilder.1619887

Research Article

Modeling and Experimental Analysis of Bias Voltage Effects on Hardness and Thickness of TiN Coatings Produced by PVD Process

Ahmet Uğur Kaya

Kocaeli University, Faculty of Science, Department of Physics, Kocaeli, Türkiye, ugurk@kocaeli.edu.tr

ARTICLE INFO

Keywords:
PVD coating
TiN
Bias voltage
Film thickness
Hardness
Theoretical models

Article History:
Received: 14.01.2025
Revised: 04.02.2025
Accepted: 25.02.2025
Online Available: 28.02.2025

ABSTRACT

This study examines the impact of bias voltage on the mechanical properties and film thickness of TiN coatings deposited on cold work tool steel via the PVD process. TiN coatings, known for their excellent hardness and wear resistance, were deposited at varying bias voltages (100–300 V). Hardness measurements and SEM analyses were conducted to evaluate the relationship between bias voltage, hardness, and film thickness. Theoretical models, including hardness-load and indentation hardness relationships, were developed to provide a comprehensive understanding of these trends. The results demonstrate that increasing the bias voltage enhances coating hardness up to 250 V due to improved atomic mobility and nucleation density. However, beyond this threshold, grain coarsening and defect formation contribute to a reduction in hardness. A monotonic decrease in film thickness was observed with higher bias voltages, attributed to ion bombardment and re-sputtering effects. The developed models showed strong alignment with experimental results, particularly for indentation hardness behavior, while discrepancies in the hardness-load relationship were noted under high loads and higher bias voltages. These findings underscore the importance of precise bias voltage control and theoretical modeling in enhancing TiN coating performance for industrial applications.

1. Introduction

High-speed steels (HSS) are widely used in industrial applications due to their excellent thermal stability, durability, wear resistance, and resistance to chemical interactions. However, during drilling operations, chip formation and its impact on the drill surface negatively affect the performance of HSS tools. To address these issues, HSS tools are often enhanced with coatings such as TiN, TiCN, and CrN to improve their wear resistance and overall performance [1, 2].

Physical Vapor Deposition (PVD) technology is commonly used for coating HSS tools due to its low processing temperatures and environmentally friendly nature. TiN coatings are preferred for their high hardness and low friction coefficients. Studies have shown that PVD coatings such as TiN, Ti(Y)N, and TiAlN significantly enhance the mechanical properties of HSS tools, leading to improved performance in various machining applications [3, 4]. For instance, the addition of yttrium to TiN coatings (Ti(Y)N) increases adhesion and corrosion resistance, providing a 36% increase in tool life compared to standard TiN coatings [5].

Further studies have explored the impact of coating parameters such as cathode current and bias voltage on film thickness and hardness. Higher bias voltages increase ion bombardment, producing denser and harder coatings, while increased cathode currents enhance deposition rates and influence microstructure [6]. Additionally, duplex coatings, which combine nitriding and PVD coatings, offer the advantages of both methods, extending tool life and increasing wear resistance [7-9].

Cite as: A. U. Kaya (2025). Modeling and Experimental Analysis of Bias Voltage Effects on Hardness and Thickness of TiN Coatings Produced by PVD Process, *Sakarya University Journal of Science*, 29(1), 113-124. https://doi.org/10.16984/saufenbilder.1619887

Cold work tool steels are frequently used in applications requiring high wear resistance and hardness due to their high carbon and chromium content. For example, it has been reported that PVD coatings, including TiN, on DIN 1.2379 and 1.2080 steels significantly improve tool life and mechanical performance [1, 2]. Recent studies have further expanded the understanding of TiN coatings in various industrial applications. For instance, researchers have studied the tribological optimization of titanium-based PVD multilayer hard coatings on steels used for cold rolling applications, highlighting the critical role of deposition parameters in enhancing wear resistance and mechanical performance [10].

Similarly, the wear behavior of uncoated, TiN, and AlTiN coated cold work tool steel (1.2379) was optimized using response surface methodology, providing valuable insights into how coating compositions influence durability under operational conditions [11]. Additionally, the mechanical behavior of PVD coatings during manufacturing processes was investigated, emphasizing the significance of coating-substrate interactions in determining overall performance [12]. These studies underline the continuous advancements in PVD coating technologies and the growing emphasis on optimizing mechanical properties through controlled deposition parameters.

Previous studies have extensively examined the relationship between coating thickness and hardness for PVD-deposited TiN coatings, highlighting the critical role of deposition parameters such as bias voltage. However, this study uniquely combines experimental findings with theoretical modeling approaches, including energy-based ion bombardment modeling and static/dynamic analysis methods. By integrating hardness and indentation models, this research offers a comprehensive understanding of the effects of bias voltage on both mechanical properties and indentation behavior, offering new insights into the optimization of PVD coatings for industrial applications [13–18].
Similarly, the wear behavior of uncoated, TiN, and AlTiN coated cold work tool steel (1.2379) was optimized using response surface methodology, providing valuable insights into how coating compositions influence durability under operational conditions [19, 20]. Additionally, the mechanical behavior of PVD coatings during manufacturing processes was investigated, emphasizing the significance of coating-substrate interactions in determining overall performance [21, 22]. Studies have demonstrated that PVD coatings such as TiN and AlTiN exhibit improved wear resistance due to optimized deposition conditions and substrate interactions [23, 24]. Furthermore, advancements in coating techniques have led to the development of enhanced tribological performance, particularly in cold rolling applications where surface integrity is crucial [25-27]. These studies underline the continuous advancements in PVD coating technologies and the growing emphasis on optimizing mechanical properties through controlled deposition parameters.

Additionally, it was investigated the mechanical behavior of PVD coatings during manufacturing processes, emphasizing the significance of coating-substrate interactions in determining overall performance [28]. These studies underline the continuous advancements in PVD coating technologies and the growing emphasis on optimizing mechanical properties through controlled deposition parameters.

Previous studies have extensively examined the relationship between coating thickness and hardness for PVD-deposited TiN coatings, highlighting the critical role of deposition parameters such as bias voltage. However, this study uniquely combines experimental findings with theoretical modeling approaches, including energy-based ion bombardment modeling and static/dynamic analysis methods. By integrating hardness and indentation models, this research offers a comprehensive understanding of the effects of bias voltage on both mechanical properties and indentation behavior, offering new insights into the optimization of PVD coatings for industrial applications [10-15].

2. Materials and Methods

2.1. Materials

The substrate material used for the coating process was 1.2080 (D3 AISI/SAE) Böhler-Edelstahl cold work tool steel Disc-shaped

samples were cleaned using a KLN ultrasonic cleaner operating at a frequency of 40 kHz. The cleaning process was performed in deionized water at room temperature for 15 minutes to effectively remove surface contaminants. After ultrasonic cleaning, the samples were dried using clean, pressurized air to prevent any residual moisture. TiN coatings were deposited using a Multiarc (US.A.) and Siemens (Germany) PVD coating system at OPAŞ-Titanit Coatings Center. The coating parameters, including the applied bias voltages, are presented in Table 1.

2.2. Hardness measurements

Hardness measurements were performed using a Fischerscope microindentation hardness tester. The tests utilized a four-sided pyramidal (Vickers) diamond tip, which was brought into contact with the sample surfaces under fixed loading rates. The residual indent areas were measured after a constant loading period to calculate hardness values.

The bias voltage range of 100 V to 300 V was selected based on preliminary experimental observations and insights from previous studies on TiN coatings deposited via the PVD process. This range was chosen to cover both low and high bias conditions to observe the transition in coating properties. Lower bias voltages (100–150 V) were included to evaluate the initial stages of ion bombardment and its effect on coating density and hardness, while higher voltages (200–300 V) were selected to investigate potential grain coarsening, defect formation, and changes in mechanical properties due to increased ion energy [6, 9, 14].

The optimal performance observed at 250 V is attributed to enhanced atomic mobility and increased nucleation density, which significantly improved hardness and coating uniformity. This voltage represents a threshold where the beneficial effects of ion bombardment are maximized without inducing excessive defects or grain coarsening, as supported by similar findings in prior research [13, 23, 24].

The indentation depth range was between 0.05 to 2.85 µm. Additionally, we clarified that each hardness measurement was averaged from five replicates to ensure data reliability and consistency.

Table 1. Coating parameters

Bias Voltage (V)	Cathode Current (A)	Press (mTorr)	Coating Duration (min.)	Coating Temp. (°C)
100	50	2.1×10^{-2}	45	450
150	50	2.1×10^{-2}	45	450
200	50	2.1×10^{-2}	45	450
250	50	2.1×10^{-2}	45	450
300	50	2.1×10^{-2}	45	450

2.3. Film thickness measurement

Cross-secitonal scanning electron microscope (SEM) images were captured using a JEOL JSM 840 microscope at the Brisa R&D Center analytical laboratories. Film thicknesses were measured from cross-sectional SEM images at 3000× magnification under a 15 kV accelerating voltage.

2.4. Modeling approaches

2.4.1. Indentation hardness model

The indentation hardness H_{meas} was modeled based on the composite hardness approach commonly used in thin-film mechanics [10, 11].

The hardness at various indentation depths was modeled using the following equation:

$$H_{meas} = \left(H_{coat} \cdot (1 - f)\right) + (H_{subs} \cdot f) \quad (1)$$

Where; H_{meas}: Measured hardness (theoretical, based on the model),

H_{coat}; Coating hardness, H_{subs}: Substrate hardness, $f = \frac{d}{d+t}$: with d as the indentation depth and t as the coating thickness.

2.4.2. Hardness-load relationship model

The load-dependent hardness model (H_{load}) follows methodologies proposed for analyzing mechanical properties of thin films under varying loads [10, 12, 13].

The hardness-load relationship was evaluated using the following expression:

$$H_{load} = \left(H_{coat} \cdot \left(1 - \frac{P}{P_{\max}}\right)\right) + \left(H_{subs} \cdot \frac{P}{P_{\max}}\right) \quad (2)$$

where; H_{load}:Load-dependent hardness (theoretical, based on the model),

P_{max}: Maximum load,
$H_{coating}$: Coating hardness,
$H_{substrate}$: Substrate hardness.

2.4.3. Energy-based ion bombardment model

To analyze the effects of bias voltage on coating properties, the energy-based ion bombardment model was employed [14, 15]. This model calculates the energy imparted to the coating surface using the equation:

$$E = \frac{1}{2}mv^2 \quad (3)$$

Where; m is the ion mass [14], and v represents the ion velocity derived from the applied bias voltage [15]. These high-energy ions significantly influence coating density, hardness, and re-sputtering effects.
The ion velocity (v) is calculated based on the applied bias voltage, using:

$$v = \sqrt{\frac{2qV}{m}} \quad (4)$$

Where; q is the ionic charge, V is the applied bias voltage, and m is the mass of the ion (e.g., titanium or nitrogen ions in this study) [16].

This modeling approach has been previously used in similar studies to explain the effects of ion bombardment on film growth and mechanical properties. For instance, studies have shown that energy transfer mechanisms during ion bombardment enhance surface diffusion and grain refinement [14, 15].

3. Results and Discussion

Hardness measurements of TiN-coated samples were carried out using a Fischerscope micro indentation hardness tester under the coating parameters listed in Table 1. The results for hardness-load and hardness-indentation depth relationships are presented in Figures 1 and 2. The initial observations indicate a significant dependence of the hardness values on the applied bias voltage during the coating process.

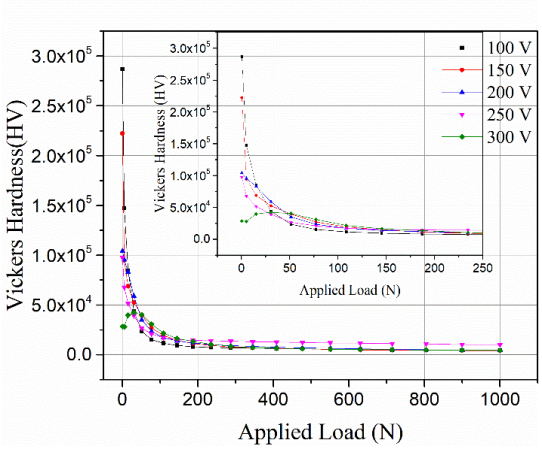

Figure 1. Variation of Vickers hardness of TiN-coated samples as a function of applied load for different bias voltages (100–300 V). The inset shows the detailed view for the load range 0–250 N.

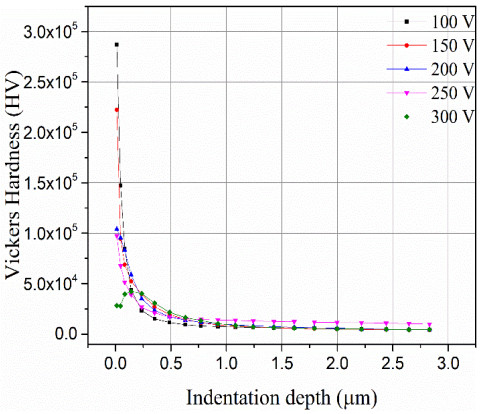

Figure 2. Variation of Vickers hardness of TiN-coated samples as a function of indentation depth

At low loading rates (<50 N), hardness values were high for coatings with low bias voltage. When the load amount increased up to 200 N, an increase in hardness values was observed in coatings with high bias voltage (Figure 1 inset). At loads above 200 N, the decrease in hardness values significantly slowed for all samples. After this load value, the hardness of the samples coated with a 200 and 250 V bias voltage was higher compared to the other samples.

Studies have shown that increasing the bias voltage generally leads to higher hardness values due to enhanced atomic mobility and compressive stress during the coating process [6,

12]. However, after reaching a certain threshold, further increases in bias voltage or coating current can result in grain coarsening and increased defects, which may reduce hardness and wear resistance [1, 3, 14]. Researchers have observed that while bias voltages around 100 V can significantly improve the mechanical properties of TiN coatings, bias voltages beyond this level may lead to increased friction and reduced coating integrity due to structural changes such as grain coarsening or the formation of defects [3, 4, 17, 21, 22].

In this study, hardness values increased up to a bias voltage of 250 V; beyond this value, a significant decrease in hardness was observed. Similar threshold values have been reported in the literature for comparable bias voltages and loading rates [1, 9, 13, 23, 24]. After this voltage value, the decrease in hardness was associated with grain size and defect formation in the coating [1]. The slight decrease or stabilization of hardness values after a loading rate of 200 N was also linked to defect formation in the coating as the bias voltage increased [9].

The observed trend of increasing hardness up to 250 V, followed by a subsequent decrease, aligns with findings from previous studies [26, 27]. Carabillò et al. [26] and Bülbül et al. [27] also reported that increasing bias voltage enhances hardness due to increased atomic mobility and compressive stress. However, beyond a certain threshold, grain coarsening and defect formation become dominant, leading to a decline in hardness. These discrepancies are often attributed to changes in coating microstructure, residual stress accumulation, and the influence of substrate interactions under higher bias voltages.

Additionally, it is important to explain the relationship between indentation depth and film thickness with hardness, which forms the basis of this study. A similar behavior observed in the hardness-bias voltage relationship was also evident in the hardness-indentation relationship (Figure 2). Up to an indentation depth of 0.15 micrometers, hardness values were directly proportional to the bias voltage. Higher hardness values were observed at higher bias voltage levels. Between indentation depths of 0.15 and 0.7 micrometers, the sample coated at a bias voltage of 300 V exhibited the highest hardness value. However, beyond 0.7 micrometers, a trend similar to that observed in the hardness-bias voltage relationship emerged, where the sample coated at 250 V demonstrated the highest hardness. These findings highlight the transition from coating-dominated hardness behavior at lower indentation depths to substrate-dominated behavior as the indentation depth increased.

These transitions have been extensively studied, highlighting the relationship between coating thickness, mechanical properties, and the effects of deposition parameters and substrate interactions. [12-14].

Figure 3 illustrates the thickness of the TiN coatings. The film thicknesses were determined by averaging multiple measurements obtained from SEM cross-sectional images using screen scale calibration. The results are presented in Table 2, showing the variation of coating thickness with respect to bias voltage.

Table 2. Film thickness of TiN coatings under varying bias voltages

Bias Voltage(V)	Thickness(µm)
100	1.64
150	1.55
200	1.47
250	1.03
300	0.9

The data indicate a monotonic decrease in film thickness as bias voltage increases. This observation aligns with previous studies that attribute the reduction in thickness to ion bombardment effects, which lead to resputtering of surface atoms and reduced deposition rates at higher bias voltages [6, 16, 17]. Furthermore, the observed monotonic decrease in film thickness with increasing bias voltage aligns with the findings of in the study, which was reported similar trends in titanium-based PVD multilayer hard coatings [26].

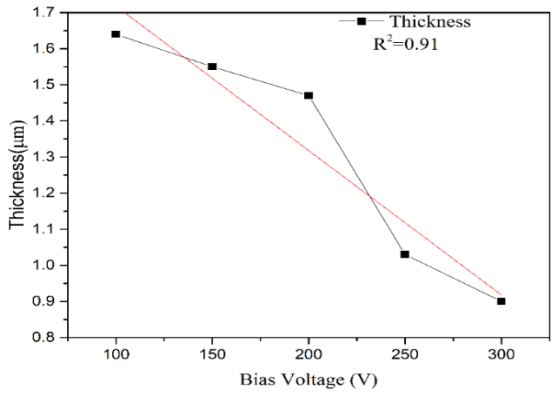

Figure 3. Film thickness of TiN coated samples with respect to Bias Voltage

Additionally, It was emphasized that deposition parameters, particularly bias voltage, significantly influence the wear behavior of TiN coatings, corroborating the hardness variations observed in this study [27]. It was further highlighted how substrate interactions under varying coating conditions affect mechanical properties, which parallels the substrate influence identified in our indentation hardness analysis [28].

This trend is accompanied by a rise in hardness values up to a certain threshold. The thickness reduction is monotonic up to a bias voltage of 200 V; however, a sharper decline is observed for coatings prepared at 250 V and 300 V. These observations align with findings from earlier studies, which reported similar behavior under varying bias voltage conditions [5, 6, 7, 16, 17].

The decrease in coating thickness with higher bias voltages is primarily attributed to the energy delivered by high-energy ions during deposition. These ions strike the coating surface, leading to re-evaporation or resputtering of surface atoms. This phenomenon slows down the growth rate of the coating and results in a thinner, denser structure. Ion bombardment plays a critical role in determining the coating's microstructure. The resputtering effect induced by high-energy ions can refine grain structures by promoting densification but also introduces defects such as voids or microcracks when the ion energy exceeds optimal levels. This process alters grain size distribution, contributing to hardness variations. Additionally, pseudo-diffusion layers formed due to ion bombardment can affect coating thickness and mechanical properties. In this study, SEM cross-sectional analysis was employed to qualitatively assess coating thickness and structural uniformity.

However, quantitative analysis of pseudo-diffusion effects was not performed due to the limitations of the available data. Future studies incorporating advanced characterization techniques such as EDX or TEM could provide deeper insights into these effects. The energy-based ion bombardment model, as discussed earlier, supports this explanation by demonstrating how higher ion energies disrupt coating growth dynamics [18]. While the energy-based ion bombardment model provides a robust framework for understanding the effects of bias voltage on coating properties, the energy calculations could be further supported by comparative studies.

Incorporating references related to ion energy distribution and its impact on microstructural evolution in TiN coatings would strengthen the model's validity. Future studies could enhance this model by integrating experimental data on ion flux density and energy transfer efficiency during the PVD process, allowing for more precise predictions of coating behavior under varying deposition conditions. Additionally, coatings deposited at higher bias voltages exhibit enhanced grain refinement, contributing to their increased hardness and density despite reduced thickness.

Energetic particles directed towards the substrate surface deposit a portion of their energy through inelastic collisions, leading to localized heating of the substrate surface. This heating plays a critical role in surface diffusion and determines the composition and structure of the formed coating. Impurity atoms, such as embedded carbon or oxygen in the recoil surface region, can form a pseudo-diffusion layer that affects coating thickness. When the energy of the particles is sufficiently high, these impurities are sputtered before the pseudo-diffusion layer can form, resulting in thinner and harder coatings [6, 15, 20].

Continued ion bombardment enhances physical mixing, diffusion, and nucleation modes while removing unbound atoms from the surface, thus improving the surface quality. High-energy

impacts also restrict the mobility of condensing atoms on the surface, increasing nucleation density. Coatings deposited at bias voltages exceeding 200 V typically exhibit higher nucleation densities, which correlate with enhanced hardness and refined microstructures [7, 9, 12, 25].

Studies have demonstrated that higher substrate temperatures, induced by energetic particle impacts, facilitate diffusion processes, promote uniform coating, and enhance hardness properties. PVD coatings, such as TiN, processed under controlled high-temperature conditions, show increased hardness and reduced defects [10, 16]. Moreover, it has been reported that pseudo-diffusion layers formed by trapped impurities can alter both coating thickness and hardness.

High-energy particle impacts effectively sputter these impurities, leading to coatings with superior mechanical and tribological properties, as well as reduced surface roughness [5, 6, 17]. Many researchers have reported similar results on film thickness and hardnes affected by substrate temperature and nucleation formation. Higher substrate temperatures facilitate the diffusion process, promoting uniform coating and enhancing hardness properties. They observed that PVD coatings like TiN exhibit increased hardness when processed under controlled high-temperature conditions [7, 18, 19].

Figures 4–8 show the cross-sectional SEM images of the samples, highlighting the structural differences and coating integrity at varying bias voltages. The microstructural evolution of TiN coatings with increasing bias voltage is summarized in Table 3. At lower bias voltages (100–150 V), the coatings exhibit a fine-grained, dense structure with minimal defects. As the bias voltage increases beyond 200 V, grain coarsening becomes evident, and minor porosity is observed. The highest bias voltage (300 V) results in a rougher morphology with visible cracks, indicating a potential increase in internal stress. These observations emphasize the influence of bias voltage on coating microstructure and mechanical stability.

Table 3. The microstructural evolution of TiN coatings with increasing bias voltage and film thicness

Bias Voltage (V)	Grain structure	Thickness (µm)	Observed defects
100	Fine grains	1.64	None
150	Dense structure	1.55	Minor voids
200	Dense structure	1.47	Slightly porosity
250	Coarse grains	1.03	Voids&micr ocracks
300	Coarse grains	0.90	Cracks observed

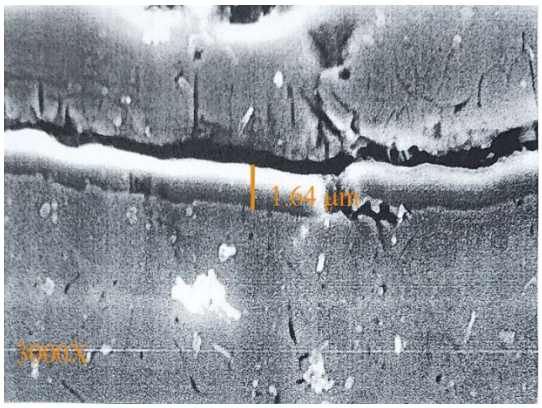

Figure 4. SEM cross-section of TiN coating deposited at 100 V bias voltage, indicating the measured coating thickness (1.64 µm) and its interface with the substrate

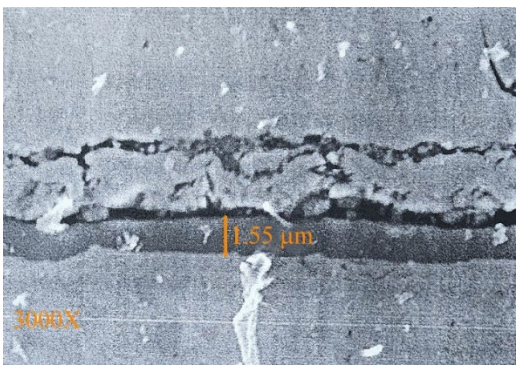

Figure 5. SEM cross-section of TiN coating deposited at 150 V bias voltage, indicating the measured coating thickness (1.55 µm) and its interface with the substrate

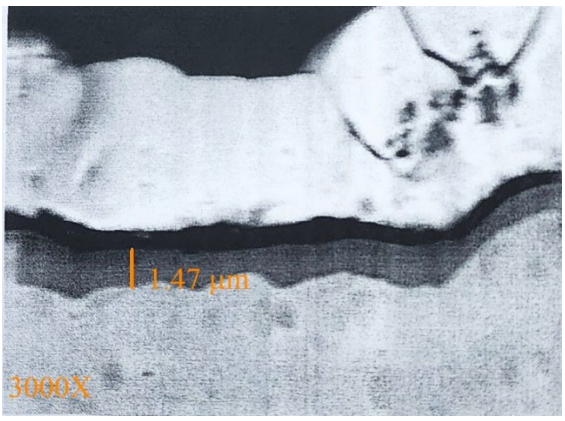

Figure 6. SEM cross-section of TiN coating deposited at 200 V bias voltage, indicating the measured coating thickness (1.47 µm) and its interface with the substrate

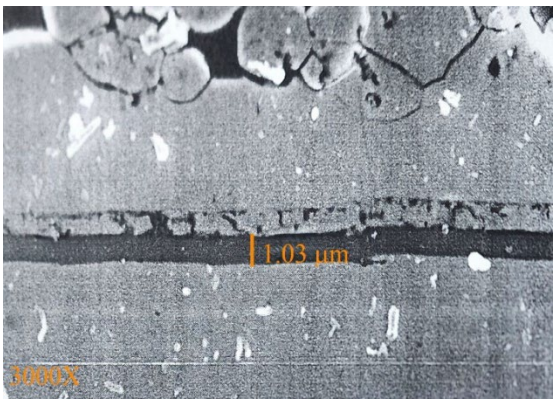

Figure 7. SEM cross-section of TiN coating deposited at 250 V bias voltage, indicating the measured coating thickness (1.03 µm) and its interface with the substrate

The revised hardness-load model shows a strong correlation with experimental data across all bias voltages, demonstrating its robustness in capturing the mechanical behavior of TiN coatings. As illustrated in Figure 9, the experimental hardness values (represented by the straight lines) closely follow the calculated model predictions (dashed lines), particularly at lower loads.

However, for coatings prepared with bias voltages above 150 V and under high loads (>200 N), minor deviations persist. These small differences are likely due to increased substrate influence as indentation depth surpasses the coating thickness, leading to an overestimation of hardness values at high loads. This effect is well-documented in literature and is an inherent limitation of simplified hardness models that do not fully account for layered elastic-plastic interactions. Future improvements could involve a more advanced layered mechanical model that explicitly incorporates substrate effects, as well as alternative indentation analysis methods such as the Oliver-Pharr approach for nanoindentation. Despite these minor deviations, the model provides a reliable framework for understanding the hardness-load relationship in TiN coatings. The findings of this study indicate that at high loads exceeding 200 N, particularly for coatings deposited at bias voltages above 150 V, slight deviations between the experimental hardness values and the predictions of the hardness-load model are observed.

These discrepancies are primarily due to the increasing influence of the substrate as the indentation depth becomes comparable to or exceeds the coating thickness.

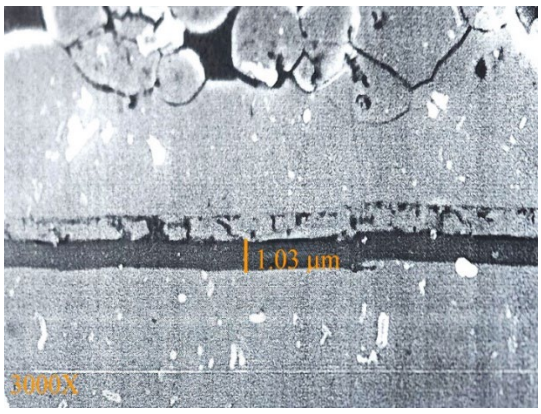

Figure 8. SEM cross-section of TiN coating deposited at 300 V bias voltage, indicating the measured coating thickness (0.90 µm) and its interface with the substrate

While the model remains highly effective in representing the overall hardness-load relationship, these observations emphasize the importance of incorporating substrate effects in mechanical property evaluations, especially for thin coatings.

Additionally, ensuring precise measurement and control of coating thickness before hardness testing could further improve the accuracy and reliability of mechanical property assessments

The examination of the hardness-indentation depth relationship reveals a strong correlation between the experimental data and the theoretical model predictions across all bias voltage levels and indentation depths (Figure 10). This agreement suggests that the indentation hardness

model effectively captures the localized mechanical behavior of the coatings, including the transition from coating-dominated to substrate-influenced regions.

While minor deviations can occur due to localized microstructural variations, the indentation model demonstrates a consistent ability to represent hardness behavior across different conditions. Compared to the hardness-load relationship, where substrate influence becomes more significant at higher loads, indentation hardness measurements provide a more localized assessment, making them less susceptible to macroscopic factors such as substrate effects or inhomogeneities.

Additionally, the robustness of the indentation model is supported by its dependence on well-characterized parameters such as coating thickness and indentation depth, further reinforcing its reliability in mechanical property evaluations. These findings emphasize the importance of precise modeling in understanding thin-film mechanics while also acknowledging the inherent differences between various hardness measurement methodologies.

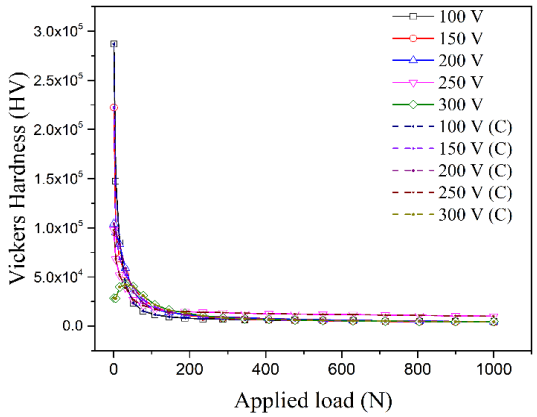

Figure 9. Variation of Vickers hardness of TiN-coated samples as a function of applied load (straight line: experimental, dashed line: calculated)

The calculated model exhibits a strong correlation with the experimental trend at low to moderate loads, accurately capturing the coating-dominated behavior. At higher loads (>200 N), minor deviations are observed, which can be attributed to the increasing influence of the substrate and potential microstructural variations such as grain coarsening. These variations, which lead to a maximum discrepancy of approximately 0.3%, are consistent with findings from previous

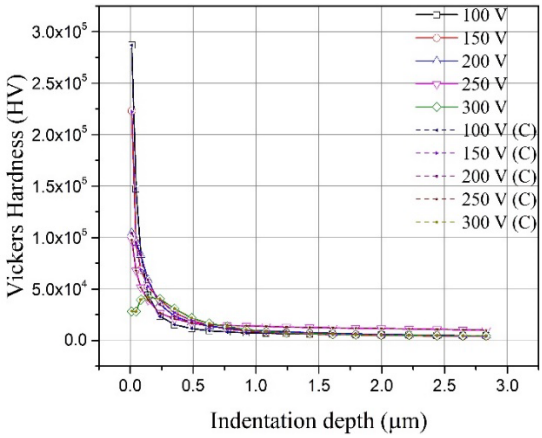

Figure 10. Variation of Vickers hardness of TiN-coated samples as a function of indentation depth (straight line: experimental, dashed line: calculated)

microindentation studies [29, 30]. While such discrepancies are inherent in thin-film mechanical characterization, they highlight the importance of considering substrate effects and material heterogeneities in hardness modeling.

Unlike the hardness-load relationship, where macroscopic factors and substrate contributions introduce variability, the indentation model provides a robust framework for evaluating the intrinsic properties of thin coatings. These findings emphasize the importance of utilizing multiple models to capture different aspects of mechanical behavior comprehensively.

The observed trends in hardness and film thickness with varying bias voltages highlight the significant influence of deposition parameters on the mechanical properties of TiN coatings. The monotonic decrease in film thickness with increasing bias voltage is consistent with ion bombardment effects, leading to re-sputtering and reduced growth rates. Additionally, the enhanced hardness observed up to 250 V bias voltage can be attributed to increased atomic mobility and nucleation density, while the decline beyond this threshold is likely due to grain coarsening and defect formation. These results align with previous studies, confirming the complex interplay between coating parameters and mechanical behavior.

4. Conclusion

This study systematically investigated the influence of bias voltage on the mechanical properties and film thickness of TiN coatings

deposited on cold work tool steel using the PVD process. The key findings and implications of this research are summarized as follows: A strong correlation between bias voltage and coating properties was observed, with optimal mechanical performance achieved at a bias voltage of 250 V. This bias voltage facilitated enhanced atomic mobility and nucleation density, resulting in coatings with improved hardness and structural integrity.

Film thickness decreased monotonically with increasing bias voltage, consistent with the predictions of the energy-based ion bombardment model. The reduction in coating thickness at higher bias voltages was attributed to resputtering effects caused by ion bombardment, which also contributed to refined microstructures and increased hardness. The hardness-indentation relationship exhibited excellent agreement between experimental data and theoretical model predictions across all bias voltage levels. This finding underscores the robustness of the indentation hardness model in capturing localized mechanical behavior and transitions between coating-dominated and substrate-influenced regimes. Slight deviation between experimental data and model predictions were observed in the hardness-load relationship for coatings prepared at bias voltages above 150 V under high loads (>200 N). These deviations were primarily attributed to the increased contribution of substrate effects as the indentation depth approached or exceeded the coating thickness.

These findings underscore the potential of TiN coatings to enhance tool life and improve wear resistance in industrial applications. The optimal control of deposition parameters, particularly bias voltage, is critical for tailoring coatings to specific performance requirements. The study highlights the importance of combining experimental measurements with theoretical models to gain a comprehensive understanding of thin film behavior.

To address the limitations identified in this study, future research should focus on: Refining the hardness-load model to better account for substrate effects and high-load scenarios. Integrating precise coating thickness measurements prior to hardness evaluations to enhance the reliability of experimental data. Exploring advanced ion bombardment models to further understand the interplay between deposition parameters, coating microstructure, and mechanical performance.

Future research could expand on the findings of this study by exploring different PVD coating compositions, such as TiAlN and TiCN, under similar bias voltage conditions to evaluate their mechanical and tribological properties. Additionally, investigating the effects of deposition temperature on coating hardness, microstructure, and adhesion could provide deeper insights into the thermal dynamics of the PVD process. Furthermore, evaluating the tribological performance of TiN coatings in real-world applications, such as machining and cutting tools, would help bridge the gap between laboratory-scale studies and industrial applications. These future studies will contribute to a more comprehensive understanding of the interplay between deposition parameters and coating performance. In summary, this study offers valuable insights into the mechanical behavior of TiN coatings and emphasizes the potential of PVD coatings to enhance tool life and wear resistance in industrial applications.

Article Information Form

Acknowledgments

This study is derived from the master's thesis completed in the Department of Physics at the Institute of Natural Sciences, Kocaeli University. I would like to take this opportunity to thank my thesis advisors, Prof. Dr. Yüksel Bektöre (retired) and Dr. Hasan Alanyalı (retired). Additionally, I would like to thank Brisa Inc., for providing the SEM images and OPAŞ Inc., for their assistance in the implementation of the coatings.

Funding

The author has no received any financial support for the research, authorship or publication of this study.

The Declaration of Conflict of Interest/ Common Interest

No conflict of interest or common interest has been declared by the author.

The Declaration of Ethics Committee Approval

This study does not require ethics committee permission or any special permission.

The Declaration of Research and Publication Ethics

The author of the paper declare that they comply with the scientific, ethical and quotation rules of SAUJS in all processes of the paper and that they do not make any falsification on the data collected. In addition, they declare that Sakarya University Journal of Science and its editorial board have no responsibility for any ethical violations that may be encountered, and that this study has not been evaluated in any academic publication environment other than Sakarya University Journal of Science.

References

[1] A. Ali, M. Hamzah, “Effects of bias voltage on TiN coatings,” Surface and Coating Technology, vol. 204, no. 5, pp. 1234–1240, 2008

[2] K. M. Gupta, K. Ramdev, S. Dharmateja, S. Sivarajan., “Microstructure and mechanical properties of PVD TiN coatings,” Thin Solid Films, vol. 516, pp. 450–457, 2018

[3] J. M. Wilson, A. T. Alpas, “Wear mechanisms of PVD TiN coatings,” Wear, vol. 225, pp. 126–133, 1999.

[4] H. Malik, R. Bradley, B. Mills, “PVD coatings on high-speed steels,” Thin Solid Films, vol. 374, pp. 254–263, 2000

[5] X. Zheng, L. Yu, “Enhancement of TiN coatings with yttrium,” Journal of Coatings Technology, vol. 82, pp. 142–148, 2010

[6] E. Yiğit, İ. Şenocak, “Bias voltage effects on PVD coatings,” Materials Science and Engineering, vol. 19, no. 3, pp. 452–460, 2022

[7] A. F. Rousseau, J. G. Partridge, E. L. H. Mayes, J. T. Toton, M. Kracica, D. G. McCulloch, E. D. Doyle, “Duplex coatings on tool steels,” Surface Engineering, vol. 31, pp. 86–95, 2015

[8] J. L. Endrino, G. S. Fox-Rabinovich, C. Gey, “Mechanical properties of duplex PVD coatings,” Surface and Coating Technology, vol. 198, pp. 181–187, 2005

[9] M. A. Çakır, “Katodik ark PVD yöntemi ile TiN kaplanmış 316L paslanmaz çelik implant malzemesinin elektrokimyasal ve ıslanabilirlik özelliklerinin belirlenmesi”, Gümüşhane Üniversitesi Fen Bilimleri Dergisi, vol. 13. pp. 106-115, 2023

[10] B. Jonsson, S. Hogmark, "Hardness measurements of thin films", Thin Solid Films, vol. 114, no. 2, pp. 257-269, 1984

[11] D. Tabor, Hardness of Metals, 1st ed. Clarendon Press, Oxford, 1951

[12] M. Pharr, "Measurement of thin film mechanical properties using nanoindentation," MRS Bulletin, vol. 17, no. 7, pp. 28-33, 1992

[13] S. Suresh, A. E. Giannakopoulos, "A new method for estimating residual stresses by instrumented sharp indentation," Acta Materialia, vol. 46, no. 16, pp. 5755-5767, 1998

[14] A. Thornton, "Influence of apparatus geometry and deposition conditions on the structure and topography of thick sputtered coatings," Journal of Vacuum Science & Technology A, vol. 4, no. 6, pp. 3059-3065, 1986

[15] S. M. Rossnagel, J. Hopwood, "Magnetron sputter deposition with high levels of metal ionization," Journal of Vacuum Science & Technology B, vol. 12, no. 1, pp. 449-453, 1994

[16] R. F. Bunshah, Handbook of Deposition Technologies for Films and Coatings, 1 st ed. Noyes Publications, Park Ridge, NJ, 1994

[17] A, Hörling, L. Hultman, M. Odenb, J. Sjölen, L. Karlsson, "Mechanical properties and machining performance of $Ti_{1-x}Al_xN$-coated cutting tools", Surface & Coatings Technology, vol. 191, pp. 384-392, 2005

[18] M. Ö. Öteyaka, M. M. Yıldırım, "Investigation of the Surface properties of hardened and PVD coated DIN 115CRV3 steel for cutting tools application", Journal of Science and Technology of Dumlupınar University, vol, 032, pp. 91-102, 2013

[19] R. H. N. Reddy, M. Alphonse, V. K. B. Raja, K. Palanikumar, D. R. S. Krishna, "Evaluating the wear studies and tool characteristics of coated and uncoated HSS drill bit, A review", Materials Today Proceedings, vol. 46, pp. 3779-3785, 2021

[20] L. Urtekin, Ö. Keleş, "Biyomedikal Uygulamalar İçin TiN Kaplı Ti6Al4V Alaşımının Mekanik Özelliklerinin Araştırılması", Savunma Bilimleri Dergisi The Journal of Defense Sciences, vol.18, pp. 91-108, 2019

[21] H. Dempwolf, M. Proft, A. Baumann, S. Malz, O. Keßler, "The impact of bias and nitrogen pressure on TiNbN coatings in Arc-PVD processes-A multifactorial study", Coatings, vol. 12, pp. 935-953, 2022

[22] D. K. Devarajan, B. Rangasamy, K. K. Amirtharaj Mosas, "State-of-the-art developments in advanced hard ceramic coatings using PVD techniques for high-temperature tribological applications", vol. 6, pp. 301-329, 2023

[23] M. Piska, P. Sliwkova, "Surface parameters, tribological tests and cutting performance of coated HSS taps" 25th DAAAM International Symposium on Intelligent Manufacturing and Automation, DAAAM, Austria, 2015, 125-234

[24] H. Hoche, S. Groß, T. Troßmann, J. Schmidt, M. Oechsner, "PVD coating and substrate pretreatment concepts for magnesium alloys by multinary coatings based on Ti(X)N" Surface and Coatings Technology, 228(Supplement 1), 336-341, 2013

[25] M. Sahin, C. Misirli, D. Özkan, "Characteristic properties of AlTiN and TiN coated HSS materials" Industrial Lubrication and Tribology. 67/2, pp.172–180, 2015

[26] A. Carabas depitedillo, F. Sordetti, A. Querini, M. Magnan, O. Azzolini, L. Fedrizzi, Lanzutti, M "Tribological optimization of titanium-based PVD multilayer hard coatings deposited on steels used for cold rolling applications" Materials today Communitacations, vol. 34, pp. 105043-105053, 2022

[27] A. E. Bülbül, H. Dilipak, M. Sarıkaya, V. Yılmaz, "Optimization of the wear behavior of uncoated, TiN and AlTiN coated cold work tool steel 1.2379 using response surface methodology", Materials Testing, vol. 58, pp. 12-19, 2016

[28] C. Ould, X. Badiche, P, Monmitonnet, Y. Gachon, "PVD coated mill rolls for cold rolling of stainlesssteel strips-Tribological and mechanical laboratory tests", Journal of Manufacturing Processes, vol.15, pp. 77-86, 2013

[29] W. C. Oliver, G. M. Pharr, "An improved technique for determining hardness and elastic modulus using load and displacement sensing indentation experiments" Journal of Materials Research", 7(6), pp. 1564–1583, 1992

[30] S. J. Bull, T. F. Page, "Contact phenomena in nanoindentation studies", Surface and Coatings Technology, 54–55, pp. 173–181, 1992

Sakarya Üniversitesi Fen Bilimleri Dergisi
Sakarya University Journal of Science

ISSN : 2147-835X
Publisher : Sakarya University

Vol. 29, No. 1, 125-139, 2025
DOI: https://doi.org/10.16984/saufenbilder.1589238

Research Article

Air-Exposure-Driven Color and Optical Variations in Hydroxyapatite Extracted from Fish Scales

H. Esma Okur

Bursa Technical University, Faculty of Engineering and Natural Sciences, Department of Chemistry, Bursa, Türkiye, esma.okur@btu.edu.tr

ARTICLE INFO

Keywords:
Hydroxyapatite
Fish scales
Band gap
Air exposure
Rietveld refinement

Article History:
Received: 21.11.2024
Revised: 21.02.2025
Accepted: 25.02.2025
Online Available: 28.02.2025

ABSTRACT

The disposal of fish scales as waste presents an environmental challenge and an untapped opportunity for resource recovery. In this study, hydroxyapatite (HAp) was extracted from European seabass (Dicentrarchus labrax) scales to explore how air exposure during calcination affects its optical and surface properties. HAp powders were prepared under two distinct calcination conditions: fully exposed to air (producing white powder) and partially shielded from air (resulting in gray powder). Rietveld refinement of X-ray powder diffraction (XRPD) data confirms that both powders crystallize in the hexagonal HAp structure, with a minor Mg-whitlockite impurity. Despite these differences in air exposure, the bulk structure of the HAp remains unchanged. The color variations are linked to surface oxidation, as subsurface layers in the partially shielded scales retain a grayish tone while the exposed surfaces turn completely white. Scanning electron microscopy reveals subtle differences in particle morphology: the white powder had a smoother surface compared to the slightly rougher gray powder. Fourier transform infrared spectra confirm the presence of characteristic phosphate and hydroxyl groups in both powders, indicating that the core chemical structure of HAp is intact in both cases. The Ca/P ratios—1.504(7) for the white powder and 1.505(7) for the gray powder obtained from the Rietveld analysis—further support the stoichiometric integrity of the material. UV-Vis spectroscopy reveals direct bandgap values of 3.99 eV for the white powder and 3.87 eV for the gray powder. These bandgap values, which are lower than those typically reported for defect-free HAp (5–6 eV), suggest that the optical differences between the powders are driven by surface effects, such as oxygen vacancies or trace impurities. This study highlights how calcination conditions, particularly air exposure, influence surface properties and optical behavior, paving the way for potential applications of fish-scale-derived HAp in electronic and optical materials.

1. Introduction

Hydroxyapatite (HAp) is a calcium phosphate mineral composed of calcium cations (Ca^{2+}), orthophosphate (PO_4^{3-}), and hydroxide (OH^-) ions, with a stoichiometric formula of $Ca_{10}(PO_4)_6(OH)_2$, resulting in a calcium-to-phosphorus ratio (Ca/P) of 1.67. HAp is widely regarded as one of the most valuable bioceramic materials due to its close structural similarity to natural bone, where the inorganic component consists of approximately 60 wt% HAp. Therefore, since the 1980s, HAp has gained widespread recognition for its exceptional chemical stability and biocompatibility, making it a prominent material in dental and orthopedic applications [1–5].

HAp is known to exist in two crystallographic structures: the hexagonal (space group $P6_3/m$) [6] and monoclinic crystal systems (space group $P2_1/b$) [7], with subtle differences in atomic arrangement, particularly in the orientation of the hydroxyl groups, while both

Cite as: H. E. Okur (2025). Air-Exposure-Driven Color and Optical Variations in Hydroxyapatite Extracted from Fish Scales, *Sakarya University Journal of Science*, 29(1), 125-139. https://doi.org/10.16984/saufenbilder.1589238

maintain a Ca/P ratio of 1.67. In the hexagonal structure, the hydroxyl groups are oppositely oriented. However, in the monoclinic structure, the hydroxyl groups are oriented in the same direction within the same column but are oppositely oriented between columns [8]. Therefore, accurate structural determination is crucial for specific applications.

Synthetic methods are commonly employed to produce HAp [9], as they offer a controlled process that minimizes the risk of defects, impurities, vacancies, and deficiencies. However, there is growing interest in extracting HAp from natural sources [10, 11], such as fish scales, which are a by-product of the seafood industry. The use of fish scales in the production of an important bioceramic material like HAp holds significant value for sustainability.

Additionally, recycling this by-product, which would otherwise be considered waste, plays a crucial role in reducing environmental impact.
As a result, there has been growing interest in optimization of the extraction of HAp from natural sources to minimize structural anomalies such as defects, cation or anion deficiencies, or deviations from stoichiometry. It is well known that biological apatites often deviate from the stoichiometric composition of HAp and contain some amount of ion substitutions, including Na^+, Mg^{2+}, K^+, HPO_4^{2-}, CO_3^{2-}, Cl^-, and F^- [12]. It is therefore crucial to extract HAp free from the aforementioned structural anomalies, as defects, vacancies, and deficiencies significantly impact the electronic and optical properties of HAp. For instance, recent studies have applied various pre-treatment methods to examine the morphological and structural characteristics of HAp derived from fish scales. One such study found that boiling the scales prior to calcination significantly impacted the morphology and crystallinity of the extracted HAp powder [13].

Fish scales that were boiled before calcination produced spherical particles at higher temperatures, while non-boiled scales led to the formation of nanorods, underscoring the major influence of pre-treatment on microstructure and potential defect formation. Notably, the study also reported differences in color between the boiled and non-boiled samples, indicating that the pre-treatment affected not only the structure but also the appearance of the HAp powder [13]. This underscores the importance of the extraction method in determining the structural properties of HAp, which ultimately has a significant effect on the electronic properties of material.

A recent study by Okur [14] further contributed to this field by employing a straightforward yet effective calcination method to extract HAp from recycled European seabass scales. In that work, the scales were calcined at 800 °C, resulting in the formation of highly crystalline HAp with minimal secondary phases, as verified by Rietveld refinement of X-ray powder diffraction data. Magnesium whitlockite was identified as a minor impurity, which may be beneficial for biomedical applications owing to its positive influence on bioactivity and osteoconductivity. In addition, HAp was incorporated into polyvinyl alcohol composite films, demonstrating improved adsorption efficiency for methylene blue dye and underscoring the material's potential for environmental remediation. Building on these findings, the same calcination parameters (800 °C for 2 hours) were applied in the present study to systematically examine the influence of air exposure on the surface and optical properties of HAp, while minimizing additional confounding factors.

In addition to the structural studies, numerous theoretical and experimental studies have been conducted to uncover the electronic and optical properties of HAp considering the defect levels, vacancies, *etc.* [15–21]. Unfortunately, due to the lack of accurate structural characterization and/or poor sample quality, it has been challenging to elucidate fundamental properties such as the electronic band structure and band gap. This has led to significant discrepancies in the obtained values, especially for the band gap. For instance, the measured width of the forbidden electronic gap (E_g) ranges from above 6 eV down to 3.95 eV.

Recent investigations have shed light on how the optical and electronic properties of HAp influence its bioactivity and broader applications. Rosenman et al. [15] demonstrated that HAp possesses distinct bulk and surface-localized electron-hole states, as revealed by

photoluminescence (PL) and surface photovoltage spectroscopy (SPS). Their findings suggest that these deep electron-hole charged states may contribute to enhanced cell attachment, bone regeneration, and overall biocompatibility. Avakyan et al. [19] later explored how oxygen vacancies and structural defects impact the electronic structure and optical absorption of HAp, indicating that processing conditions and surface modifications can be instrumental in tuning these properties.

Computational studies have also provided valuable insights into the influence of defects on HAp behavior. Bystrov et al. [22] examined oxygen and hydroxyl vacancies as well as atomic substitutions, showing that such defects alter the band structure, optical transparency, and mechanical stability of HAp. Their work highlights how oxygen-related defects in particular can create localized electronic states within the bandgap, thus affecting the material's electronic response. In an earlier study, Bystrov et al. [23] used first-principles calculations to investigate various defect types—including oxygen and hydroxyl vacancies, cation substitutions, and interstitials—and their effects on the density of electronic states (DOS) and bandgap. These modifications introduce additional energy levels in the forbidden zone, which may prove beneficial for biomedical coatings, implant materials, and nanomedical applications.

Rial et al. [24] further underscored the versatility of nanosized HAp for environmental remediation, catalysis, and drug delivery, where the electronic surface properties play a key role. Collectively, these studies illustrate that the optical and electronic properties of HAp are not merely static material characteristics; rather, they can be actively tailored through defect engineering, synthesis conditions, and doping strategies to support a range of applications. As research progresses, the potential for HAp in optoelectronics, bioactive materials, and environmental technologies continues to expand, making detailed knowledge of its band structure more relevant than ever.

This study focuses on a detail that has not been addressed in previous research on the extraction of HAp from fish scales. It offers a new perspective by investigating the effects of both pre-treatments before calcination and the level of air exposure during calcination. In this process, the fish scales were boiled in water before calcination to remove organic matter. Subsequently, two different calcination methods were employed: in the first scenario, each fish scale was in direct contact with air inside the furnace, while in the second scenario, only the surface scales were in direct contact with air, and the scales beneath the surface were shielded from air exposure by the top layer.

In other words, the first group was fully exposed to air, while the second group underwent calcination as partially shielded beneath the surface. After calcination, it was observed that the fully exposed fish scales on the surface were completely white, whereas the partially shielded scales beneath the surface were white-gray/black in color. After grinding the calcined fish scales, white and gray HAp powders were obtained. The main objective of this research is then to investigate how different calcination environments influence the formation of HAp, focusing on the resulting color, optical and structural differences between the white powder, produced from fully exposed scales, and the gray powder, obtained from partially shielded scales.

The structural characterisation was performed through Rietveld refinement of X-ray powder diffraction (XRPD) data, Fourier transform infrared spectroscopy (FTIR), and scanning electron microscopy (SEM). Additionally, UV-Vis spectroscopy was used to examine the optical properties of both samples, specifically to understand how varying air exposure during calcination affects the band gap and light absorption. This study delves deeper into the mechanisms of HAp formation from fish scales, while also examining how different calcination conditions affect its structural and optical properties. These insights are valuable for applications where natural HAp's color and structural integrity play key roles.

2. Materials and Methods

2.1. Preparation of hydroxyapatite powder from European seabass (Dicentrarchus labrax) scales

Scales from European seabass (Dicentrarchus labrax), sourced as a by-product from Bursa Kocamanlar Seafood. The same batch of fish scales used in [14] was employed here, where the detailed structural characterization of the raw scales is documented. Relevant information can be found in the Electronic Supplementary Information (ESI) of [14]. The choice of calcination temperature (800 °C) and duration (2 hours), with a heating rate of 10 °C/min, was based on thermogravimetric analysis results presented in [14].

Two groups of calcined samples were prepared: one in which the scales were placed in a single layer for full air exposure, and another in which the scales were stacked, reducing air contact for inner layers. This straightforward yet controlled arrangement ensures repeatable differences in oxidation and thermal decomposition between the two groups.

Prior to calcination, the scales were boiled in deionized water for 4 hours to remove organic matter and collagen. They were then filtered and allowed to dry in a fume hood for 24 hours. Once dry, the scales were divided into two groups. In the *fully exposed* group, the scales were arranged in a single layer to maximize air contact during calcination. In the *partially shielded* group, the scales were stacked so that inner layers were covered by surface scales, reducing their direct exposure to air. Both groups were calcined at 800 °C for 2 hours with a heating rate of 10 °C/min, as specified in [14].

Following calcination, the fully exposed group turned completely white, while the partially shielded group exhibited both white and gray regions (Figure 1). In both groups, the outermost (surface) scales remained white. After cooling to room temperature, the scales were initially ground using a coffee grinder and then further reduced in size with a mortar and pestle. The resulting white powder (from fully exposed scales) and gray powder (from partially shielded scales) were sieved through a 150 µm sieve and stored for subsequent analyses.

2.2. Structural characterisation

2.2.1. X-ray powder diffraction (XRPD)

X-ray powder diffraction (XRPD) measurements were conducted using a Bruker D8 Advance diffractometer in Bragg-Brentano geometry. Data were collected at room temperature over an angular range of $2\theta = 5-60°$, with a step size of 0.02°, utilizing Cu Kα radiation ($\lambda = 1.54056$ Å). The collected XRPD data were analyzed through Rietveld refinement, employing the General Structure Analysis System (GSAS), a widely used software suite written in FORTRAN [25]. Throughout the refinement process, various key factors were carefully optimized, such as peak intensities, background fitting, and lattice parameters, to ensure accurate results.

The quality of the refinement was evaluated through *R*-factors, including the weighted profile *R*-factor (R_{wp}) and the expected statistical *R*-factor (R_{exp}), with the goodness-of-fit determined by the χ^2 value. A pseudo-Voigt function [26], which combines Gaussian and Lorentzian components, was used to model the peak shapes, while the background was fitted using a Chebyshev polynomial function. Anomalous X-ray scattering factors, such as corrections to form factors (f' and f''), were computed with the DISPANO program [27] and incorporated into the GSAS refinement. The iterative refinement cycles included adjustments to profile shape parameters, zero-point corrections, background modeling, and scale factors, along with atomic thermal displacement parameters for the phases analyzed.

Figure 1. Schematic representation of hydroxyapatite (HAp) powder preparation from European seabass scales. The top image shows the cleaned fish scales after removing dirt and debris. The central image depicts the scales after boiling for 4 hours and drying in a fume hood for 24 hours. The left image shows the gray powder obtained from partially shielded scales, where inner scales were shielded from air exposure during calcination. On the right is the white powder, derived from fully exposed scales calcined in a single layer, allowing full air exposure. The bottom images show the final powders after grinding, highlighting the distinct color differences between the gray and white powders

2.2.2. Fourier transform infrared spectroscopy (FTIR), scanning electron microscopy (SEM) and UV-Visible spectroscopy

The functional groups in the extracted powders were identified using a Fourier transform infrared (FTIR) spectrometer equipped with an Attenuated Total Reflectance (ATR) diamond probe. Spectra were collected over the range of 4000–400 cm^{-1} on a Thermo Nicolet iS50 FTIR system. For morphological analysis, scanning electron microscopy (SEM) was performed using a Zeiss Gemini 300 microscope with a Bruker XFlash 6I100 detector in In-Lens mode. Prior to imaging, the samples were coated with a thin layer of gold-palladium (Au-Pd) alloy (60:40 ratio), applying a 15 nm conductive coating using a Leica EM ACE600 high-vacuum sputter coater to enhance surface conductivity. Optical absorbance measurements of the powders, across the wavelength range of 200–800 nm, were conducted using an Agilent Cary 60 UV-Vis spectrophotometer.

3. Results

3.1. Rietveld analysis

Ambient temperature XRPD data for the fully exposed white and partially shielded gray powders confirmed the successful extraction of crystalline hydroxyapatite, HAp, from fish scales, as shown in Figure 2**.** The figure highlights the crystalline similarity between the two samples: white HAp powder (fully exposed to air), gray HAp powder (partially shielded). Minor variations in peak intensities are observed, but no significant differences in overall crystallinity are present.

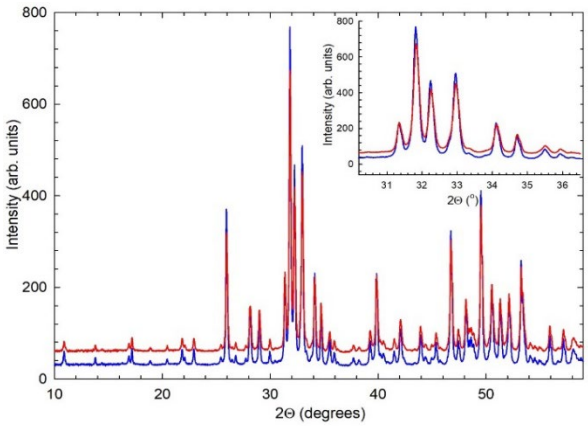

Figure 2. X-ray powder diffraction (XRPD) patterns of hydroxyapatite (HAp) extracted from the fish scales collected at ambient temperature with λ = 1.5406 Å. The red curve represents the white powder (fully exposed) the blue curve corresponds to the gray powder (partially shielded). The inset shows a magnified view of the 2θ = 30.2–36.5°, emphasizing the crystalline similarity among the samples, with minor differences in peak intensities

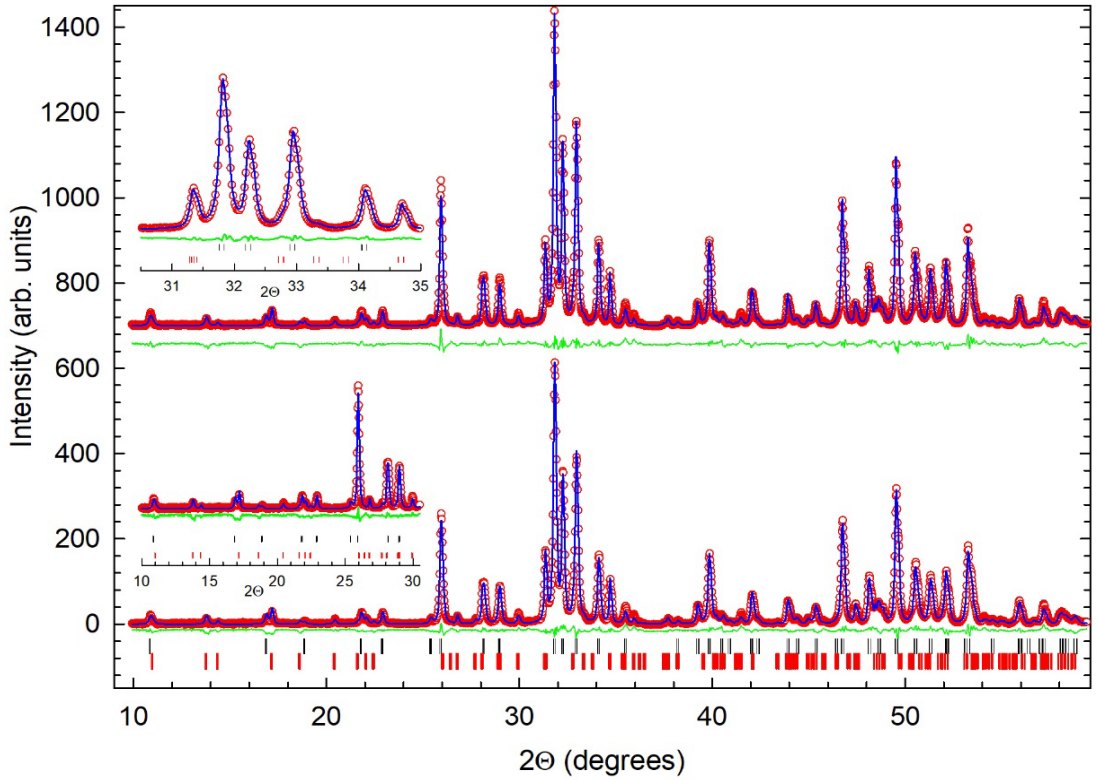

Figure 3. Rietveld fits to XRPD data for the gray (partially shielded, upper profile) and white (fully exposed, lower profile) hydroxyapatite (HAp) powders collected at ambient temperature with λ = 1.5406 Å. The red circles represent the observed data, blue lines the calculated profile, and green lines the difference between observed and calculated profiles. Black and red ticks mark the reflection positions of the majority phase hexagonal HAp $Ca_{10}(PO_4)_6(OH)_2$ (space group $P6_3/m$) and minority rhombohedral Mg-Whitlockite $Ca_{18}Mg_2H_2(P0_4)_{14}$ (space group $R3c$), respectively. The weighted-profile and expected R-factors for the upper fit are R_{wp} = 4.54% and R_{exp} = 1.15% while for the lower fit they are R_{wp} = 3.88% and R_{exp} = 1.13%. The insets highlight different 2θ regions of the corresponding profiles, emphasizing the peak fitting and the contribution of the secondary Mg-Whitlockite phase

The Rietveld refinement (Figure 3) reveals that both the white and gray powders crystallize in the hexagonal space group $P6_3/m$ (no. 176) [28], along with a secondary phase, identified as magnesium whitlockite ($Ca_{18}Mg_2H_2(PO_4)_{14}$) as in the previous study [14]. This impurity is modeled using the rhombohedral space group $R3c$ (no. 161) [29]. Previous studies on extracting HAp from natural sources using calcination have commonly reported the formation of HAp in a hexagonal structure, consistent with the findings of this study. However, these works often identified β-tricalcium phosphate (β-TCP, $Ca_3(PO_4)_2$) as the secondary phase, typically without employing detailed Rietveld refinement [13, 30, 31]. The similarity in the chemical composition and crystal structure of β-TCP and whitlockite (WH) frequently leads to their confusion in discussions regarding calcium phosphate phases [29]. Both minerals share the same space group ($R3c$) but have distinct unit cell parameters, making them difficult to differentiate through standard XRPD analysis, especially as their Bragg reflections can overlap.

Magnesium incorporation into whitlockite causes slight distortions in the crystal lattice, resulting in subtle variations in bond lengths, angles, and the overall structural stability compared to pure β-TCP. The f' and f'' corrections applied in GSAS were: Ca (f' = 0.340, f'' = 1.235), P (f' = 0.283, f'' = 0.433), Mg (f' = 0.165, f'' = 0.177), and O (f' = 0.046, f'' = 0.032). The refined unit cell parameters, P–O bond lengths, and weight fractions of HAp and WH phases for both the white and gray powders are summarized in Table 1.

The unit cell parameters for both phases – $a = b$ = 9.4235(1) Å, c = 6.8800(1) Å for the white powder, and $a = b$ = 9.4232(1) Å, c = 6.8806(1) Å for the gray powder – are nearly identical within experimental uncertainty, despite the color differences. These values are consistent

with previously reported data [14]. Similarly, the weight fractions of HAp (83.27(3) wt% for the white and 83.57(3) wt% for the gray) and Mg-whitlockite (16.7(1) wt% for the white and 16.4(1) wt% for the gray) phases show no notable differences between the fully exposed and partially shielded powders. Additionally, the P–O bond lengths in the HAp structure are virtually identical for both powders, with minimal variation within experimental error.

Table 1. Refined structural parameters and weight fractions of the major hydroxyapatite and minor Mg-Whitlockite phases present in the white and gray powders obtained from the fully exposed and partially shielded region of the fish scales

	structural parameters	white – fully exposed	gray – partially shielded
Hydroxyapatite ($P6_3/m$)	$a = b$ (Å)	9.4235(1)	9.4232(1)
	c (Å)	6.8800(1)	6.8806(1)
	V (Å^3)	529.106(9)	529.120(8)
	P−O1 (Å)	1.577(4)	1.575(4)
	P−O2 (Å)	1.536(4)	1.529(4)
	P−O3 (Å)	1.631(2)	1.625(2)
	weight fraction (%)	83.27(3)	83.57(3)
Mg-Whitlockite ($R3c$)	$a = b$ (Å)	10.3474(3)	10.3474(3)
	c (Å)	37.084(2)	37.079(2)
	V (Å^3)	3438.7(2)	3438.1(2)
	weight fraction (%)	16.7(1)%	16.4(1)

Table 2. Refined structural parameters for hexagonal biogenic hydroxyapatite (space group $P6_3/m$) from Rietveld analysis of XRPD data collected at ambient temperature from the partially exposed gray (upper) and fully exposed white (lower) powders, at room temperature with λ = 1.5406 Å. Site multiplicities and ocuupancies are listed in columns *M and N,* respectively. Values in parentheses are estimated errors from the least-squares fitting. The weighted-profile and expected *R*-factors for the white and gray powders are R_{wp} = 3.88%, R_{exp} = 1.13% and R_{wp} = 4.54%, R_{exp} = 1.15%, respectively

Atoms	*x/a*	*y/b*	*z/c*	*M*	*N*
Ca(1)	0.3333	0.6667	0.0017(5)	4	0.998(3)
Ca(2)	0.25572(24)	0.99784(27)	0.25	6	0.963(6)
P	0.4015(4)	0.35716(33)	0.25	6	1.082(4)
O(1)	0.3404(5)	0.4850(5)	0.25	6	1
O(2)	0.5868(5)	0.4748(10)	0.25	6	1
O(3)	0.3394(4)	0.2430(4)	0.0566(4)	12	1
O-h	0	0	0.19500	4	0.5
H	0	0	0.06080	4	0.5
Atoms	*x/a*	*y/b*	*z/c*	*M*	*N*
Ca(1)	0.3333	0.6667	0.0014(5)	4	0.999(3)
Ca(2)	0.25537(23)	0.99740(27)	0.25	6	0.963(3)
P	0.40203(32)	0.35686(32)	0.25	6	1.083(4)
O(1)	0.3415(5)	0.4855(5)	0.25	6	1
O(2)	0.5881(5)	0.4744(9)	0.25	6	1
O(3)	0.3408(4)	0.2433(4)	0.0553(4)	12	1
O-h	0	0	0.19500	4	0.5
H	0	0	0.06080	4	0.5

The refinement of the site occupancies of the Ca(1), Ca(2), and P atoms for the white and gray powders yielded stoichiometric values of Ca:P = 9.77(2): 6.50(3) yielding Ca/P: 1.504(7) and

Ca:P = 9.77(2): 6.49(3) yielding Ca/P: 1.505(7), respectively. Although these values fall below the ideal Ca/P ratio of 1.67 for stoichiometric HAp, such deviations are typical of biogenic HAp owing to ionic substitutions [10, 11].

In a previous study, the Ca/P ratio for HAp derived from the same fish scales was refined as 1.474(7), reinforcing the notion that naturally sourced HAp often exhibits a Ca-deficient profile. Crucially, the Ca/P ratios remain similar for both the fully exposed (white) and partially shielded (gray) powders. It should be noted that, during the refinement process, the P–O bond lengths were constrained to 1.55 Å [28] due to the limitations of X-rays in accurately determining the positions of light elements.
The fractional atomic coordinates of P, O(1), O(2), and O(3) were refined with a tolerance of 0.05 and a bond length restraint weight of 100 (presented in Table 2). Variations in air exposure during calcination do not significantly alter the fundamental structural characteristics of the extracted HAp. Full air exposure primarily affects the surface, leading to color changes likely caused by surface oxidation or the interaction of trace impurities with an oxygen-rich environment. These surface effects, potentially creating oxygen vacancies or defects, modify the electronic structure, contributing to the color differences observed.

However, these modifications remain confined to the surface, leaving the bulk crystal structure unaffected. Additionally, the consistent Ca/P ratios across the fully exposed (white) and partially shielded (gray) powders confirm that air exposure does not influence the stoichiometry of the calcium and phosphorus atoms. This indicates that the observed color changes due to air exposure are limited to surface properties and do not impact the bulk structure or stoichiometric composition of the HAp.

3.2. FTIR analysis

The FTIR spectra shown in Figure 4 confirm the presence of key functional groups characteristic of HAp. The observed bands correspond to distinct infrared absorption modes of the free orthophosphate ion (PO_4^{3-}), which has nine degrees of freedom that simplify into four normal modes of vibration. The ν_1 mode, associated with P–O symmetric stretching, is detected around 964 cm^{-1}, confirming the presence of the HAp phase, consistent with previously reported values [32]. The ν_3 mode, attributed to the antisymmetric P–O stretching, appears as bands at 1088, 1030, and 980 cm^{-1}, representing triply degenerate stretching vibrations. The ν_4 mode, corresponding to antisymmetric P–O bending, is identified by the bands at 600 and 565 cm^{-1}, typical of HAp.

Additionally, the OH^- group is characterized by a distinct band around 3600 cm^{-1}, indicating the stretching vibrations of the O–H bond, while the band near 630 cm^{-1} corresponds to the librational motion of the OH^- ion [13], a feature specific to HAp and absent in related phases such as fluorapatite and chlorapatite [32]. These spectra confirm the successful formation of HAp in both the fully exposed and partially shielded samples, While the characteristic bands for the PO_4^{3-} groups are consistent across both samples, slight differences in intensity are observed.

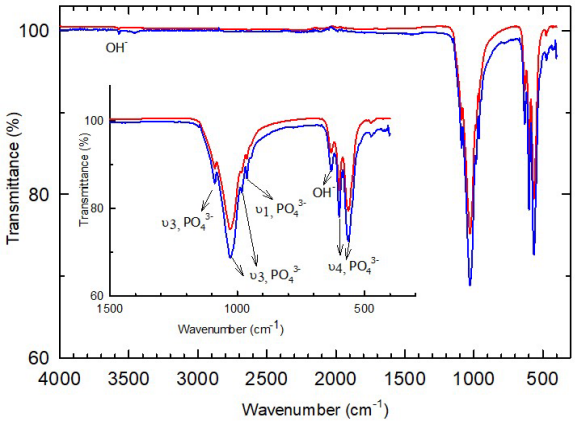

Figure 4. FTIR spectra of the hydroxyapatite (HAp) powders. The red spectrum represents the white HAp powder (fully exposed), while the blue spectrum represents the gray HAp powder (partially shielded). The labeled bands correspond to characteristic functional groups, with further details provided in the main text. The inset shows an expanded view of the wavenumber range 1500–300 cm^{-1}, focusing on the absorption modes of the PO_4^{3-} groups in HAp, which are labeled and indicated by arrows

3.3. SEM analysis

The SEM images in Figure 5 provide a morphological analysis of the white and gray HAp powders, revealing variations in particle

shape, crystallite size, and degree of surface crystallization. At lower magnifications (Figures 5a and 5c), both powders exhibit aggregated particles, though the gray powder shows more pronounced irregularities in particle shape compared to the smoother, more uniform appearance of the white powder. At higher magnifications (Figures 5b and 5d), individual HAp particles, ranging from approximately 45 nm to 135 nm in size, are observed in both powders, confirming the nanoscale nature of the crystallites. Observed differences in particle morphology and surface texture may result from variations in air exposure during calcination, with the fully exposed white powder showing a more uniform and smoother surface. The presence of nanoscale crystallites in both powders indicates the potential for increased surface area, which could be advantageous for applications requiring high surface interactions, such as adsorption or various biomedical uses.

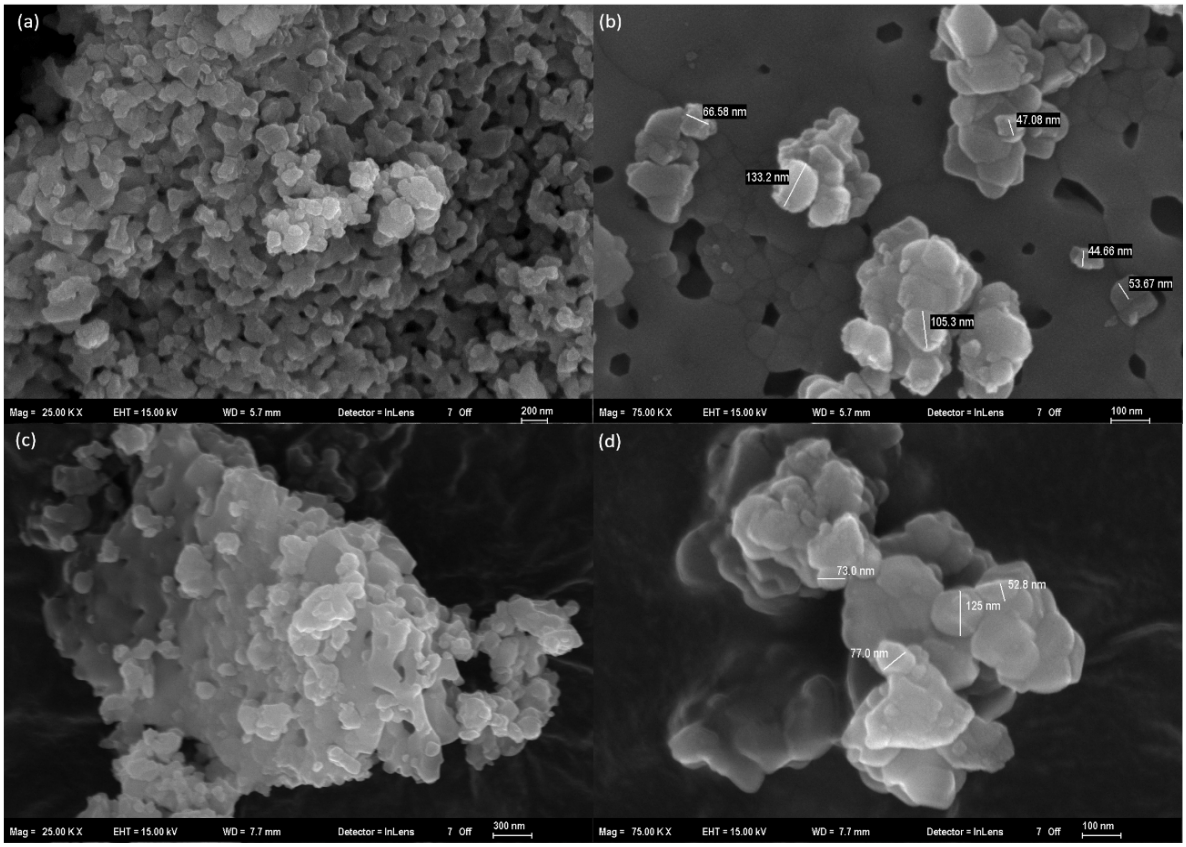

Figure 5. SEM images of hydroxyapatite (HAp) powders extracted from fish scales, comparing white (fully exposed, upper panels) and gray (partially shielded, lower panels) powders at different magnifications. (a, c): Low-magnification (25.0 kX) overviews of the white (a) and gray (c) powders. (b, d): High-magnification (75.0 kX) close-ups of the white (b) and gray (d) powders, highlighting individual HAp crystallites ranging in size from approximately 45 nm to 135 nm

3.4. UV-Vis spectroscopy

The optical properties of the white and gray HAp powders were analyzed using UV-Vis spectroscopy. To determine the direct bandgap E_g of the samples, Tauc plots were constructed using the relation $(\alpha hv)^2 = C(hv - E_g)$ where α is the absorption coefficient, C is a constant, and hv represents the photon energy. This method, widely applied for estimating optical bandgaps in semiconducting materials, allowed for the calculation of the bandgaps [33].

As shown in Figure 6, the linear portion of the Tauc plot, which corresponds to the absorption edge, was extrapolated to the x-axis to obtain the direct bandgap values. The white HAp powder has a bandgap of 3.99 eV, while the gray powder exhibits a slightly lower bandgap of 3.87 eV. These differences can be attributed to surface properties, as the XRPD and FTIR analyses show

no significant differences in the bulk structure of the powders. The higher bandgap of the white powder aligns with its reflective nature, while the lower bandgap of the gray powder suggests greater absorption of visible light, likely due to surface effects.

Although HAp is typically considered an insulator with a bandgap in the 5–6 eV range, the observed values of 3.99 eV and 3.87 eV fall within a range that indicates possible semiconducting behavior. Bandgap variations reported in the literature can be attributed to the presence of defects and the choice of theoretical methods for bandgap calculations.

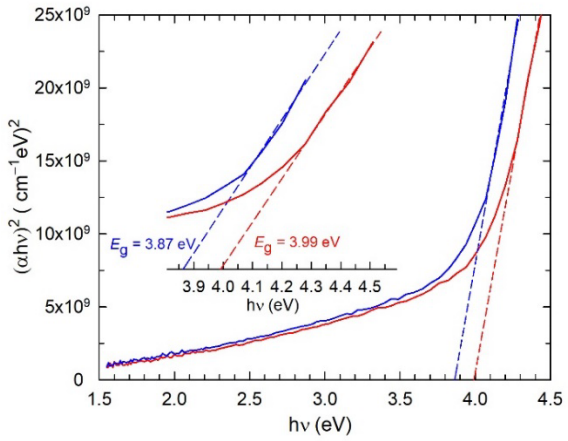

Figure 6. Tauc plot showing the relationship between $(\alpha h\nu)^2$ and photon energy ($h\nu$) for the white and gray hydroxyapatite (HAp) powders. α represents the absorption coefficient. Linear fitting was applied to the absorption edge region, and the extrapolation of the fitted lines to the *x*-axis reveals the direct bandgap (E_g) values. The white powder shows a bandgap of 3.99 eV (red line), while the gray powder has a bandgap of 3.87 eV (blue line). The inset highlights the extrapolation area, illustrating the slight bandgap difference

For example, Rosenman et al. used photoluminescence (PL) and surface photovoltage spectroscopy to study HAp and determined a bandgap of 3.95 eV from the PL spectra. They also determined E_g as 3.94 eV from the contact potential difference (DCPD) curves treatment method [15], consistent with our findings. The comparison between DCPD and PL spectra in [15] demonstrates that the energy levels of electron-hole states obtained from the two spectroscopy techniques are remarkably similar.

This suggests that all HAp samples share an identical electron-hole state structure, comprising five bulk states and one surface state. It is proposed that these deep electron (hole) charged states could be a key factor contributing to the high bioactivity observed in HAp nanoceramics. In contrast, theoretical studies based on density functional theory (DFT) often predict larger bandgap values, ranging from 4.5 to 5.4 eV for HAp, even higher values for defect-free samples [16-18].

It is important to consider the level of defects in HAp, as defect-free HAp is transparent to visible light, with electronic excitations only occurring for photon energies greater than 6 eV. Therefore, accurately determining the fundamental properties of HAp—such as its crystalline structure, phonon dispersion, electronic band structure, dielectric response, and electronic band gap—with minimal error margins is essential for a reliable evaluation of both spectroscopic and theoretical results [19].

Previous studies have demonstrated that doping, as well as the presence of defects and vacancies, can lower the E_g of HAp. For example, the optical bandgap of HAp/TiO_2 composite thin films was found to decrease from 4.1 eV to 3.8 eV with varying dipping cycles [20]. Another study, which combined experimental and theoretical approaches, examined the impact of Ti substitution in HAp on the bandgap. Diffuse reflectance spectroscopy revealed optical bandgap values of 3.65 eV for Ti-HAp, greater than 6 eV for pure HAp, and 3.27 eV for TiO_2. However, bandgaps calculated using DFT yielded lower values, specifically 2.74 eV for Ti-HAp, 4.95 eV for HAp, and 2.23 eV for TiO_2 [21].

A first-principles study on the optoelectronic properties and defect levels in HAp found that donor and acceptor transitions calculated with semi-local DFT differed from those obtained using hybrid-DFT by nearly 2 eV. This large discrepancy underscores the importance of using high-precision methods to describe electron-electron interactions when calculating electronic and optical transitions in HAp defects. Accurate determination of electronic states requires high-quality computational approaches [19].

In this study, the observed bandgap reduction may be attributed to surface effects, oxygen vacancies, or trace impurities introduced during calcination. The presence of the Mg-whitlockite phase could also contribute to the bandgap narrowing, as previous research suggests that defects and impurities significantly influence the bandgap of HAp. Magnesium substitution in whitlockite can lead to lattice distortions and defects, such as oxygen vacancies, which may introduce localized energy states within the bandgap.

These changes could alter the electronic structure and reduce the bandgap. While these observations point towards the potential for semiconducting properties in the modified HAp, further research is required to confirm this behavior and fully understand the influence of the Mg-whitlockite phase, along with other surface effects, on the material's electronic properties.

4. Discussion

This study examines how air exposure during calcination affects the optical and structural properties of hydroxyapatite. While the white and gray powders show distinct color differences, structural analysis confirms that both crystallize in the hexagonal HAp structure with a minor Mg-whitlockite impurity. This indicates that varying calcination conditions do not alter the bulk composition. The Rietveld refinement verified the crystalline structure remained consistent in both powders. The color differences between the white and gray powders are most probably due to surface oxidation occurring during calcination. SEM analysis revealed slight differences in particle morphology, with the white powder displaying a smoother surface than the gray powder. However, these variations are confined to the surface, as no significant deviations in bulk structure were detected. FTIR spectra further confirmed the presence of characteristic phosphate and hydroxyl groups in both powders, indicating that the fundamental chemical structure of HAp was preserved. Additionally, the consistent Ca/P ratios across both powders suggest that the calcination process did not affect the stoichiometric composition, reinforcing the conclusion that the observed color and bandgap differences are surface-driven rather than due to changes in the bulk structure.
Regarding phase composition, both this study and previous investigation [14] confirmed that HAp is the primary phase, with a minor Mg-whitlockite impurity present. However, the study on Nile tilapia scales identified biphasic calcium phosphates, specifically HAp and β-tricalcium phosphate, at higher calcination temperatures [13]. These discrepancies may arise from differences in the source material or the calcination conditions, which can impact the resulting phase composition.

When comparing optical properties, the bandgap values obtained in this study—3.99 eV for the white powder and 3.87 eV for the gray powder—are lower than the 5.5 eV reported in [13] for the white powder obtained after boiling pre-treatment and calcination at 800°C. The same study also reported two bandgap values, 2.87 eV and 3.97 eV, for the blue powder obtained from dry fish scales without pre-treatment, which was calcined at 800°C [13]. These variations in bandgap values likely due to the differences in sample preparation and elemental composition. For example, the tilapia study linked the blue color of dry samples (which lacked boiling pre-treatment) to higher concentrations of Na, Cl, S, and Mn. In contrast, our results suggest that surface effects, particularly air exposure during calcination, are key factors driving the observed color and bandgap differences between the white and gray powders rather than the structural variations in the bulk. This comparison reinforces the significant role that surface conditions, such as air exposure and calcination environment, have on the optical properties of HAp, even when the bulk structure remains mostly unaffected. The difference in the electronic states of HAp between the surface and bulk, as highlighted in [15], further supports this conclusion.

Although the white and gray powders show noticeable color differences, XRPD, FTIR, and SEM analyses reveal no major variations in their bulk crystal structures. This suggests that the color differences are surface-related rather than due to changes in the core crystalline properties. The white color in the outer layers of the calcined scales is likely due to full air exposure, allowing

for complete oxidation and the removal of organic matter. In contrast, the inner gray/black layers, shielded from direct air exposure, may retain carbon residues from incomplete combustion of organic materials like collagen. This could explain the color contrast between the two layers. Localized temperature variations during calcination may also contribute, with the outer layers reaching higher temperatures, ensuring complete decomposition of organic matter, while the inner layers, lacking sufficient air exposure, experience incomplete combustion, leading to the gray hue [34].

The elemental composition of HAp powder obtained from the same fish scales and calcined at 800 °C for 2 hours has been previously analyzed using EDS spectroscopy [14]. The results confirmed that, after calcination, the major elements were calcium, phosphorus, and oxygen, with minor contributions from other trace elements such as magnesium and sodium. However, in the earlier study [14], all the calcined scales were combined, causing the white fraction to be masked by the gray fraction, which yielded an overall gray appearance. Only through the controlled separation of fully exposed and partially shielded scales in the present study was the role of air exposure in color formation definitively identified. In the earlier work, the gray-colored HAp powder exhibited approximately 3.8% residual carbon, indicating that some organic remnants remained in the sample—possibly attributable to reduced air contact during calcination [14].

While the lab-based X-ray diffraction provides useful insights into the bulk crystal structure, it is limited in detecting fine details like oxygen vacancies or other surface defects. High-resolution methods, such as synchrotron X-ray or neutron diffraction, would offer better sensitivity to light elements like oxygen and could give a clearer picture of structural defects responsible for the observed bandgap narrowing. These advanced techniques could help confirm whether oxygen deficiencies or other defects are influencing the surface properties, giving us a deeper understanding of the material's electronic and optical behavior.

5. Conclusion

This research highlights the critical impact of surface effects on the optical properties of hydroxyapatite (HAp) powders extracted from fish scales. Structural analysis confirms that both the white and gray powders crystallize in the hexagonal HAp structure along with a minor Mg-whitlockite impurity, indicating that the bulk crystalline structure remains unchanged despite variations in air exposure. Although the gray powder may retain slightly more residual carbon, Rietveld refinements confirm no significant deviation in space group or lattice parameters. These results suggest that air exposure primarily affects surface properties—particularly those linked to optical characteristics—rather than inducing detectable changes in the bulk structure of the HAp. UV-Vis spectroscopy shows bandgap values of 3.99 eV for the white powder and 3.87 eV for the gray powder. These values, while lower than those typically reported for defect-free HAp (5–6 eV), align with previously reported bandgaps for HAp containing surface defects. This suggests possible semiconducting behavior in the extracted HAp, influenced by surface phenomena rather than changes in the bulk structure. These findings can contribute to a deeper understanding of how calcination conditions impact the optical, surface and structural properties of biogenic HAp, which has important implications for its use in biomedical applications and environmental remediation, where surface characteristics play a critical role in performance.

Article Information Form

Acknowledgments
The author would like to express sincere thanks to Kocamanlar Seafood for providing the fish scales used in this study and Tabii Soğuk Hava Depoculuk Limited Co. for their financial support.

Funding
The author has no received any financial support for the research, authorship or publication of this study.

The Declaration of Conflict of Interest/ Common Interest

No conflict of interest or common interest has been declared by the author.

The Declaration of Ethics Committee Approval

This study does not require ethics committee permission or any special permission.

The Declaration of Research and Publication Ethics

The author of the paper declares that she complies with the scientific, ethical and quotation rules of SAUJS in all processes of the paper and affirms that no falsification has been made on the data collected. In addition, the author declares that Sakarya University Journal of Science and its editorial board have no responsibility for any ethical violations that may be encountered, and that this study has not been evaluated in any academic publication environment other than Sakarya University Journal of Science.

References

[1] P. W. Brown, B. Constantz, Hydroxyapatite and related materials, USA:CRC press Boca Raton, 1994.

[2] H. Cölfen, "A crystal-clear view," Nature Materials, vol. 9, no. 12, pp. 960–961, 2010.

[3] S. F. Jackson, J. T. Randall, "The fine structure of bone," Nature, vol. 178, no. 4537, p. 798, 1956.

[4] R. Murugan, S. Ramakrishna, "Development of nanocomposites for bone grafting," Composites Science and Technology, vol. 65, no. 15, pp. 2385–2406, 2005.

[5] N. Eliaz, N. Metoki, "Calcium phosphate bioceramics: A review of their history, structure, properties, coating technologies and biomedical applications.," Materials (Basel, Switzerland), vol. 10, no. 4, 2017.

[6] A. S. Posner, A. Perloff, A. F. Diorio, "Refinement of the hydroxyapatite structure," Acta Crystallogr., vol. 11, no. 4, pp. 308–309, 1958.

[7] J. C. Elliott, P. E. Mackie, R. A. Young, "Monoclinic hydroxyapatite," Science, vol. 180, no. 4090, pp. 1055–1057, 1973.

[8] G. Ma, X. Y. Liu, "Hydroxyapatite: hexagonal or monoclinic?," Crystal Growth & Design, vol. 9, no. 7, pp. 2991–2994, Jul. 2009.

[9] M. Sadat-Shojai, M.-T. Khorasani, E. Dinpanah-Khoshdargi, A. Jamshidi, "Synthesis methods for nanosized hydroxyapatite with diverse structures," Acta Biomaterials, vol. 9, no. 8, pp. 7591–7621, 2013.

[10] P. Arokiasamy, M. M. A. B Abdullah, S. Z. Abd Rahim, S. Luhar, A. V. Sandu, N. H. Jamil, M. Nabiałek, "Synthesis methods of hydroxyapatite from natural sources: A review," Ceramics International, vol. 48, no. 11, pp. 14959–14979, 2022.

[11] N. A. S. Mohd Pu'ad, P. Koshy, H. Z. Abdullah, M. I. Idris, T. C. Lee, "Syntheses of hydroxyapatite from natural sources," Heliyon, vol. 5, no. 5, p. e01588, 2019.

[12] V.-R. Maria, D. A. Navarrete, D. Arcos, Biomimetic Nanoceramics in Clinical Use: From Materials to Applications. Cambridge: Royal Society of Chemistry, 2008.

[13] T. Eknapakul, S. Kuimalee, W. Sailuam, S. Daengsakul, N. Tanapongpisit, P. Laohana, W. Saenrang, A. Bootchanont, A. Khamkongkaeo, R. Yimnirun, "Impacts of pre-treatment methods on the morphology, crystal structure, and defects formation of hydroxyapatite extracted from Nile tilapia scales," RSC Advances, vol. 14, no. 7, pp. 4614–4622, 2024.

[14] H. E. Okur, "Rietveld refinement-based structural analysis of biogenic hydroxyapatite and its PVA composite for dye removal," Mater. Today Commun., vol. 43, p. 111723, 2025

[15] G. Rosenman, D. Aronov, L. Oster, "Photoluminescence and surface photovoltage spectroscopy studies of hydroxyapatite nano-Bio-ceramics," Journal of Luminescence, vol. 122–123, pp. 936–938, 2007.

[16] K. Matsunaga, A. Kuwabara, "First-principles study of vacancy formation in hydroxyapatite," Physical Review B, vol. 75, no. 1, p. 14102, 2007.

[17] L. Calderin, M. J. Stott, A. Rubio, "Electronic and crystallographic structure of apatites," Physical Review. B, vol. 67, no. 13, p. 134106, 2003.

[18] P. Rulis, L. Ouyang, W. Y. Ching, "Electronic structure and bonding in calcium apatite crystals: Hydroxyapatite, fluorapatite, chlorapatite, and bromapatite," Physical Review B, vol. 70, no. 15, p. 155104, 2004.

[19] L. A. Avakyan, E. V Paramonova, J. Coutinho, S. Oberg, V. S. Bystrov, L. A. Bugaev, "Optoelectronics and defect levels in hydroxyapatite by first-principles," Journal of Chemical Physics, vol. 148, no. 15, 2018.

[20] K. Kaviyarasu, A. Mariappan, K. Neyvasagam, A. Ayeshamariam, P. Pandi, R. R. Palanichamy, C. Gopinathan, G. T. Mola, M. Maaza "Photocatalytic performance and antimicrobial activities of HAp-TiO_2 nanocomposite thin films by sol-gel method," Surfaces and Interfaces, vol. 6, pp. 247–255, 2017.

[21] M. Tsukada, M. Wakamura, N. Yoshida, T. Watanabe, "Band gap and photocatalytic properties of Ti-substituted hydroxyapatite: Comparison with anatase-TiO_2," J. Mol. Catal. A-Chemical, vol. 338, no. 1–2, pp. 18–23, 2011.

[22] V. S. Bystrov, E. Paramonova, L. Avakyan, J. Coutinho, N. Bulina, "Simulation and computer study of structures and physical properties of hydroxyapatite with various defects,"Nanomaterials" vol. 11, no. 10, 2021,

[23] V. S. Bystrov, J. Coutinho, A. V. Bystrova, D. Y. Dekhtyar, R. C. Pullar, A. Poronin, A. Palcevskis, A. Dindune, B. Alkan, B. C. Durucan, E. V. Paramonova, "Computational study of hydroxyapatite structures, properties and defects," J. Phys. D. Appl. Phys., vol. 48, no. 19, pp. 195302, 2015

[24] R. Rial, M. Gonzalez-Durruthy, Z. Liu, J. M. Ruso, "Advanced materials based on nanosized hydroxyapatite," Molecules, vol. 26, no. 11, 2021

[25] A. C. Larson, R. Von Dreele, "General Structure Analysis System (GSAS)," Los Alamos National. Laboratory Rep. LAUR, pp. 86–748, 2004.

[26] P. Thompson, D. E. Cox, J. B. Hastings, "Rietveld refinement of Debye-Scherrer synchrotron X-ray data from A1203," Journal of Applied Crystallography, vol. 20, no. 2, pp. 79–83, 1987.

[27] J. Laugier, B. Bochu, "LMGP-suite of programs for the interpretation of X-ray experiments." ENSP/Laboratoire des Matériaux et du Génie Physique, 1999.

[28] K. Sudarsanan, R. A. Young, "Significant precision in crystal structural details. Holly Springs hydroxyapatite," Acta Crystallographica Section B, vol. 25, no. 8, pp. 1534–1543, 1969.

[29] R. Gopal, C. Calvo, J. Ito, W. K. Sabine, "Crystal structure of synthetic Mg-Whitlockite, $Ca_{18}Mg_2H_2(PO_4)_{14}$," Canadian Journal of Chemistry, vol. 52, no. 7, pp. 1155–1164, 1974.

[30] E. Hosseinzadeh, M. Davarpanah, N. H. Nemati, S. A. Tavakoli, "Fabrication of a hard tissue replacement using natural

hydroxyapatite derived from bovine bones by thermal decomposition method," International Journal of Organ Transplantation Medicine, vol. 5, no. 1, pp. 23–31, 2014.

[31] R. X. Sun, Y. Lv, Y. R. Niu, X. H. Zhao, D. S. Cao, J. Tang, J., K. Z. Chen, "Physicochemical and biological properties of bovine-derived porous hydroxyapatite/collagen composite and its hydroxyapatite powders," Ceram. Int., vol. 43, no. 18, pp. 16792–16798, 2017.

[32] J. M. Stutman, J. D. Termine, A. S. Posner, "Vibrational spectra and structure of the phosphate ion in some calcium phosphates," Trans. N. Y. Academic Science, vol. 27, no. 6 Series II, pp. 669–675, 1965.

[33] J. Tauc, "Optical Properties and Electronic Structure of Amorphous Semiconductors," in Optical Properties of Solids, S. Nudelman and S. S. Mitra, Eds., Boston, MA: Springer US, 1969, pp. 123–136.

[34] M. Šupová, "Problems associated with the assessment of organic impurities in bioapatites isolated from animal sources: A review," Journal of the Australian Ceramic Society, vol. 58, no. 1, pp. 227–247, 2022.